UNIVERSIDAD DE CHILE
FACULTAD DE CIENCIAS FÍSICAS Y MATEMÁTICAS
DEPARTAMENTO DE INGENIERIA ELECTRICA

INSTRUMENTATION DEVELOPMENT OF INNOVATIVE RADIO-DEVICES TO IMPROVE THE COMING CYCLES OF RADIO ASTRONOMY OBSERVATIONS

TESIS PARA OPTAR AL GRADO DE DOCTOR EN INGENIERÍA ELÉCTRICA
EN COTUTELA CON LA UNIVERSIDAD DE GRONINGEN

DANIEL ARTURO MONTOFRÉ POBLETE

PROFESOR GUÍA:
FAUSTO PATRICIO MENA MENA

PROFESOR CO-GUÍA:
ANDREY MIKHAILOVICH BARYSHEV

MIEMBROS DE LA COMISIÓN:
ERNEST MICHAEL
ALVARO GONZALEZ GARCIA
SHINICHIRO ASAYAMA
KARINA CAPUTI

Este trabajo ha sido parcialmente financiado por Conicyt mediante los fondos Basal AFB-170002 y CONICYT-PCHA/DoctoradoNacional/2015-23190035

SANTIAGO DE CHILE
2020

RESUMEN DE LA TESIS PARA OPTAR AL GRADO DE
DOCTOR EN INGENIERÍA ELÉCTRICA EN DOBLE
TITULACIÓN CON LA UNIVERSIDAD DE GRONINGEN
POR: DANIEL ARTURO MONTOFRÉ POBLETE
FECHA: 2020
PROF. GUÍA: FAUSTO PRATICIO MENA MENA
PROF. CO-GUÍA: ANDREY MIKHAILOVICH BARYSHEV

INSTRUMENTATION DEVELOPMENT OF INNOVATIVE RADIO-DEVICES TO IMPROVE THE COMING CYCLES OF RADIO ASTRONOMY OBSERVATIONS

La radio astronomía representa una de las herramientas más útiles para investigar objetos celestiales tales como emisiones sicrontrónicas de cuásares, nubes moleculares del medio interestelar y eventos de horizonte de agujeros negros. Todo esto se debe, principalmente, a la gran sensibilidad que los receptores astronómicos pueden alcanzar y la gran resolución angular que puede ser lograda mediante técnicas interferométricas. Sin embargo, la radio astronomía no está exenta de limitaciones que le impiden desplegar su máxima capacidad en términos de resolución. Las fluctuaciones de fase atmosférica, inducidas primordialmente por corrientes turbulentas, son el principal responsable. No corregir dichas fluctuaciones impedirá que el máximo potencial de la radio astronomía pueda ser alcanzado.

En este trabajo de tesis, una novedosa solución para sortear los inconvenientes relacionados a las fluctuaciones de fase en observaciones de alta frecuencia es presentado. El telescopio ALMA ha sido seleccionado como objetivo. La idea es utilizar un sistema óptico externo a temperatura ambiente el cual permitirá iluminar un receptor de baja y uno de alta frecuencia, simultáneamente. De este modo, la solución para la fluctuación de fase podrá ser transferida desde la baja hacia la alta frecuencia, permitiendo así extender las líneas de bases en observaciones interferométricas a altas frecuencias.

RESUMEN DE LA TESIS PARA OPTAR AL GRADO DE
DOCTOR EN INGENIERÍA ELÉCTRICA EN DOBLE
TITULACIÓN CON LA UNIVERSIDAD DE GRONINGEN
POR: DANIEL ARTURO MONTOFRÉ POBLETE
FECHA: 2020
PROF. GUÍA: FAUSTO PRATICIO MENA MENA
PROF. CO-GUÍA: ANDREY MIKHAILOVICH BARYSHEV

INSTRUMENTATION DEVELOPMENT OF INNOVATIVE RADIO-DEVICES TO IMPROVE THE COMING CYCLES OF RADIO ASTRONOMY OBSERVATIONS

Radio astronomy represents one of the most useful tools for investigating celestial objects such as psychrontronic emissions from quasar, molecular clouds in the interstellar medium, and a black hole event horizon. All this is possible due to the great sensitivity that astronomical receivers can achieve, and the high angular resolution that can be reached using interferometric techniques. However, despite the great effort made, radio astronomy is not exempt of limitations that prevent it from deploying its maximum capability in terms of resolution. Atmospheric phase fluctuations, mainly induced by turbulent currents, are primarily responsible. Failure to correct these phase fluctuations will impede that the maximum potential of radio astronomy can be realized.

In this thesis work, a novel solution to solve the drawbacks related to phase fluctuations in high frequency observations is presented. The ALMA telescope has been selected as a target. The idea is to use an external optical system at room temperature which can illuminate a low and a high frequency receiver, simultaneously. In this way, the solution for the phase fluctuation can be transferred from low to high frequency, thus, extending the maximum baseline for interferometric observations at high frequencies.

Dedicado a

Todos aquellos que creyeron en mi durante todo este proceso. En especial a quienes, sin entender un ápice de lo que hacía, fueron quienes más devotamente depositaron su fe en mi persona y mi trabajo. Les agradezco de todo corazón.

Especial agradecimientos a mi madre, quien debió sacrificar parte de su vida y felicidad para poder educarme. Tampoco quiero dejar de lado a mi padre, quien con sus excentricidades me ha dejado claro los caminos que hay -y especialmente los que no hay- que recorrer en la vida.

Agradecimientos

Lo primero que se me viene a la mente es el día que comencé a pensar que quería hacer un doctorado, en esos momentos recibí todo el apoyo de mi familia, quienes me dieron apoyo económico y emocional y, a mis profesores de la USACH quienes complementaron el apoyo familiar con su experiencia académica y profesional. A todos ustedes, madre, Samuel, Dinesh, Juliano es a quienes agradezco en primera instancaia, ya que sus esfuerzos hicieron que todo esto pudiese ponerse en marcha.

Ya iniciado el semestre académico del año 2015, tuve la oportunidad de conocer a maravillosos seres humanos que pasaron de ser compañeros de curso a buenos amigos y colegas. Les estoy eternamente agradecidos a todos ustedes Rocío, Taky, Perroni Alvear, Ignacio, Javier (the sapo), Pelaito, Nicolas (el capitán), Pi-kingo, Gonzalin, Alex, Orteguita, Sebin. Haberlos conocido y haber entablado amistad con ustedes hizo que mi paso por Beauchef fuese muchísimo más que solo un asunto académico. Nuevamente, gracias por todos aquellos lindos momentos.

Durante mi paso por Groningen tuve la oportunidad de hacer muchos amigos, los cuales me enseñaron cosas que me eran desconocidas, las cuales me ha permitido convertirme en el hombre que actualmente tiene el agrado de escribir estas palabras. Sobre todo aquellos amigos que hice en el instituto de astronomía y, en especial, a mis compañeros de oficina que, mediante consejos y conversaciones, pudieron ayudarme en una infinidad de cosas. Infinitas gracias a todos Justine, Stephan, Rodrigo (el gringo), Aitor, Rafael, David, Maha, Luiz, Lisa, Ferdinard (alemansito), Bleen, Elina, Jorrit, Ajinkya, Davide, William (Jey), Olmito (el gitano), Katya, Enrico, Bram.

Para finalizar, quisiera agradecer a Ronald H., quien me mostró que la ciencia es un juego que debe ser disfrutado. A la hora de hablar de trabajo duro, las enseñanzas de Andrey Kh. fueron de las mejores. Y, si tuviese que elegir a alguien por quien siento admiración, ese puesto sería ocupado por Shin'ichiro quien mediante sus simples consejos me ayudo a resolver problemas que parecían no tener solución. Tampoco puedo dejar fuera de esto a Nico R. quien se hizo cargo de mi tutela en un momento de alta turbulencia e incertidumbre. Finalmente, no puedo sino terminar esta lista con las dos personas quienes oficialmente estuvieron a cargo de todo esto, Patricio y Andrey. Ellos me brindaron consejos muy valiosos y conocimiento que no puede ser hallado en libros ni la internet. Patricio, gracias por enseñarme que la responsabilidad y la constancia es algo fundamental en la carrera científica. Andrey, gracias por mostrarme que es importante elegir bien tus palabras antes de verbalizar alguna idea.

Table of Contents

List of Tables

List of Figures

Chapter 1

Introduction

This chapter starts with a brief introduction of radio astronomy, its importance, and the technological tools that make the observation of radio waves possible. Currently, radio astronomy is one of the most useful tools to study the cold and early universe. This is mainly due to the high sensitivity that the receiver can reach, and the high angular resolution that can be achieved. On one hand, the high level of sensitivity has been reached due to the continuous development in solid-state physics and radio engineer. On the other hand, high angular resolution is possible to achieve by means of interferometric measurements.

Next, the sources of noise -mainly phase noise due to atmospheric distortion- that limit the usage of radio interferometry observations will be reviewed. Not correcting this phase noise leads to a limitation in the maximum achievable resolution of an interferometer array, and thus, the full potential of radio astronomy would be unexploited. Therefore, the techniques developed to mitigate these effects over the phase stability, and their limitations, are subsequently discussed.

Besides elaborating on new calibration techniques in order to improve the phase stability, one novel idea is proposed. This is the development of dual-frequency receivers. Since phase noise correlates between observation bands (as it will be explained later on) due to its dependence only on the structure of the atmosphere through the line of sight of each telescope in a baseline, phase correction can be obtained at low-frequencies and then transferred to a high-frequency band. Finally, experimental evidence of the efficiency of this method using ALMA -currently, the biggest radio astronomy project on Earth- is presented. Science drivers for ALMA will be also discussed. Nevertheless, those are in general valid for any radio astronomy measurements, no matter the instrument used.

Throughout this thesis work, when the term "radio astronomy" (or radio waves) is used, it refers to electromagnetic radiation whose wavelength spectrum lies on both the radio band and the millimeter/submillimeter band. It is important to highlight this point here because our intention is keeping the nomenclature as clear as possible in order to avoid confusing the reader.

1.1 Radio astronomy and radio-astronomical instrumentation

The discovery of radio emission from the Milky Way by Karl Jansky in 1930s [1] is considered as the beginning of radio astronomy. This new observation window obtained its indisputable importance in the 1950s with the first observation of the 21-cm hydrogen line [2]. Nowadays, radio astronomy represents one key tool to observe celestial objects such as pulsar beams, synchrotronic emission of quasars, molecular clouds of the interstellar medium and the event horizon of black holes.

In the last decades, the millimeter/submillimeter wavelengths spectrum have been uncovered due to the continuum effort of instrumentation scientists to improve the technology of the receivers. Many areas have been favoured such as atmospheric physics, medical applications or remote sensing [3–5]. However, astronomy has been one of the most benefited fields since astronomical observation made in this part of the spectrum has allowed studying many unexplored areas of astrophysics, e.g. cosmic microwave background (CMB), formation and evolution of galaxies, protoplanetary disk survey, gravitational lensing, and black-hole physics. Moreover, many important molecules (including but not limited to hydrogen, carbon and oxygen based) have strong absorption/emission lines in the millimeter/submillimeter spectrum. The study of these lines (unseen in other wavelength spectra) has allowed astronomers to enhance our grasp about the physics and chemistry of the early stage of the universe.

1.1.1 Radiation processes and radio observations

Radio astronomy addresses a broad range of phenomena produced by sources of different nature. These sources can be classified into three main categories, as follows.

- **Black-body source:** it corresponds to thermal emission and depends exclusively on the physical temperature of the source. An example of this type of emission is the Cosmic Microwave Background (CMB), whose temperature is ~ 2.74 K.
- **Continuum source:** this type of emission comes from high-energy charged particles deaccelerating and releasing energy as electromagnetic radiation (Bremsstrahlung). Another way to produce this type of emission is by electrons moving in the presence of a strong magnetic field (Synchroton). An example of this emission is the strong radiation beam generated by quasars.
- **Spectral line source:** at certain specific frequencies, the resonance mechanism of atoms and molecules generates this type of emission. As an example, consider the spectral line generated by neutral atomic hydrogen at 1420.405 MHz, which results from the transition between two energy levels of the atom.

It is important to mention that some celestial objects can radiate simultaneously in many of the afore-mentioned mechanisms. Neutron stars are a very good example since they behave as strong X-ray sources by thermal emission and, at the same time, they behave as non-thermal radio sources (pulsars).

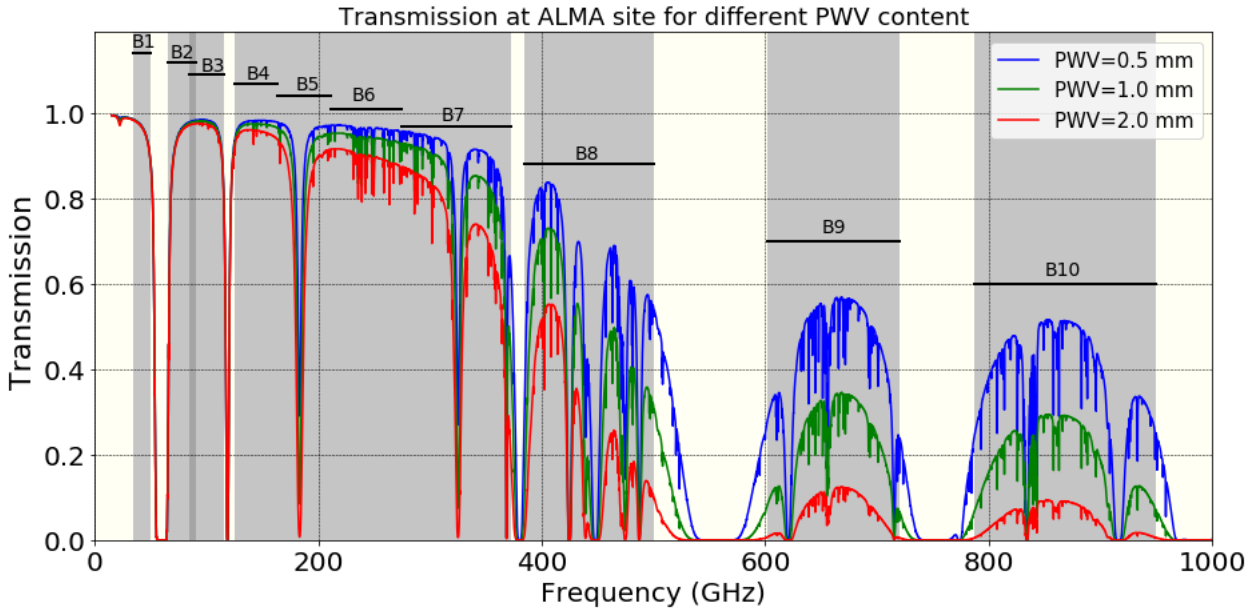

Figure 1.1: ***Atmospheric windows at Chajnantor.***
Below 30 GHz the absorption is dominated by the weak transition of H_20 at 22.2 GHz, and rarely exceeds 20% in the zenith direction [7]. The oxygen bands in the 53-67 GHz band are considerably stronger, and no astronomical observation can be made from the ground in this band. A similar effect happens with the isolated 118 GHz O_2 line, which makes observations impossible in the 116-120 GHz band. There is a series of strong water vapor lines at 183, 325, 380, 448, 475, 557, 621, 752, 988 and 1097 GHz and higher. Observations can be made in the windows (as indicated by the black bars) between these lines at dry locations. This is where the different ALMA observing Bands have been defined. Data retrieved from APEX web-page: *http://www.apex-telescope.org/sites/chajnantor/atmosphere/transpwv/*

Observations from Earth

One of the main limitations to perform radio astronomy observation from ground base facilities is the low transparency of this spectrum at sea level. Earth's atmosphere is responsible for the absorption of a big portion of the radiation, where the main absorbing agent corresponds to water vapor and molecular oxygen. This issue can be mitigated if the instrument is located in a place with very dry air conditions and high altitudes. These conditions are satisfied in sites like the Chajnantor plateau, a desert plain located 5000 m over the sea level in the driest place in the world, the Atacama Desert in the north of Chile. The Chajnantor plateau represents one of the best places in the world to take astronomy observation in the millimeter/submillimeter spectrum due to its high transmission [6]. Figure 1.1 shows the transmission as a function of frequency at the Chajnantor plateau for different concentrations of precipitable water vapor (PWV) content.

Cosmic signals

The strength of the electromagnetic waves received from a discrete celestial source is expressed as the flux density and is measured in watts per square meter per hertz ($\mathrm{W\,m^{-2}\,Hz^{-1}}$). The unit most commonly used in astronomy for flux density is the jansky Jy; $1\,\mathrm{Jy} = 10^{-26}\mathrm{W\,m^{-2}\,Hz^{-1}}$. In producing an image of a radio source, the desired quantity is the power flux density emitted per unit solid angle subtended by the radiating surface, which is

measured in units of $\mathrm{W\,m^{-2}\,Hz^{-1}\,sr^{-1}}$. This quantity is variously referred to as the intensity, specific intensity, or brightness of the source.

The electric responses (or voltages) induced in a radio receiver system by the electromagnetic radiation coming from a cosmic source are generally referred to as signals. Nonetheless, these signals do not contain information as usually understood in an engineering sense. The information they carry on comes -almost universally- in the form of Gaussian random noise. In other words, the induced voltage in the receiving system as a function of time can be described as a package of stochastic short pulses that when combined take a waveform whose amplitude is described by Gaussian distribution. If a bandwidth $\Delta\nu$ is used, the envelope of the waveform has the appearance of random variations with a timescale of the order $1/\Delta\nu$. For most of the radio sources, this characteristic of the signal is invariant in timescales of minutes or hours. However, it is important to note that there are radio sources whose nature do not follow this characteristic, for instance, bear in mind a signal coming from pulsars.

Reception of cosmic signals

Radio astronomy receivers (explained in the following subsection) are not free of noise. As electromagnetic radiation is detected by the receiver, the generated voltage must pass through an electronic chain. This process -of course- is not free of noise since some amount will be added to the system. A good quality receiver makes this noise level as little as possible. However, quantum mechanics laws impose a limit to the minimum achievable noise level [8]. The total noise level in a receiver system can be conveniently associated with a system noise temperature T_S. This relation between noise and temperature comes from the fact that resistors intrinsically generate noise, and the level of this noise per unit bandwidth is proportional to the physical temperature. This way to describe the noise level of a receiver has a practical advantage since typical radio signals that astronomers deal with are quite faint. Therefore, they can be conveniently calibrated using the noise generated by a cold/hot resistive load as a reference.

The received power P_{in} delivered by an antenna, with collecting area A, to a matched load in a bandwidth $\Delta\nu$, from a randomly polarized source of flux density S, assumed to be small compared to the beam width, is given by

$$P_{in} = \frac{1}{2} SA\Delta\nu \equiv k_B T \Delta\nu \tag{1.1}$$

where k_B corresponds to the Boltzmann constant. The factor 1/2 in the middle term of equation 1.1 takes account of the fact that the antenna responds to only one-half the power in the randomly polarized wave. The right term in equation 1.1 is just a convenient way to express the received noise power, P_{in}, in terms of an effective temperature T. Bearing in mind this relationship between power and temperature, the noise power in a receiver system can be specified in terms of system temperature T_S. Analogically, the term antenna temperature T_A refers to the component of the power received by the antenna that results from a cosmic source under study. Those powers can be related to a system/antenna temperature by

$$P_S = kT_S\Delta\nu \tag{1.2}$$

and

$$P_A = kT_A\Delta\nu, \tag{1.3}$$

respectively.

The ratio of the signal power from a source to the power in the receiving amplifier is T_A/T_S. Because of the random nature of the signal and noise (described above), measurements of the power level made at time intervals separated by $2\Delta\nu^{-1}$ can be considered independent [9]. A measurement in which the signal level is averaged for a time τ contains approximately $2\Delta\nu\tau$ independent samples. The signal-to-noise (SNR) level at the output of a power measuring device attached to the receiver is increased in proportion to the square root of the number of independent samples, and takes the form

$$SNR = C\frac{T_A}{T_S}\sqrt{\Delta\nu\tau}. \tag{1.4}$$

with $C \geq 1$. Typical values for radio astronomical measurements of $\Delta\nu$ and τ are of the order 1 GHz and 6 hrs (considering the capabilities of current radio-receivers). This results in a value of 4×10^6 for the factor $\sqrt{\Delta\nu\tau}$. As a consequence, it is possible to detect a signal for which the power level is less than 10^{-6} times the system noise (considering that a SNR level of 4 is good enough for that specific astronomical purpose). This capability of radio astronomy receivers to detect such faint sources makes them the ideal tool to study the cold and early universe.

1.1.2 Radio astronomy receivers

As it occurs in optical astronomy, radio astronomy also has as instrumental goals increasing the resolution and the sensitivity of the detectors. Nevertheless, the feature that makes radio astronomy distinguishable from its optical counterpart is the fact that the electromagnetic radiation collected by the telescope is previously amplified and processed before being stored. This process is called detection and there are different ways in which radio waves can be detected.

Direct detection

Direct detection corresponds to the measurement of the total power coming from a celestial radio frequency (RF) source. For this detection mode, bolometers are the most used device. There are different technologies using the bolometric operation principle, among them, the best known are neutron transmutation doped germanium (NTD-Ge), transition edge sensor (TES), and microwave kinetic inductance detectors (MKIDS) [10].

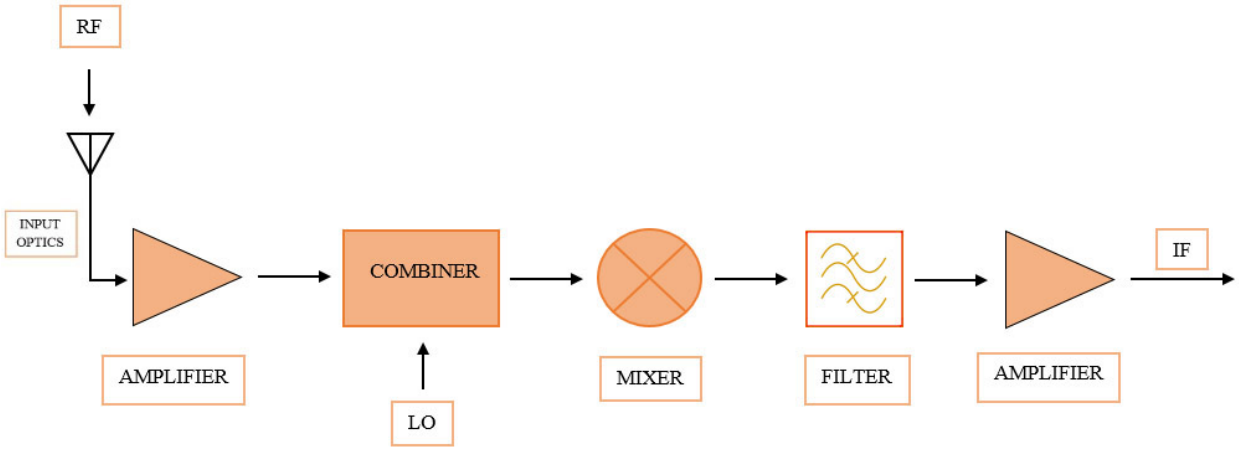

Figure 1.2: ***Types of heterodyne receivers***

The RF signal is collected by the input optics, amplified by a low noise amplifier, and then combined with the local oscillator. The combined beam then reaches the mixer, where the spectral components are down-converted. The IF signal is filtered an then amplified again before it is analyzed by the back-end spectrometer. The LO source must also be stabilized by a phase reference system.

The operation principle of direct detectors is described as follows. The electromagnetic radiation coming from the sky is collected by a reflector antenna and then transferred to a transmission line, e.g. a feed horn. Once the radiation is highly focused, it strikes upon a thin film of a photosensitive device with a non-linear I-V curve. The device is designed to either change its electrical resistance or inducing an additional electrical current. If a constant bias current is additionally supplied across the film, then the input RF radiation beam will change this bias current. The current variation across the thin film is proportional to the power of the detected radiation. The frequency band over which the radiation can be properly absorbed is limited by many factors, among them, the most significant contributions come from the optical properties of the thin film and the optical system used to focus the radiation. This frequency band is commonly called the instantaneous bandwidth.

Direct detectors can be very efficient in detecting radiation due to the high sensitivity that they can reach. However, given a certain bandwidth $\Delta\nu$, they are unable to distinguish between signals with equal power but at different frequencies within $\Delta\nu$. This feature limits its use as spectrometers, nonetheless, this issue can be overcome by using a set of narrow band-pass filters in front of it. Due to the nature of their working principle, direct detectors are unable to resolve the phase of the detected radiation. This makes them unsuitable for being used in radio interferometric observations since interferometry is based on combination of signals, where the relative phase is preserved (this will be discussed in more detail in the next sections).

Heterodyne detection

Heterodyne detection allows radio interferometric observation on Earth possible due to its high frequency resolution and sensitivity, and, more importantly, its capacity for preserving the phase of the input RF signal. The mixing principle to downconvert the RF signal requires

the integration of several electronics components into the heterodyne receiver system [11, 12]. Figure 1.2 shows a typical block-diagram of a heterodyne receiver with all the vital components.

As it was afore mentioned, heterodyne detection is the process of measuring power and resolving the phase of the incoming RF celestial source. To do so, the input RF signal, with a frequency F_{RF}, is combined with a strong monochromatic local oscillator (LO), with a frequency F_{LO}. The signals are combined using a device called mixer, which has a non-linear I-V curve and, due to this non-linearity, many frequencies are generated in the mixer. The generated frequencies are described by

$$|m \times F_{RF} - n \times F_{LO}| \tag{1.5}$$

where m and n are integers whose values depend on the type of non-linearity and response time of the mixer device, so that, only a limited number of combinations for m and n are allowed. In the most fundamental case, we are only interested in the case $m = n = 1$, so the mixer behaves as a frequency conversion device whose desired output, called intermediate frequency (IF), is a signal with a frequency $F_{IF} = F_{RF} - F_{LO}$. At this point is important to highlight that frequencies for other combinations of m and n are also generated by the mixer. Those frequencies are normally not wanted, so they must be eliminated using an adequate band-pass filter.

When F_{LO} is chosen to be close to F_{RF}, the input RF signal is converted to an IF signal with a much lower frequency that preserves the phase information. This working principle can also be extended for an input RF signal consisting of a continuous range of frequencies. Therefore, the output IF spectrum will have an amplitude spectrum proportional to the input RF signal but shifted down in frequency by F_{LO}, and the same relative phase for the whole bandwidth. This process is known as downconversion and it is one of the key technology tools that makes interferometry at millimeter/submillimeter wavelengths possible.

In practice, the IF output signal at a frequency F_{IF} may originate from a signal at either of the two frequencies

$$F_{RF} = F_{LO} \pm F_{IF}. \tag{1.6}$$

In other words, there are two bands of signal frequencies, placed on either side of the LO frequency. The band with higher frequencies is conventionally referred to as the upper sideband, while the band with lower frequencies is referred to as the lower sideband. There are different ways to deal with the upper and lower sidebands, those are schematically represented in figure 1.3.

1.2 Interferometry in astronomy

The main difference between interferometric measurements and direct imaging – e.g. an optical telescope equipped with a CCD sensor- is that interferometry takes samples of the

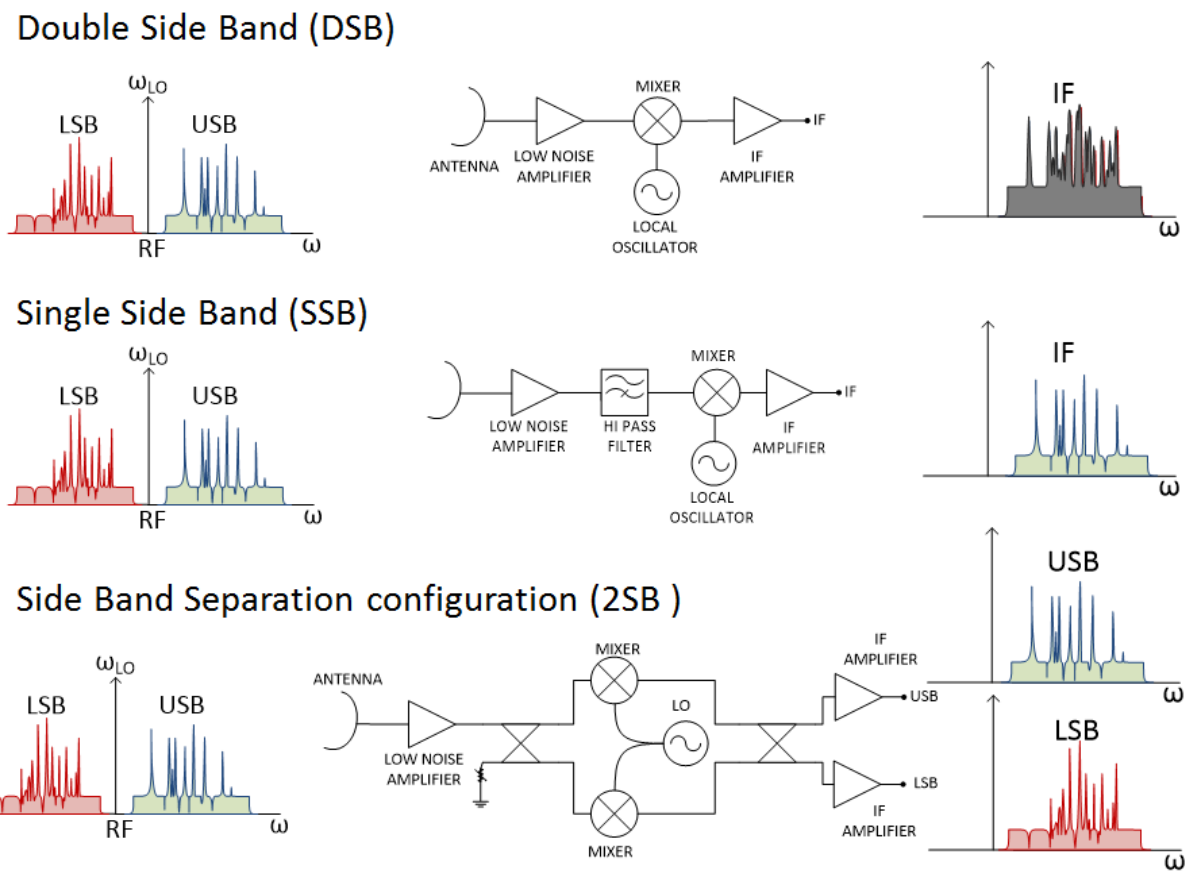

Figure 1.3: ***Types of heterodyne receivers***

(Top) A receiver system which responds to both bands is called a double-sideband (DSB). Note that noise coming from one sideband of the detector decreases the signal-to-noise ratio of the other sideband of a heterodyne detector and, in addition, some unwanted signals could be added. (Center) A filter in front of the receiver can be used to suppress the unwanted sideband -and so- reduce the noise level. The use of such a filter makes the receiver a single-sideband (SSB) receiver system. (Down) Another way to improve the sensitivity of a DSB receiver can be achieved using two heterodyne DSB mixers, this gives rise to the so-called sideband-separating receiver (2SB).

power spectrum of the sky brightness distribution. This is called visibility and is equivalent to measuring the Fourier transform of the region of the sky where the source under study is located. To do this, interferometry makes use of baselines, where each of one is, simply, a pair of antennas separated by a distance $s_{\rm i}$. Each baseline samples a single point of the power spectrum in the Fourier space, which is related to the distance $s_{\rm i}$ and the angle of position of the baseline vector. Since the interferometric resolution depends on the inverse of the distance, a short baseline will sample large-scale angular structures (or equivalently large field of view with low angular resolution), while a long baseline will sample short-scale angular structures (or equivalently small field of view with high angular resolution). By combining visibilities took from a large number of baselines, which includes short and long baselines, the Fourier space can be properly sampled (uv-plane coverage). This procedure allows an accurate reconstruction of the image by means of inverse Fourier transformation. The quality of this reconstructed image depends on how well the uv-plane is covered, i.e., how well the Fourier space is sampled in the interferometric measurement. In this section,

we will take a brief look at the fundamental concepts of interferometry and their application in astronomical observations [13].

1.2.1 Michelson stellar interferometry

The use of interferometric techniques for the observation of astrophysical objects was first proposed in 1868 by H. Fizeau in order to measure the diameter of stars [15]. Several years later, in 1891, A. Michelson measured the size of the moons of Jupiter using the technique. However, it took until the construction of the Mount Wilson Observatory in California for Fizeau's original idea to be realized, when the angular size of the photosphere of the massive star Betelgeuse was measured [16].

Figure 1.4 shows the scheme of a modern interferometric facility. The concepts here explained in the framework of interferometry are equally valid in any band of the electromagnetic spectrum. Thus, the interferometric principles apply for optical, infra-red, millimeter/submillimeter and radio waves. Nevertheless, receivers operating at different wavelengths will be ruled by different physical principles.

1.2.2 The demand for higher resolution: single dish v/s interferometer

The astronomical observation of celestial sources can be done in two modes, i.e., using a single dish telescope or an interferometer. However, interferometry offers several advantages. The main one is the higher angular resolution achievable by an interferometer. To put this in context, consider the theoretical diffraction limit (using Rayleigh criterion [14]) of a single dish telescope with a diameter D,

$$\theta_{min} = 1.22\frac{\lambda}{D}. \tag{1.7}$$

For $D = 10$ m and an operating wavelength of $\lambda = 1$ mm, the maximum achievable resolution is ~ 25 arsec. Now, consider a young stellar system in a star-forming region located at a distance of 100 pc, whose diameter is the order $\theta_{min} \sim 250$ au. The angle subtending such a system is ~ 2.5 arsec. Additionally, consider the case of a planet within the system at a distance of 25 au from the central star, such a planet would subtend an angle of ~ 0.25 arsec. At this point, using a single dish telescope to achieve that resolution will require a diameter of $D = 1$ km, which is absolutely not feasible.

This simple example illustrates the limitation of single-dish telescopes to achieve such a small angular scale. Therefore, it is mandatory to look for an alternative option in order to reach the necessary resolution. Rather than using a huge single dish, an array of the multiple smaller telescopes can be used. When combined, they can simulate a single dish telescope with the necessary size to achieve the desired resolution. This combination of smaller and linked telescopes is called interferometer. Now, the maximum achievable resolution is no longer dominated by the size of single telescopes in the interferometer, but rather the distance between them – also known as the baseline length. In the simplest case, consider an

interferometer composed of two telescopes separated by a distance B (baseline length). The maximum achievable resolution is now

$$\theta_{min} \propto \frac{\lambda}{B}. \tag{1.8}$$

As the name suggests, interferometers work using interferometry principles. To understand this, we can think in Young's two slits experiment in a screen, where the interference between wavefronts produced by each slit generates a fringe pattern, with maxima and minima of intensity. Now imagine that instead of two slits we have two telescopes forming a baseline pair, and they are receiving plane wavefronts from a celestial source (as shown in figure 1.4). The constructive interference fringes represent the space at which the signal from the telescopes can be combined coherently. On the other hand, the angular distance between fringes is analogous to the resolution that the interferometer is sensitive to. Hence, increasing the baseline length B will increase the maximum achievable resolution. This means that for an interferometer, the limiting factor of the angular resolution (for a given wavelength) is dominated by the baseline length. A more detailed discussion about the interferometry framework can be found in [17].

The use of many baseline pairs, i.e. multiple antennas forming different combinations of varied lengths, is possible. This combination of baselines, referred to as a synthesis array (explained later on in this chapter), is used to build up an image of the celestial source. Additionally, observation using separate single dish telescopes can be added to interferometric observations, providing information on large scale structures, e.g. the southern Galactic plane survey [18].

1.2.3 The uv-plane and visibility

Before discussing how interferometry is applied to astronomical observations, it is useful to define a reference frame of work which helps to clarify how the output from an interferometer is converted into an image of the sky. This reference frame is called the uv-plane and relates the coordinate system used for each telescope location with the image plane that contains the target celestial source in the sky. Figure 1.5 shows a baseline pair tracking the target celestial. Considering only one polarization, and a receiver system with a bandwidth $\Delta\nu$, an element of the source of solid angle $\Delta\Omega$ contributes a component of power

$$\frac{1}{2}A_{eff}I_\nu(x,y)\Delta\nu\Delta\Omega, \tag{1.9}$$

where A_{eff} is the effective collecting area of each telescope, and $I_\nu(x,y)$ is the brightness distribution of the source. The coordinates x and y represent right ascension and declination, respectively. The vector w points directly to the centre of the observations from the first antenna. The vectors u and v are respectively the East-West and North-South components of the projected baseline of the interferometer onto the plane of the sky. The points of this baseline are therefore located at $(0,0,0)$ and (u',v',w') in what is known as the uv-plane.

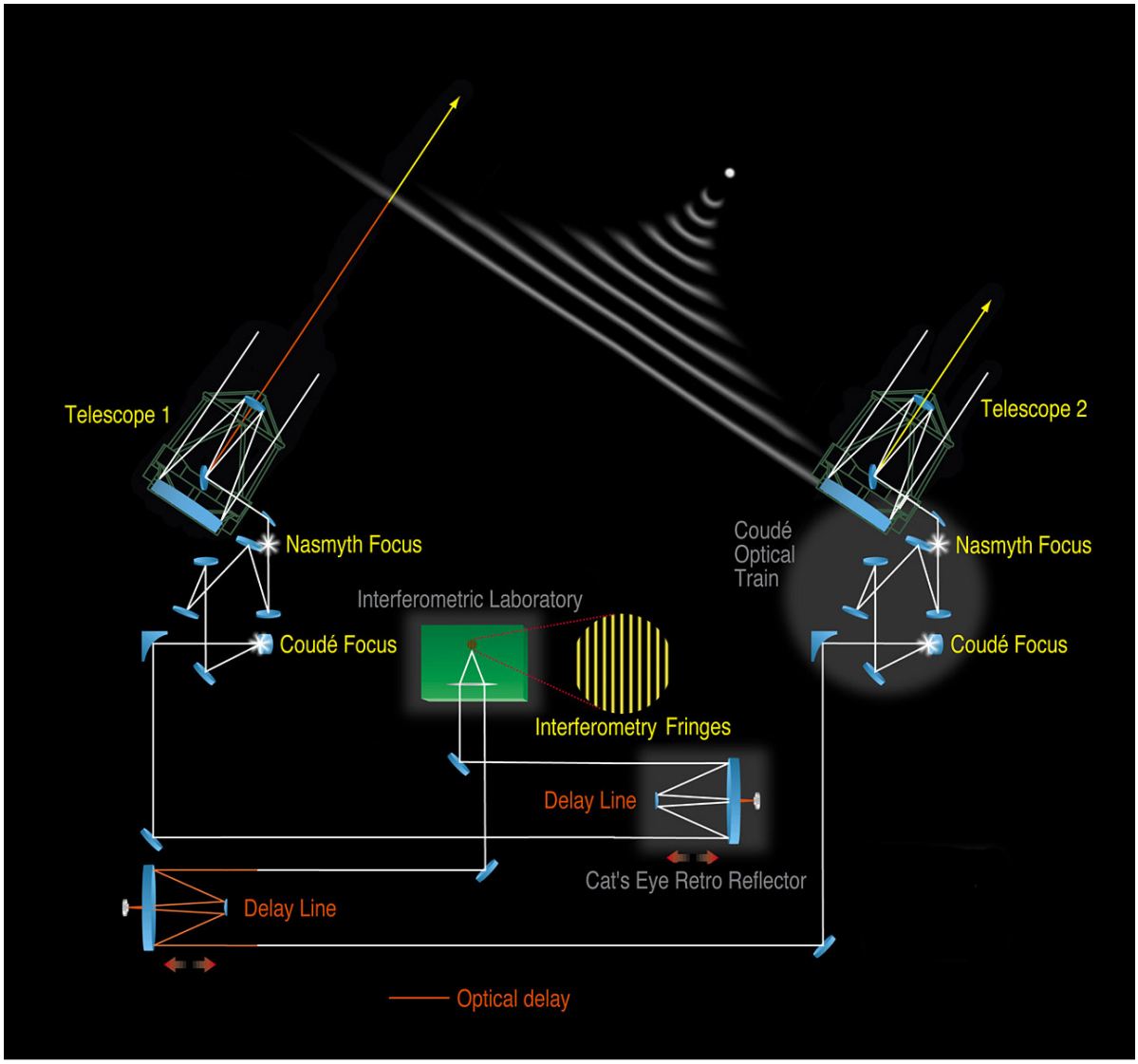

Figure 1.4: ***Schematic representation of an interferometric measurement using the Very Large Telescope (VLT).***
A plane wavefront coming from a celestial source is simultaneously detected by two telescopes. In order to produce a fringes pattern, the signal detected by each telescope must be coherently combined. This is realized by using delay lines, which are adjusted until clear fringes are generated. *This image has been taken and adapted from [14].*

1.2.4 Fringes and coherence

Astronomical observations using a single dish optical telescope take an image of the target celestial source by measuring directly its brightness distribution $I_\nu(x, y)$. However, the situation is different when an interferometer is used since $I_\nu(x, y)$ cannot be directly measured in this way. What is actually measured by an interferometer is the coherence between signals detected by each telescope in the array. This quantity is called visibility and is defined as

$$V = \frac{I_{max} - I_{min}}{I_{max} + I_{min}}, \tag{1.10}$$

where I_{max} and I_{min} correspond to the maximum and minimum of the interference pattern, respectively. The Young's two slits experiment can be used again in order to give a simple explanation of visibility. As in Young's experiment, the signal from the slits will create a constructive and destructive interference pattern on a screen if they are combined coherently. This gives a $I_{max} = 1$ and $I_{min} = 0$, which result in $V = 1$ and clear fringe pattern is created on the screen. However, in case that the distance between slits is now shifted at a certain distance where the two sets of interference patterns are out of phase with respect to each other, then $I_{max} = I_{min}$ and $V = 0$, which means that the wavefronts are combined incoherently, and fringes are not created. In other words, the generation of fringes can be used as an indicator to measure the degree of coherence between signals. Additionally, the quality of the fringes produced by an interferometer can be quantitatively described using the visibility.

A more general situation must consider the case where a more complex brightness distribution is sampled by a baseline pair. This distribution can be approximated to a set of point-like sources and, thus, the relative phase ϕ of the produced interference pattern must be considered. This phase term is related to the delay of the signal reaching each telescope and therefore provides information on the angular separation of the sampled object. In the following section, we will give a more detailed explanation of the phase of visibility. The interested reader can find a thorough analysis of this subject in [19].

1.2.5 The van Cittert-Zernike theorem

For a more detailed analysis, the visibility V is usually expressed as a complex quantity, this is, in terms of the fringe amplitude $|V|$ and the phase difference ϕ between the terms that build up the fringe pattern. The complex representation of visibility is given by

$$V = |V| \, \mathrm{e}^{-\mathrm{i}\phi} \tag{1.11}$$

It is possible to relate this quantity (measured by the telescopes that make up the interferometer) with the sky brightness distribution $I_\nu(x, y)$. This involves a transformation from xy-coordinates, on a plane in the sky, to the uv-plane coordinates. The mathematical tool that allows relating these coordinates system is the Fourier transform,

$$V(u, v) = \int\int I_\nu(x, y) \mathrm{e}^{-2\pi\mathrm{i}(ux+vy)} \mathrm{d}x\mathrm{d}y. \tag{1.12}$$

Analogically, equation 1.12 can be undergone to an inverse Fourier transformation, and so giving the desired brightness distribution of the sky,

$$I_\nu(x, y) = \int\int V(u, v) \mathrm{e}^{2\pi\mathrm{i}(ux+vy)} \mathrm{d}u\mathrm{d}v. \tag{1.13}$$

Equation 1.13 is known as the van Cittert-Zernike theorem, which simply states that the output signal of an interferometer is the Fourier transform of the sampled brightness distribution

of a celestial source on the sky [9].

A well-filled (u,v) plane is crucial for high fidelity imaging. While aperture synthesis can be used to recover more (u,v) space, the effect of an incompletely sampled visibility domain still presents issues in the recovery of the information from the observations. In practice, the full (u,v) space can never be completely recovered, and what is actually recovered is known as the "dirty image" I_D. Many methods have been developed in order to obtain a reliable image of the brightness distribution. Discussing of those methods goes beyond the scope of this chapter; however, a further explanation can be found in [20].

1.2.6 Aperture synthesis

As it was stated above, the quality of the brightness distribution image, obtained by Fourier transform of the complex visibility, $V(u, v)$, depends on how well the uv-plane is filled. In the ideal case, the uv-plane is fully sampled, and the quality of the image is totally reliable. However, when using an interferometric array this is not the case since the array is made up of a set on individual antennas forming a combination of baseline pairs. Inasmuch as the antennas do not fully cover the uv-plane, gaps are generated, inevitable leading to quality degradation of the synthesized image. For an array made up of N antennas, the number of baselines in the array is N_b ,i.e., the number of discrete uv-samples is given by $N_b = \frac{1}{2}N(N-1)$. This N antennas combined to produce N_b samples in the uv-plane is called aperture synthesis.

Since increasing the number of uv-samples is fundamental in order to guarantee a reliable approximation to the true sky brightness distribution, aperture synthesis makes use of two additional "tricks". To exemplify the first one, consider a celestial object under observation for a certain number of hours. The rotation of the Earth changes the orientation of the array with respect to the source, increasing the uv-plane coverage. Nonetheless, even after using the rotation of the Earth, there are still gaps in the uv-plane coverage. The second way to fill those gaps is by changing the antenna configuration layout during the observation. This allows previously unsampled regions in the uv-plane to be now covered. Thus, the combination of the rotation of the Earth and reconfigurable telescope positions are useful tools that, when used together, help to build up a more complete uv-plane coverage for interferometric observations.

1.2.7 ALMA: the eye to look into the hidden universe

Cutting edge radio interferometry makes use of aperture synthesis which, as discussed above, is simply an ensemble of baseline pairs. This technique is used for detecting radio emission from a source with fine angular details since the resolution of a single dish telescope is insufficient for some specific astronomical purposes. New astronomical discoveries will demand measurements with sufficient accuracy in their angular resolution to allow a clear identification of parameters such as intensity, polarization, and frequency spectrum of the detected objects. Radio interferometry can achieve this resolution by means of observation using very long baselines and high-frequency receivers.

The newest generation of millimeter/submillimeter receivers have a considerably improved

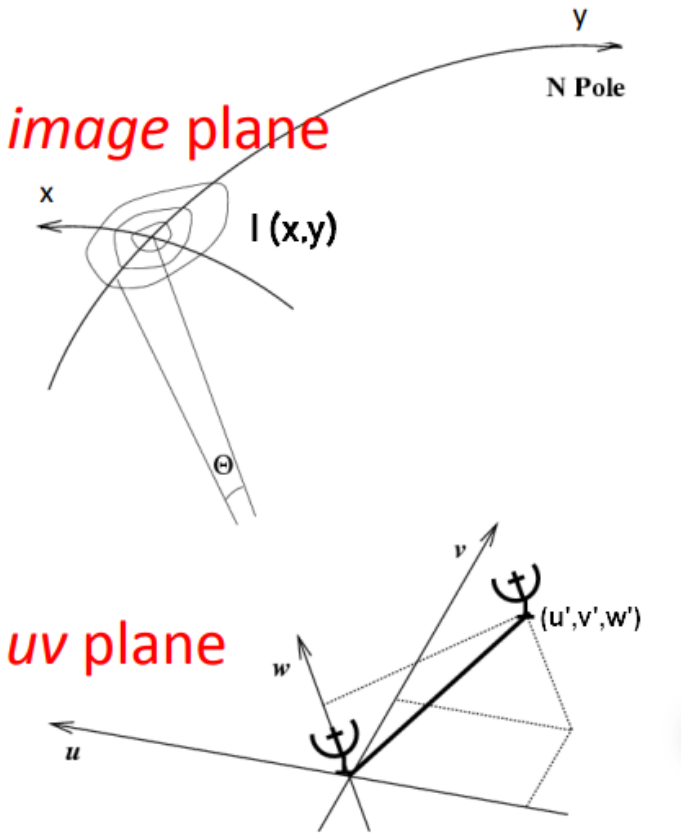

Figure 1.5: ***Relationship between uv-plane and image plane.***
The image shows a pair of antennas, in the uv-plane, making up a baseline. This baseline pair is used to sample the brightness distribution $I(x, y)$ in the xy-plane in the sky.

performance due to the recent technological developments in fields like astronomical instrumentation, solid-state physics, and fiber-optic communications. Most of the telescopes using this cutting edge receivers have demanded a large investment in human and economic resources. The only feasible way to implement them is by international cooperation. The best example is the Atacama Large Millimeter/submillimeter Array (ALMA), which is a cooperation between the European Southern Observatory (ESO), the National Radio Astronomy Observatory (NRAO) and the National Astronomical Observatory of Japan (NAOJ) in collaboration with the Republic of Chile. The success of existing radio astronomy facilities – like ALMA, shown in figure 1.6- have demonstrated what can be achieved by all these new technologies incorporated into the newest radio astronomy receivers. Very good examples of these achievements are the picture taken by ALMA of the HL-Tau protoplanetary disk; and the first image ever taken of the event horizon of a black hole (note that this image was taken using telescopes all over the world, but without ALMA, this could not have been possible). Both images are shown in figure 1.7.

Currently, ALMA represents the largest astronomical millimeter/submillimeter wavelengths observatory in existence. One of the most important technical developments of ALMA is to produce accurate images with resolutions of tens of milliseconds, which at submillimeter wavelengths require baselines up to ~ 15 km. This resolution was achieved for the first time at the ALMA Long Baseline Campaign (LBC), obtaining angular resolutions as fine as 19

Figure 1.6: ***Image of ALMA site by night.***
This image has been taken from the ALMA website: *https://www.almaobservatory.org*

Table 1.1: ***Optical parameters of the ALMA antennas***

Symbol	Description	Data
D	Primary Aperture	12.0 m
f_p	Focal Length of Primary	4.8 m
	f/D of Primary	0.40
d	Secondary Aperture	0.75 m
	Final f/D	8.00 m
e	Secondary Eccentricity	1.10526
θ_p	Primary Angle of Illumination	128.02 ^{o}
θ_s	Secondary Angle of Illumination	7.1 6^o
$2c$	Distance Between Primary and Secondary Foci	6.177 m
v	Primary Vertex Hole Clear Aperture	0.75 m

mas at $\sim$ 350 GHz [21].

ALMA consists of fifty-four 12-meter and twelve 7-meter diameter antennas with a focal beam f/D ratio of 8.0. The geometry of these antennas corresponds to a Cassegrain telescope and is shown in figure 1.8 and its optical parameters are listed in table 1.1. The incoming light from the sky impinges upon the primary reflector. Then, it reflects the light towards the front of the telescope where it is reflected again by the secondary reflector. Then, the light travels back through a hole in the primary reflector to the rear part of the telescope focusing the beam into one of the available receivers, where the electromagnetic radiation is transformed into an analogue signal and, subsequently, into a digital signal.

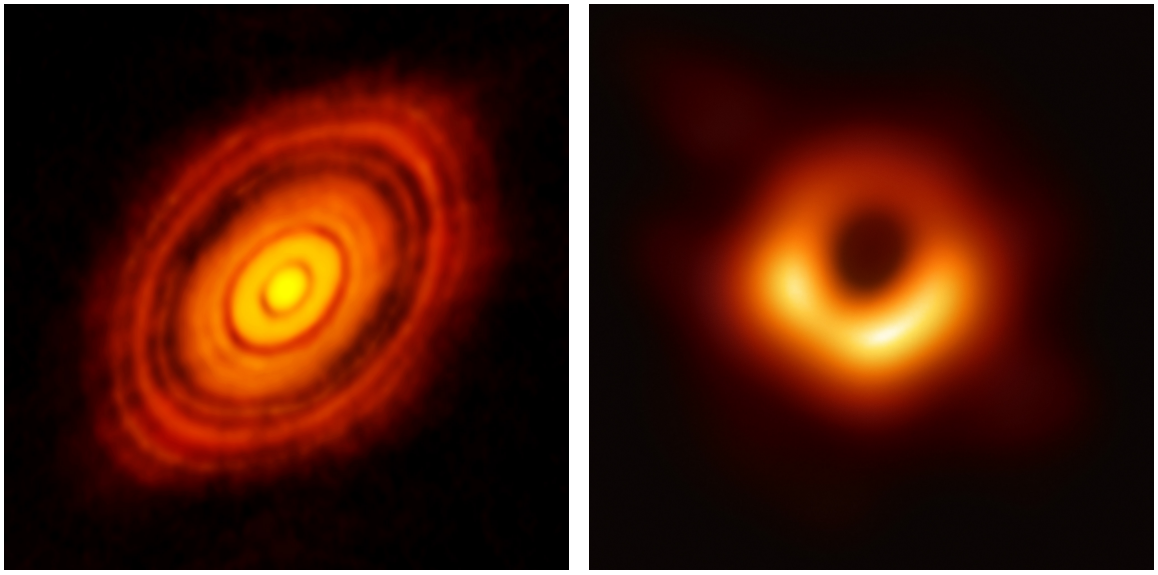

Figure 1.7: ***Images of the HL-Tau protoplanetary disk (left) and the event horizon of black hole (right).***
These images were taken from ESO web page *https://www.eso.org/public/*

The principal sources of atmospheric attenuation for electromagnetic radiation are the molecular resonances of water vapor, oxygen, and ozone [23]. Figure 1.1 shows the absorption lines of water vapor and oxygen at the ALMA site for different content of precipitable water vapor (PWV), which are pressure broadened and cause attenuation far from the absorption line center frequencies. This feature establishes the frequency intervals at which astronomical observations can be made, known as observation bands. ALMA established ten bands in order to cover efficiently the atmospheric windows between 35 and 950 GHz. The frequency range for each band of ALMA is shown in table 1.2.

1.3 Interferometric measurements in radio astronomy: loss of coherence and correction techniques

When the telescopes used in an interferometric measurement are steered an angle θ for sampling a celestial source, an optical path difference (OPD) between the signal arriving at each telescope is generated. As the signals are combined to generate a fringe pattern, the phase difference -produced by the OPD- must be compensated. A good quality fringe pattern demands phase stability over time. However, this phase is generally corrupted by the atmospheric layer of the Earth. For radiation in the spectrum of MHz, the charged particles in the ionosphere are the main responsible for phase fluctuation. As the frequency increases above ~ 10 GHz the main factor that produces phase fluctuations is the PWV, mostly located in the troposphere. These phase fluctuations can decrease the degree of coherence, causing as a result that the fringes will be more difficult to detect. For instance, the coherence time -i.e. the maximum integration time which still produces detectable fringes- might be reduced to seconds for millimeter/submillimeter wavelengths, and thus, the SNR will also be reduced.

Figure 1.9 shows a scheme of how PWV content in the atmospheric layer produces loss of

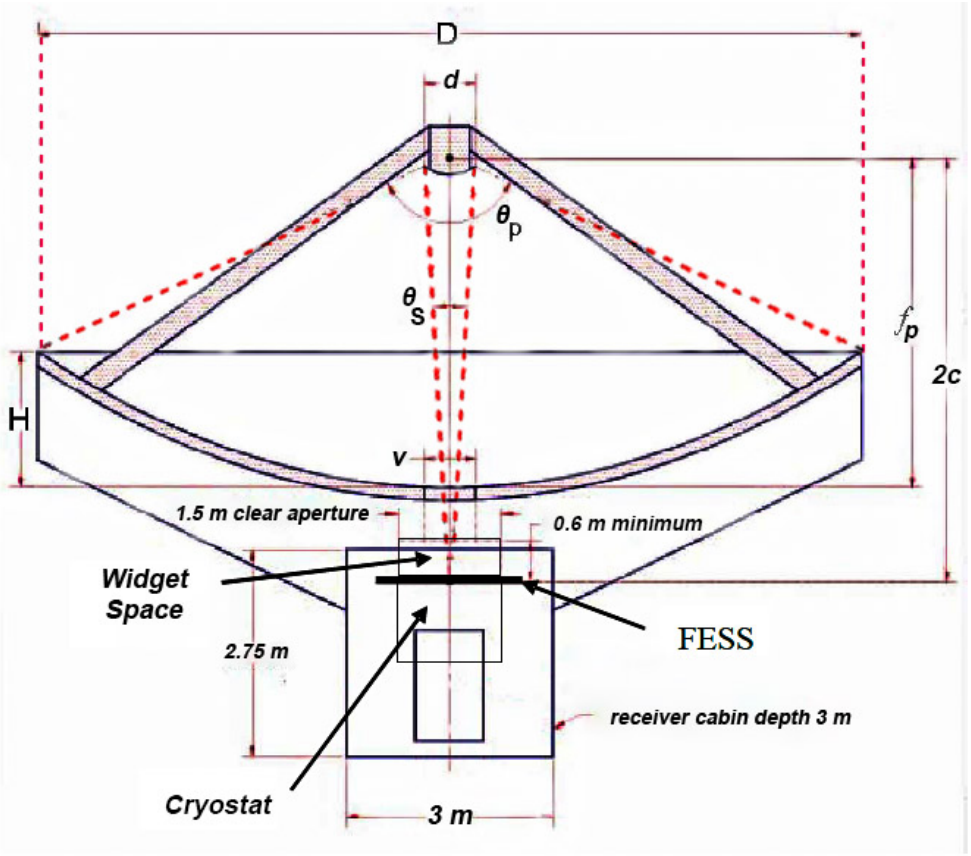

Figure 1.8: ***Schematic of an ALMA antenna.***
This type of antenna has a Cassegrain configuration. It is composed by a parabolic dish surface (primary reflector) and a hyperbolic dish surface (secondary reflector) [22]

coherence when antennas are combined for interferometric measurements. The mechanism of how this loss takes place is explained in the following subsection.

1.3.1 Atmospheric distortion and its wavelength dependence

All the concepts previously described about interferometry have been stated for an idealized situation, i.e., where the overall delay (or equivalently, phase fluctuation) induced in the beams- combined by a baseline pair- are known and stable. If that is the case, the relative phase difference of the interference fringes of an observed source, like a point-like object, at a given position in the sky will be known. Therefore, a correction can be applied in order to preserve the coherence and make fringes observable. Nevertheless, real-life interferometric measurements are way far from this ideal approach, and phase noise becomes a fundamental limitation that might make interferometry measurements unsuitable.

Like in optical astronomy, where the mechanical tolerances of the telescope optics are critical, in millimeter/submillimeter astronomy the phase fluctuation is mainly induced by the passage of the light, from the celestial source, through the Earth's atmosphere before arriving at the interferometer. These phase fluctuation induced by the Earth's atmosphere, which are large and rapidly varying, put a limit to the maximum achievable baseline length. Thus, the maximum resolution of an interferometry will be limited if this phase fluctuation

Table 1.2: ***ALMA frequency bands***

Band	Lowest Frequency GHz	Mid-Band Frequency GHz	Highest Frequency GHz
1	31.3	38	45
2	67	78	90
3	84	100	116
4	125	144	163
5	163	187	211
6	211	243	275
7	275	323	373
8	385	442	500
9	602	661	720
10	787	868	950

is not corrected.

The optical effects which cause these rapidly changing phase fluctuations are known in astronomy as seeing. The effects of seeing are different for single-dish and interferometric observations. In the former, the maximum angular resolution that can be achieved is mainly affected. In the later, the resolution is little affected by seeing but the sensitivity can be dramatically affected. In the following subsection, we will give a brief but illustrative explanation of the seeing, and how interferometers mitigate its effects over the phase fluctuation. Special emphasis will be put on ALMA since it represents the biggest interferometer on Earth right now.

The wavefront perturbation model

Consider a pair of telescopes making a baseline pair separated by a distance B. These telescopes are steered to a celestial source in the sky. However, as shown in figure 1.9, the separation makes the line of sight, connecting each telescope with the source, different. The OPD, i.e. phase delay, experienced by a wavefront coming from the source depends on the refractive index of the material it is passing through, in this case mainly air. The refractive index of air varies with pressure, humidity, and temperature. Thus, assuming a constant pressure along the line of sight for each telescope, it seems quite reasonable assuming that the overall phase delay of the interferometer depends on the detailed humidity and temperature distribution along each line of sight. A first approximation model to deal with this situation is to assume that Earth's atmosphere is build-up of a set of horizontal layers, where the refractive index is homogeneous within each layer. In this scenario, the phase delay introduced by each layer will be equivalent for each line of sight. Therefore, the only contribution to the overall phase delay will be simply the angle at which the telescopes are steered. Nevertheless, the validity of this approach fades away as the distance B increases, since seems unlikely to assume that humidity and temperature in the air remain unchanged for very long horizontal distances.

Horizontal inhomogeneities in the refractive index of the atmospheric layers introduce fluctuation into the OPD of a baseline pair and, hence, the relative phase of the fringe pattern will be noisy. The most problematic inhomogeneities in the refractive index come

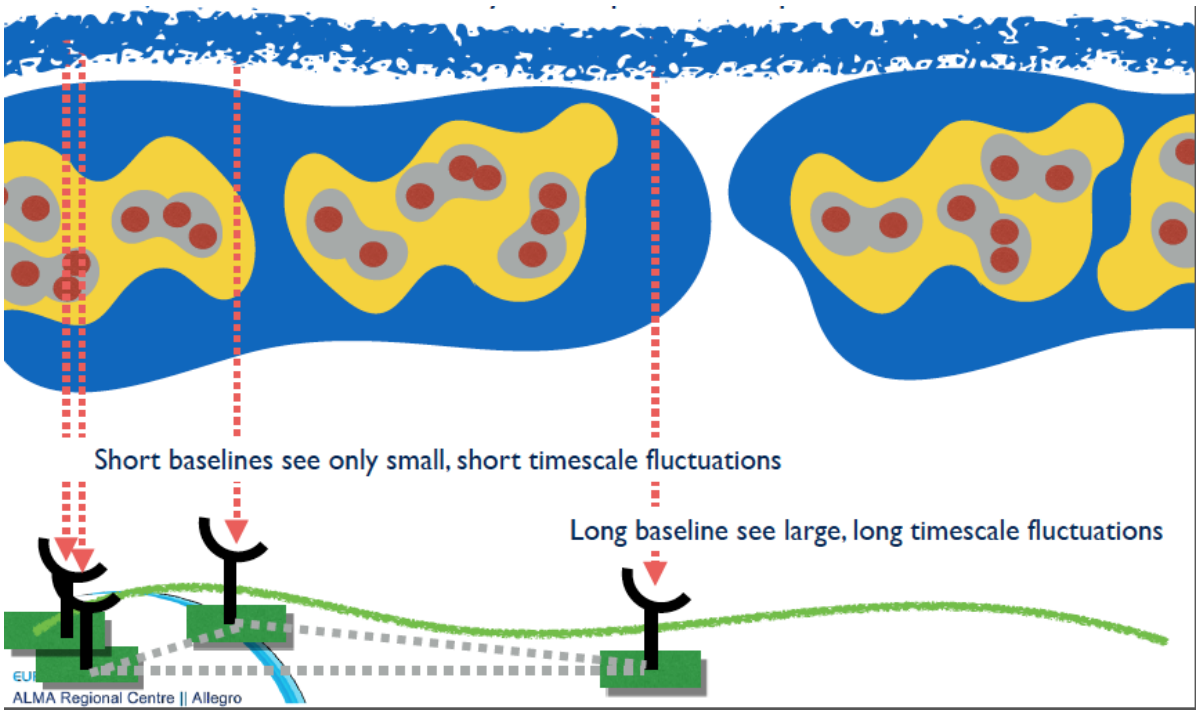

Figure 1.9: ***Atmospheric distortion producing lost of coherence***

The image shows many antennas making up an aperture array. As baseline length increases, the atmospheric structure (rendered in red, yellow and blue) over each antennas changes, decreasing the phase stability through that line of sight.

from turbulent mixing of atmospheric layers, which produces changes in the refractive index of random nature. Furthermore, the wind moves this random fluctuation, increasing, even more, the randomness of this process. An accurate model to describe astronomical seeing must consider the turbulent nature of the mixing of these layers and their time evolution. A more detailed discussion about this subject can be found in [24])

Turbulence model

Turbulence, whatever the reason of its cause, has a characteristic structure, consisting of random vortexes (or "eddies") of moving air, as shown in figure 1.10. As they randomly move in the air, they continuously split into smaller pieces like in a fractal type structure. The statistical properties of such turbulent eddies are described by the so-called Kolmogorov turbulence model [24]. According to this model, turbulence will produce a significant change in the refractive index along the path of a propagating beam, when those eddies coincide with pre-existing gradients of refractive index. For example, consider the interface region between two layers of air at different temperatures. When this happens, the turbulent motion mixes the air creating regions of higher and lower refractive index. This process mimics the structure of the turbulence itself, consequently, producing a clear distortion in the initial wavefront.

1.3.2 Effects of precipitable water vapour

At millimeter/submillimeter wavelengths, there are three main contributions to fluctuations in the refractive index: [1]

- "Dry": these are mainly linked to density and thermal fluctuations.
- "Wet": fluctuations due to variations in the amount of precipitable water vapour (PWV).
- "Instrumental": fluctuations due to variations in the signal propagation through cables and instrumentation.

Of these, under all but the driest observing conditions, wet fluctuations dominate. For this reason, interferometer -like ALMA- installed a fast water vapour radiometer (WVR) in each antenna to measure the PWV fluctuations along the line of sight of the telescope and subtract a residual "wet" phase delay from the observed signal between each telescope pair. Typically, this technique significantly reduces the rms phase fluctuation, by a factor of 2 or better for data where the precipitable water vapour PWV >2 mm. In drier conditions the WVRs become less effective and the typical improvements is <1.6 in conditions where PWV <1.0 mm [25].

The Kolmogorov behaviour of the atmospheric fluctuations above ALMA are illustrated in figures 1.11 and 1.12, showing the temporal and the spatial structure function, respectively. Figure 1.11 shows a measure of the phase fluctuation, using a two-point-deviation statistic, as a function of time for the raw data (blue) and WVR corrected data (red) for one chosen baseline (~ 7000 m long) from long-baseline ALMA testing data [26]. It clearly indicates that the phase fluctuation increases as longer and longer time-scales are used for the phase fluctuation calculation, even for the WVR-corrected data (red). Figure 1.12 plots the rms phase fluctuation (in terms of path length noise as indicated in [26]) calculated over a 10 minute observation, as a function of baseline length from one of the driest long baseline test observations (PWV $= 0.28$ mm). The phase fluctuation increases towards larger baselines as the differential signal between two antennas is increasingly affected by larger scale fluctuations.

Fig. 1.12 also illustrates a critical aspect for ALMA science observations (and therefore for radio interferometric measurements). For reliable imaging at the full resolution of the array configuration used, **for all baseline pairs** the phase rms needs to be below a critical value, which for ALMA is typically set at 30^o, corresponding to a coherence of 87 % [26]. The horizontal lines indicate this limit of 30^o imposed on the phase rms for reliable imaging at the central frequencies of Band 3 (100 GHz), Band 6 (230 GHz), Band 7 (350 GHz), Band 9 (650 GHz). The conditions for meeting the phase rms limit become more stringent with increasing frequency. Specifically, figure 1.12 shows the phase rms as a function of baseline length in the best given conditions for observations throughout the 2014 long baseline tests (PWV $= 0.28$ mm) [21]. Here the WVR correction is hardly effective. The green and purple lines indicate the expected phase rms values after phase referencing to reduce the phase fluctuation. The green line represents cycling with a nearby calibrator < 1 deg away over a 2 minute time-scale, while the purple line represents cycling on a 20 second time-scale (as

[1] The results and plots presented in this subsection were part of a research proposal presented to ESO in the year 2017. Here, we provide only a brief overview of the work developed by our partners of Allegro group

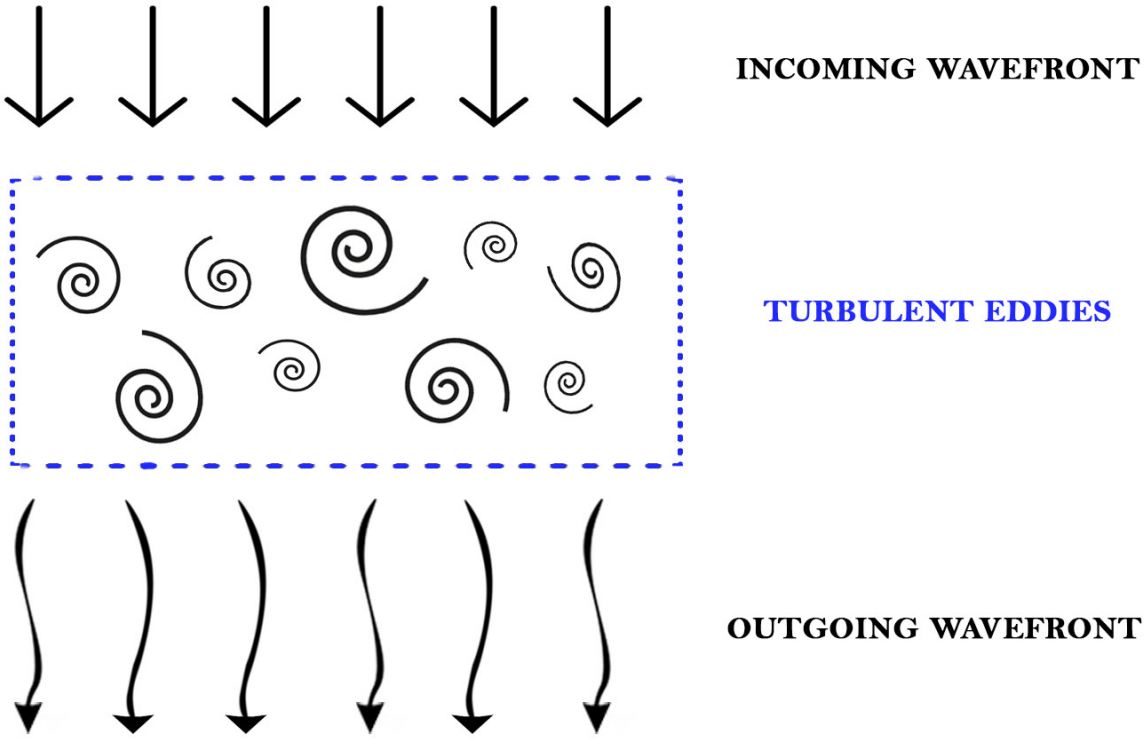

Figure 1.10: ***Schematic illustration of Kolmogorov turbulence model***
A plane wavefront arriving from a source enters to a layer with turbulent eddies. As it travels through the turbulently mixed air, different parts of the wavefront are slowed down by depending on the line of sight through the layer. As a consequence, the wavefront becomes randomly "corrugated" by the time it arrives at the interferometer.

estimated from [27]).

When considering only the WVR correction to the data shown in figure 1.12, the phase rms is only reduced to the 30^o rms level for Band 3 observations. However, this is the phase RMS as measured over>10 min, such that if one applies phase calibration solutions from referencing the phase RMS after is more noticeably reduced. The green band in figure 1.12 illustrates phase referencing on a 2 minute time-scale. It shows that the phase rms would decrease sufficiently to allow Band 6 observations. To observe at higher frequency bands, techniques like fast switching (cycling to a calibrator on time-scales faster than 1 minute - e.g. purple line in figure 1.12) are required. Although this fast switching increases the overheads, it removes all phase fluctuations occurring on time-scales longer than the switching time, such that faster switching removes more variations. Although Band 9 observation could now be achieved, there are only a few tens of calibrators that would allow the fast switching to be employed. The likelihood of such a strong calibrator within 1 deg of a PI science target is however very low. It has been shown that if the calibrator is >3-5 deg the fast switching no longer has an effect as the line-of-sight of the antennas point through a totally different bit of atmosphere - the phase fluctuation level is close to that expected with 2 minute cycling [26]. Therefore, it is highly unlikely that high frequency band -like Band 9- will be observed using only fast switching (FS) and phase referencing. The later option is

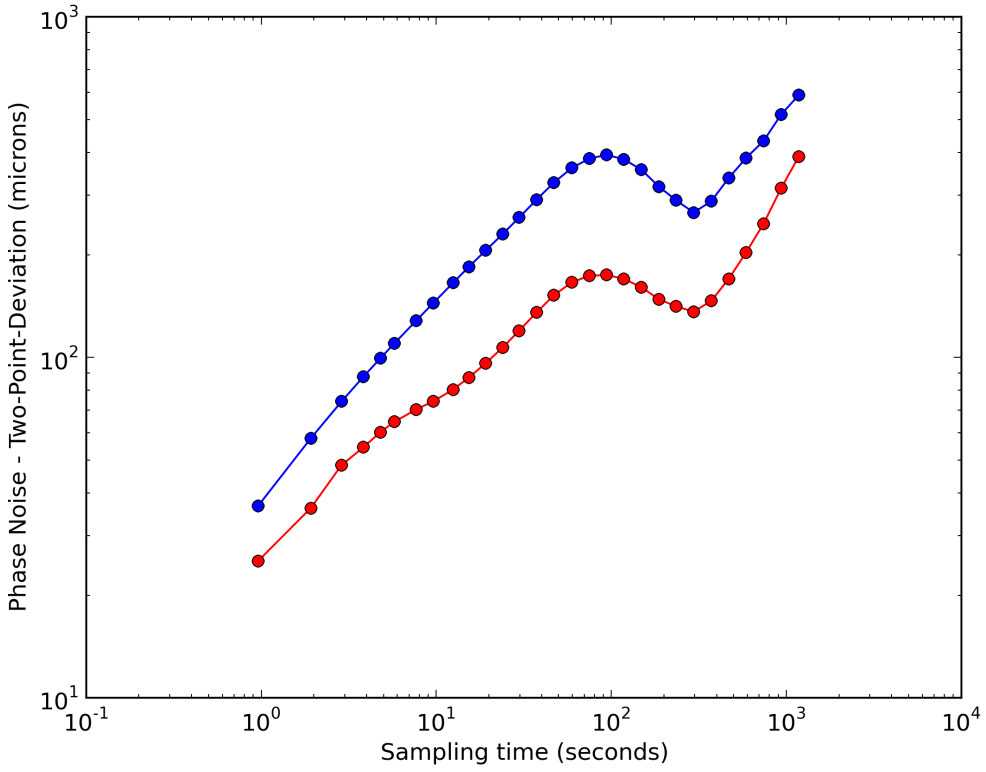

Figure 1.11: ***Temporal dependence of atmospheric fluctuation***
This plot shows the phase fluctuation (measured by the two-point-deviation) as a function of time for one baseline from the dataset Xa59 [26] of ~ 7000 m with PWV $= 0.61$ mm. The blue is the raw phase and the red is after WVR corrections are applied.

the standard phase fluctuation correction used by ALMA and we give a brief explanation in the following subsection.

1.3.3 Phase referencing

ALMA uses another phase referencing technique, which consists of switching to a close-on-the-sky strong point source for phase calibration. The observations are interleaved with the science target on the order of every few minutes (60-90 seconds for the long baselines at Band 6 and Band 7) to remove any phase variation that is not removed by the WVR system (as it is not perfect), particularly large fluctuations by longer time-scale. In combination with WVR and fast switching, the phase calibration and correction procedures work very well at the lower observing frequencies of ALMA (< 500 GHz), allowing for reliable imaging. However, for high-frequency observations this is problematic since the brightness of the reference sources typically drops as a function of frequency, leaving the vast majority of the high-frequency observations without a suitably nearby phase standard subject to comparable atmospheric conditions.

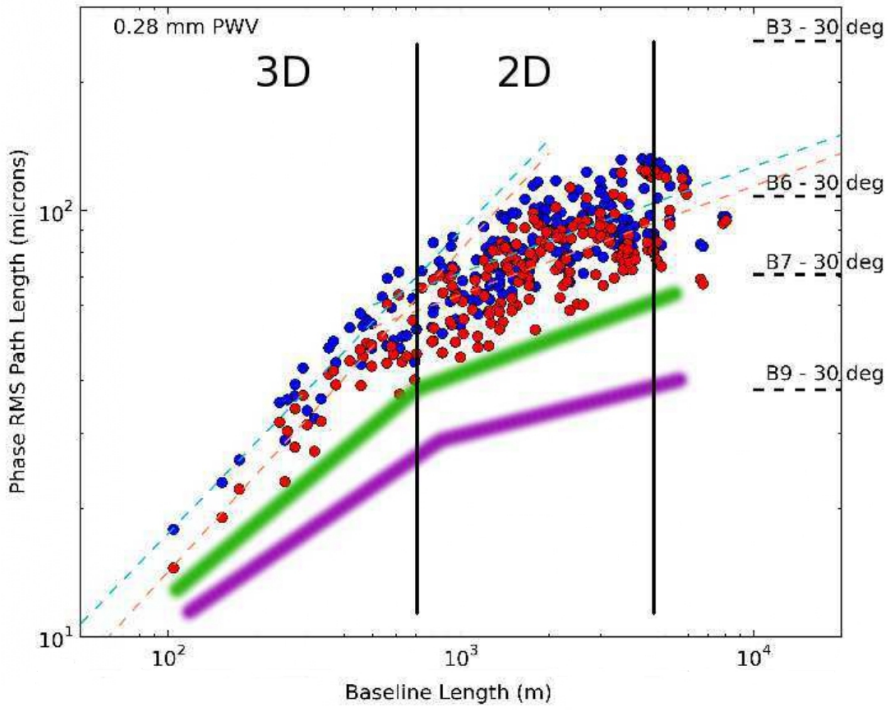

Figure 1.12: ***Spatial dependence of atmospheric fluctuation***

Typical atmospheric structure functions for ALMA showing the rms phase fluctuation, expressed as a path length difference, as a function of baseline (up to ~ 7 km). Blue: WVR uncorrected; Red: WVR corrected. The breaks in the slope of the structure function indicate 3D fluctuations to be dominant up to 1–2 km,a subsequent change to 2D fluctuations, and a baseline-length independent rms on the largest scales. The break at 1–2 km is thought to be associated with the thickness of the water vapour layer above ALMA. The horizontal lines illustrate a typical limit of 30^o at the central frequency of Band 3 (100 GHz), Band 6 (230 GHz), Band 7 (350 GHz), Band 9 (650 GHz). In this case, WVR correction is hardly effective.

1.3.4 Band to Band calibration

A basic version of dual-frequency observations is already in use at ALMA, in the form of Band-to-Band (B2B) calibration that, while not truly a dual-frequency, switches between low-frequency (LF) and high-frequency (HF) ALMA bands. As suitable and close-by HF phase calibrators are typically difficult to find, B2B observations observe a phase calibrator at LF and then transfer (by scaling) the observed phase for use with the science target observed at HF. Employing B2B for calibration using a strong LF calibrator can allow faster phase referencing to be used, less than 1 min cycle times. In particular, a fast frequency switching is required to most accurately obtain the important B2B phase off-set solution. Although B2B may allow a 20 second cycle time, there are still stringent requirements of calibrator strength and separation with the science target. Furthermore, as with any phase referencing, only an interpolated solution is applied, thus, fluctuations shorter than the cycle time will still remain uncorrected [28]. Nevertheless, this technique provides an insight into the benefits of using a dual-frequency receiver for solving the phase fluctuation troubles when long baseline and high-frequency are combined in an interferometric measurement.

1.3.5 Sub-array experiment: self calibration transfer technique

As a true dual-frequency observing-mode is not currently possible at ALMA, Allegro [1] in collaboration with staff at the Joint ALMA observatory (JAO) proposed to use a paired-antenna setup. This took place during a compact array configuration with the antennas in each pair observing at LF and HF respectively, as shown in figure 1.13. The paired-antenna set-up, observing at different frequency bands, was new to ALMA, thus, it was chosen to start with Bands 3 & 6 and Band 3 & 7 tests before attempting to use a frequency band > 500 GHz.

The successful Bands 3 & 6 and 3 & 7 sub-array paired antenna tests were undertaken in water dominated conditions > 2 mm PWV. Under these conditions, the WVR does give a considerable improvement in the phase stability. However, the results from these tests of a continuous dual-frequency phase transfer are encouraging. It was found that one can directly transfer the scaled-up phase solutions from the low to high frequency. They also mimicked more unstable conditions by excluding the WVR correction and find that it is possible to produce a better image after transferring the simultaneous LF to HF phase solution than what can be achieved with an in-band calibration with 2 min referencing. A full explanation of this method is available on [29].

The conclusion of this sub-array experiment is that when typical phase reference scheme is applied (with a 2 minutes cycling time), the coherence is very low at a level of only 35%. In contrast, when simultaneous phase transfer of the self-cal solution from the low-frequency (Band 3 in this case) is applied, the coherence is improved to over >60% and the SNR is increased in $\sim$ 12%. In this experiment, the WVR was intentionally not applied in these cases to mimic the even worse phase fluctuations that would exist at higher frequency bands (for instance Band 9).

Albeit Band 9 measurements were not taken, this paring-antennas experiment gives an idea of how beneficial the phase transfer technique can be; ergo, the benefits of implementing a true dual-frequency receiver for ALMA.

1.4 Benefits of allowing ALMA to operate in a dual-frequency observation mode

As it was stated in the previous section, the implementation of a true dual-frequency receiver for ALMA seems to be a practical solution for the phase calibration problems that currently impede reaching the higher achievable resolution. By simultaneously observing one LF and one HF band, all aspects of ALMA science at high frequencies are significantly enhanced by the improved calibration and observing speed that this development would allow. In particular, this technique will speed up spectral line surveys.

Besides all the conceivable benefits, it is possible identify three main science drivers for a dual-frequency receiver aimed to connect a low with a high-frequency band:

- **Improvement in phase calibration** for the high-frequency band. In the case of

[1] https://www.alma-allegro.nl/

low atmospheric water vapour content where the conventional phase correction scheme using the water vapour radiometers breaks down. This may potentially enable much more efficient observations at longer baselines.

- **Enabling highest resolution imaging with ALMA**. Since for a given array configuration, Band 9 always provides 3 times better resolution than Band 6, ALMA's highest resolution imaging is reserved for high-frequency bands like Band 9. However, occasions where phase stability is so exceptional that even Band 9 data can be self-calibrated up to 15 km are scarce. A dual-frequency receiver offers the unique possibility to correct the Band 9 for sources that can be self-calibrated at Band 6.
- **Observation of transient phenomena** that occur over wide frequency ranges. Eliminating the overhead of band switching represents a big advantage for solar chromosphere research, where simultaneous multi-band coverage is desired.

These science drivers will be explained in more details in the following subsections.

1.4.1 Improvement in phase calibration

ALMA is currently able to employ baselines of up to 16 km with observing frequencies up to about 380 GHz [25]. In particular, at higher frequencies, observations are sensitive to atmospheric effects that attenuate and decorrelate the data. As an example, in nearby galaxies, Band 9 observations provide unique spectral line information and high resolution. However, the rate at which these high-quality Band 9 results can be obtained has limitations. The main difficulties, related to phase stability, when observing with Band 9, or any high-frequency band, are the following.

- Phase fluctuations scale linearly with frequency, atmospheric fluctuations that result in a phase rms of 20^o at Band 6 (230 GHz), that are nicely within the specification for imaging, will cause 60^o of phase rms at Band 9 (690 GHz), making imaging difficult if not impossible.

- To reduce atmospheric phase fluctuations, high-frequency observations are only carried out under the driest conditions, typically when the precipitable water vapour (PWV) is below 1 mm. Under such conditions "wet" fluctuations are often no longer dominant and Water Vapour Radiometer (WVR) corrections may not significantly improve, or possibly even worsen, as shown in figure 1.14.

- Phase calibrators are significantly weaker at higher frequencies leaving less usable sources and ones that typically are much further away from the target, introducing systematic errors in the phase calibration [27].

Moreover, this variability appears to be uncorrelated with phase variations measured by the Water Vapour Radiometers (WVRs) that provide the primary method to correct for rapid atmospheric phase fluctuations. This is illustrated in figure 1.14. The exact reason for which the WVR fluctuations under some dry conditions no longer trace the phase fluctuations seen in the observations is not clear. A possible explanation is that at those times the phase fluctuations are no longer dominated by water vapour but instead by thermal instabilities of the "dry air component".

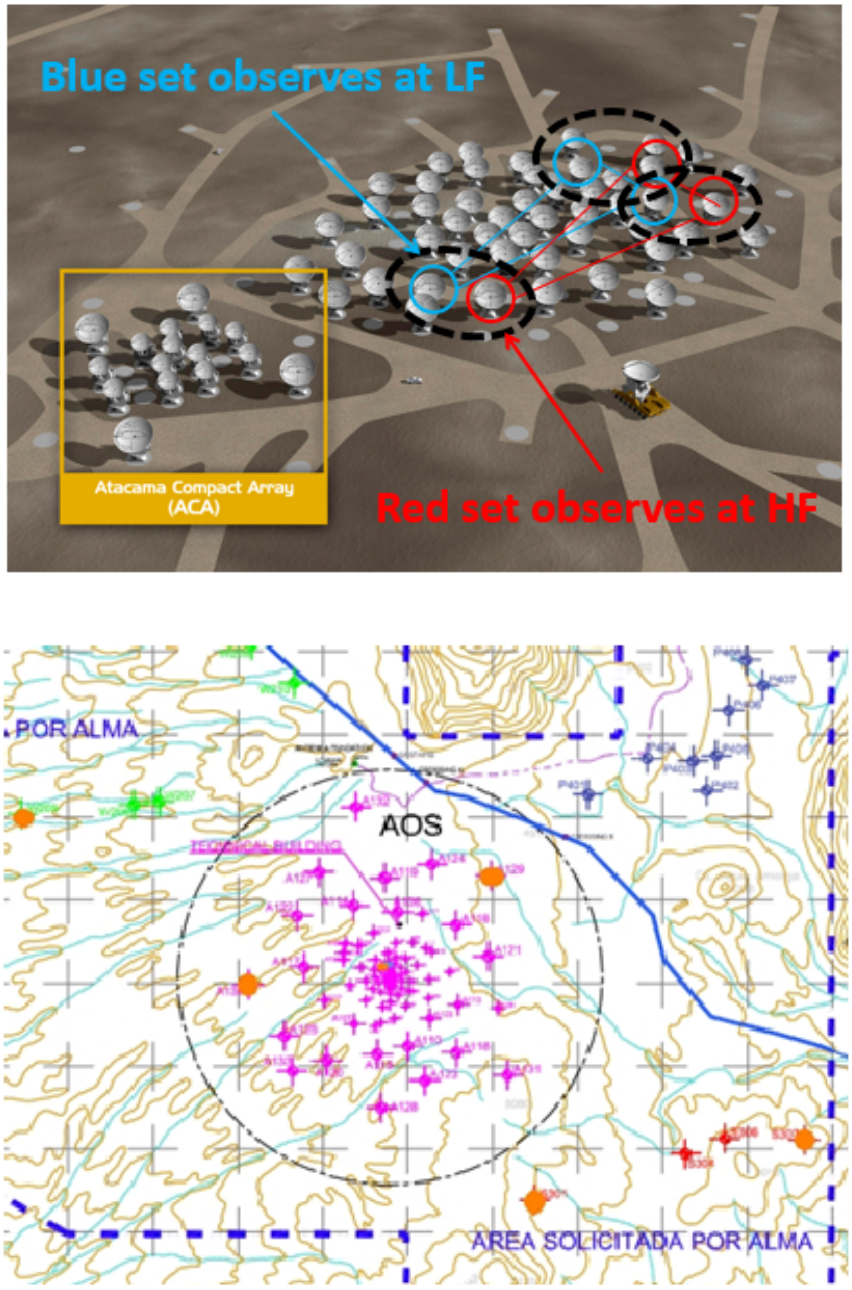

Figure 1.13: ***Antennas paired for sub-array experiment***
A sketch of sub-array setup illustrating the concept of pairing antennas is shown in the upper panel. This idea can be done only for short baselines setup, where the antenna pad density is high enough to find good pairs (as shown in the lower panel by purple crosses). However, due to the low density of antenna pads in the outer region, good pairs are not available and therefore sub-arrays are not feasible for the longest baselines that ALMA can reach.

1.4.2 Enabling the highest resolution for ALMA

To date, ALMA's highest resolution images, employing baselines up to 15 km, were obtained at Bands 7 or lower, where fast (<60 s) atmospheric phase fluctuations can be corrected

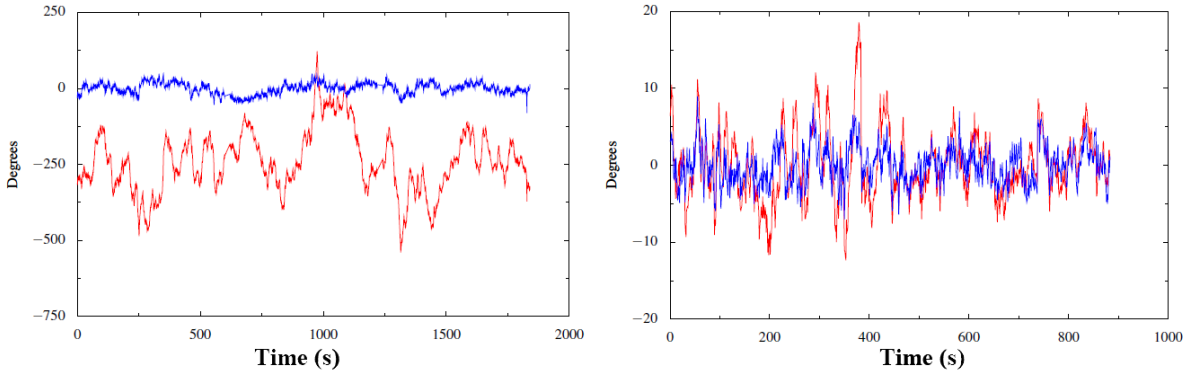

Figure 1.14: ***Atmospheric calibration problem.***
Test observation of a strong quasar at 90 GHz with ALMA. The red line is the phase of the observed (complex) visibility on the test baseline, expected to be a constant in time for a point-like source. The blue line is the visibility phase after correction of the data based on the WVR signals. Left: Test observations on a longish baseline (650 m) under relatively humid conditions (PWV$\sim$ 2.2mm), showing almost a 10x reduction of the phase variations; Right: Test observation on a short (25 m) baseline in dry conditions (PWV$\sim$ 0.5mm), achieving only a 30-50% improvement [30].

through self-calibration. The best-known example of such observations are the iconic images of HL Tau in Bands 3, 6 and 7 (see figure 1.7). These were obtained under very good weather conditions and employed self-calibration at these three bands. This self-calibration was essential to reach the resolution and signal-to-noise to produce the spectacular images that, in a way, have defined ALMA.

At the same time that the Band 3, 6 and 7 data were taken on HL Tau, observations at Band 9 were also obtained. However, at Band 9, self-calibration was limited to baselines < 300 m, resulting in far worse angular resolution than the 15 km Band 7 observations. Clearly, even under very good weather conditions, the frequency-dependent increase in phase variation by factors 2–3 pushed the decorrelation over the limit where the signal was essentially lost on time scales of minutes.

1.4.3 Observation of transient phenomena

ALMA is a new powerful tool for observing the Sun at high spatial, temporal, and spectral resolution. These capabilities can address a broad range of fundamental scientific questions in solar physics [32]. The radiation observed by ALMA originates mostly from the chromosphere, a complex and dynamic region between the photosphere and corona, which plays a crucial role in the transport of energy and matter and, ultimately, the heating of the outer layers of the solar atmosphere.

Dual-frequency receivers will play a key role in fully unlocking ALMA's diagnostic potential. First of all, it is fundamental to realize that the height in the solar atmosphere from where the millimeter/submillimeter radiation is emitted generally increases with wavelength (see red arrow in figure 1.15). Different receiver bands thus effectively map different layers in the solar atmosphere. In Band 9, the low chromosphere is observed, whereas Band 6 allows

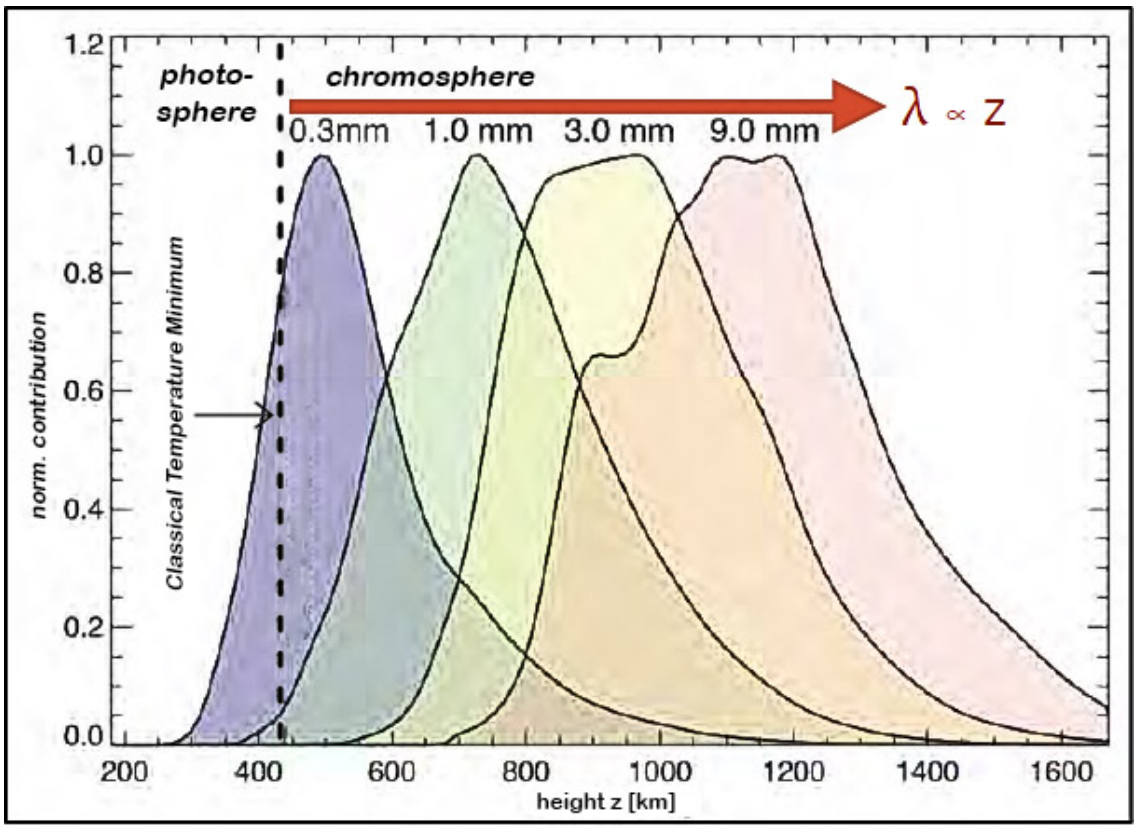

Figure 1.15: ***Contribution functions of the continuum intensity***
Contribution functions of the continuum intensity at four selected wavelengths between 0.3 mm and 9.0 mm. They correspond to the solar disk-center and are based on a numerical model snapshot of the solar atmosphere under quiet Sun conditions [31]. The height in solar atmosphere from where the radiation is emitted generally increases with wavelength. The dashed vertical line labelled "classical temperature minimum" marks the boundary between the photosphere and the model chromosphere.

for studying the middle chromosphere. Currently, observations can only be carried out in one band at a time (corresponding to one height range) and changing bands might lead to interruptions of many minutes. The time needed for a typical (acoustic) shock wave to propagate from its photospheric excitation site through the whole chromosphere is on the order of only 2–3 min. The time delay between a shock wave appearing in Band 9 and Band 6 is accordingly even less (due to the smaller difference in effective formation height). Following a propagating event throughout the atmosphere is impossible with ALMA's current single-band observations and instead requires ultra-fast band switching or preferably multi-band receivers. Only the latter option enables strictly simultaneous observations without sacrificing spatial resolution or time coverage.

The combination of at least two receiver bands would allow for novel techniques such as atmospheric tomography (giving the instantaneous 3D structure of the solar atmosphere) and chromospheric seismology (by using atmospheric waves and oscillations at high cadence), which have unprecedented diagnostic capabilities and would result in important results and high-impact publications (e.g., concerning the role of waves for the coronal/chromospheric heating problem) [33].

1.5 Proposed research

An overview of the importance of radio astronomy has been presented. This included the technological tools that make possible to detect radio signal, and how interferometric techniques can be applied to increase the maximum achievable resolution. The fundamental concept to bear in mind is that the output image from an interferometer (or equivalently, the sky brightness distribution) corresponds to the Fourier transform of the visibility sampled by the ensemble of antennas making up the interferometric array.

Despite the big effort involved in the development of state of the art radio astronomy -as previously discussed for ALMA-, this field is not exempt of limitation of its maximum theoretical capabilities. Specifically, phase fluctuations induced by atmospheric turbulence seems to be the limiting factor. Although there always may be occasions of phase stability so exceptional that even high-frequency bands -for instance Band 9- can be self-calibrated out to 15 km, such occurrences are very rare. Since for a given array configuration, Band 9 always provides 3 times better resolution than Band 6 (because of a scale factor of ~ 3 between the frequencies that define each band), ALMA's highest resolution imaging is reserved for high-frequency bands like Band 9 or Band 10. It is therefore paramount that a solution to correct the phase variations at high frequencies must be found and, as proposed by the Allegro group, the best way to get to this solution is by the implementation of true dual-frequency receiver for ALMA. A dual-frequency system offers the unique possibility to correct the Band 9 phase variations down to time scales of the individual integrations, at least for sources that can be self-calibrated at Band 6. Such a dual-frequency system simultaneously measures the visibilities at Band 6 and Band 9 on all baselines. By finding the self-calibration solution at Band 6 on each baseline, and scaling the phase correction to Band 9, the latter data can be corrected as well. This instantaneously provides an image at three times (= the frequency ratio) the resolution compared to the Band 6 image, i.e., a large and significant increase.

1.5.1 Objectives

Considering the aforementioned reasons for a true dual-frequency system for ALMA, the following objectives for this thesis work are proposed:

- Designing and construction of an optical system that once integrated into ALMA's cryostat will allow a true dual-frequency observation mode.
- Designing, fabrication and characterization of a frequency selective surface aimed to split the incoming from the secondary reflector of ALMA and, thus, illuminating the two target receivers.
- Designing, construction and characterization of a horn antenna aimed to operate in the frequency range of ALMA Band 6 (211-275 GHz). This antenna can be further used in a near-field beam pattern measurement system in order to test the quality of the constructed optical system.

1.5.2 Hypothesis

The integration of this optical system on a few antennas will allow ALMA to operates on a true dual-frequency observation mode. In this way, the longest baseline that ALMA can

reach using Band 6 will be as well available for Band 9. Hence, if the phase calibration is successfully transferred from low to high-frequency, ALMA will observe with its highest resolution ever achieved so far.

1.5.3 Structure of this thesis work

The above-mentioned objectives will be developed as follows. In chapter 2, we start with a revision of the state of art of dual-frequency receivers, followed by an overview aimed to describe the ALMA antennas specification within the quasioptics formalism. Then, the results obtained of the designed optical system are shown and the optical layout that makes possible splitting the beam for dual-frequency observation is presented. Additionally, the fabricated optical system is presented along with the calculated impact over the performance of the involved receivers. Then, in chapter 3, the frequency-selective surface that will allow splitting the electromagnetic for dual-frequency observation mode is designed and optimized for maximum transmission in the frequency range of Band 9 ($602-725$ GHZ). Several designs are presented, constructed and characterized by Fourier transform spectroscopy. Chapter 4 presents the design, development and further characterization of a novel kind of horn aperture antenna, the so-called spline-profile horns. A comparison of two types of geometries will be done and the one with the best performance will be identified. The antennas here presented have been designed to operate in the ALMA Band 6 frequency range ($211-275$ GHz). Once constructed, the characterization of the far-field radiation pattern will be done. The goal is to demonstrate that the constructed antenna is suitable to be integrated into a set-up aimed to characterize the designed optical system. Finally, in chapter 5 the conclusions of this thesis work are presented.

Chapter 2

Conceptual Design of a Dual-Frequency Receiver for ALMA

2.1 Introduction

To ensure that ALMA operates at its full potential during the next years, it is necessary to maintain a continuous instrumentation development program. Such a program is also motivated by the new technologies in the field of millimeter/submillimeter waves receivers, which can extend the current ALMA capabilities. As a part of this program, this project proposes to investigate the feasibility of simultaneous dual-frequency observations, using the existing Band 6 (211–275 GHz) and 9 (602–720 GHz) receivers of ALMA. This combination, or more generally for any combination of a low/middle and a high-frequency ALMA band, could permit an increase of accuracy in determining phase correction, due to transferring the phase calibration between bands, and double instantaneous frequency coverage for line surveys. In order to make possible these improvements, it is necessary to design an optical system that allows the combination of existing Band 6 and 9 beams and, also, having no impact on the normal operation of the telescope in its traditional single-frequency mode.

We start this chapter with a review of state of the art on dual-frequency receivers for radio astronomy. Then, the layout of the ALMA's bands is presented. This will justify why the combination of Bands 6 and 9 seems to be one of the best candidates to design a dual-frequency receiver. An analysis of the available space outside the cryostat is also fundamental if we want to introduce a new piece of hardware in it. Afterwards, we proceed with a brief description of the theory involved in the optical design for long-wavelength electromagnetic waves, the so-called Quasi-optical approximation. Finally, we conclude the chapter with our proposed layout of an optical beam combiner system along with a discussion of its constraints and limitations. A detailed tolerance analysis, which has fundamental importance when choosing the elements of the optical system that will be used to correct any possible misalignment in the optical system is also included.

2.2 State of the art of dual-frequency receivers

In this section, a review of radio-astronomical facilities that can perform dual-frequency measurements is presented. The most relevant telescopes and some array systems are mentioned.

- **SMA:** The Submillimeter Array is an eight-element radio interferometer designed to operate throughout the major atmospheric windows from about 180 to 900 GHz. In an effort to mitigate the effects of atmospheric instabilities, which limit the phase coherence of the array especially in the higher frequency bands, the array was designed to allow simultaneous operation of a low-frequency receiver (< 350 GHz) with a high-frequency receiver (> 600 GHz), by means of polarization diplexing. The overlap region of 330-350 GHz was included to facilitate dual-polarization measurements in the frequency range considered to offer the highest sensitivity for continuum observations with the array [34].

- **GREAT:** the German REceiver for Astronomy at Terahertz is a modular dual-color heterodyne instrument for high resolution far-infrared (FIR) spectroscopy covering the frequency windows between 1,25 and 2,5 THz on board of SOFIA. GREAT as a dual-color receiver records two frequencies simultaneously (the two beams must co-align on the sky within a fraction of their beam sizes). The signal from the telescope is separated into the two frequency channels by means of a beam splitter [35].

- **IRAM:** The EMIR receiver in operation at the 30 m telescope offers four frequency bands: B1: $83 - 117$ GHz, B2: $129 - 174$ GHz, B3: $200 - 267$ GHz, and B4: $260 - 360$ GHz. In each band, the two orthogonal polarizations are observed simultaneously. Dual-band combinations B1/2, B1/3, and B2/4 are available. In dual-band configuration, including sideband separation and polarization diplexing, up to eight IF channels are delivered to the spectrometers, totaling up to 64 GHz of signal bandwidth. Frequency diplexing relies on dichroic mirrors, also known as frequency selective surfaces (FSS) [36].

- **LLAMA:** The Large Latin American Millimeter Array (LLAMA) is a Vertex 12 m class telescope that will be located in the Puna de Atacama in the northwestern part of Argentina. It will have ALMA equivalent optics but with two APEX style Nasmyth Cabins (labeled as A and B). It has also been deemed scientifically desirable to have a simultaneous observation in cabin A and cabin B, by means of a dichroic filter (reflecting the low-frequency bands to Nasmyth cabin B and the high-frequency channels to Nasmyth cabin A.). For this reason, the long-term plans are to have ALMA bands 1, 3, 5 routed to cabin B, and ALMA bands 6, 7, 9 to cabin A [37].

- **VERA:** The VLBI Exploration of Radio Astrometry (VERA) is a Japanese VLBI array to explore the 3-dimensional structure of the Milky Way based on high-precision astrometry of Galactic maser sources. VERA is composed of four 20 m radio telescopes everyone of each is equipped with a dual-beam receiver system that can simultaneously observe two sources at 22 GHz and 43 GHz. The dual-band observations carried out with VERA have effectively cancelled out atmospheric fluctuations that usually undermine VLBI [38].

- **KVN:** The Korean VLBI Network (KVN) is a Korean array composed of three 21 m radio telescopes. KVN has developed an innovative multi-frequency band receiver system to observe four different frequencies at 22, 43, 86 and 129 GHz simultaneously. KVN capabilities have given astronomers a tool to study the formation and death of stars, and the structure and dynamics of the Milky Way. Additionally, alike VERA, KVN has also overcome the fundamental limitation due to atmospheric fluctuations that undermine VLBI observations [39].

After this study of the art of multi-frequency receiver facilities, we see that the idea of multi-band observation is not new. Furthermore, some interferometers have already overcome the phase fluctuation problem in this way. In the following section, we will proceed with an exploration of ALMA's receiver system. Mechanical and electronic constraints will be studied in order to determine which combination of bands is the best at the time of designing a dual-band receiver for ALMA.

2.3 Why using the Band 6 and 9 of ALMA?

As was discussed in chapter 1, ALMA is not exempt from image degradation caused by atmospheric effects or instabilities in the instruments. Even after phase correction under good weather conditions, phase fluctuations reach values that do not allow achieving the minimum coherence limit of 87% for reliable imaging. This effect is more notorious in observations at high frequencies, which directly restrict the maximum resolution that ALMA can achieve. One potential solution to solve this problem is by means of implementing a dual-frequency receiver. Thus, using the phase calibrator at low frequencies and then transferring the solution to the target at higher frequencies.

Figure 2.1 shows the receiver's layout of the ALMA cryostat. The relative positions for the windows and cartridges of each band are given with respect to the center of the circular surface. This information is vital for designing the optical system aimed to combine the two target ALMA bands. A preliminary analysis shows that a very limited impact on the ALMA system is needed. However, if the connected bands are aimed to be used simultaneously, they must share the input LO feed in order to preserve the relative phase after down-conversion. Another important factor to bear in mind is that the target bands must be close to each other, thereby, reducing the volume of the external hardware to be mounted on top of the cryostat. We deem that the pair of bands that best satisfy these two conditions are Band 6 and Band 9 (labelled in red in figure 2.1). Since there is a factor 3 in the frequency operation range between Band 6 and Band 9, an optical system that allows simultaneous observation with those bands will increase ALMA resolution in factor 3 (if phase solution is successfully transferred). Thus, when adding an optical beam combiner system to the ALMA phase correction process, it is expected that the telescope will produce the best possible images to date at high frequencies. Nevertheless, the feed LO range for the chosen bands does not fully overlap. In this way, the combination of these two bands will reduce the operating frequency range of each band. This issue will be addressed in more detail later in this chapter.

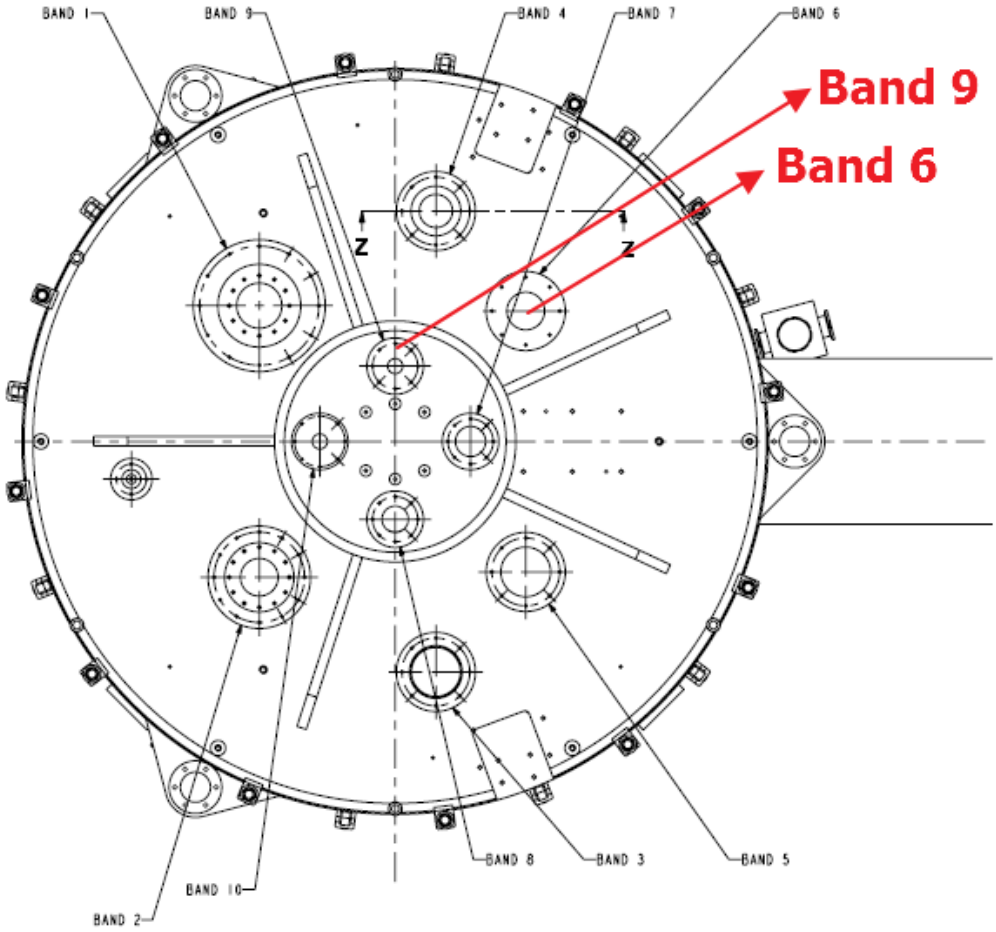

Figure 2.1: ***ALMA cryostat layout***

Due to wavelength dependence of diffraction, the four bands with the higher operation frequency (Band 7,8,9 and 10) are located at the center of the cryostat. The geometrical center corresponds to the origin of the coordinates system used in table 2.1.

Table 2.1: ***ALMA cryostat design specification***

Specifications of the ALMA cryostat for its ten observation bands. The wavelength here showed correspond to that at central frequency point for each band.

Band [GHz]	Frequency [GHz]	Wavelength λ [mm]	Cartridge Location [mm,deg]	Window Location [mm,deg]
1	35-50	7.89	(295,135^o)	(255,135^o)
2	65-90	3.85	(295,-135^o)	(255,-135^o)
3	84-116	3.00	(335,-80^o)	(310.7,-80^o)
4	125-163	2.08	(335,80^o)	(310.7,80^o)
5	163-211	1.60	(295,-45^o)	(245,-45^o)
6	211-275	1.23	(295,45^o)	(245,45^o)
7	275-373	0.93	(150,0^o)	(100,0^o)
8	385-500	0.68	(150,-90^o)	(103.3,-90^o)
9	602-720	0.45	(150,90^o)	(100,90^o)
10	787-950	0.35	(150,180^o)	(100,180^o)

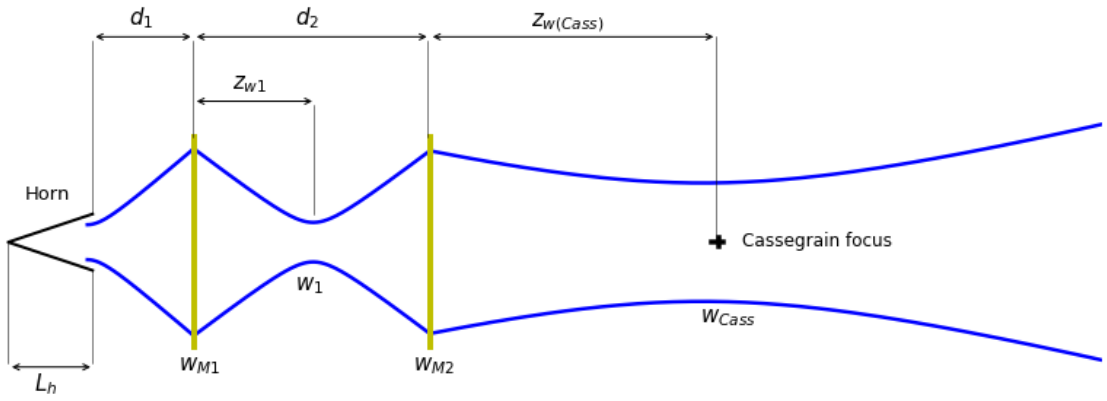

Figure 2.2: ***Optical train representation.***
Schematic representation of the general cold optics system for each ALMA Band. This optical system is presented in each of ten bands and it is located between the feed horn and the secondary reflector. All the focusing elements (represented with yellow lines) correspond to off-axis mirrors, except for Bands 1 and 2, where the first focusing element corresponds to a lens and the second is absent. Tables 2.2 and 2.3 show the specific values for each band.

2.3.1 Specifications of Band 6 and 9 receivers

Now, we proceed to the detailed description of the bands of interest for this project, i.e., Bands 6 and 9. It is important to highlight that all the optical components for both bands are inside the cryostat. This is known as "cold optics" since those optical components are at a temperature close to 4 K.

An important tool to characterize and represent any optical system is the so-called "Optical Train", which is a beam diagram that shows how the properties of that beam change as it propagates through an optical system. Since all the ALMA bands were designed in a coherent way, there is a general optical train that is used to characterize each of the ten ALMA Bands and it is shown in figure 2.2. The parameters d_i correspond to the distance between focusing elements, w_{Mi} are the beam radius at a specific focusing element, w_{cass} is the beam waist and L_h is the horn axial length.

The description of Bands 6 and 9, following the optical train context, are shown in tables 2.2 and 2.3, respectively. Additionally, schematics of the cold optics are shown in figure 2.3. Any optical system aimed to combine bands 6 and 9 must be thought in such a way that the existing cold optics for each band must be coupled (optical matched) to the new optical system to be mounted on the top of cryostat.

2.3.2 Analysis of available space to introduce additional hardware

As a starting point, it is important to highlight that not all the space above the cryogenic chamber is available to be used in this optical system. There already exists many optical, electronic and calibration devices, like, WVR, warm optic elements, and lenses. For this

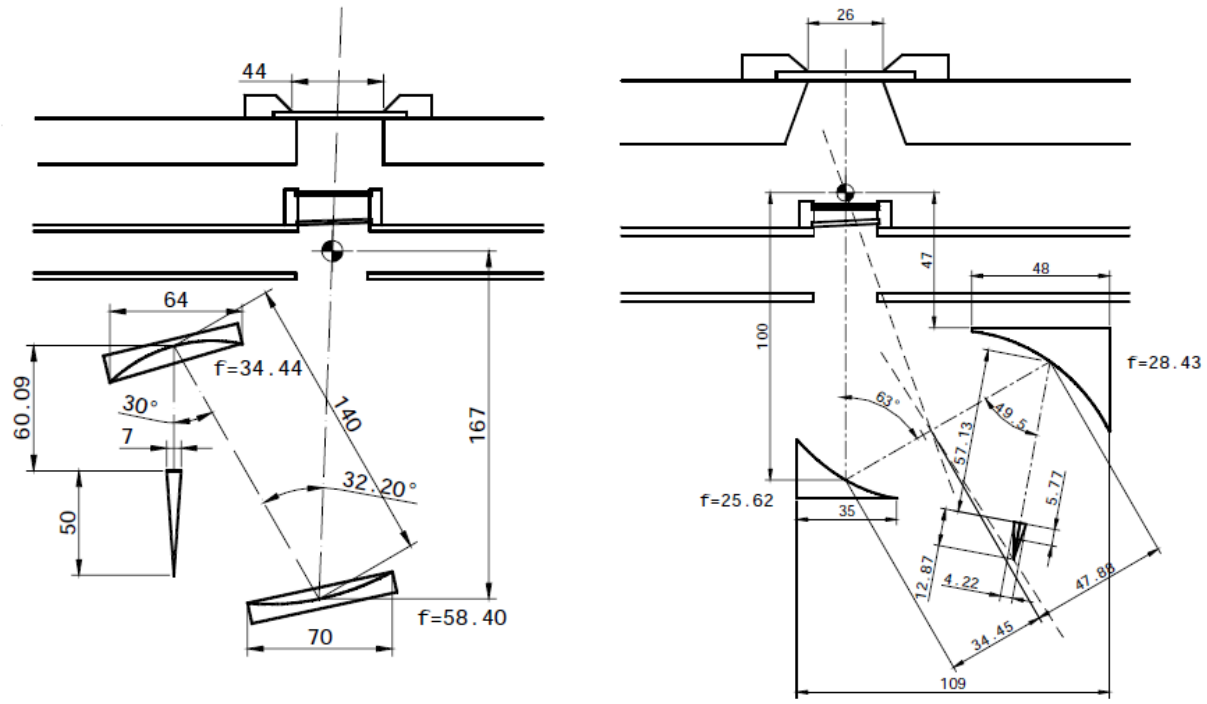

Figure 2.3: ***Cold optics drawing of Band 6 and 9.***
Schematic of Bands 6 (left) and 9 (right). These optic systems are located within the cryostat and term "cold" makes reference to the fact that the surrounding temperature has been set-up to 4 K.

reason, it is important to define a Safe Working Zone (SWZ) which will guarantee that the beam will not crash with any object in its path, producing undesirable effects such as diffraction or interference. Figure 2.4 shows the path taking a straight line from Band 6 to Band 9 window. This figure shows that there is a bracket partially blocking the path. To avoid this obstacle, and any other that could show up in the optical path of the beam, the first goal is to clearly identify the SWZ by means of inspecting the CAD file of the cryogenic chamber (which is available in the ALMA database). Figure 2.5 shows the SWZ, whose volume shape corresponds to a cylinder of diameter Φ and length L. The cylinder goes from Band 6 to 9 passing above the Band 4 bracket structure, however, the height cannot exceed a certain maximum given by H. The parameters that define the SWZ are given in table 2.4.

Since the SWZ has been defined, we can now proceed with the design of the optical system aimed to combine the target ALMA bands. Nevertheless, since we are dealing with long-wavelength electromagnetic beams, the effects of diffraction must be taken into account in order to come out with a low-distortion system that will not reduce the sensitivity of the involved ALMA bands. In the following section, we introduce the concept of Gaussian Optics, which is indispensable at the time of designing any optical system for radio astronomical applications.

2.4 Quasi-Optics and Gaussian beam approximation

Gaussian beams play an important role in large-wavelength systems such as laser, microwave, and radio-astronomical systems. In this section, we give a brief derivation of the Gaussian

Table 2.2: ***Optical train description of ALMA Band 6***

Frequency [GHz]		211	243	275
λ [mm]		1.420817	1.233714	1.090154
Horn diameter	7.0			
Horn axial length (L_h)	50.0			
Horn slant length	50.122			
Horn waist, w_0		2.198	2.181	2.162
Horn waist offset, $\Delta z(w_0)$		-2.3902	-3.1216	-3.9292
Waist at horn aperture, w_{ha}		2.252	2.252	2.252
d_1	59.89			
R_{s1}	65.277	64.112	65.340	66.663
f_1	34.44			
$R_{\mathrm{i}1}$	72.905	74.414	72.825	71.249
Waist at mirror 1, w_{M1}	(dia.=64)	13.003	11.553	10.468
z_{w1}		71.577	69.629	67.798
w_1		2.539	2.420	2.304
d_2	140.00			
R_{s2}	73.421	71.389	73.533	75.443
f_2	58.397			
$R_{\mathrm{i}2}$	275.39	320.874	283.696	258.458
Waist at mirror 2, w_{M2}	(dia.=70)	12.452	11.671	11.116
$z_{w(Cass)}$	166.86	171.035	169.986	169.281
w_{Cass}		8.509	7.389	6.530
$\mathrm{d}_{mirror-subrefl}$		6166.76	6166.76	6166.76
$w_{subrefl}$	(dia.=750)	318.796	318.796	318.796
$R_{subrefl}$	6000.00	5999.999	5999.997	5999.996
Edge Taper ($\mathrm{d}B$)	12.00	12.02	12.02	12.02

beam formulas following the methodology used in [40].

2.4.1 Gaussian beam theory

Diffraction is the tendency of radiation to change its spatial distribution as the distance from the source varies. This effect dominates the propagation of electromagnetic radiation when the wavelength is comparable to the dimensions of the system. Quasioptic theory deals with those beams whose diameters are moderately large when is measured in wavelengths. In this situation, Gaussian-beam formalism can be used. It allows modeling a realistic situation within not highly restrictive limits. Gaussian beams correspond to electromagnetic waves that spread out transversely as they propagate. The energy distribution of this type of waves can be accurately modeled by using a Gaussian fit, whose parameters change as the wave propagates. Thus, it is impossible to have a perfectly collimated beam from a Gaussian beam source. For this reason, it is important to deal with these waves using the formulas given by Gaussian-beam formalism. Otherwise, the spill-over experimented by the beam, as it propagates through the -here presented- optical system, can lead to a significant reduction in the sensitivity of the overall system.

2.4.2 The paraxial wave equation

In very specific cases, the propagation of an electromagnetic wave results in a distribution of field amplitudes that is independent of position, as for example a plane wave. A simplified

Table 2.3: ***Optical train description of ALMA Band 9***

Frequency [GHz]		602	661	720
λ [mm]		0.497994	0.453544	0.416378
Horn diameter	4.22			
Horn axial length (L_h)	12.87			
Horn slant length	13.042			
Horn waist, w_0		1.358	1.358	1.358
Horn waist offset, $\Delta z(w_0)$		-5.7771	-6.3836	-6.9405
Waist at horn aperture, w_{ha}		1.013	0.970	0.929
d_1	57.13			
R_{s1}	64.15	63.574	64.183	64.731
f_1	28.43			
$R_{\mathrm{i}1}$	51.06	51.428	51.037	50.695
Waist at mirror 1, w_{M1}	(dia.=48)	9.892	9.501	9.191
z_{w1}		51.0740	50.6993	50.3766
w_1		0.821	0.773	0.729
d_2	82.33			
R_{s2}	32.13	31.835	32.172	32.456
f_2	25.62			
$R_{\mathrm{i}2}$	126.546	131.229	125.799	121.640
Waist at mirror 2, w_{M2}	(dia.=35)	6.089	5.958	5.857
$z_{w(Cass)}$	100.00	99.8028	99.7058	99.6317
w_{Cass}		2.980	2.714	2.491
$\mathrm{d}_{mirror-subrefl}$		6099.27	6099.27	6099.27
$w_{subrefl}$	(dia.=750)	319.198	319.198	319.198
$R_{subrefl}$	6000.00	5999.990	5999.998	6000.004
Edge Taper (dB)	12.00	11.99	11.99	11.99

Table 2.4: ***Dimension of the SWZ***

Symbol	Quantity	Value (mm)
Φ	Maximum Radius	73
L	Maximum Length	188
H	Maximum Height	200

problem comes across when a beam of radiation that is largely collimated, i.e., it has a well-defined direction of propagation but has also some transverse variation. The paraxial wave equation, which forms the basis for Gaussian beam propagation, describes a beam with a limited transverse variation compared to a plane wave.

Consider now a single electromagnetic wave propagating in a uniform medium, whose electric or magnetic field ψ satisfies the Helmholtz wave equation,

$$(\nabla^2 + k^2)\psi = 0, \tag{2.1}$$

where a time variation at angular frequency ω of the form $\exp(j\omega t)$ has been assumed. For a beam of radiation that is similar to a plane wave but for which some variation perpendicular to the axis of propagation is allowed, it is possible to assume that the electric and magnetic fields are mutually perpendicular to the direction of propagation. Setting the direction of

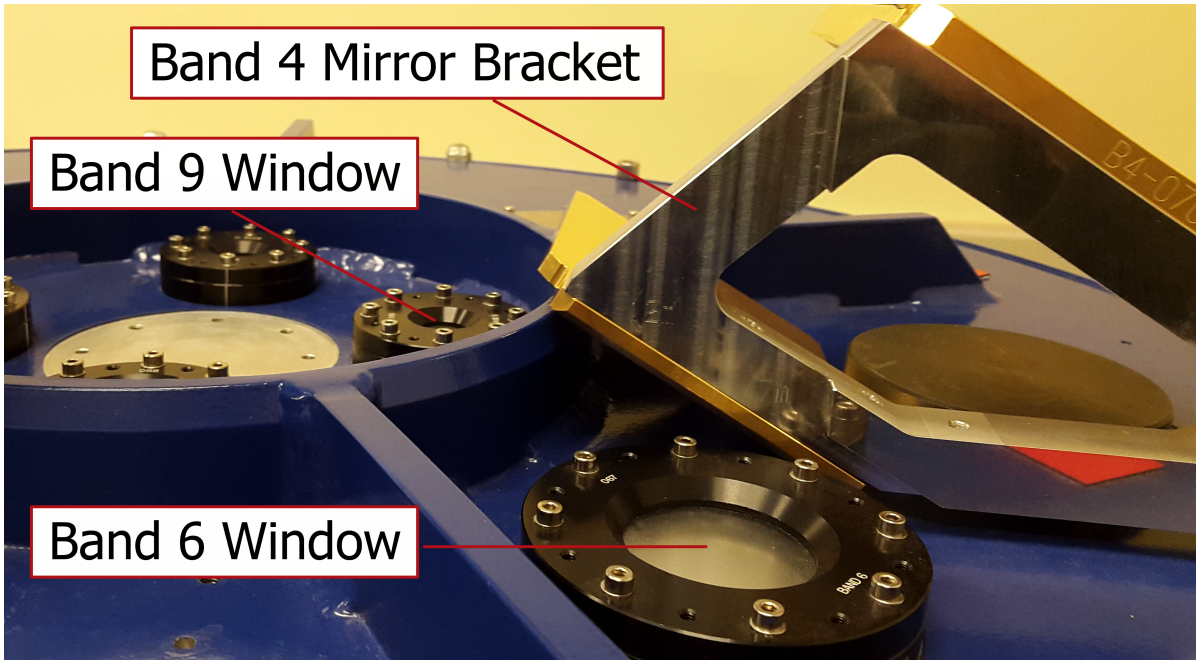

Figure 2.4: ***Images of the cryostat.***
It is possible to see that the straight line that connects the centers of Band 6 and 9 is not completely clear. In fact, there is a metallic bracket in the middle of the path. Hence, the available space to design the structure that will support the optical system must be identified.

propagation in the positive z direction, the distribution for any component of the electric field takes the form

$$E(x, y, z) = u(x, y, z) \exp(-jkz) \tag{2.2}$$

where u is a complex scalar function that defines the non-plane wave part of the beam. Let us assume that:

- The variation along the direction of propagation of the amplitude u (due to diffraction) is small over a distance comparable to a wavelength, and
- The axial variation is small compared to the variation perpendicular to this direction.

Then we can obtain the **paraxial wave equation** in rectangular coordinates,

$$\frac{\partial^2 u}{\partial x^2} + \frac{\partial^2 u}{\partial y^2} - 2jk\frac{\partial u}{\partial z} = 0. \tag{2.3}$$

Solutions to the paraxial wave equation are the Gaussian beam modes that form the basis of the design of the quasi-optical system.

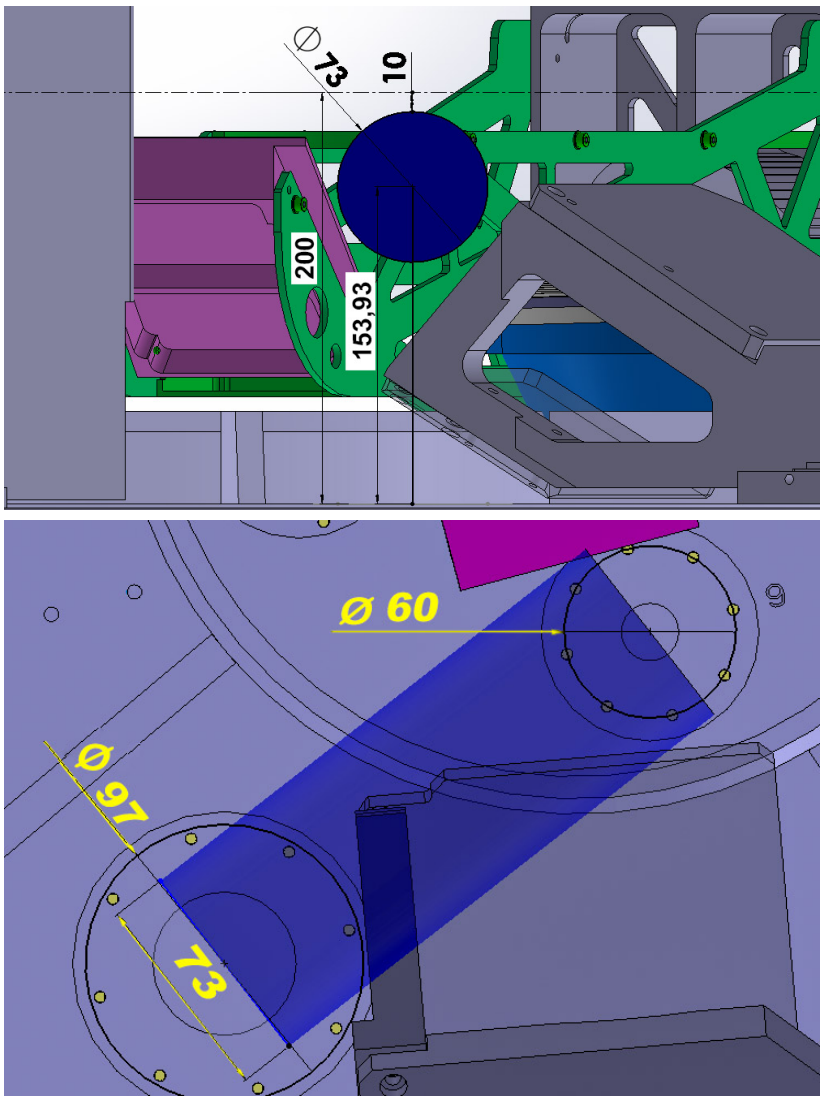

Figure 2.5: ***The Safe Work Zone***
The shaded region represents the maximum available space that we have to design the beam combiner system and its support structure. This region has a cylindrical shape and its specifications are listed in table 2.4.

2.4.3 Gaussian beam propagation

It is more convenient to express the solutions of the paraxial wave equation in cylindrical coordinates, as the axial symmetry characterizes many situations encountered in practice (e.g., corrugated feed horns and lenses). In this coordinate system, r represents the perpendicular distance from the axis of propagation, taken again to be the z axis, and the angular coordinate is represented by φ. Assuming axial symmetry, that is, u is independent of φ, we obtain the **axially symmetric paraxial wave equation**,

$$\frac{\partial^2 u}{\partial r^2} + \frac{1}{r}\frac{\partial u}{\partial r} - 2jk\frac{\partial u}{\partial z} = 0. \tag{2.4}$$

The simplest solution of equation 2.4 can be written in the form,

$$u(r,z) = A(z)\exp\left[\frac{-jkr^2}{2q(z)}\right] \tag{2.5}$$

where A and q are two complex functions (of z only), which remain to be determined. The function q is called the complex beam parameter, but it is often referred to simply as the beam parameter or **Gaussian beam parameter**.

This wave can be characterized by its radius of curvature R, the beam radius w and the beam phase shift ϕ_0 as a function of position along the axis of propagation. Respectively we have

$$R(z) = z\left[1 + \left(\frac{\pi w_0^2}{\lambda z}\right)^2\right], \tag{2.6}$$

$$w(z) = w_0\left[1 + \left(\frac{\lambda z}{\pi w_0^2}\right)^2\right]^{1/2}, \tag{2.7}$$

$$\phi_0(z) = tan^{-1}\left(\frac{\lambda z}{\pi w_0^2}\right). \tag{2.8}$$

The beam radius w is the value of the radius at which the field falls to 1/e relative to its on-axis value, and w_0 denotes the beam radius at $z = 0$, which is called the **beam waist radius**. We see that the beam waist radius is the minimum value of the beam radius and that it occurs at the beam waist, where the radius of curvature is infinite, characteristic of a plane wave-front. Now with all these definitions, it is possible to express the fundamental Gaussian beam mode $u(r,z)$ and the electric field $E(r,z)$ by means of

$$u(r,z) = \frac{w_0}{w}\exp\left(\frac{-r^2}{w^2} - \frac{j\pi r^2}{\lambda R} + j\phi_0\right), \tag{2.9}$$

and

$$E(r,z) = \frac{w_0}{w}\exp\left(\frac{-r^2}{w^2} - jkz - \frac{j\pi r^2}{\lambda R} + j\phi_0\right). \tag{2.10}$$

Figure 2.6 shows the typical behaviour of a Gaussian beam, which is given by equation 2.10. This figure shows how the beam diffracts as it propagates.

2.4.4 Asymptotic behaviour of Gaussian beams

The description of a Gaussian beam has a particularly simple form when expressed in terms of the confocal distance z_c (or Rayleigh range). This parameter z_c will help us to distinguish

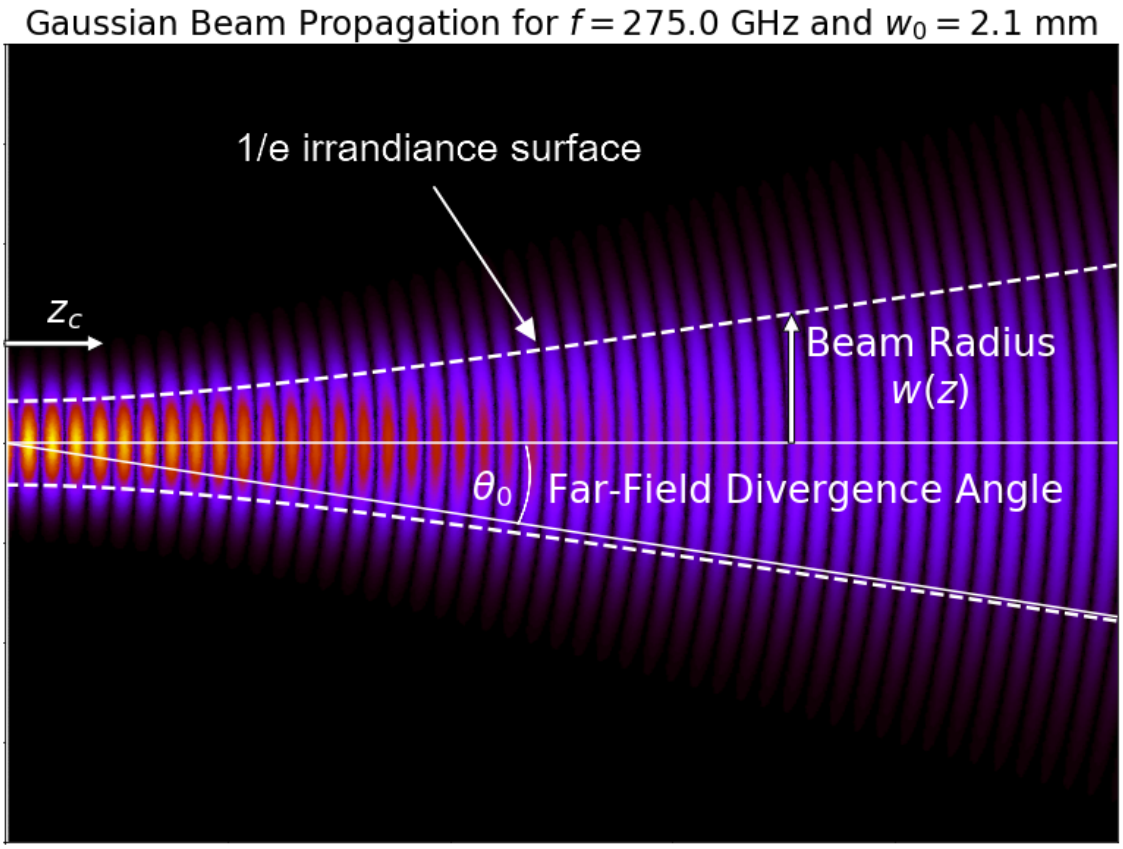

Figure 2.6: ***Gaussian beam representation.***
In a Gaussian beam spreading, it is possible to observe how the beam changes its radius of curvature (and also its beam radius) as it propagates. The beam waist w_0 represents the region where the beam radius has its minimum value. The confocal distance z_c defines the interface between near-field and far-field regions.

between Near-Field (NF) and Far-Field (FF) for the Gaussian beam propagation (a more detailed description about NF and FF will be given in chapter 4), and it is defined as

$$z_c = \frac{\pi w_0^2}{\lambda}. \tag{2.11}$$

Using this definition, the Gaussian-beam parameters given by equations 2.6, 2.7 and 2.8, can be written as

$$R = z + \frac{z_c^2}{z}, \tag{2.12}$$

$$w = w_0 \left[1 + \left(\frac{z}{z_c}\right)^2\right]^{0,5}, \tag{2.13}$$

$$\phi_0(z) = \tan^{-1}\left(\frac{z}{z_c}\right), \tag{2.14}$$

Respectively. It is evident that the radius of curvature R, the beam radius w, and the Gaussian beam phase shift ϕ_0, all of them change considerably between the beam waist and the confocal distance z_c. It is possible to define certain regions along the beam propagation, specifically the 'near field', defined by $z \ll z_c$ and a 'far-field', defined by $z \gg z_c$, making an analogy with a more general diffraction theory. The "transition region" takes place at the confocal distance z_c. The beam radius w attains its minimum value w_0 at the beam waist, and the electric field is highly concentrated in that point, as shown in figure 2.6. This means that the electric field and power distributions have their maximum values at the beam waist. Regarding the radius of curvature R and phase shift ϕ_0, they are infinite and zero, respectively, at the beam waist.

Far from the beam waist (i.e. in the far-field), the beam radius increases monotonically as described by equation 2.13. Close to the beam waist (in the near field) the beam radius is essentially unchanged from its value at the beam waist. This leads us to the conclusion that the confocal distance establishes the distance over which the Gaussian beam propagates without significant growth, i.e it is essentially collimated. As we move away from the waist, the radius of curvature decreases until we reach a distance z_c. At distances from the waist equal to z_c, the beam radius is equal to $\sqrt{2}w_0$, the radius of curvature attains its minimum value equal to $2z_c$, and the phase shift is equal to $\pi/4$. At distances from the waist greater than z_c, the beam radius grows significantly, and the radius of curvature increases.

In the far-field, $z \gg z_c$, the beam radius grows linearly with the distance. The growth of the 1/e radius of the electric field can be defined in terms of the angle $\theta = \tan^{-1}(w/z)$ (see figure 2.6), and in the far-field limit we obtain the asymptotic beam growth angle θ_0 given by

$$\theta_0 \cong \frac{\lambda}{\pi w_0}. \tag{2.15}$$

Equation 2.15 is quite useful when we attempt to estimate the beam waist of an optical system, for instance, the beam waist of a feed horn used to illuminate a telescope.

2.4.5 Edge Taper

The field distribution and the power density of the fundamental Gaussian beam mode are both maxima on the axis of propagation ($r = 0$) at the beam waist ($z = 0$). The field amplitude and power density diminish as z and r vary from zero. The power density always drops monotonically as a function of r for fixed z, reflecting its Gaussian form. The fundamental Gaussian beam mode has a Gaussian distribution of the electric field perpendicular to the axis of propagation. The distribution of power density is proportional to this electric field squared and given by

Table 2.5: ***Reference Values for the Gaussian beam*** T_e ***and*** F_e

r_e/w	$T_e(r_e)$	$F(r_e)$	$T_e(\mathrm{d}B)$
0.0	1.000	0.0000	0.0
0.2	0.9231	0.0769	0.4
0.4	0.7262	0.2739	1.4
0.6	0.4868	0.5133	3.1
0.8	0.2780	0.7220	5.6
1.0	0.1353	0.8647	8.7
1.2	0.0561	0.9439	12.5
1.4	0.0198	0.9802	17.0
1.6	0.0060	0.9940	22.2
1.8	0.0015	0.9985	28.1
2.0	0.0003	0.9997	34.7
2.2	0.0001	0.9999	42.0

$$\frac{|P(r)|}{|P(0)|} = \exp\left[-2\left(\frac{r}{w}\right)^2\right], \tag{2.16}$$

where r is the distance from the propagation axis. Since the basic description of the Gaussian beam mode is in terms of its electric field distribution, it is most natural to use the width of the field distribution to characterize the beam, although it is true that the power distribution is more often directly measured.

A straightforward way to characterize a Gaussian beam in terms of the relative power level at a specified radius is given by the edge taper T_e. It corresponds to the relative power density at a radius r_e and is defined as

$$T_e(r_e) = \exp\left(\frac{-2r_e^2}{w^2}\right). \tag{2.17}$$

The edge taper is often expressed in decibels to accommodate efficiently a large dynamic range,

$$T_e(\mathrm{d}B) = -10\log_{10}(T_e). \tag{2.18}$$

It is also convenient to define the parameter $F(r_e)$, which corresponds to the fractional power of the Gaussian beam that falls inside the radius r_e, and is defined as

$$F_e(r_e) = \int_{r=0}^{r=r_e} |E(r)|^2 2\pi r \mathrm{d}r = 1 - T_e(r_e). \tag{2.19}$$

Table 2.5 shows some reference values for T_e. Note that a diameter of $4w$ truncates the beam at a level of 34.7 dB on the axis of propagation and includes 99.97% of the power in the fundamental mode of a Gaussian beam. Such diameter is generally sufficient to make the effects of diffraction (over the power distribution) negligible. This criterion will be used to define the proper size of each mirror in the optical system to be designed. Thus, the power loss due to beam truncation will be reduced.

2.4.6 Quasioptical design: ABCD matrix formalism

Quasi-optical systems can be analyzed in a manner analogous to the treatment of rays in a linear geometrical optics system. In this approach, the location and slope of a ray at the output plane of a paraxial system are defined to be linear functions of the parameters of the input ray. Denoting the position as p and the slope as s for a beam that travels through a general optical system, we can write the linear relationship between input and output ray position and slope as

$$\begin{pmatrix} p_{out} \\ s_{out} \end{pmatrix} = \begin{pmatrix} A & B \\ C & D \end{pmatrix} \begin{pmatrix} p_{\mathrm{in}} \\ s_{\mathrm{in}} \end{pmatrix}, \tag{2.20}$$

where array algebra notation has been adopted. The extension of this ray transformation approach to Gaussian beams leads to the "$ABCD$" law in which the four parameters characterizing an optical system element operates in a manner similar to geometrical optics elements. Parameters A, B, C and D are the same as for the geometrical optic system element. The $ABCD$ elements, combined into a 2×2 matrix, form the ray transfer matrix of the system.

The $ABCD$ law is an enormous aid to quasioptical analysis since all of the geometrical optics ray theory can be applied to the Gaussian-beam representation of a system. Setting the convention that rays incident from the left, we obtain the matrix that represents the total effect of a sequence of elements just by multiplying the respective individual $ABCD$ matrices. Starting with that for the first element encountered by the beam and multiplying by the matrix for each subsequent element placed on the left in the matrix equation.

To find the beam transformation properties of a Quasioptical system by means of the $ABCD$ law, let us consider the situation illustrated in figure 2.7. We find the matrix $\mathbf{M}$, which represents the propagation of a beam a certain distance d_{in} in direction to a certain optical system, the transformation of its properties by that system, and finally, propagation a distance d_{out} moving away from the optical system is described by

$$\begin{aligned} \mathbf{M} &= \begin{pmatrix} 1 & \mathrm{d}_{out} \\ 0 & 1 \end{pmatrix} \begin{pmatrix} A & B \\ C & D \end{pmatrix} \begin{pmatrix} 1 & \mathrm{d}_{in} \\ 0 & 1 \end{pmatrix} \\ \mathbf{M} &= \begin{pmatrix} A + C\mathrm{d}_{out} & A\mathrm{d}_{in} + B + \mathrm{d}_{out}(C\mathrm{d}_{in} + D) \\ C & C\mathrm{d}_{in} + D \end{pmatrix}. \end{aligned} \tag{2.21}$$

From this expression, we can obtain the distance from the system output plane to the output beam waist and the output waist radius,

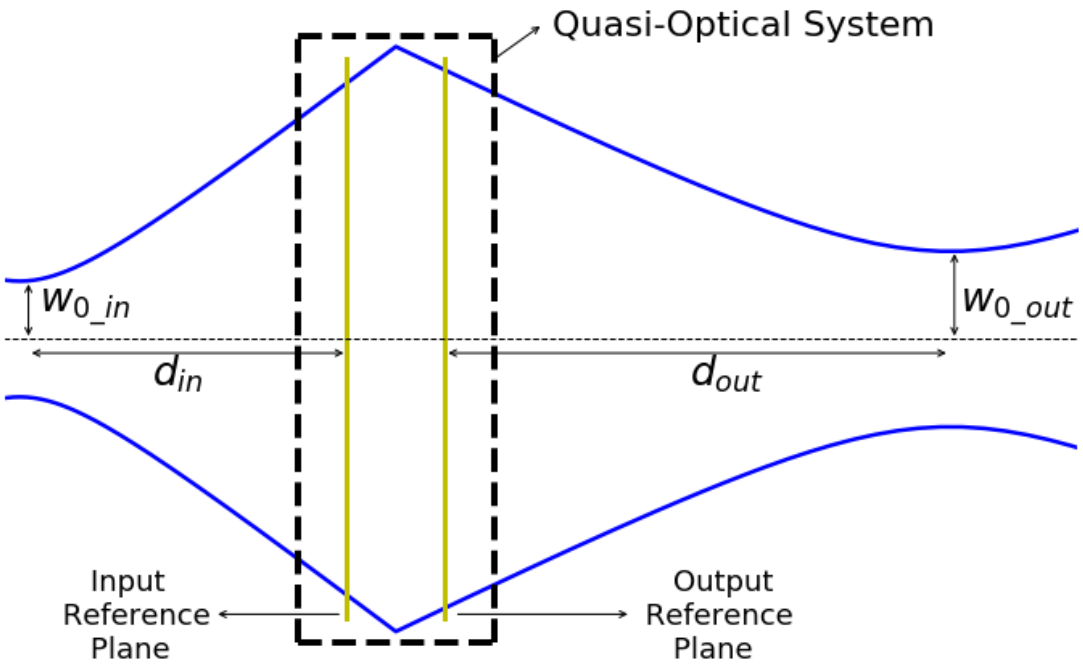

Figure 2.7: ***Transformation of a Gaussian-beam.***
Representation of a Gaussian-beam which travels through a certain optical system. The input waist w_{0_in} is located at a distance d_{in} from the system input reference plane. The output beam has a new beam waist w_{o_out} which is located at a distance d_{out} from the output reference plane.

$$\mathrm{d}_{out} = \frac{(A\mathrm{d}_{in} + B)(C\mathrm{d}_{in} + D) + ACz_c^2}{(C\mathrm{d}_{in} + D)^2 + C^2 z_c^2}, \tag{2.22}$$

$$w_{0out} = \frac{w_{0in}}{[(C\mathrm{d}_{in} + D)^2 + C^2 z_c^2]^{0,5}}. \tag{2.23}$$

These equations apply to any quasioptical system, and to any Gaussian beam mode in the paraxial limit. The system itself can be arbitrarily complicated, and all we have to do is to obtain its $ABCD$ matrix from a cascaded representation of its constituent elements. A more detailed explanation of this formalism, along with the matrix representation for any optical element (e.g. flat mirrors, lenses, etc) can be found in [41].

The ABCD formalism represents a convenient form to deal with a Gaussian beam propagating through an optical system. Thus, the size of the mirrors that will build-up the optical system for combining the Bands 6 and 9 of ALMA will be calculated by this formalism.

2.5 Sensitivity losses and beam distortion

Other important considerations for any astronomical facility are the losses present in the receivers. Among all the existent losses the most relevant for the ALMA receivers are listed below

- **Ohmic losses in metallic reflectors and grids:** they depend on the material, temperature and surface roughness [42].
- **Dielectric losses:** strongly depends on the material parameters [43].
- **Ruze's loss:** produced by scattering due to surface random imperfections [44].
- **Truncation losses:** product of the aperture efficiency and diffraction [45].
- **Aberration due to phase center shift:** this happens when a beam is refocused and hence forced to change its phase [46].
- **Cross-polarization losses and distortion:** they occur when part of the power comes in a non desired polarization component [47].
- **Beam coupling losses:** they are product of misalignment in a optical system aimed to refocus the beam into a feed system [48].

It is important to keep in mind all these losses when working in the design of an optical system. These can be reduced by optimizing the geometry of the system or, by choosing a different material. Among the contributions listed above, there are two types of losses that are extremely important when designing an optical system. Those contributions are the cross-polarization and the beam coupling. Therefore, one goal for our optical system will be making these loss contributions as little as possible, which can be done by optimizing the geometrical configuration of the optical system.

2.5.1 Cross-polarization

Let us consider an electromagnetic beam with a linear polarization state (co-polar component). Cross-polarization (or cross-polar) corresponds to the polarization orthogonal to the polarization being discussed [47]. For instance, if the beam is vertically polarized, the cross-polar component is meant to be horizontal polarization[1]. This definition of cross-polar arises from the fact that an antenna is never fully polarized in a single polarization state. Therefore, cross-polar can be understood as an undesirable polarization state which leaks a certain amount of power from the desired co-polar component. This takes significant importance when an antenna is used as a feed system for an astronomical receiver because this cross-polar component will be added to the total noise of the system. Hence, keeping this cross-polar component as little as possible is one of the main goals at the time of designing an optical system aimed for astronomical applications.

Conic section reflectors (e.g. parabolic, ellipsoidal, or hyperbolic) are widely used in radio frequency engineering and radio astronomy systems. They allow an optimal electromagnetic coupling between waves coming from a source and a detection system. In particular, we focus on the implementation of the elliptical mirror, which is simply a plane mirror with an elliptical-shaped face. This kind of mirror is ideal for research and astronomical applications because of its property of bending and folding light at precise angles with minimum wave distortion. Elliptical mirrors are widely used in the high-frequency ALMA bands since they allow to match the incident beam coming from the secondary reflector to their respective mixer horn. An example of the utility of these mirrors is the cold optical system of Band 9 [49], which is schematically represented in figure 2.8. Here, the main ray is given by blue

[1]Ditto, if the polarization is Right Hand Circularly Polarized (RHCP), the cross-polarization is Left Hand Circularly Polarized (LHCP).

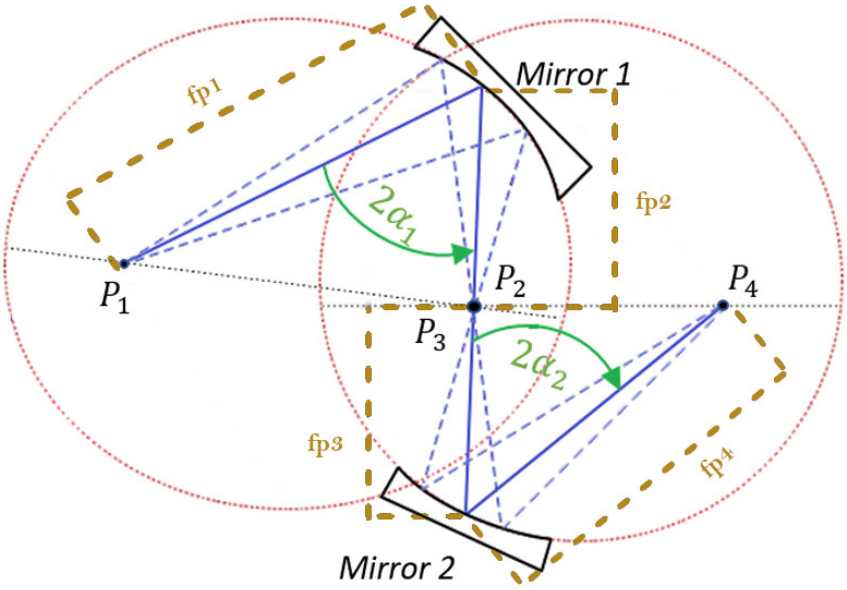

Figure 2.8: ***General elliptical mirror configuration.***
Optical layout to minimize distortion using two elliptical mirrors. The main ray is represented by the blue solid line and the marginal rays are represented by the blue dashed lines. The point P_1, P_2, P_3, P_4 correspond to focal points of the ellipse defined by the mirror 1 and 2 respectively.

solid line and the deflected ray is given by the red dashed line. Two elliptical mirrors M_1 and M_2 with focal points P_1, P_2 and P_3, P_4 respectively are arranged in such a way that P_2 coincides with P_3, this configuration is known as Gaussian beam telescope. The telescope focal plane is located at fp_1. The mixer horn is located at fp_4. Distances (R_1, R_2 , R_3, R_4) are usually defined by Quasioptics calculations and are chosen for optimal matching. Two bending angles (α_1,α_2) are also required to define an ellipse shape. These two angles are usually chosen as small as possible in order to minimize distortion losses (L_{dist}) and cross-polar losses (L_{cp}), introduced to the system by the simple fact that those mirrors are off-axis reflecting elements, which produces changes in the phase front of the beam [50].

These losses for a Gaussian beam that concentrates all its power in the fundamental mode (ideal situation), can be estimated expressing the beam profile, after reflection, by a linear combination of higher-order propagation modes. A common assumption is considered a Hermite Gaussian set of modes [51]. The distortion (or scalar) losses due to the amplitude and phase transformation are given by

$$L_{\text{dist}} = \frac{w^2 \tan^2(\alpha)}{8f^2}. \tag{2.24}$$

On the other hand, the cross-polar (or vectorial) losses, for any incident polarization is given

by

$$L_{cp} = \frac{w^2 \tan^2(\alpha)}{4f^2}, \tag{2.25}$$

where w is the Gaussian beam radius at the mirror, α is a bending angle and f is the focal distance of a mirror.

When more than one off-axis mirror is used in a system (as shown in figure 2.8), it is necessary to calculate how the phases of the initial beam vary as the beam propagates through the optical system. The sign of the phase variation, after reflection in an off-axis mirror, depends on the orientation of the coordinate system, which is defined by the reflection at the target mirror relative to the previous mirror. In the worst case (considering the simplest system consisting of two off-axis mirrors) the losses from the two mirrors sum up. On the other hand, in the best case, the field profile incident on the second mirror must be an inverted image of the profile of the reflected beam from the first mirror, fully cancelling the overall beam distortion. Hence, the design of a low-distortion optical system must be done in such a way that the overall distortion introduced by off-axis mirrors is left at a negligible level.

For a more general situation, consisting of a certain number of off-axis mirrors, the losses in power L_{sys} can be calculated by

$$L_{sys} = \mid [\Sigma_1^n [\beta(w_m/f)_{\mathrm{i}}. \tan(\theta_{\mathrm{i}}). \exp(-j\Sigma_1^n \alpha.\Delta\phi_{k\to k+1})] \mid^2, \tag{2.26}$$

where $\Delta\phi_{k\to k+1}$) is the fundamental mode phase slippage between mirror k and $k+1$, with $\alpha = 3$, $\beta = 1/2\sqrt{2}$ for scalar losses and $\alpha = 1$, $\beta = 1/2$ for cross polarisation losses. However, equation 2.26 can be approximated to [50]

$$\alpha_2 = \arctan\left(\frac{(1+M_1)\tan(\alpha_1)}{1+\frac{1}{M_2}}\right), \tag{2.27}$$

$$L_{cp} = \left|\frac{w_1^2 \tan^2(\alpha_1)}{8f_1^2} - \frac{w_2^2 \tan^2(\alpha_2)}{8f_2^2}\right|. \tag{2.28}$$

Equation 2.27 gives an approximated relation for bending angles, where $M_1 = R_2/R_1$ and $M_2 = R_4/R_3$. Thus, the full beam distortion can be calculated by the approximation given by equation 2.28.

2.5.2 Beam coupling efficiency

When designing a quasi-optical system many factors could eventually reduce the fraction of transmitted power from the source to the receiver system. The most common factors that arise are a mismatch between beams, errors in the construction of the system or misalignment

of the quasi-optical system. These factors reduce the efficiency of the beam coupling and, hence, the efficiency of the quasi-optical system [41]. Bearing this in mind, it is of fundamental importance to at the time to analyze the resulting coupling, and therefore, being able to specify tolerances for the construction and assembly of different parts in a quasi-optical system.

The two-dimensional field coupling coefficient between two Gaussian beams labeled as a and b, is defined as the overlap integral of the normalized electric field distribution of both beams over a traverse reference plane S perpendicular to the axis of propagation. This coefficient is given by

$$c_{ab} = \int\int_S E_a^* E_b \mathrm{d}S. \tag{2.29}$$

The power coupling coefficient between the two beams represents the fraction of incident power flowing in the first beam that ends up in the second. In equation 2.29, scalar fields have been assumed, however, special attention must be taken with polarization effects and normalization, due to the true field coupling is a vector equation. Therefore, it is assumed that both fields are polarised in the same sense (since a scalar approximation has been used), i.e.,

$$K_{ab} = |c_{ab}|^2. \tag{2.30}$$

In this equation it is assumed that the polarization states of the beams are the same. If this is not the case, the coupling coefficient is a fixed quantity that does not depend on the Gaussian beam aspect of the propagating radiation.

Axially aligned beams

In the case of axially aligned beams, as shown in figure 2.9, the two Gaussian-beams have a common axis of propagation. In the most general case of the fundamental mode in two dimensions, the beam coupling coefficient is given by

$$c_{ax}^2 = \frac{2j\lambda \exp\left[j(\Delta\phi - k\Delta z)\right]}{\pi w_a w_b \left(\frac{1}{q_a}^* - \frac{1}{q_b}\right)}, \tag{2.31}$$

where $\Delta\phi$ corresponds to the phase shift between the beams. However, it is more convenient to express the coupling coefficient c_{ax}^2 in terms of beam radius as

$$c_{ax}^2 = \frac{2\exp\left(-jk\Delta z\right)}{\left(\frac{w_{0a}}{w_{0b}} + \frac{w_{0b}}{w_{0a}}\right) - \frac{j\lambda\Delta z}{\pi w_{0a} w_{0b}}}. \tag{2.32}$$

Then, the power coupling coefficient K_{ax} is given by

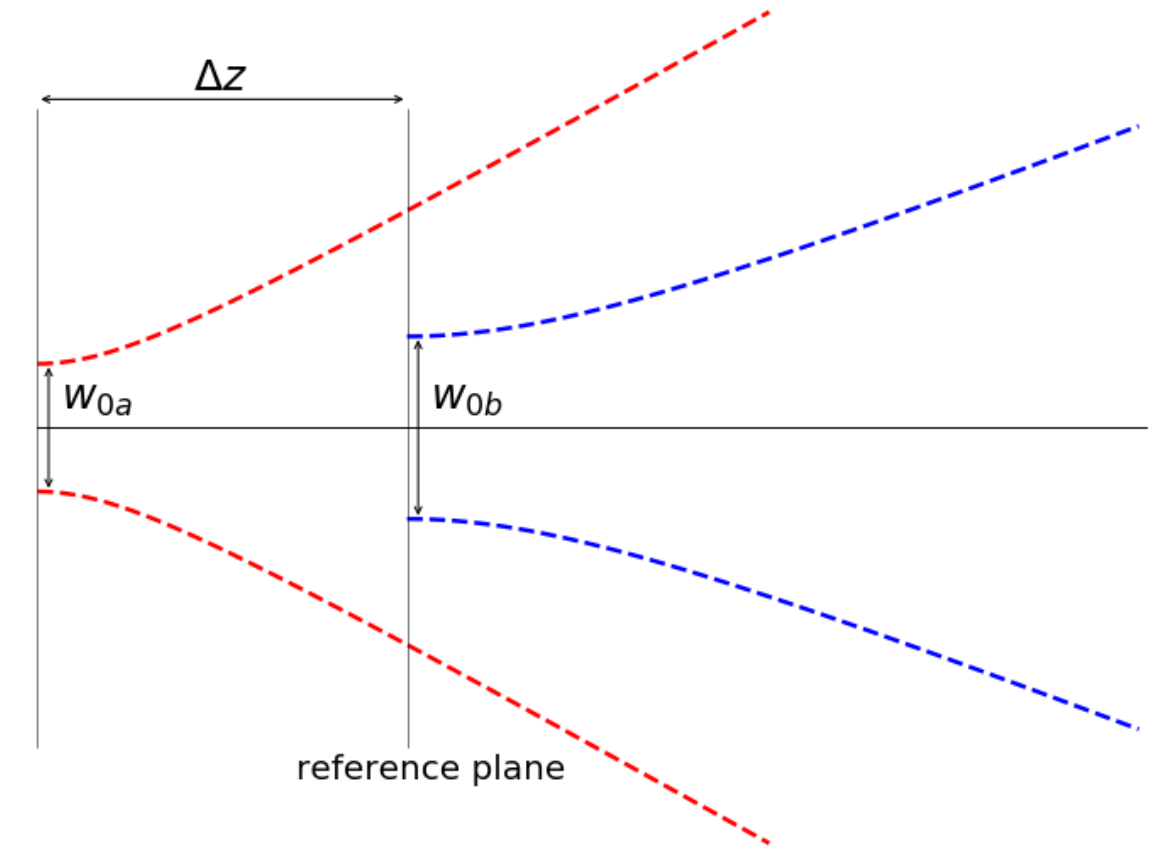

Figure 2.9: ***Axially aligned beam missmatch***
The two Gaussian beams have a common axis of propagation. However, the beams have a different waist, and hence, different beam radius at any specific point along the propagation axis.

$$K_{ax} = |c_{ax}^2|^2 = \frac{4}{\left(\frac{w_{0b}}{w_{0a}} + \frac{w_{0a}}{w_{0b}}\right)^2 + \left(\frac{\lambda \Delta z}{\pi w_{0a} w_{0b}}\right)^2}. \tag{2.33}$$

Tilted beams

When the axis of propagation of one beam is tilted with respect to that of the other beam, the symmetry of axially symmetric Gaussian beams is destroyed. Let us the axis of propagation of beam b to be tilted by an angle θ in the xz plane relative to that of beam a (as it is shown in figure 2.10). Taking the reference plane to be perpendicular to the z axis, the coupling coefficient c_{tilt}^2 for a small angle is given by

$$c_{tilt}^2 = \frac{2j\lambda}{\pi w_a w_b \left(\frac{1}{q_a^*} - \frac{1}{q_b}\right)} \exp\left(\frac{-\pi\theta^2}{j\lambda\left(\frac{1}{q_b} - \frac{1}{q_a^*}\right)}\right). \tag{2.34}$$

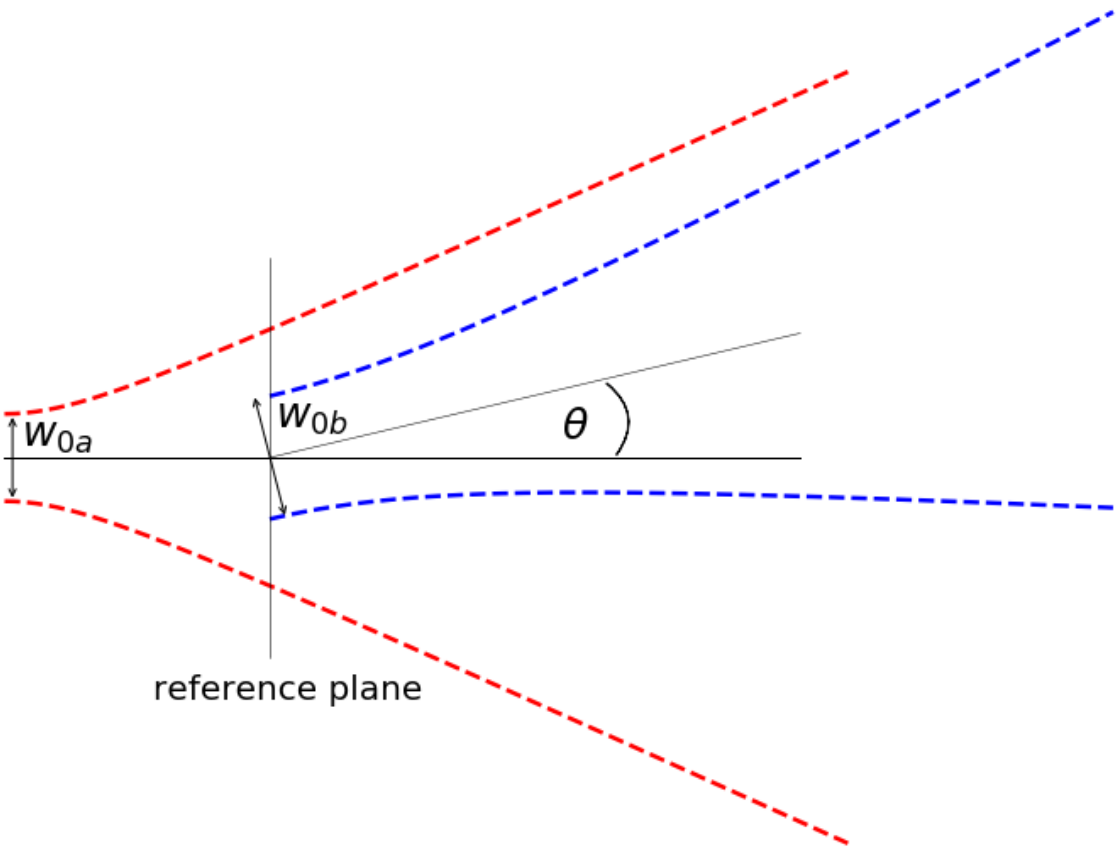

Figure 2.10: ***Tilted beam missmatch***

The axis of propagation of one beam is tilted with respect to that of the other beam by angle θ in the plane xz, which is supposed to be perpendicular to the propagation axis z.

The factor on the right-hand side of equation 2.34, preceding the exponential term, is identical to that for axially aligned beams in equation 2.31. It represents the effect of different beam sizes and curvatures. To isolate the effect of tilt, it is possible to set this factor equal to unity, and getting a coupling power coefficient K_{tilt}, in terms of w and R as

$$K_{tilt} = \exp\left(\frac{\frac{-2\pi^2\theta^2}{\lambda^2}\left(\frac{1}{w_a^2}+\frac{1}{w_b^2}\right)}{\left(\frac{1}{w_a^2}+\frac{1}{w_b^2}\right)^2+\frac{\pi^2}{\lambda^2}\left(\frac{1}{R_b}-\frac{1}{R_a}\right)^2}\right). \tag{2.35}$$

Off-set beams

This situation occurs when two beams propagate in parallel but their axis are relatively displaced to one other, as shown in figure 2.11. Calculating the coupling between such beams, the offset direction is chosen to be the x-axis and the magnitude of the offset to be x_0. Neglecting the phase factor, the coupling coefficient c^2_{offset} is given by

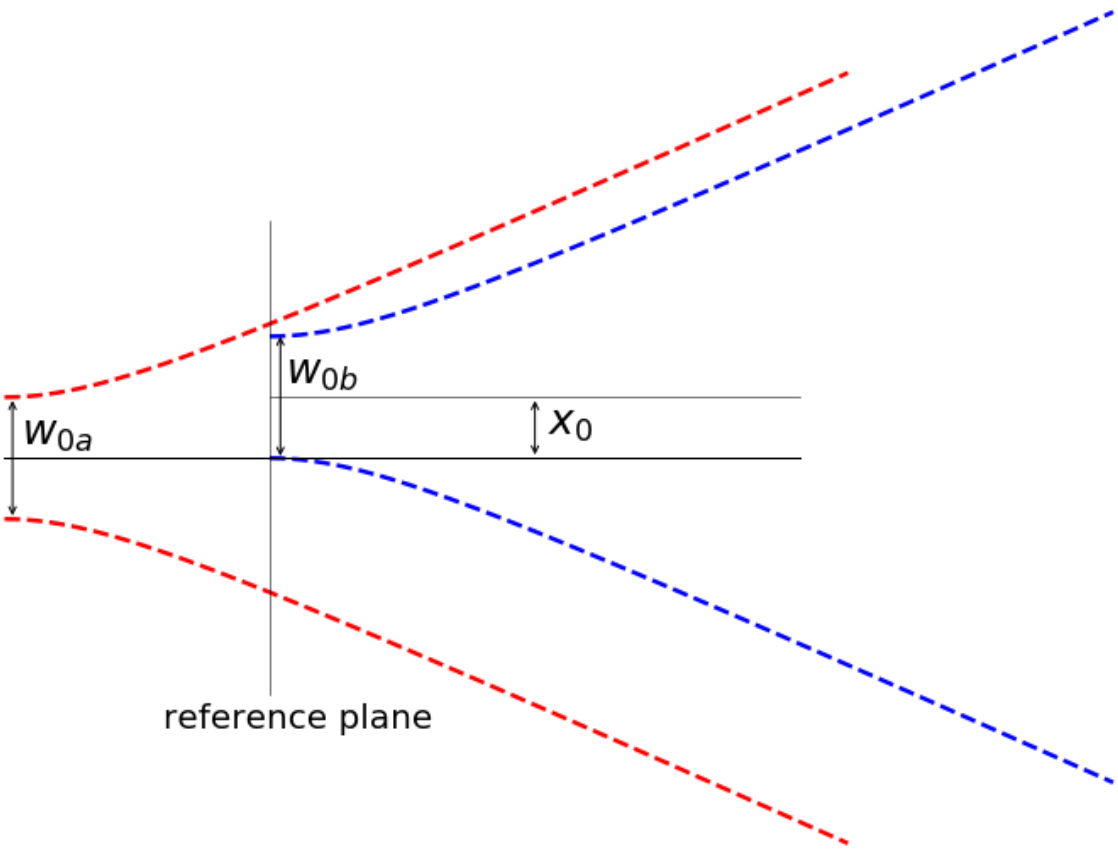

Figure 2.11: ***Offset beam missmatch***
The representation of two beams in an off-set configuration. The axes of propagation are parallel but one is displaced relative to the other a distance x_0.

$$c^2_{offset} = c^2_{ax} \exp\left(\frac{j\pi x_0^2}{\lambda(q_a^* - q_b)}\right), \tag{2.36}$$

where c^2_{ax} represents the coupling coefficient contribution of the axially aligned beams. The power coupling coefficient K_{offset}, expressed in terms of the waist parameters of the two beams is

$$K_{offset} = K_{ax} \exp\left(\frac{-2x_0^2(w_{0a}^2 + w_{0b}^2)}{(w_{0a}^2 + w_{0b}^2)^2 + (\lambda\Delta z/\pi)^2}\right), \tag{2.37}$$

where K_{ax} corresponds to the power coupling coefficient contribution of the axially aligned beams.

Equations 2.33, 2.35 and 2.37 have vital importance at the time deciding which elements will be used to align the system, therefore, compensate losses by misalignment. This is made

Optical Element	w_i [mm]	Diameter ($5w$) [mm]
Dichroic	10.03	50.17
Flat Mirror 1	8.66	43.29
Flat Mirror 2	8.52	42.64
Flat Mirror 3	8.92	44.58
Elliptical Mirror 1	10.79	53.98
Elliptical Mirror 2	11.66	58.31

Table 2.6: ***Values of diameter for each element forming the beam combiner optical system.***

by means of a tolerance analysis, which will be presented in the following section.

2.6 Beam combiner assembly and performance analysis

Since the different bands in ALMA are spatially separated in the focal plane, as shown in figure 2.1, the beams of the two bands must be combined optically in order to perform simultaneous dual-band observations. The concept is based on using a Frequency Selective Surface (FSS), or "dichroic" in short, to separate the Band 6 and 9 beams. However, the design of this dichroic involves a different theoretical approach, which will be thoroughly explained in chapter 3. For the moment, we will consider that the beam striking upon the dichroic will ideally transmit the Band 9 beam and, it will reflect the Band 6 as it does when a flat mirror is used. For both cases, i.e., transmission and reflection a low insertion loss is assumed.

2.6.1 Zemax model

An optical first order system has been designed following a geometrical optics approximation and using Zemax [52]. Using geometrical optics rather than quasi-optics is acceptable because in the far-field approximation geometrical optics describes a beam that envelops the Gaussian beam. This condition guarantees that, in the far-field region, both beams will follow the same optical path. However, it is important to be aware that the diameter of each reflecting element in the system must be chosen following the quasi-optical approach, i.e., using at least a diameter of $4w$, where w corresponds to beam radius at any element surface. This condition guarantees that 99.97 % of the power of the beam will be transmitted after each reflection.

Figure 2.12 shows the mirror layout of the proposed beam combining optical system. The size of each mirror has been calculated using quasioptical propagation by means of a python script and using $5w$ as a diameter. Choosing $5w$ instead of $4w$ was done to compensate for any possible beam spillover due to the rotation of each mirror. The resulting values are listed in table 2.6.

Considering an ideal situation, where the dichroic filter does not introduce beam distortion, the beam of Band 9 is transmitted through the dichroic without any major changes in its

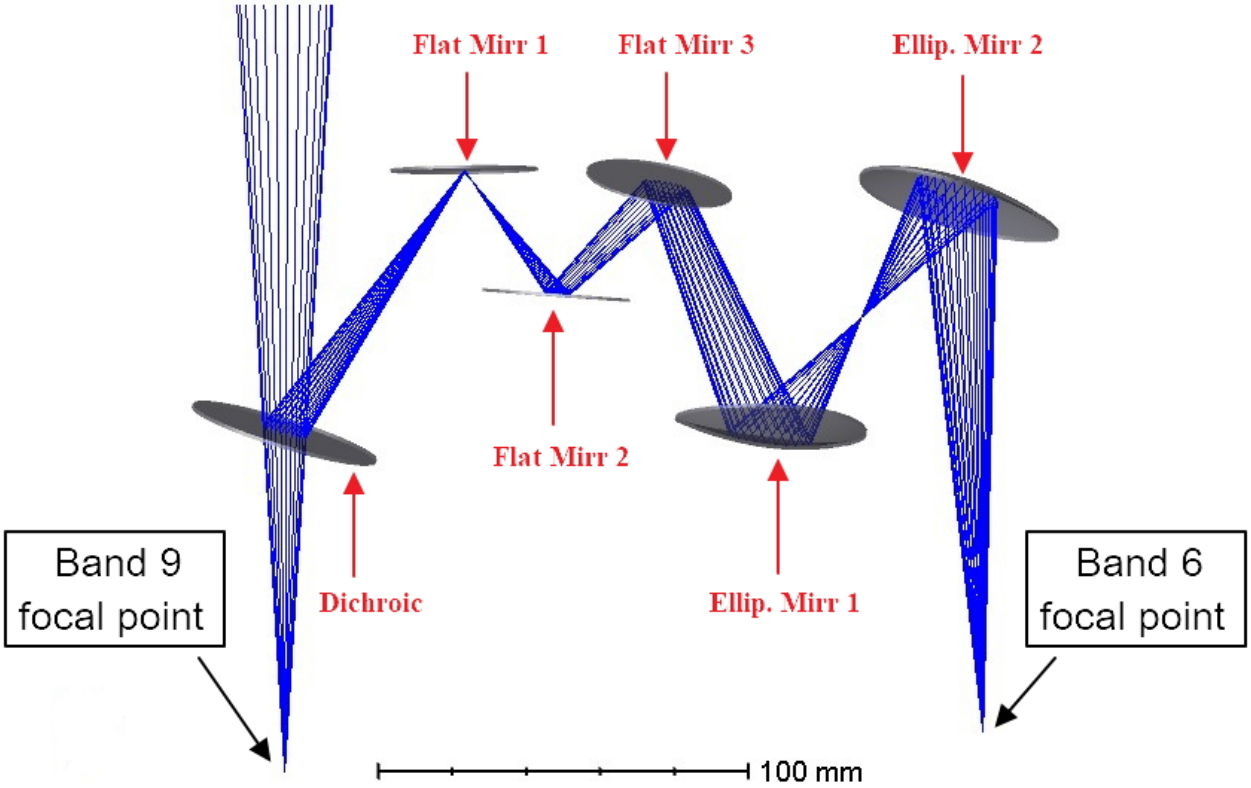

Figure 2.12: ***Proposed System.***
Design of the optical beam combiner system made using Zemax software. The secondary reflector was simulated using its F-number, which has a value of $F\# = 8$ (see table 1.1).

wavefront. One of the main reasons why we chose for this arrangement is that dichroics tend to work better when the high frequency is transmitted [53]. Moreover, the fabrication tolerances are less exigent. On the other hand, the beam of Band 6 is reflected and then redirected to its respective window by an optical re-imaging system, consisting of five mirrors, two elliptical and three flat. The incidence angle upon the dichroic filter is kept as low as possible ($\sim$ 18 degrees) in order to decrease the insertion losses [54]. The idea of using two elliptical mirrors in this system is that the beam distortion (produced by each mirror) can be compensated by properly matching their foci (see section 2.5.1). Another advantage of using a pair of elliptical mirrors is that the beam shape, after propagation through the optical system, can be easily matched to obtain an optimal coupling. In addition, the optical system has been designed to match the synthesized beam waist with the value given by the feed horn of the Band 6 receiver (see table 2.2).

2.6.2 Cross-polarization analysis

For the Band-9 beam, any deterioration of the beam as been considered to be negligible. Thus, cross-polarization contribution is vanished from the noise calculation on the Band 9 receiver. For Band 6, the situation is more complicated since the beam must go through an optical system that uses off-axis mirrors. Figure 2.13 shows the cross-polarization losses calculations, as described by equation 2.28, due to the elliptical mirror 1 and 2 for the optical system shown in figure 2.12. The plot shows a cross-polar deterioration of about -24.5 dB

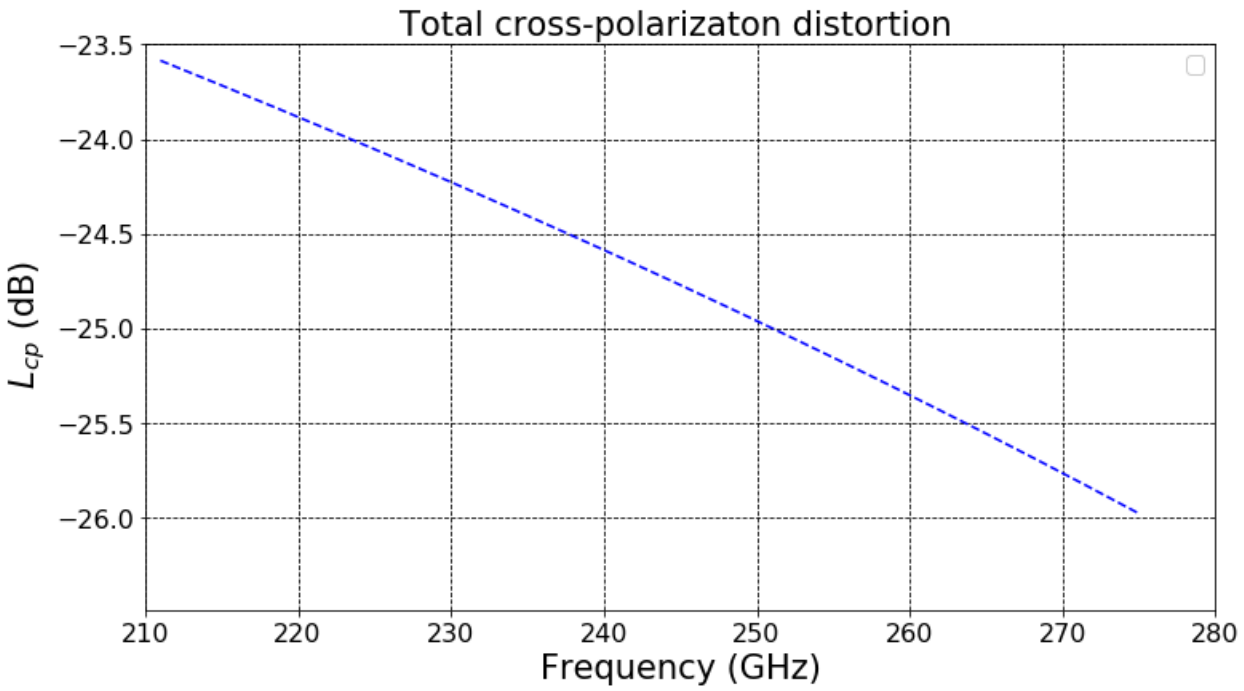

Figure 2.13: ***Cross polarization distortion calculation***
Cross-polarization distortion introduced by off-axis mirrors of the optical beam combiner assembly as calculated by using equation 2.28.

at the central frequency. For an eventual full deployment, this may be considered too high, but for a proof of concept demonstrator, we consider it acceptable. We believe that any additional loss caused by the reflection upon surfaces can be quite low when high-quality mirrors are used in the re-imaging optics.

2.6.3 Noise temperature analysis

The added noise temperature to each receiver must be calculated using the cascade method. The noise temperature of system in cascade T_{cas}, composed by n stages is given by [55]

$$T_{cas} = T_1 + \frac{T_2}{G_1} + \frac{T_3}{G_1 * G_2} + ... + \frac{T_n}{G_1 * G_2 * ...G_n}, \tag{2.38}$$

where T_{i} and G_{i} correspond to the noise temperature and gain, respectively, of each stage of the cascade. For the Band 9 beam, any insertion of noise will be purely due to the influence of the dichroic. For Band 6, the situation is more complicated since after reflection upon the dichroic the beam goes through the optical system. However, the whole optical system can be approximated to a single extra stage. Figure 2.14 illustrates the resulting cascade system in each situation. Band 6 turns into a system with three-stages, whilst Band 9 into two-stages.

Typical transmission of a modern dichroic with a mesh-type configuration is of the order of 90%, which leads to a gain of $G = 0.9$, and a noise temperatures of ~ 33 K for Band 9. Whereas, the performance in reflection is of the order to 96%, leading to a gain of $G = 0.96$,

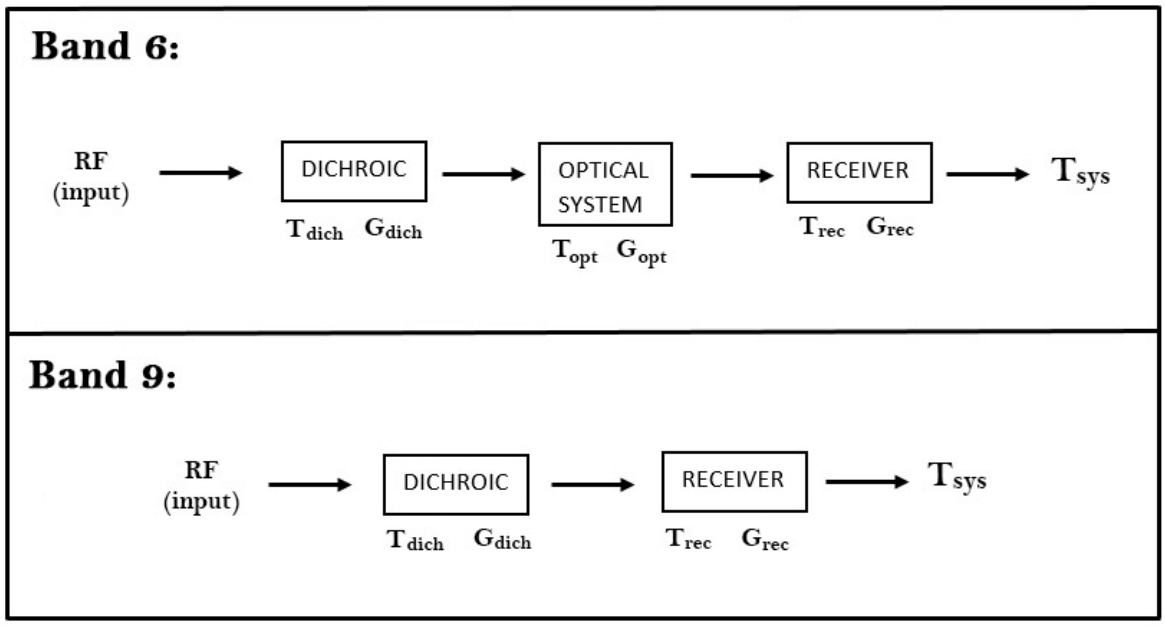

Figure 2.14: ***Resulting cascade system for each receiver,***
The RF beam coming from the secondary must go through different components before reaching Band 6 and Band 9 receivers. The resulting noise temperature for each receiver must be now calculated in cascade.

and a noise temperature of $\sim$ 13 K for Band 6 [2]. Additionally, for the case of the optical system, a total efficiency of 98% has been assumed (including cross-polarization contribution), which lead to a gain of $G = 0.98$ and a noise temperature of $\sim$ 6 K. The results of the cascade noise temperature for each receiver are presented in figure 2.15. These calculation were done considering that the noise temperature of the current Band 6 receiver exhibits a value typically between $40-60$ K at the middle of the band, and this increases to $60-100$ K at the edges of the band [56]. For Band 9, the current receiver exhibits a noise temperature lower than 170 K in 80% of the frequency range, whereas in the lower edge of the band the noise rises as high as 250 K [57].

The noise specification [3] for Band 6 and Band 9 receivers are 136 K and 261 K, respectively. On one hand, the cascade calculation shows that the total receiver noise, in the reduced noise region for each band, is $\sim$ 83 K for Band 6, and $\sim$ 222 K for Band 9. On the other hand, the total receiver noise, in the increased noise region, reaches values $\sim$ 125 and $\sim$ 311 for Band 6 and Band 9, respectively. Hence, once the optical system is integrated into the cryostat the added noise in the Band 6 receiver will not exceed its noise specification. Whilst, this condition is only guaranteed in at least 80% of the frequency range of Band 9.

2.6.4 Sensitivity analysis

All the optical components must be properly aligned in axial, lateral, and angle offset for achieving high levels of efficiency at the time of being mounted on the cryostat. However, this

[2] According to the specifications given by an external company **(http://www.qmcinstruments.co.uk/)**
[3] Values taken from the ESO web page: **https://www.eso.org/public/teles-instr/alma/receiver-bands/**

Band 6 calculation (middle of band)						
Component	Gain (Loss) [dB]	Gain(Loss) [dB]	Ambient Temp. [K]	Noise Temp. [K]	1/Gain (total)	Total Noise [K]
Dichroic	-0.177	0.96	300.0	12.50	1.0417	12.50
Optical system	-0.175	0.98	300.0	6.12	1.0204	18.88
Receiver				60.00		82.65
					Added Noise	**22.65**

Band 6 calculation (edge of the band)						
Component	Gain (Loss) [dB]	Gain(Loss) [dB]	Ambient Temp. [K]	Noise Temp. [K]	1/Gain (total)	Total Noise [K]
Dichroic	-0.177	0.96	300.0	12.50	1.0417	12.50
Optical system	-0.175	0.98	300.0	6.12	1.0204	18.88
Receiver				100.00		125.17
					Added Noise	**25.17**

Band 9 calculation (middle of the band)						
Component	Gain (Loss) [dB]	Gain(Loss) [dB]	Ambient Temp. [K]	Noise Temp. [K]	1/Gain (total)	Total Noise [K]
Dichroic	-0.46	0.9	300.0	33.33	1.1111	33.33
Receiver			300.0	170		222.22
					Added Noise	**52.22**

Band 9 calculation (edge of the band)						
Component	Gain (Loss) [dB]	Gain(Loss) [dB]	Ambient Temp. [K]	Noise Temp. [K]	1/Gain (total)	Total Noise [K]
Dichroic	-0.46	0.9	300.0	33.33	1.1111	33.33
Receiver			300.0	250		311.11
					Added Noise	**61.11**

Figure 2.15: ***Noise temperature calculation for each receiver band. For this calculation the highest reported noise temperature for each receiver has been used.***

situation is not realistic, and the misalignments presented in the system must be corrected. In order to quantify the misalignment loss, the corresponding beam coupling efficiency calculation has been done using equations 2.33, 2.35, 2.37. Figure 2.16 shows the beam coupling coefficient K_{ax}, K_{tilt}, and K_{offset} as a function of axial shift Δz, tilting angle θ, and lateral offset x_0, respectively. The calculations of K_{tilt} was done assuming that the tilt occurs at the beam waits location, whilst that for K_{offset} a coincident beam waist location was assumed. In addition, the calculations were done taking different ratios between w_{0b} (beam waist synthesized by the optical system) and w_{0a} (nominal beam waist if the feed horn.), and using a frequency of 243 GHz, which represent the central point of the Band 6 range (see table 2.2). Maximum coupling is achieved only when $w_{0b} = w_{0a}$ and, furthermore, we see that $w_{0b}/w_{0a} = 1.5$ reduces the peak of coupling to just 85%. Thus, matching the beam waist size

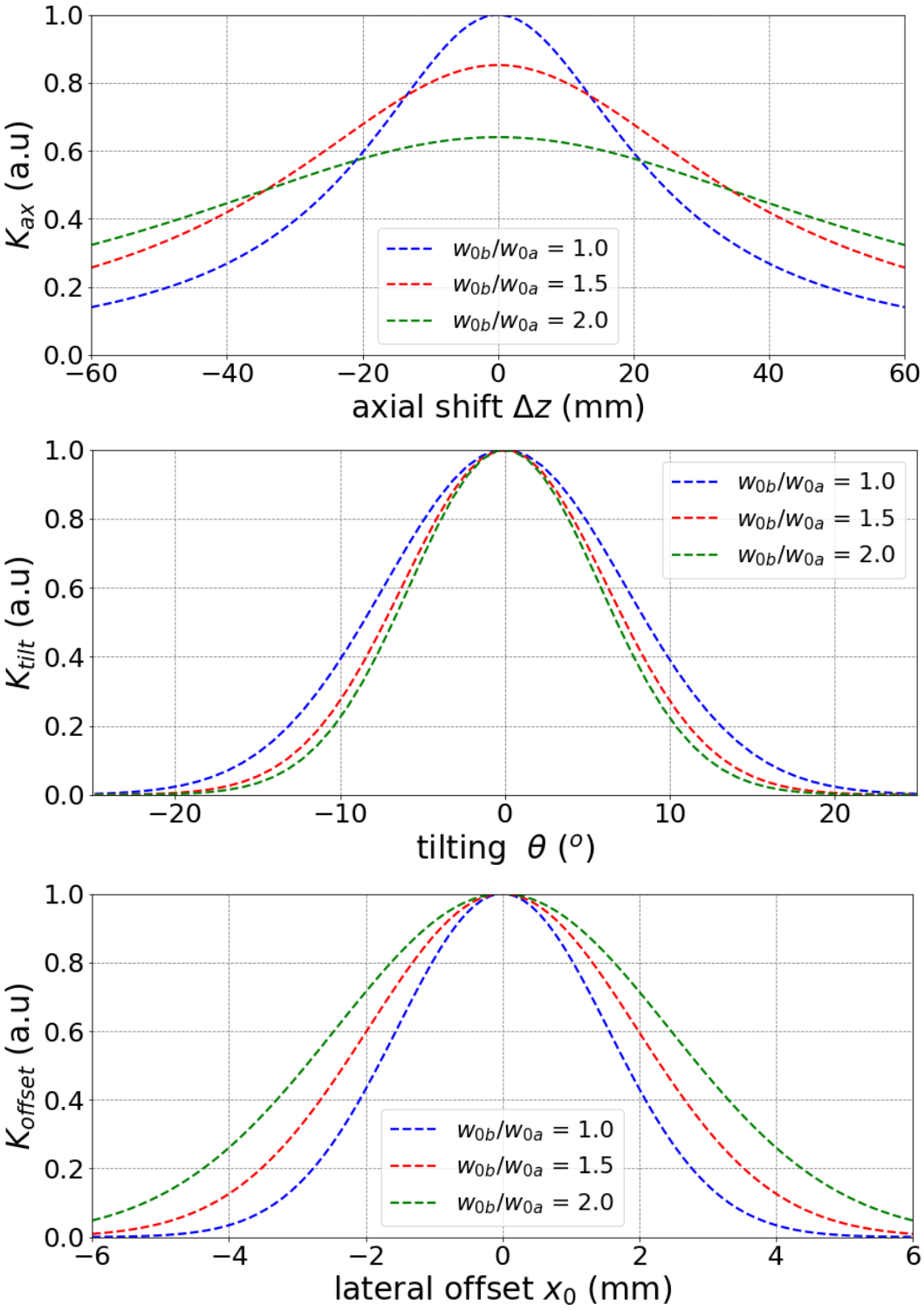

Figure 2.16: ***Coupling Efficiency Analysis***

Beam coupling calculation for the axially aligned beam configuration (top), tilted beam configuration (center), and offset beam configuration (down). For the cases of tilted and offset beam, we have also considered the simple case when the tilt occurs at the beam waist, and, the beam waist are coincident, respectively.

seems to be the most critical parameter to take into account at the time of redirecting the beam into the Band 6 receiver. However, the observed trade-off for this drop-off in peak of

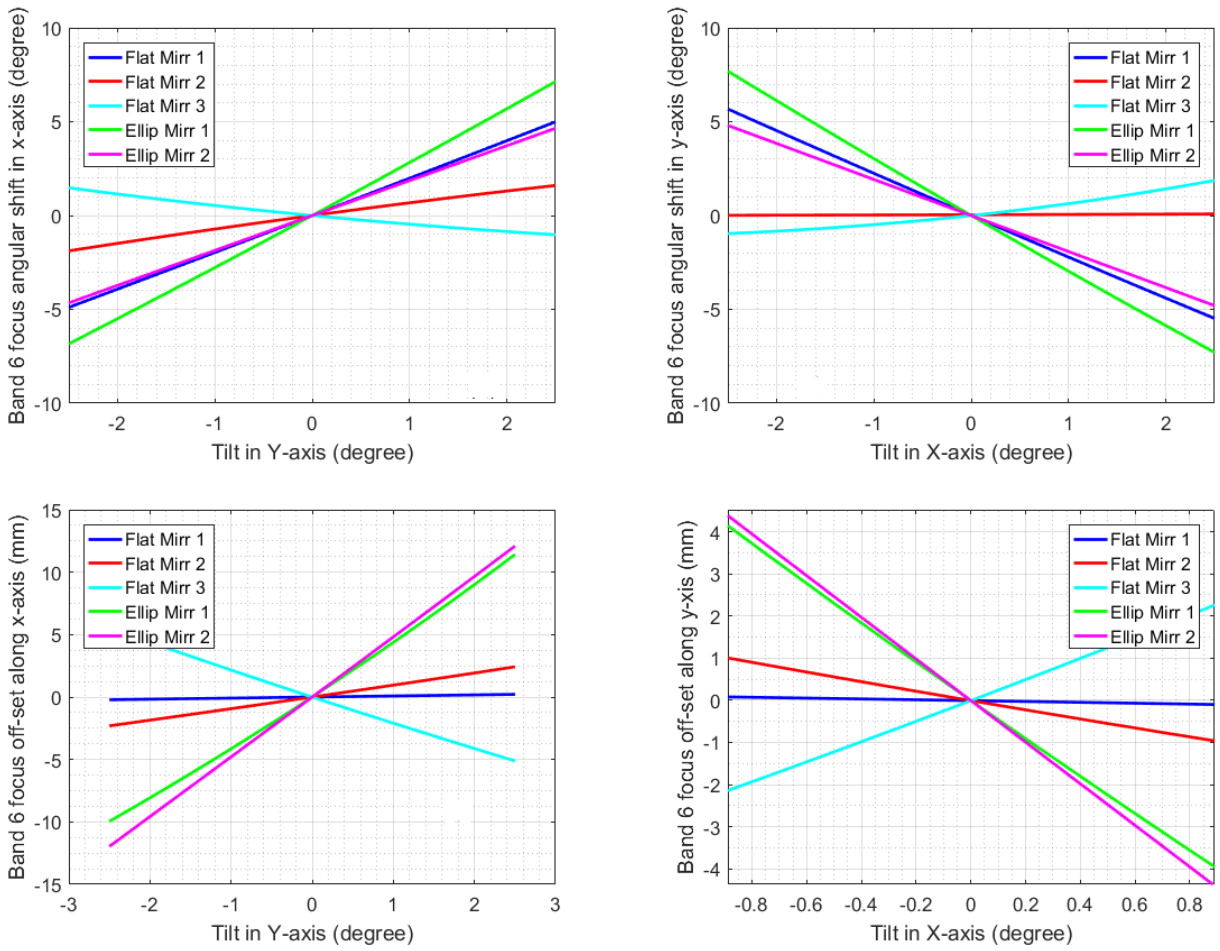

Figure 2.17: ***Tolerance Analysis***

Angular beam shift tolerance (upper row) and an off-set beam tolerance (lower row) for every reflecting surface of the optical system.

coupling seems to be that the optical system becomes less sensitive to axial shifts and lateral offsets when ${}_{0b}/w_{0a} > 1.0$. Conversely, the system becomes more sensitive to tilting angles for $w_{0b}/w_{0a} > 1.0$. A loss due to power decoupling produced by an axial misalignment in the optical system (taking $w_{0b} = w_{0a}$) is of the order of $K_{ax} = 95\%$ for a shift $\Delta z = 5.5$ mm, and 85% for $\Delta z = 13.0$ mm. In the presence of a tilt $\Delta\theta = 1.0^o$ the coupling is reduced to $K_{tilt} = 98\%$ and this values is drops to 91% for $\Delta\theta = 3.0^o$. Finally, we see that an lateral offset of only $x_0 = 0.7$ mm will reduce the coupling to $K_{offset}90\%$. Hence, we conclude that the optical system is more sensitive to lateral offset rather than axial shift or tilting. These results reveal the importance of including an alignment control device in the optical system in order to correct the misalignment, and therefore, keeping the losses in the system as little as possible.

Additional to the aforementioned power coupling calculations, a tolerance analysis has been performed. The objective is to know how sensitive the mirrors of the optical system are to any misalignment, and how the focus matching between the bands 6 and 9 will change. This analysis will show the best elements in the system to correct any misalignment. Zemax automatically generated surfaces with a length enough to contain only the beam for each

reflecting surfaces. This means that no degrees of freedom are given to the mirrors of the system under design. In the case that one of the reflecting surfaces is forced to move, part of the beam will suffer some spill-over. This issue gives no place to perform a tolerance analysis of the system. In order to sort it out, all the reflecting surfaces were increased in 35% giving some freedom to the system for adding a little shift in their angles. A tolerance analysis, for each reflecting surface of the beam combiner system, has been made and the results are shown in figure 2.17. We have divided the analysis into two parts, which correspond to angular beam shift tolerance (upper row) and off-set beam tolerance (lower row). Furthermore, we defined two rotation axis according to the coordinate system defined in figure 2.12; one along the propagation axis (within the yz plane) and one out of propagation axis (within the xz plane). The beam shift and tilt have been studied in both rotation axis. If there is any mismatch between the field of view of both bands, that implies that the bands are observing different points in the sky. Hence, it is desirable that the misalignment for each component stays as little as possible.

Figure 2.17 shows the result obtained for the tolerance analysis of the proposed optical system. The most important conclusion of this analysis is that the best pair of mirrors to control any misalignment in the optical system are the flat mirror 1 and the elliptical mirror 2. They provide a maximally decoupled adjustment in either offset or angle. Another advantage of choosing these mirrors as control devices is that they are placed on the top of the system, which will make the mechanical design easier. Therefore, these mirrors will be equipped with micrometer screws for manual adjustment. A more detailed explanation of the implementation of the alignment screws is given in the following section.

2.7 Mechanical design and fabrication

Since the different bands in ALMA are spatially separated in the focal plane, the beams of the two band must be combined optically in order to perform simultaneous dual-band observations. In the design proposed in the previous section, a dichroic is located above the Band 9 vacuum window, and pass that beam unmodified (supposing a dichroic with ideal performance). The new Band 6 beam, now coaxial with the Band 9 beam, will be reflected by the dichroic and re-imaged by a set of curved and flat mirrors into the original Band 6 focal point. Because of the spread in beam angles between the cartridges, it will be necessary to align the beams both in lateral offset and angle. For this, we have identified two mirrors in the chain that, when tilted individually, provide a maximally decoupled adjustment in either offset or angle. These mirrors will be equipped with micrometer screws for manual adjustment.

One of the most important mechanical requirement to be accomplished by the whole structure is the connection mechanism to the cryostat since no major modifications are allowed, i.e., no drilling or using pieces that could harm the optimal operation of other components previously installed. Furthermore, holes that are used in the already set-up components are not allowed. This beam combiner system has been designed to operate exclusively in the 12-meter diameter antennas. The space restrictions in those with 7-meter diameter are even tighter, due to additional components aimed to compensate the difference in the optical path length of the beam for both antennas. As those components are not present in the 12-meter configuration, some extra holes (used to link those components) are available to be used

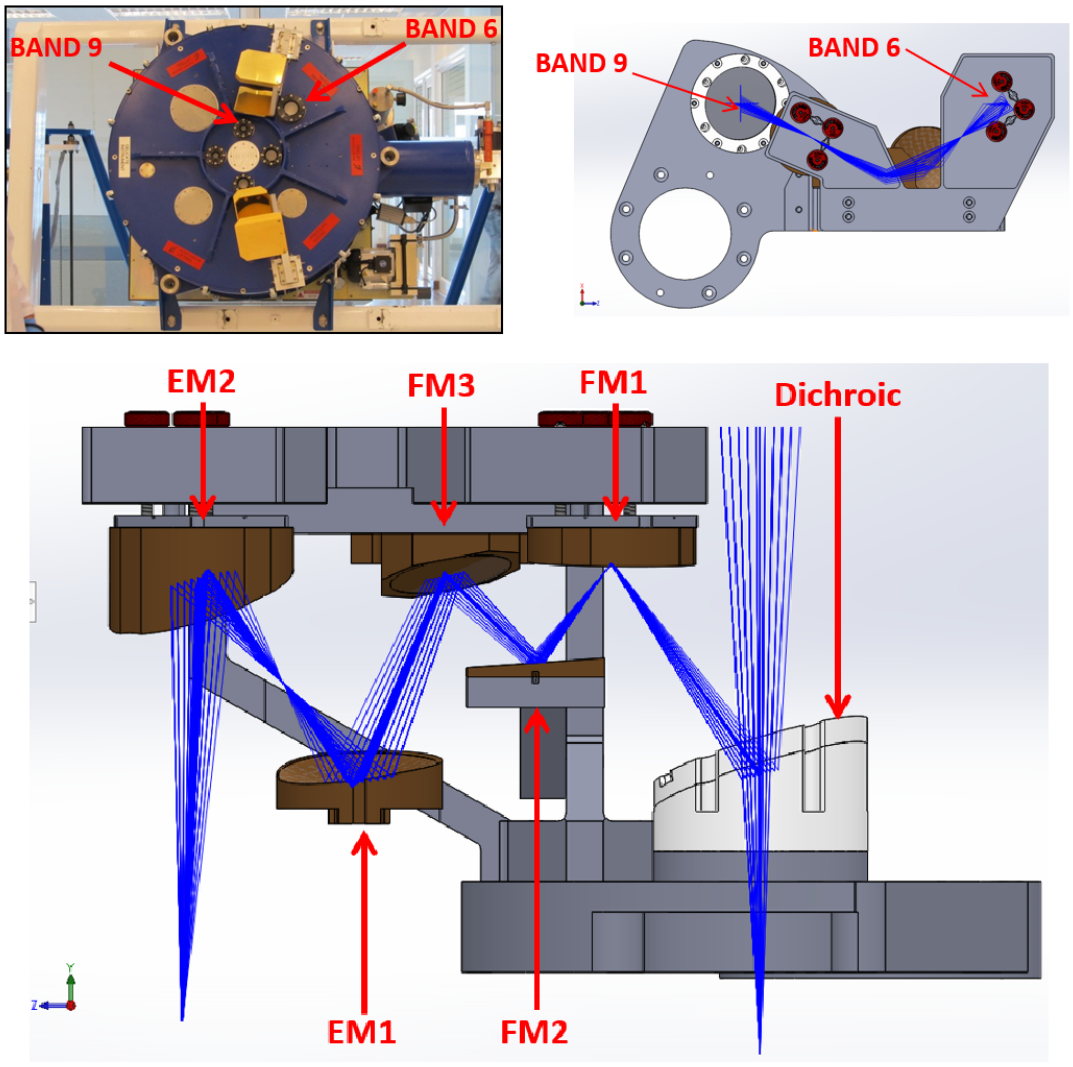

Figure 2.18: ***Layout of the bands in the ALMA cryostat and mechanical design of the optical system.***
Brown pieces correspond to the mirrors, and the blue lines correspond to geometrical optics approximation of the Band 6 and 9 beams.

green[7]. We will use those holes to link the support structure to the cryostat. Additionally, mechanical vibrations and elastic deformation of the parts that make up the structure must have a minimal impact on the alignment of the system. All these considerations led to the mechanical design shown in figure 2.20. The whole structure that supports the optical beam combiner system stands on a robust base called "vertebra", which is the only part of the system that has direct contact with the cryostat, and hence, correspond to the main abutment of the system. In order to maintain the structure stable, the vertebra was designed thick enough to resist the weight of all the other pieces.

In addition, a view of how the structure would look like once is mounted on the top of cryostat is illustrated in the figure 2.19. Table 2.7 shows the beam radius at each reflecting surface and the actual size that each element must have in order to avoid beam spillover. The optimal diameter D of each surface has been calculated using the formula $D = 5 * w_m + \Delta$,

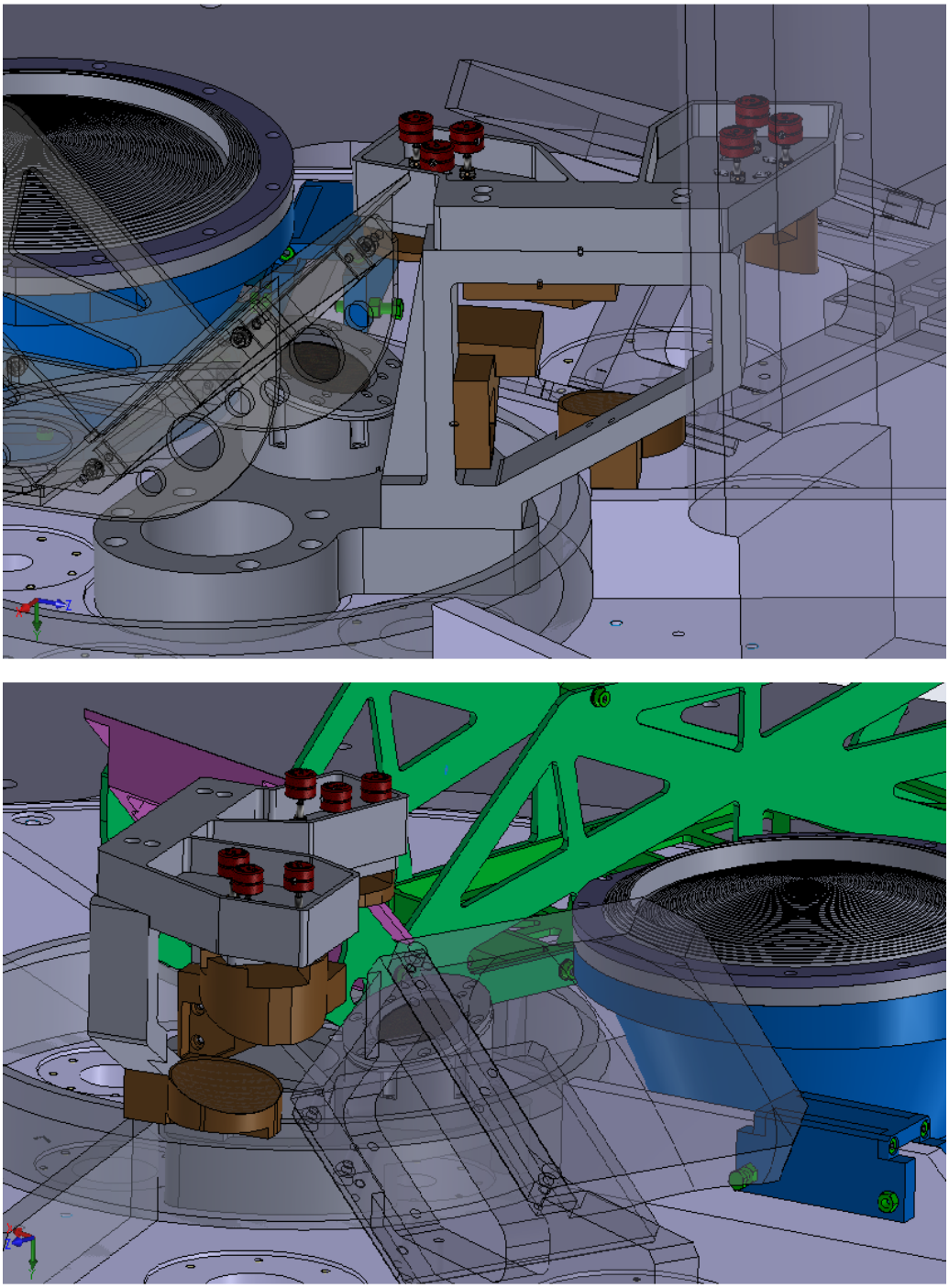

Figure 2.19: ***Rendering of the beam combiner system once is mounted on the cryostat***
The brown coloured holders corresponds to those that will hold the mirrors, the alignment screws are shown in red.

where w_m corresponds to the beam radius at the specific element and Δ is only a small tolerance included to compensate any possible beam spillover produced by the tilting of the surface.

Table 2.7: ***Beam size, requiered taper and optimal diameter at each reflecting surface***

Element	Beam Radius w_i (mm)	Element Diameter $5w_i$ (mm)	Optimal Diameter $D = 5w_i + \Delta$ (mm)
Dichroic	10.03	50.17	55.0
Flat Mirror 1	8.66	43.29	45.0
Flat Mirror 2	8.52	42.64	45.0
Flat Mirror 3	8.92	44.58	40.0
Ellip. Mir. 1	10.79	53.98	60.0
Ellip. Mir. 2	11.66	58.31	65.0

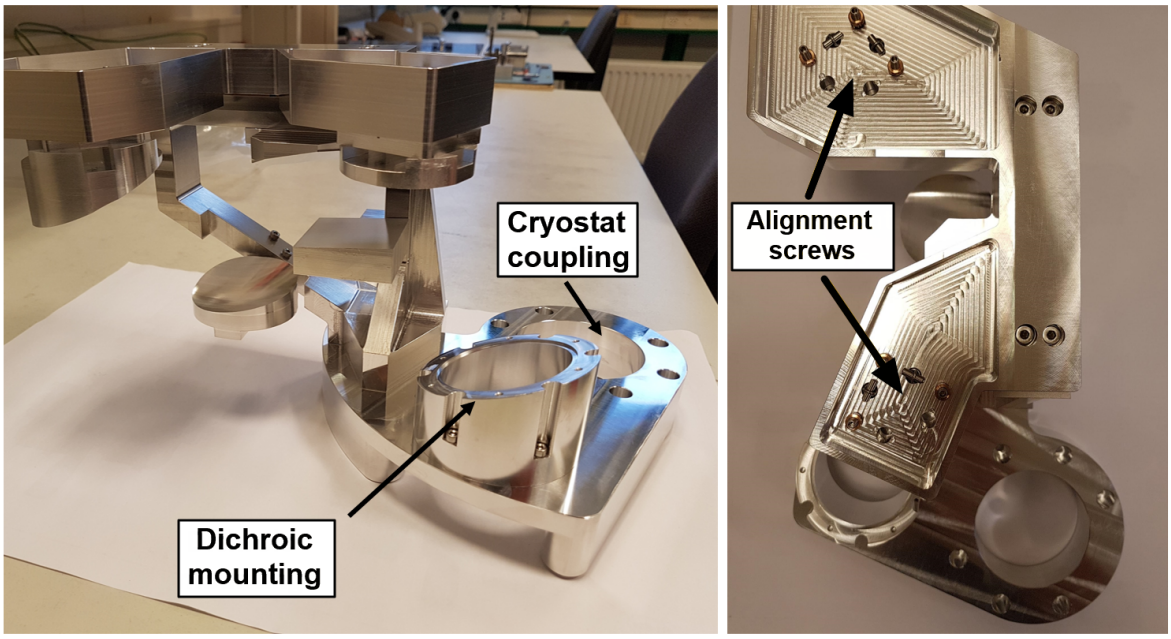

Figure 2.20: ***Constructed beam combiner optical system***
The alignment screws location is indicated in the image, however, they are not shown.

The designed mechanical structure has been fabricated by a external company [4] and it is shown in figure 2.20. The left panel indicates the space where the dichroic will be placed and, also, the piece to be used for mounting the structure into the cryostat. The right panel shows a top view, where the alignment screw holes are marked (screws are not shown in the image). We deem that the fabricated structure is ready to be mounted into the ALMA cryostat. Nonetheless, some hardware/software modifications will be necessary in order to run a true dual-frequency observation. This is a clear caveat that an additional study is necessary for successfully operating with both bands simultaneously, however, this is out of the scope of this thesis work.

[4] http://kenter-precisie.nl/

2.8 Conclusions

In this chapter, we have studied the feasibility and practical implementation of a dual-frequency observations mode for ALMA. This dual-frequency mode can be realized through an external optical system, operating at room temperature, and employing two of the existing ALMA receivers. In particular, we have proposed the combination of Band 6 and 9. For this combination, we envision several science drivers, which have been described in section 2.1.

To implement this dual-frequency receiver, a low distortion optical system has been proposed. The ray optics formalism was used and quasioptical corrections were included in order to calculate the appropriate size of each element. The designed system uses mirrors (two elliptical and three flat) and keeps the losses at a minimum level. After a tolerance analysis, we have concluded that the best mirrors to correct misalignment are the flat mirror 1 and the elliptical mirror 2. These mirrors present the higher sensitivity in one control parameter, either beam shift or beam tilt, and the lower in the other parameter. This feature makes them the best option to work as alignment control system, therefore, these mirrors were equipped with micrometer screws. Thus, any eventual misalignment presented in the system could be corrected by titling the mirrors. Moreover, both mirrors are on top of the optical system. This detail represents an advantage for the mechanical design of the optical system, from the point of view of reaching the screws once the optical system is mounted into the ALMA cryostat.

In this chapter, we have assumed that we have a dichroic with an 'ideal' performance. Under this assumption, the added noise temperature to each receiver will not exceed the maximum stipulated by the ALMA specification. However, for a true dual-frequency receiver using existing ALMA hardware, the real impact on the noise temperature produced by a dichroic must be thoroughly studied. In the following chapter, we will review the physics behind dichroics and, we will present some designs aimed to fulfill the expected high-performance.

Chapter 3

Design, Construction and Characterization of Frequency Selective Surfaces

3.1 Introduction

In chapter 1 we described how the ALMA telescope operates and its importance in radio-astronomy. However, despite of being the most powerful radio telescope in the world, ALMA is not exempt of problems, in particular for phase calibration at high frequencies using long baselines under low humidity conditions. One potential solution for this calibration problem is to implement a dual-band observation mode, which will also bring in some important astronomical benefits. The idea of observing at dual frequency has been used before in other telescopes, showing very successful outcomes. In chapter 2 we presented the design of an optical beam combiner assembly that will allow ALMA to operate in such dual-band mode. The designed optical system is made up by 5 mirrors (two elliptical and three flat) and one dichroic filter. Additionally, it was demonstrated that the dichroic filter is one of the most relevant components since most of the system noise will be introduced by this filter.

In this chapter we report the design, construction and characterization of three free-standing and single-layer Frequency Selective Surface (FSS) structures, whose spectral response is aimed to fulfil the required dichroic performance at non-normal beam incidence. A suitable FSS is required to allow transmission of electromagnetic radiation in the ALMA Band 9 range ($602 - 725$ GHz) with a transmission > 90 %, to achieve a rejection lees than -25 dB for Band 6 ($211 - 275$ GHz), and cross-polarization levels below -30 dB. All these specifications must be simultaneously satisfied at a beam incidence of 18^o. The transmission characteristics as a function of the frequency for the designed FSS were measured using a Fourier Transform Spectrometer (FTS). The experimental results of transmittance of the FSS filters are in good agreement with electromagnetic simulations made in HFSS. Nevertheless, some discrepancy is observed, which is attributed to defects in the fabrication process.

Designing a filter to operate at $600 - 725$ GHz will make us work in the THz region of the

electromagnetic spectrum (or equivalently in submillimeter waves region). For this reason, we start the chapter with a brief overview of technological applications in THz range and its importance in many scientific fields (including of course astronomy). Then, we will take a quick look to the relation between the spectral properties of FSSs with geometrical parameters. Subsequently, we continue with the proposed prototypes designed to be integrated into the optical beam combiner system. Finally, the chapter ends up with an experimental verification of the constructed FSSs to conclude whether the design specifications were achieved or not.

3.2 State of the art on Terahertz technologies

Nowadays the term terahertz (THz) is broadly applied when we refer to electromagnetic waves whose wavelength range spans between 1.0-0.1 mm (300 GHz - 3 THz). For frequencies lower than 300 GHz, we cross into the millimeter wave bands; whereas frequencies higher than 3 THz is currently one topic of high interest for stratospheric/space astronomy, thus, also for future space missions [58].

Historically, electromagnetic waves in the range of THz have remained one of the least exploited regions of the spectrum. This is basically because the technologies that deal with this type of waves are in a region between 'traditional' microwave and optical technologies. Nevertheless, this situation is currently changing since an increasing commercial emphasis has been placed on THz system in the last years [59]. Among the most benefited fields from THz technologies are high-resolution spectroscopy and remote sensing. The complementary use of THz instruments with heterodyne and Fourier transform techniques have allowed scientists from diverse fields (e.g. astronomy, chemistry, Earth planetary and space) to measure, catalog, and map thermal emission lines for a wide variety of light-weight molecules [60,61]. The thermal emission lines from gases that appear in the Earth's stratosphere and upper troposphere (for instance, water, oxygen, chlorine and nitrogen compound) have a particular importance. The spectral information of these components is vital to study the abundance, distributions, and reaction rates of elements involved in ozone destruction, global warming, and pollution monitoring [62]. Therefore, the development of new THz sensor technologies is very important to improve our understanding of the dynamics of our own Earth planet and, as well as, the atmospheric composition of new planets with conditions similar to Earth.

Astronomy in the range of THz waves has also been highly boosted by the capabilities gained through the development of novel devices. Some examples are quantum-cascade lasers for LO generation, hot-electron bolometers for detection beyond 1.2 THz, and frequency-selective surface (FSS) for THz spectroscopy and filtering [63]. In addition, FSSs are widely used as dichroic filters, which allows either dividing a beam into two or combining beams from different sources into a single beam for further processing. The idea of dividing a beam is commonly found in astronomical applications since it has enabled the deployment of multi-band receivers for radio astronomy, and multi pixel system for current and future facilities on Earth, and stratospheric/space astronomy [64–66]. The benefits of a multi-receiver systems are vast since they have allowed, so far, increasing the mapping speed and uv-plane coverage, enhance the phase calibration in high-frequency interferometric observations, and, moreover, they have the potential to provide unique information for future VLBI observations [67,68]. All these reasons, along with the continuous demand for an improved instrument sensitivity

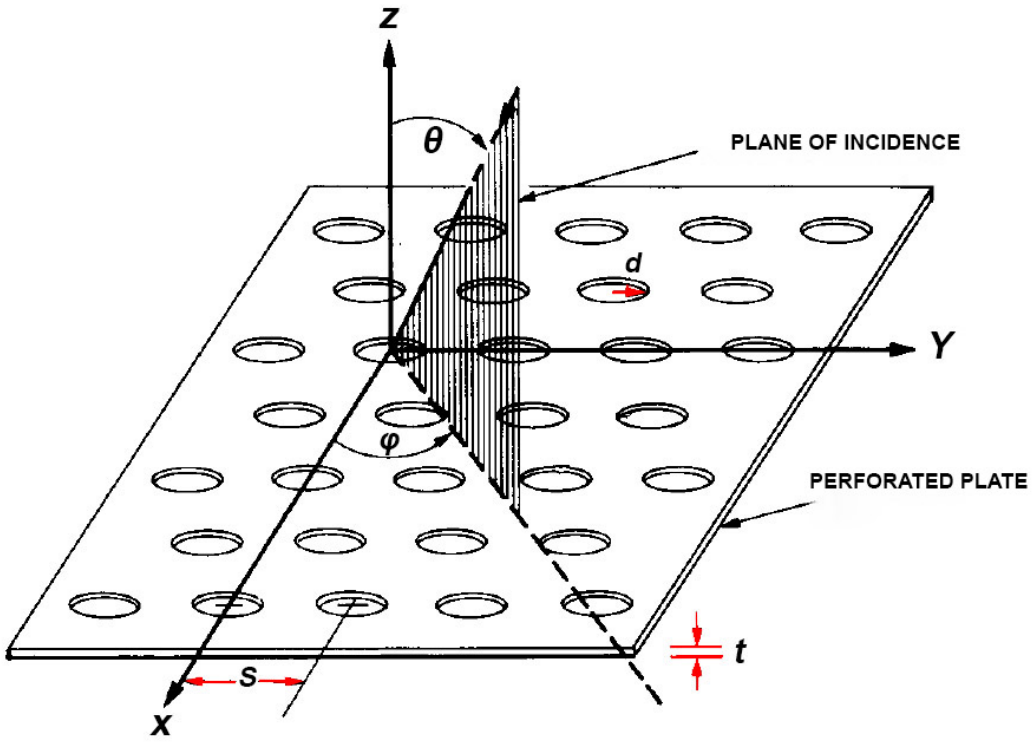

Figure 3.1: ***Dichroic plate geometry***

A dichroic consisting of a perforated metal plate with a thickness t. There are many possible shapes and spacing configuration. In this case, circular apertures of radius d with a hexagonal spacing s is shown. The angles θ and ϕ are used to indicate the direction of the incoming electromagnetic beam. (*Figure retrieved and adapted from [71]*)

and signal quality, explain the increasing interest in THz instrumentation. Furthermore, such interest seems to continue increasing as new technologies are developed and production costs are reduced [69, 70].

3.3 Dichroic filters theory

Dichroic filters are a subgroup of FSSs, which have found widespread application from the microwave to the near-infrared spectral region [72]. In the most common implementation, a dichroic consist of a metallic plate which is periodically perforated. The simplest configuration of dichroics consist of a single metal layer, perforated with circular apertures as shown in figure 3.1. However, more complicated shapes are useful for improving different relevant aspects, such as transmittance stability, cross-polarization levels, increasing the bandwidth, or the resonance frequency with the incident angle. To this aim, squares, crosses, Jerusalem crosses, tripoles, and pyle shaped apertures have been studied [73].

When we focus on commercial applications, dichroic filters have many practical uses. They span from applications for scientific research to domestic use. Frequency mixers and multipliers, laser cavities, Fabry-Perot interferometer [59, 74, 75] and simple screen door of microwave ovens (see figure 3.2) are only few examples of the many branches where dichroic filters find a proper use.

Figure 3.2: ***Applications of dichroic filters***

Two examples of applications for dichoic filters are presented: (top) the multi-frequency receiver implemented for the telescopes of the Korean VLBI Network (KVN); (down) the screen door of a microwave oven using a dichroic filter to block microwaves and transmit visible light.(*Figures retrieved from internet.*)

One of the most common uses of dichroic filters is for either divide a beam into two beams with different frequencies or combine beams from different sources into a single beam for a further process. This idea of dividing a beam is widely found in astronomical applications. For instance, we can mention once more the Korean VLBI Network, whose receivers, shown in figure 3.2, were designed to operate simultaneously in 4 different bands. Such an optical performance has been achieved thanks to the implementation of adequate low-pass dichroic filters.

We continue this section with a brief overview of the analytical approaches that allow modelling dichroic filters as lumped elements circuits. The theoretical formulas for transmittance and reflectivity will be given and we will also discuss the performance degradation due

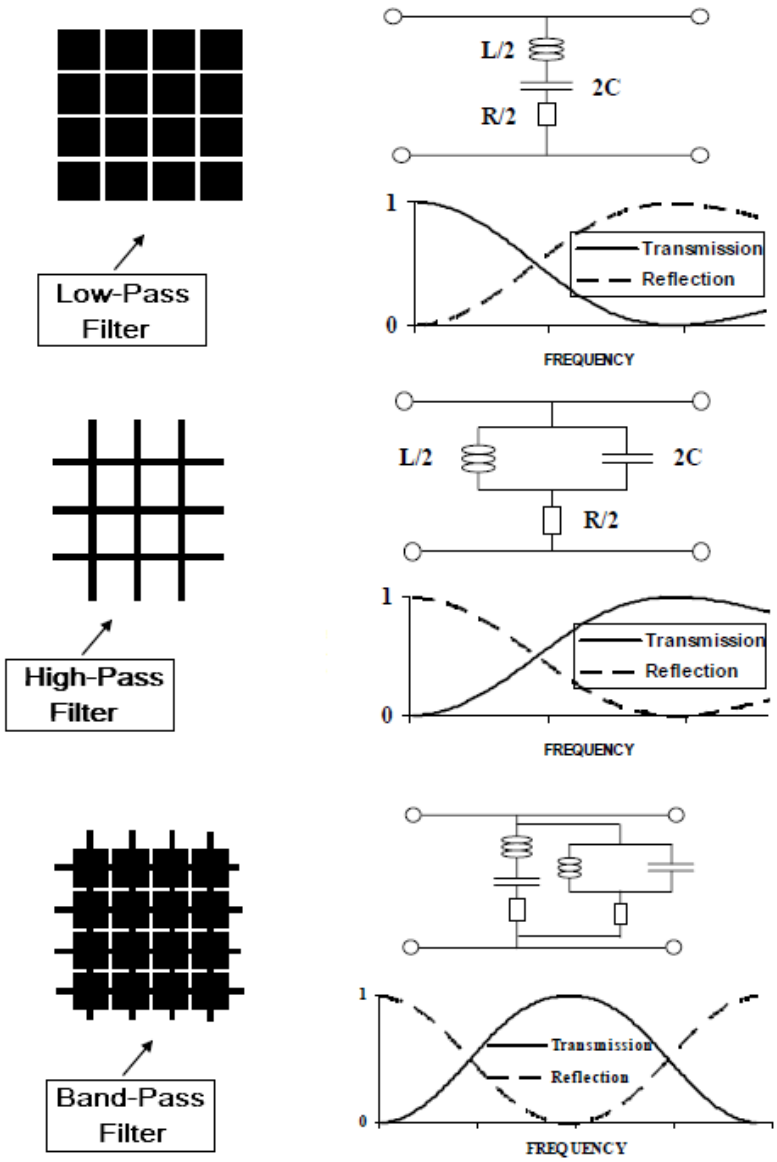

Figure 3.3: ***Metallic grids and their equivalent circuits***
Transmission line theory allows to model any specific metallic grid as a lumped element circuit. The advantage of doing so it is the clear relation between the grid geometry and its spectral properties. (*Figure retrieved and adapted from [73]*)

to non-normal beam incidence.

3.3.1 Transmission line theory for dichroics and their spectral properties

Dichroic filters have been widely used in millimeter/submillimeter wave instruments since the first publication by Ulrich of the transmission properties of metal grids [76]. The development of this approach was based on a simple argument that the spectral properties of these grids can be accurately modelled by considering each grid as a lumped circuit element in a free space transmission line. This model, which uses the transmission line method, is connected

to either a lumped inductance or lumped capacitance. Hence, we refer to these structures as inductive or capacitive grids (a mix of both is also possible). Figure 3.3 shows the relation between the metallic grid, its equivalent circuit and the respective spectral response.

It is important to remark, as it was stated in [77], that the lumped element impedance for metallic grids depend only on the geometric properties of the metallic layer. This relation between geometrical parameters and the optical response is key to reach the desired performance of any manufactured dichroic.

Dichroic filters, are typically used in the form of:

- **Low-Pass Filter (LPF):** As it is shown in figure 3.3, capacitive grids behave as low-pass filters. When several of these meshes are stacked together, with the appropriate space between layers, the cut-off can be sharpened at the expense of introducing ripples in the pass band. Those ripples can be mitigated by choosing a proper combination of meshes with different characteristic impedances, whose value depends on the mesh geometry.
- **High-Pass Filter (HPF):** The manufacture of high-pass filters can be realized by using inductive grids, as shown in figure 3.3. Analogically to capacitive meshes, inductive grids can also be mixed in a multi-layer system in order to achieve a desired performance. Nevertheless, stacking inductive grids are not exempt, either, of introducing ripples in the pass-band.
- **Band-Pass Filter (BPF):** In order to manufacture a mesh that behaves as a band-pass filter, the simplest way is by superposing the patterns of a capacitive with an inductive grid, as shown in figure 3.3. The resulting grid will have both capacitive and inductive properties and, therefore, it will exhibit a self-resonant behaviour which results in an optical band-pass. As shown in [78], either a narrow-band or a broad-band performance can be obtained. The former requires a large capacitance -i.e. large loss-, whilst the latter is better achieved by means of using a resonant grid.

The low and high-pass filters described above work well when they operate at frequencies below the diffraction region. When the frequency of the input beam is above some certain frequency ν_{diff} – which determines the beginning of the diffraction region- grating anomalies appear and, a significant part of the transmitted power is dissipated into the first diffraction lobe. A more detailed explanation of this effect can be found in [79].

3.3.2 Properties of Dichroic

As it was previously stated, dichroics consist of a metal plate dotted with equidistant apertures as shown in figure 3.1. Those apertures work as waveguides whose cut-off frequency depends on the specific shape of the aperture. In the simplest case of apertures with circular shape (or just 'holes'), each one behaves as a circular waveguide where the cut-off frequency is determined by the hole diameter.

Another important implementation of dichroic filter is in multi-layer configurations. It consists of two or more dichroics which are properly stacked. The advantage of multi-layer configuration is that it can provide more degrees of freedom. In this way, some tight design

requirements -that are not possible for a single layer dichroic- can be achieved. Thus, dichroics in a multi-layer configuration allows obtaining a more selective frequency response and, also, increasing the control over both transmission and reflection bands.

3.3.3 Theoretical analysis of dichoic filters

As it was previously mentioned, the shape and size of the apertures, their periodicity, and the thickness of metal layer determine the frequency response of any dichroic. The most common aperture shapes are circular or rectangular, however, cross-shaped apertures have also been widely used [80]. For the sake of simplicity, we will restrict our analysis to a simple configuration, i.e., a single layer system with a simple aperture shape (like circular).

The general description for the spectral response of an electromagnetic wave going through a dichroic is given by the theory of Chen [71]. In this method, it is assumed that an incident plane wave striking upon a dichroic filter can be expanded into a set of Floquet modes [81]. These modes, in turn, must be matched to the waveguide modes inside the apertures (considering that each aperture behaves as a waveguide). At the output face of the waveguide, the dichroic filter acts as an array of apertures re-radiating the incident electromagnetic wave, which is once again expanded into a set of Floquet modes. The spectral response of the dichroic filter is then obtained by matching Floquet and waveguide modes. Accordingly, the complex field transmission amplitude T and the complex field reflection amplitude R are respectively given by

$$T = \frac{1}{1 - \mathrm{i}\left(A + B\tanh\left(\frac{1}{2}\mathrm{i}\beta t\right)\right)} - \frac{1}{1 - \mathrm{i}\left(A + B\coth\left(\frac{1}{2}\mathrm{i}\beta t\right)\right)}, \tag{3.1}$$

$$R = \frac{1}{1 - \mathrm{i}\left(A + B\tanh\left(\frac{1}{2}\mathrm{i}\beta t\right)\right)} + \frac{1}{1 - \mathrm{i}\left(A + B\coth\left(\frac{1}{2}\mathrm{i}\beta t\right)\right)} - 1. \tag{3.2}$$

where β corresponds to the phase change, and the functions A and B depend on the geometrical properties of the filter, i.e. the aperture diameter d, the distance between apertures s, and the layer thickness t. A list with the values that A and B takes for different aperture shapes and array layout can be found in [71]. The thickness of the layer t determines how strongly waves in an evanescent mode are attenuated inside the waveguide. Thus, t turns into a parameter of control over the sharpness of the dichroic cut-off characteristics [82]. Additionally, equations 3.1 and 3.2 must satisfy the energy conversation condition, i.e. $RR* + TT* = 1$, bearing in mind the ideal situation where ohmic can be assumed to be negligible. Therefore, the power transmittance P_{tran} is then defined by

$$P_{tran} = TT^*, \tag{3.3}$$

where equations 3.1 and 3.2 are just an approximated value, which are valid only for the first dominant propagation mode (e.g TE_{11} for circular waveguides). These equations have been extensively used in the millimeter/submillimeter waves range and they have demonstrated to be helpful in optimizing the spectral response for various dichroic configurations by only

controlling the three geometrical parameters: aperture diameter d, aperture spacing s, and layer thickness t.

Bearing in mind the simplest case of circular apertures, each of them aperture is treated as a circular waveguide with a diameter d. The bandpass occurs above the cut-off frequency, which is given by [83]

$$\nu_c = 1.841\frac{c}{\pi \mathrm{d}}, \tag{3.4}$$

where c is the speed of light in free space. For frequencies below the cut-off frequency ν_c, the dichroic filter behaves as a plane mirror with a very low loss rate. Furthermore, the aperture array of the dichoic filter also behaves as a two-dimensional grating. This behaviour occurs for frequencies above the diffraction frequency $\nu_{\mathrm{di}ff}$, which is given by [83]

$$\nu_{\mathrm{di}ff} = \frac{2c}{s\sqrt{3}}, \tag{3.5}$$

For frequencies higher than $\nu_{\mathrm{di}ff}$ electromagnetic waves fall into a region of increased insertion loss. This increased insertion loss happens when the wavelength of the incident wave is smaller than the aperture spacing s, thus part of the power is diffracted into the first diffraction lobe [84]. It is seen from equation 3.5 that a smaller aperture spacing results in a higher $\nu_{\mathrm{di}ff}$, which establishes a clear caveat at the time of designing a dichroic filter for a specific purpose. There is an additional effect that is worth to be mentioned, specially at the time of choosing the thickness of the layer. This is the clear trade-off between thickness and spectral response. Thin layers give a poor response, whereas thick layers exhibit a large ripple in the passband. This effect might mean a tight restriction when a sharp cut-off and a low insertion noise are simultaneously desired. A more detailed reference about this effect – together with some techniques to mitigate it- can be found in [73]

In summary, the set of apertures that build up a dichroic filter act as waveguides with a certain propagating mode inside them. At the output face, these apertures collaborate together to couple power, and so, they re-radiate the incident electromagnetic wave. The spectral response of the dichroic is determined by the geometrical parameter, aperture diameter (d), aperture spacing (s) and layer thickness (t). At the time of designing a dichroic filter for a having a specific performance, special care must be taken with effect such as cut-off, diffraction, and ripples within the pass-band.

The transmittance and reflectivity of a dichroic filter also depends on both the angle of incidence and the polarization state of the incoming electromagnetic wave. On one hand, a brief explanation for non-normal beam incidence is presented in the following subsection. On the other hand, we deem that a consistent explanation of the polarization influence demands a more complete electromagnetic analysis, which is out of the scope of this chapter. For this reason, we will keep our explanation on polarization influence as simple as possible. Nonetheless, the interested reader can find a thorough analysis in [85].

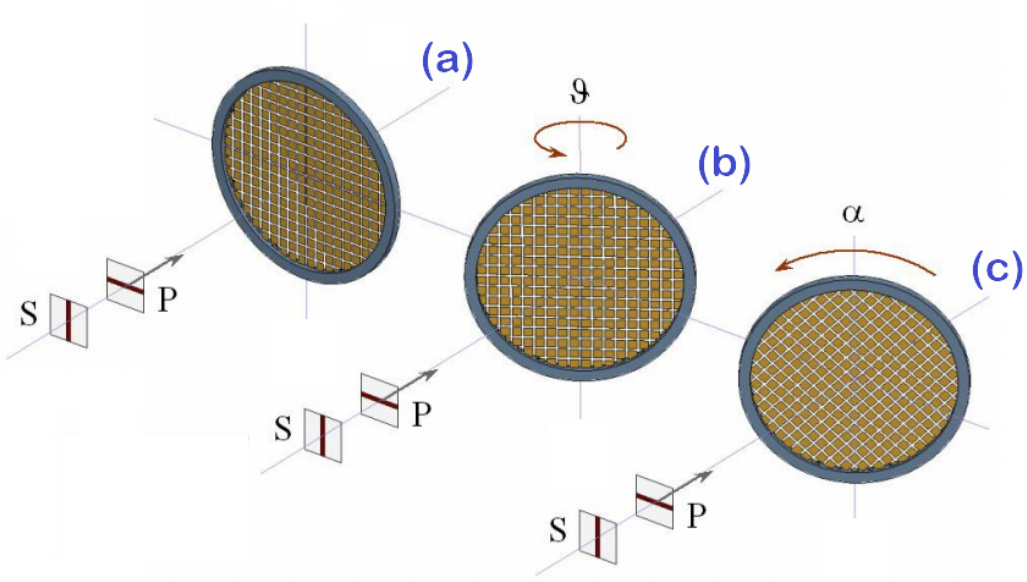

Figure 3.4: ***Angular dependence of the spectral properties of a dichroic.*** Situations (a), (b), and (c) represent different cases of beam incidence. The polarization states s and p interact differently for each situation, which will produce a change in the spectral properties of the dichroic filter. (*Image retrieved and adapted from [73]*)

3.3.4 Angular dependence

Non-normal beam incidence has a notorious impact on the spectral properties of any dichroic filter. In order to reduce those effects, several techniques have been proposed to contain the change in the aperture's shape [73]. They have proven to be very useful for incoming beam with a significant non-normal (up to 45^o). Among them, multi-layer system seems to be one of the most successful techniques to reduce the performance degradation produced by non-normal incidence.

It is also important to mention that particular care must be given to non-normal performance, when the polarization state is aimed to be maintained in transmission or reflection. To explain this point, the situation is illustrated in figure 3.4, where the S and P polarization states of the incoming beam interact with a dichroic filter. The dichroic can be rotated in two degrees of freedom (as illustrated in situation (b) and (c)), the plane tilt θ and the grid rotational orientation α. When $\theta = 0$ we call this situation normal incidence, whereas for $\theta \neq 0$ we deal with non-normal incidence. It is noticeable that for non-normal incidence both the apertures shape, and the array setup will change as a function of θ when they are projected into the plane of the incident beam. In addition, any change α will produce a similar effect, which will accentuate even more the aperture and array shape for non-normal incidence. Therefore, the spectral properties of the dichroic is expected to be a function of θ and α. As it has been previously reported [71, 73] that not taking care of non-normal incidence will lead to a break of symmetry of waveguide propagation modes. Thus, the dichroic will suffer undesired effects such as shrinking of the pass-band, leakage of transmitted power into to undesired modes or just reflected, an increasing of cross-polarization, and incrementing the insertion loss. In consequence, not paying attention to the angular dependence can lead

Table 3.1: ***Design specifications for a suitable dichroic filter.***

Parameter	Frequency	Target Goal
Transmission	$600 - 725$ GHz	$>$ 90 %
Rejection	$211 - 275$ GHz	< -25 dB
Cross-polar	$211 - 725$ GHz	< -30 dB

to an increased insertion loss. This effect is undesirable in radio astronomy applications, where maintaining the system noise as little as possible is indispensable. Nevertheless, the effects produced by non-normal incidence can be mitigated -by careful design- but never fully eliminated.

3.3.5 Calculation methods

At the time of calculating the spectral properties of dichroics filters two specific situations emerge; the hypothesis of an infinitely thin metallic film, or a metallic layer with a finite thickness. Many numerical methods can be used to calculate these two mentioned situations. Among the most used methods, we can list the Finite Difference Time Domain (FDTD), the Finite Element method (FEM), the Integral Equation Method (IEM) and the Method of Moments (MoM) [86]. FDTD and FEM can be applied for apertures with arbitrary aperture shape and spacing, however, they are quite slow. Conversely, IEM and MoM are very efficient, in terms of calculation time, but their application is usually limited to particular aperture shapes, i.e., when the analytical solution for the entire domain basis function is known in advance. As time went by, updates for the MoM were proposed. Those updates have allowed applying the MoM for solving the integral equation of unknown aperture fields for both cases thin and thick perforated layers. A detailed review of this method and, the assumptions made for infinitely thin and thick layer is presented in [85].

In the next section, the prototypes for a suitable dichroic filter are presented. The HFSS software [87], which provides an exact solution of the Maxwell's equations for unit cell of the structure will be used as designing tool. It has been reported how the solution given by this software makes a good match with the values obtained by MoM. This, at the same time, has been accompanied with experimental data of the spectral response [88]. Hence, HFSS represents a reliable calculation tool which will help to save time for finding a design that fully fit into our design specifications.

3.4 Proposed configurations

In this section, we present the results of the simulation obtained for the three different configurations: Jerusalem crosses (JC), single holes (SH) and flower-type (FT). Designing a dichroic filter that accomplish all of the design specifications listed in table 3.1 represents a very challenging task. Due to the high frequency at which this dichroic must operate, the electro-mechanical constraints are quite strict. Special emphasis must be put on the subsequent construction process since we are dealing with geometrical parameters of the order of hundreds of microns.

Table 3.2: ***Values of the optimization parameters for each dichroic configuration***

Jerusalem-cross		Single-hole		Flower-type	
parameter	(μm)	parameter	(μm)	parameter	(μm)
t	30	t	215	t	215
s	22	s	375	s	365
L	200	D	320	D	280
W	25	—	—	d	72
l	40	—	—	—	—
w	20	—	—	—	—

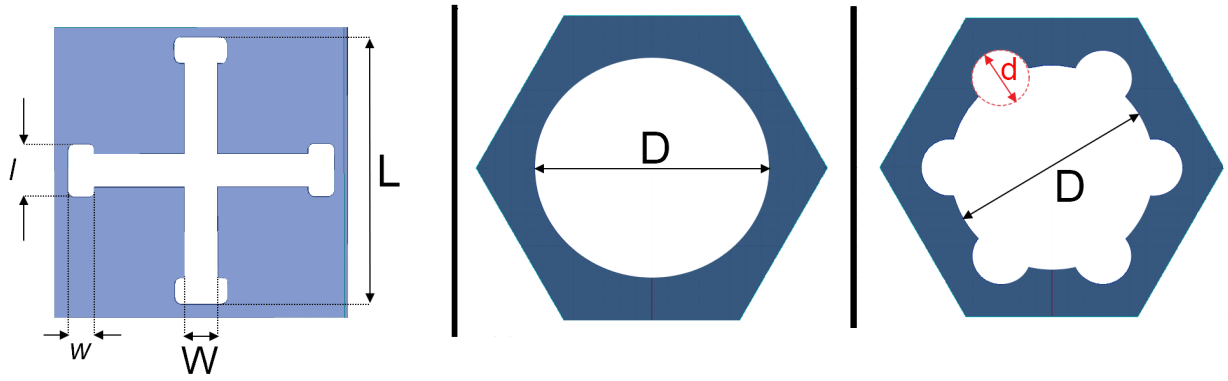

Figure 3.5: ***Proposed configurations for a dichroic filter***
In order to achieve the design specifications, we propose to implement three different configurations: Jerusalem-cross (left), single-hole (center) and flower-type (right). The thickness t, and spacing s are not shown here.

After a thorough review of the state of the art for dichroic operating at frequencies above 500 GHz [89–91], we have chosen to optimize three different configurations, all of them in a single-layer system. Two of these configurations have apertures shapes that haven extensively studied and reported, those are Jerusalem-Cross (JC) in a rectangular array, and single-hole (SH) in a hexagonal array. The third configuration brings with it a novel aperture shape – not previously reported- and is used in a hexagonal array. This configuration consists of a big hole surrounded by six small holes, equally distributed around the big one. Thus, what we have called a 'flower-type' (FT) pattern is created. Designing an aperture with this shape was motivated, mainly, because of the feasibility to be constructed using a unit cell similar in size than the single-hole case but with a smaller perforated area. This is an important feature if a photolithography process is intended to be used for its construction. In addition, a similar (or even better) performance than the single-hole configuration is expected due to the insertion of those small holes.

Figure 3.5 shows the initial unit cell structure to be optimized in order to find the set of parameters, for each design, that provides the most suitable performance according to the design specifications. The SH and FT designs are defined by a common set of design parameters, layer thickness t, aperture spacing s, and hole diameter D. Moreover, the FT geometry has an additional parameter, the small-hole diameter d. The optimization of these geometries was made using HFSS [87]. We set as main optimization goal achieving a minimum

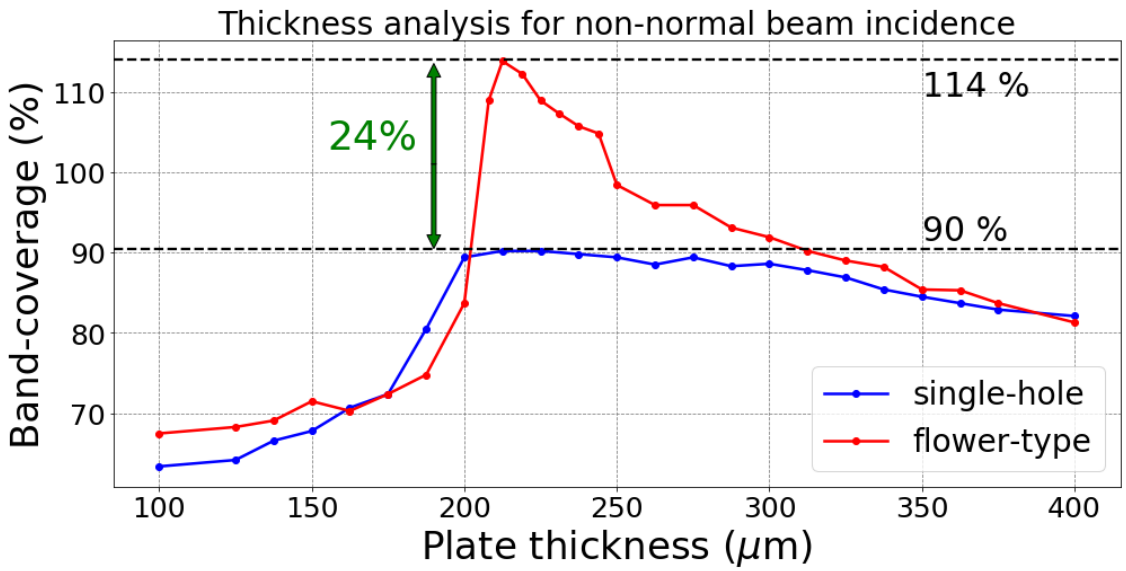

Figure 3.6: ***Simulated dichroic band-coverage as a function of the plate thickness.*** Analysis of transmission as a function of the layer thickness for the SH and FT designs. In both cases, maximum band-coverage is obtained when $t = 215\ \mu m$. The FT configuration can reach a 24 % extra band-coverage, which represents a significant improvement.

of transmission of 90 % in the pass-band ($600 - 725$ GHz). The secondary goals given to our script were keeping the rejection in the stop-band ($211 - 275$ GHz) below -25 dB to ensure a full reflection of the incoming wave, and maintaining cross-polar level below -30 dB to avoid leakage of power into high-order propagation modes.

The set of parameters that optimize the performance are given in table 3.2. It was found, for the SH and FT configurations, that a layer with a thickness of $\sim$215 μm gives the best performance, in terms of our main optimization goal (i.e. transmission), at non-normal incidence. However, due to restrictions on the manufacturing processes available to us, the minimum thickness to implement those designs was $t = 275\ \mu$m. Thus, in order to estimate whether this difference of 60 μm is detrimental in the performance or not, we analyzed the dependence of the layer thickness on the transmittance. Since a degradation in performance is expected to be larger at non-normal incidence, the analysis was restricted to only this case.

Figure 3.6 shows the band-coverage as a function of the plate thickness t. In this context, the term band-coverage is used to indicate the fraction of the pass-band whose transmittance is over 90%. The maximum coverage is reached, in both configurations, for $t \approx 215\ \mu$m. We see that the FT configuration can reach a band-coverage as high as 114% (i.e., covering more than is actually sought), whereas the SH only reaches a peak value of 90.2 %. This put in evidence the significant improvement that FT provides when compared to the SH configuration. Since the thickness to be used in both configurations is $t = 275\ \mu$m, a band-coverage of around 89.4 % and 91.1 % are expected for SH and FT, respectively. We deem that the reached performance using the available layer is good enough for a prototype aimed to validate our results.

To conclude this section, it is worthy to say that some of the effects of the fabrication

process were considered in the simulations. For the Jerusalem-cross prototype rounded corners were included (where radius depends on laser beam size used); whereas the other two prototypes -based on single holes- were endued with a slightly bigger diameter at the aperture of its back face.

3.4.1 Simulated performance for proposed prototypes

The idea of proposing so many options is that, in advance, we cannot assure that the simulation will match the experimental results. Any possible mismatch will be consequence of defects in the construction process, which is something very common when a system whose dimensions are in a scale of hundreds of microns are attempted for fabrication.

Figures 3.7 and 3.8 show the simulated performance at normal and non-normal beam incidence, respectively. These plots include the simulated transmittance, rejection (equivalent to the transmittance in dB) and cross-polar loss. Additionally, a blue and green strips were included to indicate the Band 6 and Band 9 frequency range, respectively. Purple dashed lines in the plots show the design specifications, whilst cyan and yellow dashed lines indicate the cut-off frequency ν_c and $\nu_{\mathrm{di}ff}$, respectively.

From figures 3.7 and 3.8 we can clearly see the angular dependence of the performance. A notorious reduction of the bandwidth and, a shift in the frequency cut-off (toward lower frequencies) are observed. These are unavoidable effects, however, they have been taken into consideration since the dichroic is aimed to operate at non-normal beam incidence with a fixed angle of $\theta = 18^o$. [1] Figures 3.7 and 3.8 also show that only the SH and FT configuration met the most relevant design specification, i.e., a transmittance over 90% in the frequency range of Band 9. The plots of transmittance (top panel) show that for normal beam incidence both configurations exhibits values over 90 % until frequencies beyond 0.9 THz. However, this is different for non-normal beam incidence since a shrinking in the bandwidth is observed. Nevertheless, despite this shrinking, both configurations cover almost entirely the target frequency range with a transmittance over 90 %. A degradation to values around 80 % is observed, for both configurations, at the high-frequency edge of the target range. The rejection in the Band 6 frequency range can be obtained by plotting the transmittance in logarithmic scale, which is shown in the center panels of figures 3.7 and 3.8. Once again the simulations show that only SH and FT configuration met this design specifications. In terms of cross-polar performance (down panel), we see that even with the degradation produced by non-normal incidence, the values are still below -40 dB (except for JC configuration), which is a very good result.

When the cut-off and diffraction frequencies are calculated using equations 3.4 and 3.5 respectively, we obtain the values $\nu_c = 550$ GHz and $\nu_{\mathrm{di}ff} = 930$ GHz. Looking at the top panel of figures 3.7 and 3.8 we can see that there is a good match between the analytical formulation and the simulations for ν_c at normal beam incidence. In the case of $\nu_{\mathrm{di}ff}$ there is a good match at normal beam incidence but this is missed at non-normal beam incidence. The explanation of this mismatch is due to the change in appearance produced when the

[1] All of the simulation presented here were done only for $\alpha = 0^o$ since we deem that for a proof of concept this is fine. However, we are aware that a full deployment using the ALMA's infrastructure will demand a full analysis of the α dependence.

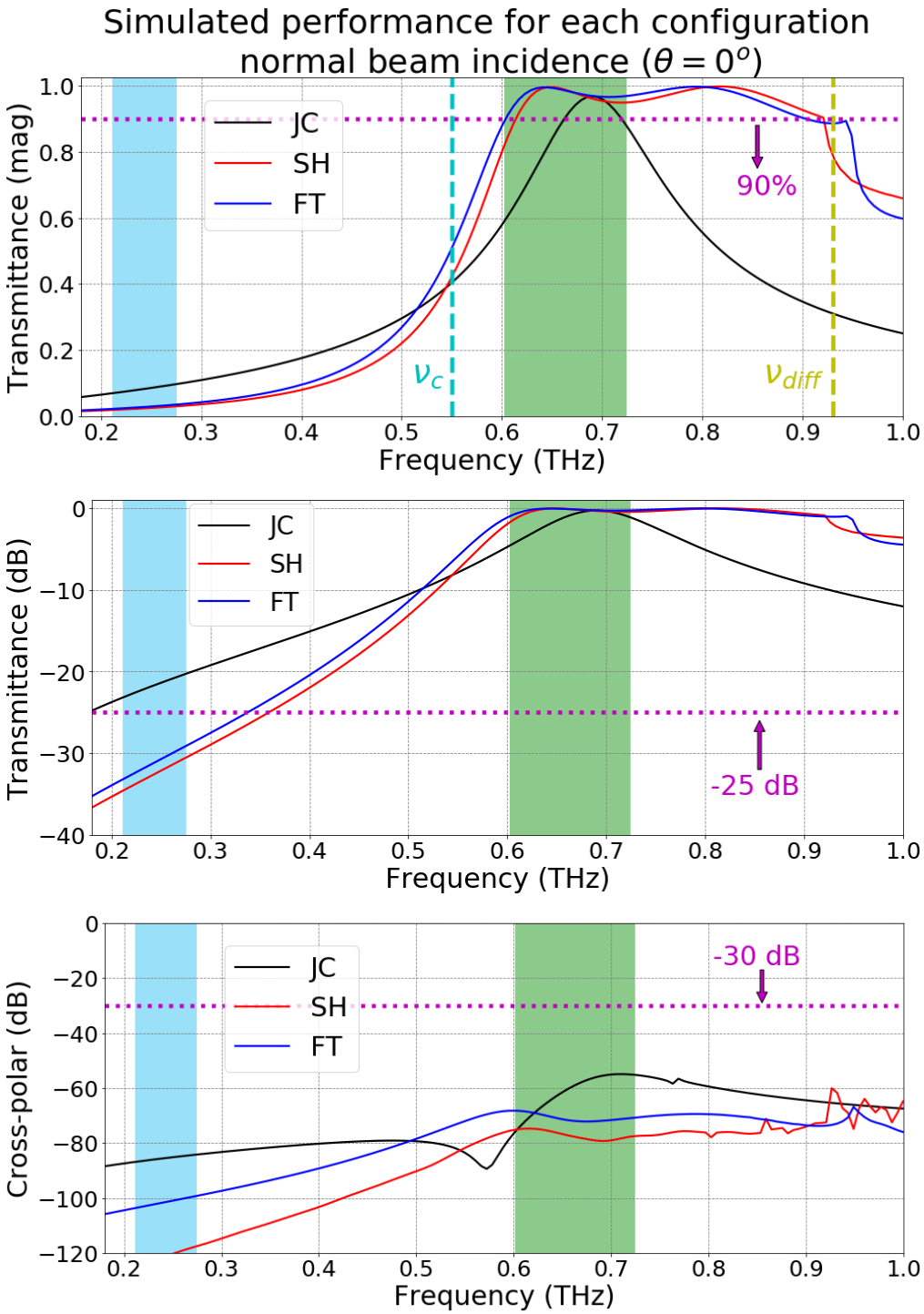

Figure 3.7: ***Simulated performance for each configuration at normal beam incidence.***

(Top) Transmittance, (center) reflectivity and (down) cross-polar loss as a function of frequency. The blue and green regions in the plot correspond to the frequency range of Band 9 (602-725 GHz) and Band 6, respectively. Vertical dashed lines are included to indicate $\nu_c = 550$ GHz and $\nu_{diff} = 930$ GHz; horizontal dashed lines mark the design specifications.

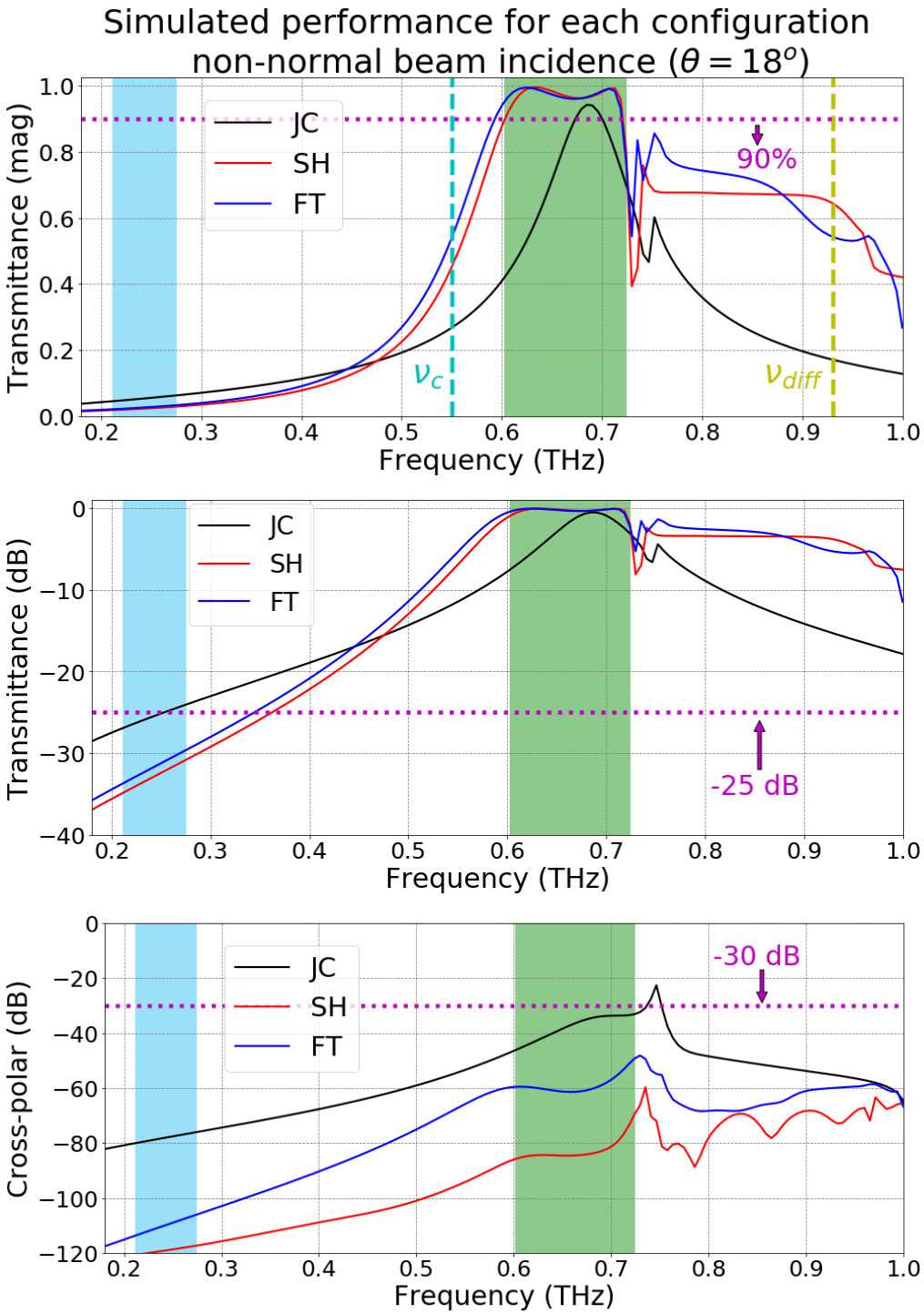

Figure 3.8: ***Simulated performance for each configuration at non-normal beam incidence.***

(Top) Transmittance, (center) reflectivity and (down) cross-polar loss as a function of frequency. The blue and green regions in the plot correspond to the frequency range of Band 9 (602-725 GHz) and Band 6, respectively. Vertical dashed lines are included to indicate $\nu_c = 550$ GHz and $\nu_{diff} = 930$ GHz; horizontal dashed lines mark the design specifications.

dichroic is tilted. It is important to highlight that both frequencies were calculated using the parameters of the SH configuration since there is no analytical solution for a system like the FT.

3.5 Fabrication of proposed prototypes

In this section, we describe the manufacturing process, which is different for each configuration. Even when the JC configuration does not fulfil the specifications, it is still a big challenge in terms of construction. Thus, it will be anyway fabricated and measured.

One of the big impediments at the time of fabricating any dichroic filter is - especially for those aimed to operate at submillimeter wavelengths - the high cost involved in the process. Several techniques have been proposed such as drilling, etching or laser cutting. However, there is no technique that can be considered as a panacea. This means that the most suitable technique will depend on the operation frequency, and the design specifications for the target dichroic filter. A good review of current available methods can be found in [85]. As it was state above, our manufacturing capabilities are limited. This is why only the Jerusalem-cross and the the single hole systems were fabricated 'at home'. The former was manufactured by using a Laser Cutter in the Millimeter Wave Lab, in Chile, whereas the latter was manufactured by drilling holes assisted by a CNC machine at Physics Department of the University of Groningen, The Netherlands. The 'flower-type' dichroic was fabricated by a commercial company, where a combination of high-precision laser cutting and etching was used.

In chapter 2, we stated that a dichroic aimed to be integrated into the designed beam combiner optical system must have a diameter of around 55 mm. However, as the production cost depends (almost exclusively) on the necessary fabrication time, we deemed that a full-size version of dichroics to be fabricated are too expensive. For this reason, all the fabricated dichroics have a diameter of only 25 mm. This allowed reducing the fabrication time in around 75%, which reduced the production cost to only one-quarter of the full-size version (only for the 'flower-type' dichroic). We are aware that for a real integration, into the beam combiner optical system, a 25 mm prototype is absolutely inappropriate. Nevertheless, we deemed that for a proof of concept the chosen size is a good trade-off.

The results of the fabrication for JC, SH and FT configurations are shown in figures 3.9, 3.10 and 3.11, respectively. It is evident that none of the fabricated dichroics are free of manufacturing errors. The most severe case is, evidently, the JC. A considerable amount of metallic residue spans all over the surface. The explanation for this lies in the lack of a process to remove the scattered metallic particles after being evaporated by the laser. For the case of the SH dichroic, the situation is more favourable but still not exempt from errors. The most notorious (and also the one that might produce an undesirable effect on the spectral properties) is the observed shift in the aperture spacing along two directions with a value $s_2 = 0.415$ mm (s_1 corresponds to the nominal value given in table 3.2). The most likely explanation for this error is due to the selection of the path and accuracy that was given to the drilling tool. Additionally, some grooves are observed on the surface, which can increase the ohmic loss of this filter [92]. Finally, the FT dichroic seems to be the constructed configuration with the highest accuracy. It is observed (see figure 3.11) that apertures and

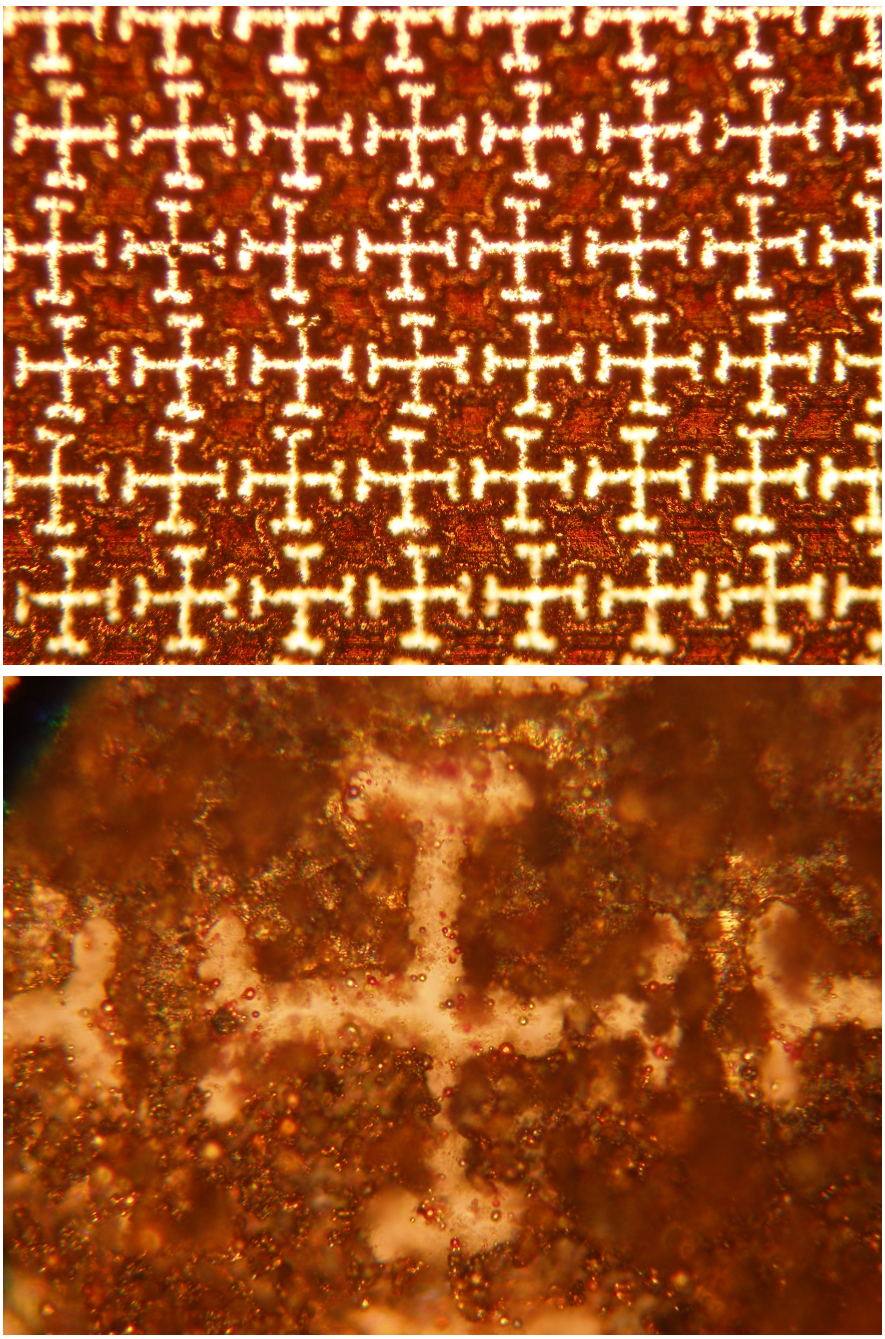

Figure 3.9: ***Constructed JC dichroic configuration.***
Misalignments and irregularities in square layout are clearly visible. Furthermore, a considerable amount of metallic residue span all over the surface.

spacing are quite homogeneous all over the surface on the front face. However, looking at the back face we see that the flower-type aperture shaped is missed and, replaced with a circular aperture. Additionally, the plate of this dichroic presents an evident curvature, which is most likely result of a thermal deformation when the laser was used to perforate the plate. A new simulation (not shown here) was made in order to include these errors and estimate their impact. An almost negligible difference of the spectral properties was observed in this new simulation. Therefore, we deem that these observed errors may not impact significantly the

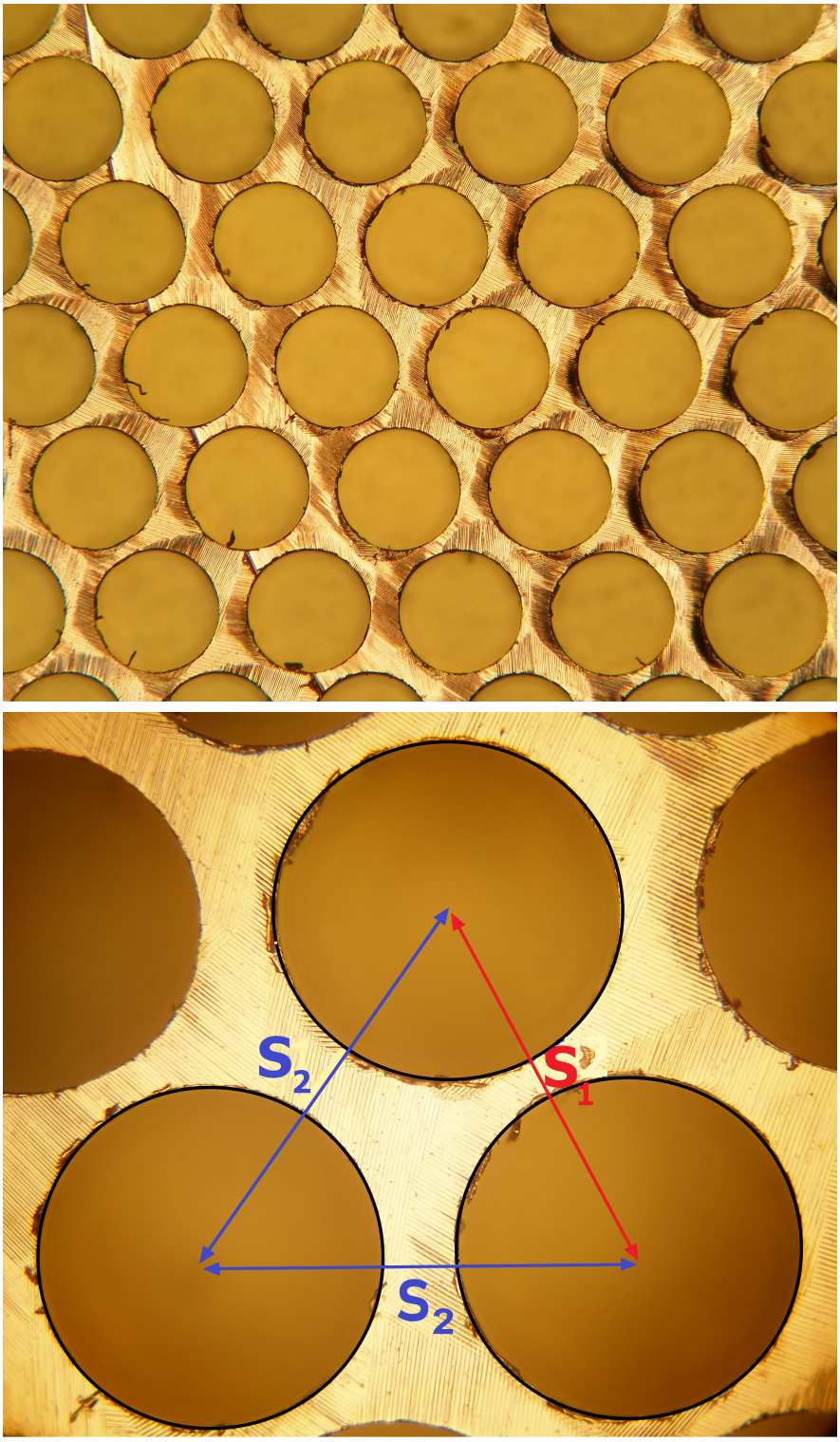

Figure 3.10: ***Constructed SH dichroic configuration.***
(top) Fabricated single-hole dichroic made of brass. (down) Close-up showing an undesirable shift in spacing along two directions. A shifted spacing $s_2 = 415\mu$ m is observed (s_1 corresponds to the nominal value given in table 3.2). This imperfection breaks the hexagonal symmetry and it will produce changes in the performance. Moreover, imperfections in the surface are observed.

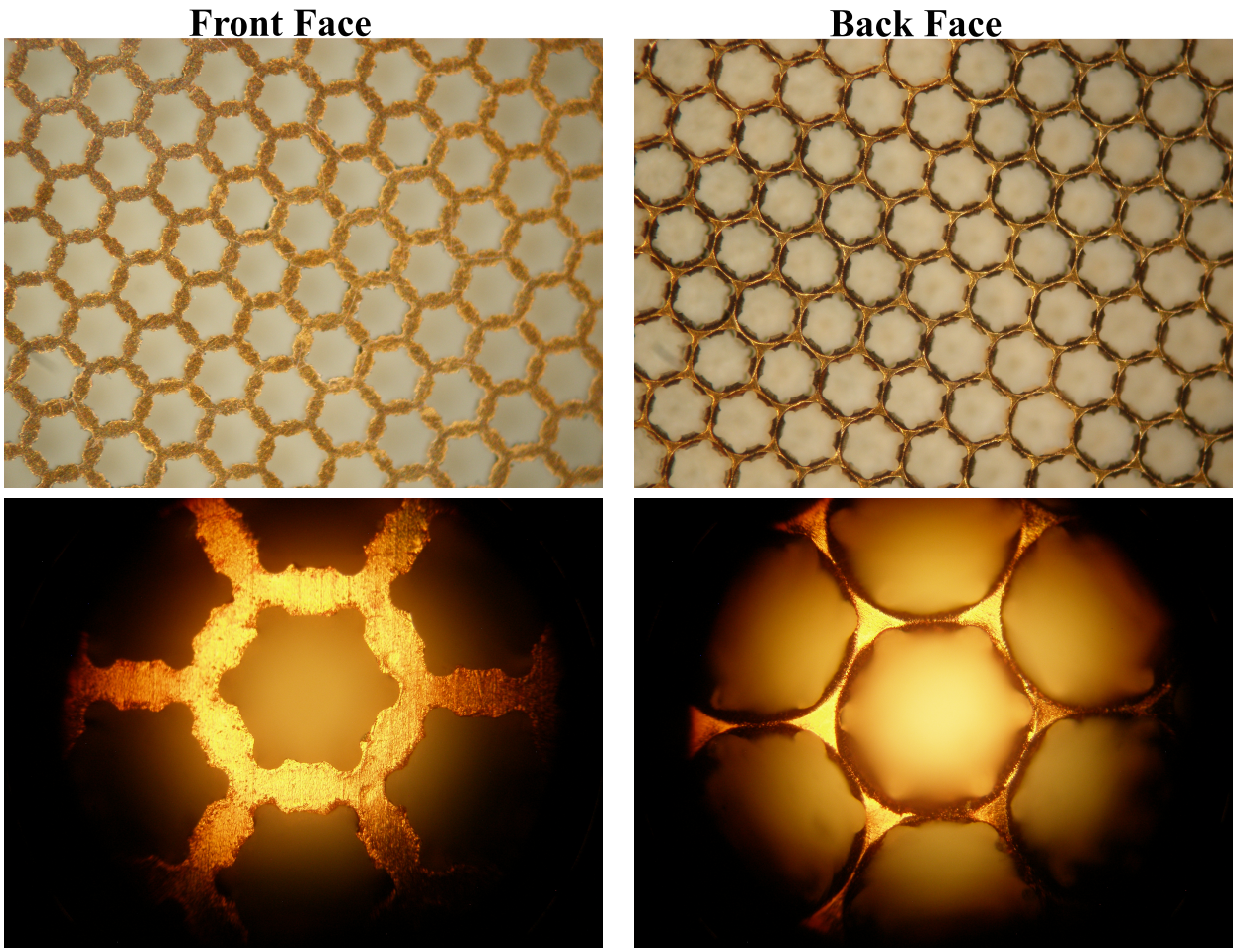

Figure 3.11: ***Constructed FT dichroic configuration viewed from its front and back face.***
The front face (left column) shows a high homogeneity in the aperture and spacing size. However, the 'flower' shape of the aperture is missed on the back face and replaced with a circular aperture. (right column).

performance (which is actually demonstrated in the next section).

3.6 Transmission characterization

In this section we explain the experimental setup to be used in the characterization of the dichroics. For a good understanding, we start with a quick review of the fundamentals of Fourier Transform Spectroscopy (FTS) theory.

Fourier Transform Spectrometer

Fourier Transform Spectrometer is a device used to analyzing the spectrum of light by means of interferometry [93] using (most commonly) a Michelson interferometer as shown in figure 3.12. When there is a difference in the optical path length between both beams, produced by moving one of the mirrors, a phase shift is introduced, which creates an interference pattern when the beams are recombined. The interference between the light beams can be either constructive or destructive. In constructive interference, the recombined beam are in phase

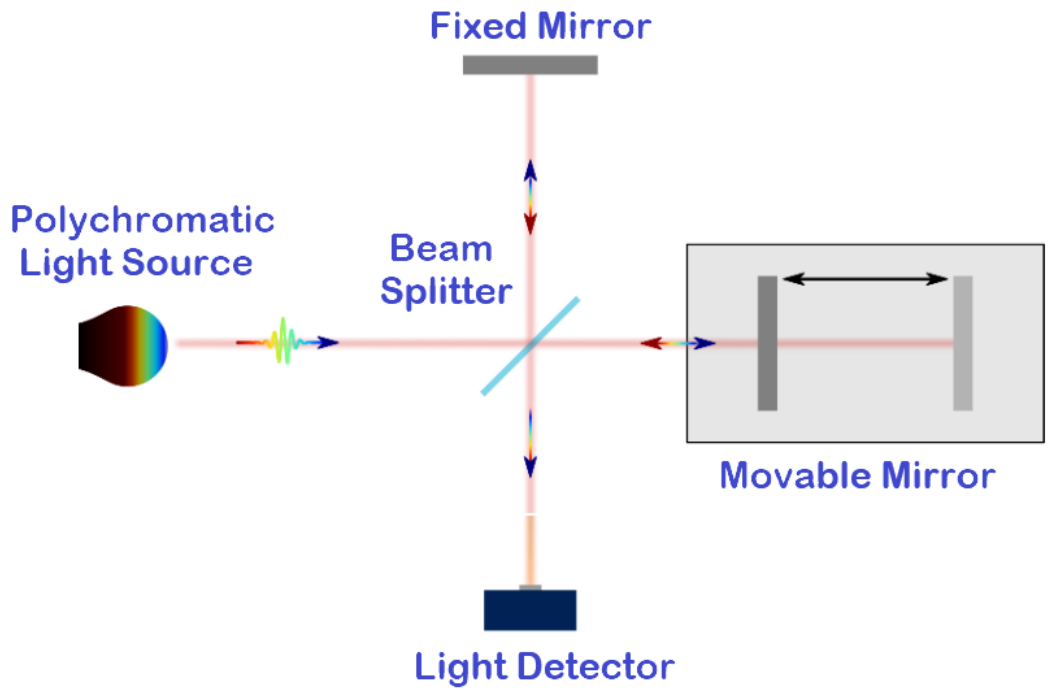

Figure 3.12: ***Michelson Interferometer***
A beam splitter is used to divide a polychromatic light beam. Then, the two produced beams are recombined by means of reflection upon two flat mirrors producing an interference pattern, which is measured using a light detector.

resulting in that the intensity at the detector is equal to the intensity of the source. On the other hand, destructive interference the intensity at the detector is zero, product of a recombination of beams out of phase. Conditions for constructive/destructive interference can be understood in terms of optical path difference (δ). This is mathematically expressed as

$$\delta = 0 \quad \text{or} \quad \delta = n\lambda, \tag{3.6}$$

$$\delta = \frac{\lambda}{2} \quad \text{or} \quad \delta = (n+1)\tfrac{\lambda}{2}, \tag{3.7}$$

where n is an integer. Equation 3.6 is for constructive interference, whilst 3.7 is for destructive interference. In case of intermediate values for δ, the intensity at the detector also takes intermediate values between maximum and zero. This intensity as function of δ is called interferogram, and for monochromatic light, takes the sinusoidal form

$$I(\delta) = \frac{I_0}{2}\left(1 + \cos\left(\frac{2\pi\delta}{\lambda}\right)\right), \tag{3.8}$$

where I_0 is the intensity of the source. In the case of having a polychromatic source of light,

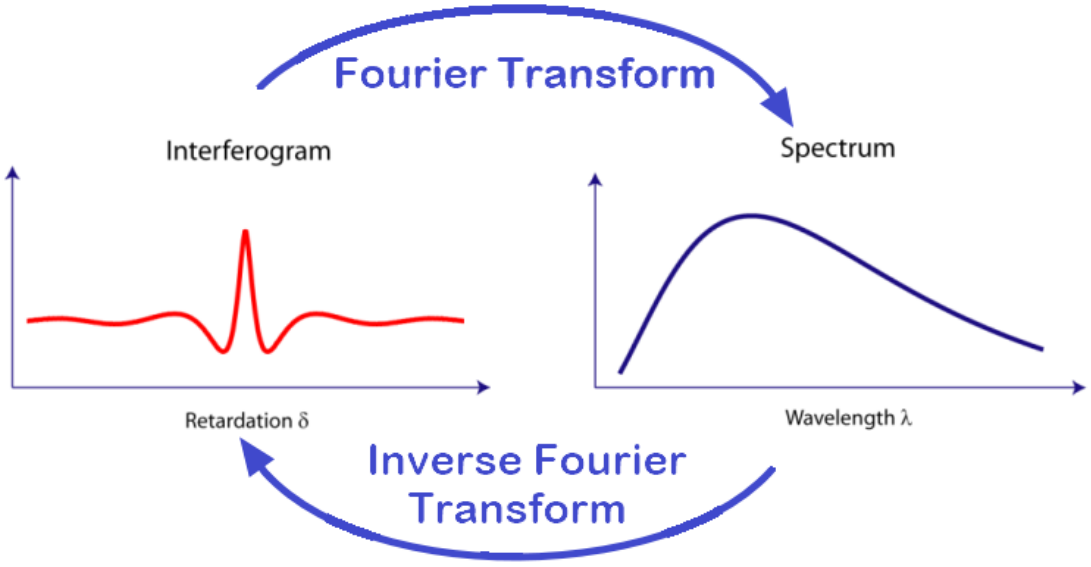

Figure 3.13: ***Relation between interferogram and polychromatic light spectrum***
Fourier transformation can be applied to the measured light intensity as a function of retardation δ (interferogram) to obtain the spectrum of the light source. The inverse relation is also possible by means of inverse Fourier transformation.

the interferogram is given by the continuum sum of each monochromatic contribution

$$I(\delta) = \int S(v)\cos(2\pi v\delta)\mathrm{d}v, \tag{3.9}$$

where $v = 1/\lambda$ and $S(v)$ is the spectrum of the light source. From equation 3.9 the spectrum can be easily obtained by inverse Fourier transformation

$$S(v) = \int I(\delta)\cos(2\pi v\delta)\mathrm{d}\delta. \tag{3.10}$$

Equation 3.10 takes the form of cosine Fourier transform (or simply the real part of Fourier transform). This relation between interferogram and the spectrum of a light source is illustrated in figure 3.13.

Experimental methodology

In order to get the transmittance for all of the fabricated dichroics, we will use the same methodology, which is described as follows. A THz beam with a flat wavefront is generated with a lamp in combination with a parabolic mirror. Then, this THz beam goes through a polarization grid before being divided by a beam-splitter (BS). The two generated beams are reflected backwards by two flat mirrors (one of them movable), and then, recombined by the BS. Since the diameter of all the constructed dichroics is 25 mm the THz beam must reduced in size. For this, a diaphragm is placed between the BS and the device-under-test

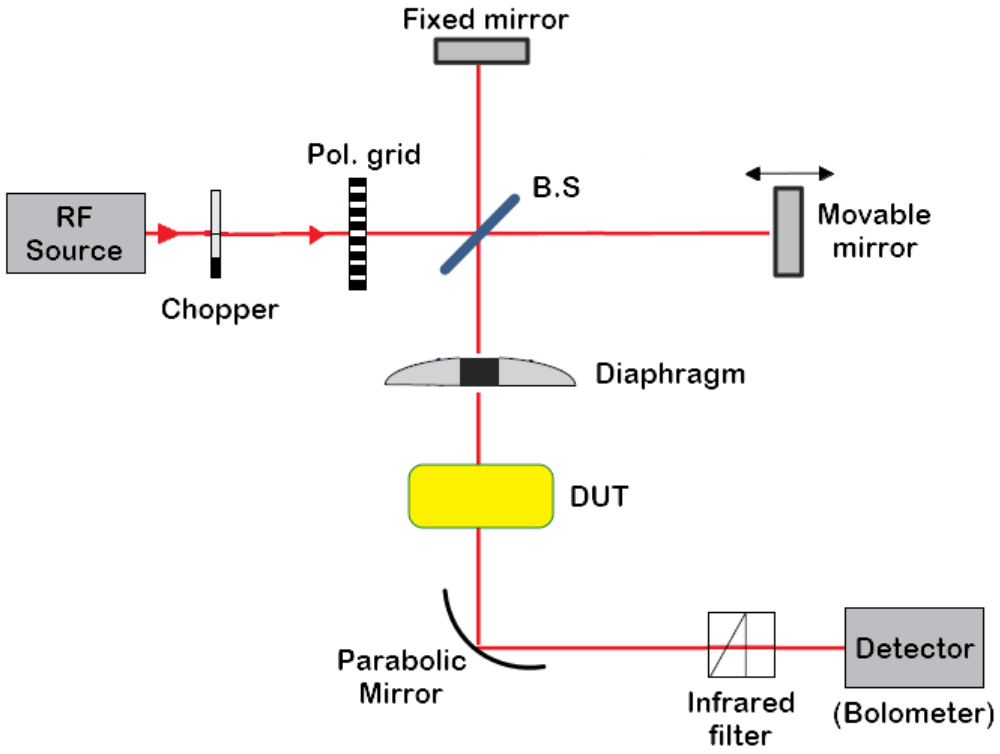

Figure 3.14: ***Diagram of the experimental setup used for the characterization.***

(DUT). Finally, the THz beam that results after passing through the DUT (in this case one of the constructed dichroics) strikes upon a parabolic mirror, which couple the beam into a bolometer detector. A diagram of this THz interferometer is shown in figure 3.14.

For each measurement we need to take a reference signal, this means, the interference pattern generated when the THz beam does not go through the DUT. This is easily realized by taking the DUT out of the setup. Once the interferograph is obtained for the reference signal, we will know the spectrum generated by the lamp (S_{ref}). Then we repeat the process, but this time including the DUT and, thus, a second sampled spectrum will be generated ($S_{sampled}$). This second spectrum corresponds to the same THz beam plus the contribution of the DUT. Therefore, the transmittance (T) of the DUT is obtained by the ratio

$$T = \frac{S_{sampled}}{S_{ref}}. \tag{3.11}$$

This procedure is applied for each dichroic at normal ($\theta = 0^o$) and non-normal ($\theta = 18^o$) incidence. The experimental setup used to take the measurement is shown in figure 3.15.

3.7 Performance analysis

It was observed that the measurements at frequencies lower < 350 GHz became very noisy. This noisy region appeared in all the measurements, but it is more noticeable in the inset (b)

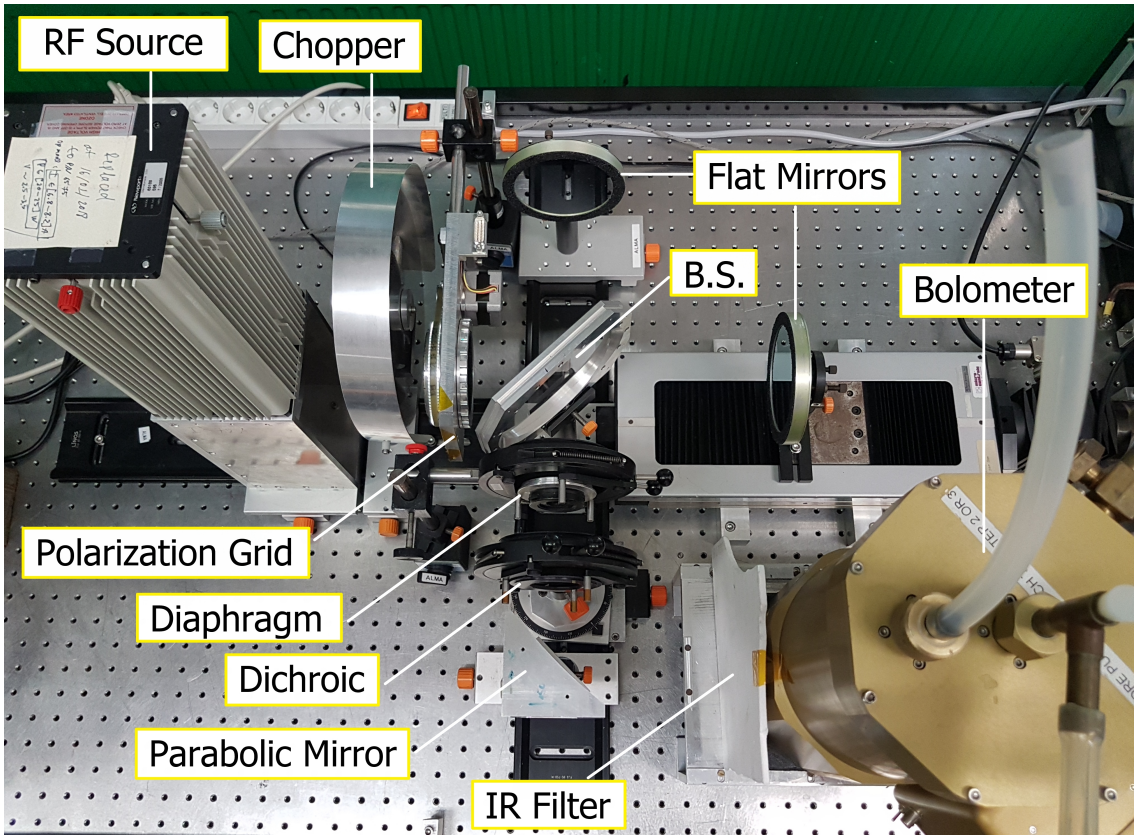

Figure 3.15: ***FTS experimental set-up.***

of figure 3.17. The reason why this happened is because the sensitivity of the used detector decreases as the frequency goes below 350 GHz and, it totally vanishes for frequencies lower than 200 GHz. Moreover, the dichroics present a rejection of < -20 dB for frequencies below 400 GHz. Thus, the ratio $S_{sampled}/S_{ref}$ for frequencies < 350 GHz resulted in a signal dominated by noise. For this reason, the experimental data at frequencies lower than 300 GHz were removed from the plots in order to enhance their visualization. We present the result starting with the FT, followed by the SH, and finishing with the JC configuration.

3.7.1 Experimental results for the flower-type configuration

Figure 3.16 shows the comparison between measurements and simulations at normal and non-normal incidence of the FT dichroic. First, an excellent agreement is observed at normal incidence. The measurements exhibit a sharper cut-off and, the frequency point where the cut-off occurs is slightly up-shifted. Second, the results at non-normal incidence are also in good agreement. A similar feature for the cut-off frequency is observed, and, additionally, there is an small decrease in the level of transmittance. Despite this drop-off, the transmittance reaches a peak value $\sim 97\%$ at 622 GHz, and a minimum of $\sim 87\%$ within the pass-band. We believe that the cut-off shift occurs due to small defects of fabrication, specifically, the slightly conical shape of the apertures at the back face. As reported in [85], the measured cut-off frequency of fabricated dichroic filters are usually sensitive to the fabrication tolerances, whilst other filter properties remain similar. The discrepancy in transmittance can be also consequence of the conical shape at the back face. Since, as reported in [94], an

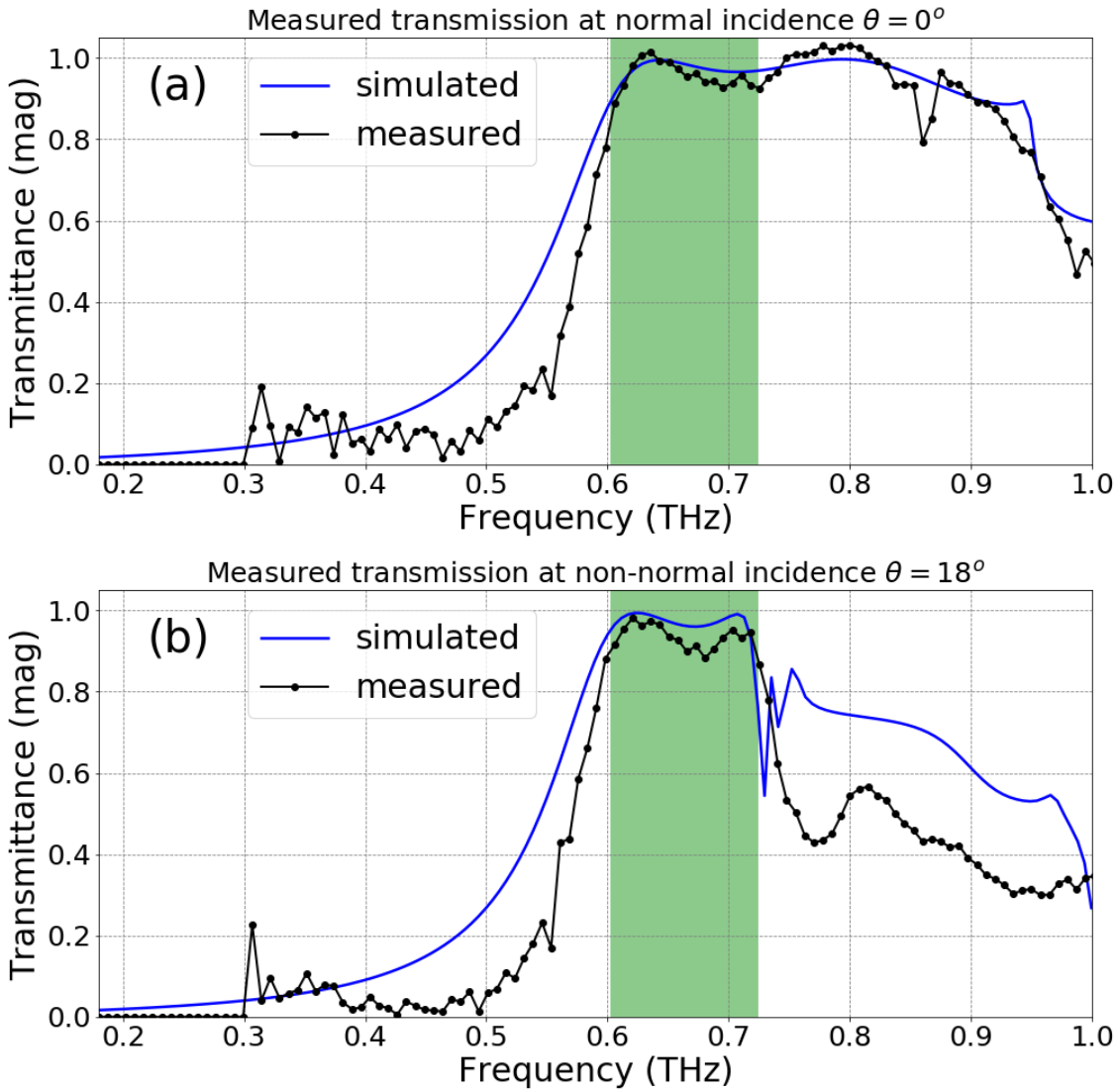

Figure 3.16: ***Experimental results for FT dichroic***
(Top) Comparison between measurements and simulation for normal beam incidence. (Down) Comparison between measurements and simulation for non-normal beam incidence.

increased loss of the propagation modes inside a circular waveguide occurs when the radius varies along the transverse direction. This loss is more evident at non-normal incidence since it depends on the relative phase of the propagation modes.

Despite of the small difference in transmittance at non-normal beam incidence, the experimental results demonstrate the advantage in performance of this novel geometry. This is particularly remarkable considering that the presented filter is a single-layer system operating at THz frequencies and with a bandwidth of $\sim$ 120 GHz. Nevertheless, there is one caveat involving the plate that contains the dichroic, which is not flat. This details will impede to integrate this dichroic into the optical system presented in chapter 2.

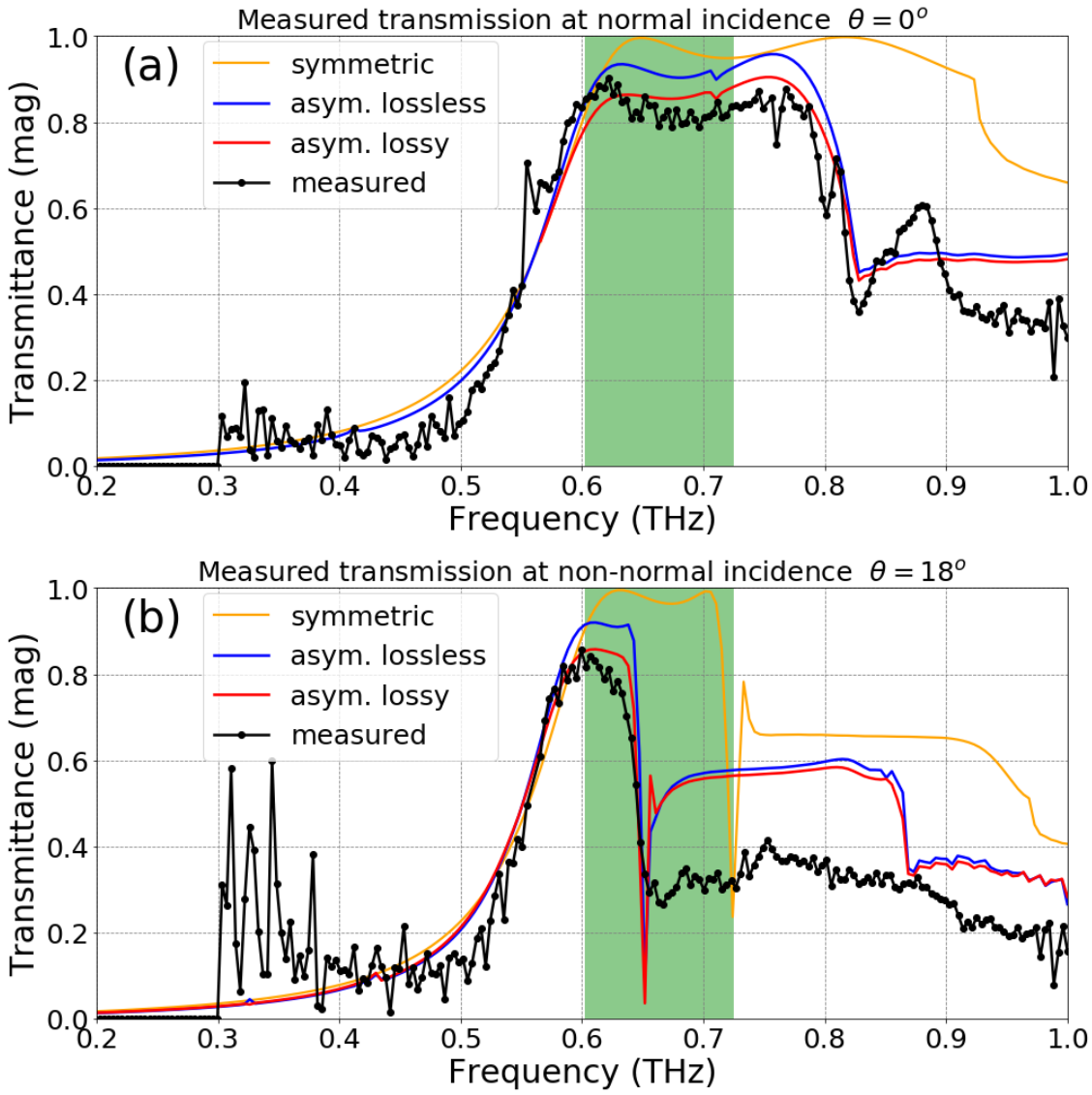

Figure 3.17: ***Experimental results for SH dichroic***

Measurements versus simulation for SH dichroic at (a) normal and (b) non-normal incidence. A better agreement is obtained when the implemented super-cell and ohmic losses were included in the simulations.

3.7.2 Experimental results for single-hole configuration

The observed shift in the spacing (see Fig. 3.10) of the fabricated SH geometry has led to discrepancies between the measurements and the expected results shown in figures 3.7 and 3.8. From figure 3.17 we observe two clear consequences of breaking the symmetry of the aperture distribution, the band-pass is considerable lowered at both normal and non-normal incidence and there is a decrease in the peak of transmittance. To explain this, new simulations were made. This time we implemented a bigger unit cell containing four apertures distributed asymmetrically as shown in figure 3.18. In order to reduce the the size of the cell, and therefore, the computation time, a rhomboidal unit cell was used (instead of a hexagonal cell). The position of each aperture was shifted a certain distance with the intention of reproducing the observed aperture distribution shown in figure 3.10. In addition, we also included in the simulations the imperfections of the surface. This was made by reducing the

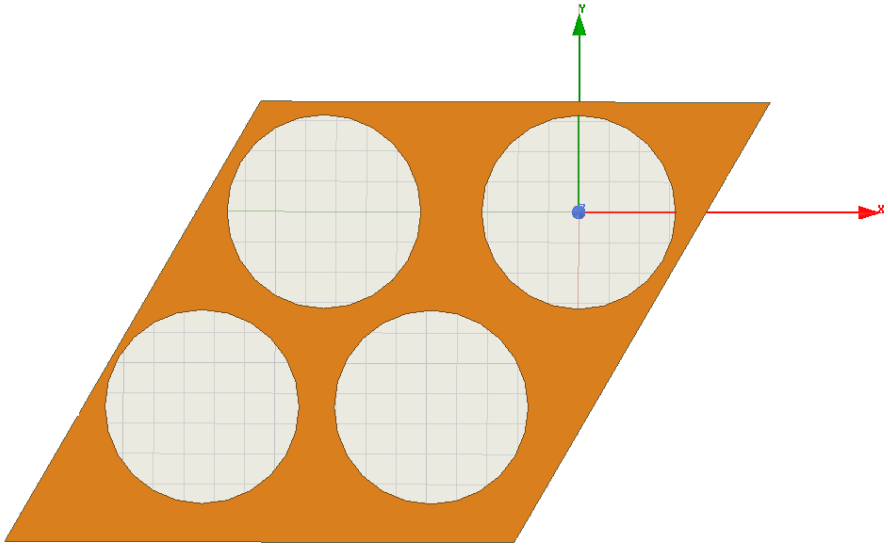

Figure 3.18: ***Implemented super-cell***
A cell with an asymmetric aperture distribution, as observed in figure 3.10, was simulated

bulk conductivity of the material to 20% of the value given in the HFSS material library [87].

Figure 3.17 compares the results of the new simulations with the experimental data. The blue line corresponds to a lossless asymmetric aperture distribution, whilst red line correspond to a lossy asymmetric distribution. We see that the former makes a fair match with the experiments but a discrepancy in the peak value of transmittance is observed. Including a finite conductivity makes a better match with the experimental data. The transmittance shown in figures 3.7 and 3.8 were included with a yellow line for comparison. The measurements reveal that at normal incidence the transmittance reaches a maximum of $\sim 87\%$, whereas at non-normal incidence the peak of value barely reaches $\sim 80\%$, This decrease in transmittance results as a consequence of the angular degradation that occurs at non-normal incidence and, it is increased by the fabricated defects presented in it.

In summary, despite being able to find a model that increases the agreement between measurement and simulation, this fabricated dichroic does not satisfy the design specifications. Hence, in order to make this dichroic suitable, for our specific goal, the fabrication process must be improved. Nevertheless, maybe this prototype is still good for application at non-normal beam incidence.

3.7.3 Experimental results for Jerusalem-cross configuration

No match between measurements and simulation is observed for the JC dichroic (see figure 3.19). However, a similar tendency is observed for normal beam incidence but with a peak transmittance of only 60% and a shift in frequency of around 100 GHz. The situation is even worse for non-normal beam incidence since no correlation between measurement and simulation is observed at all.

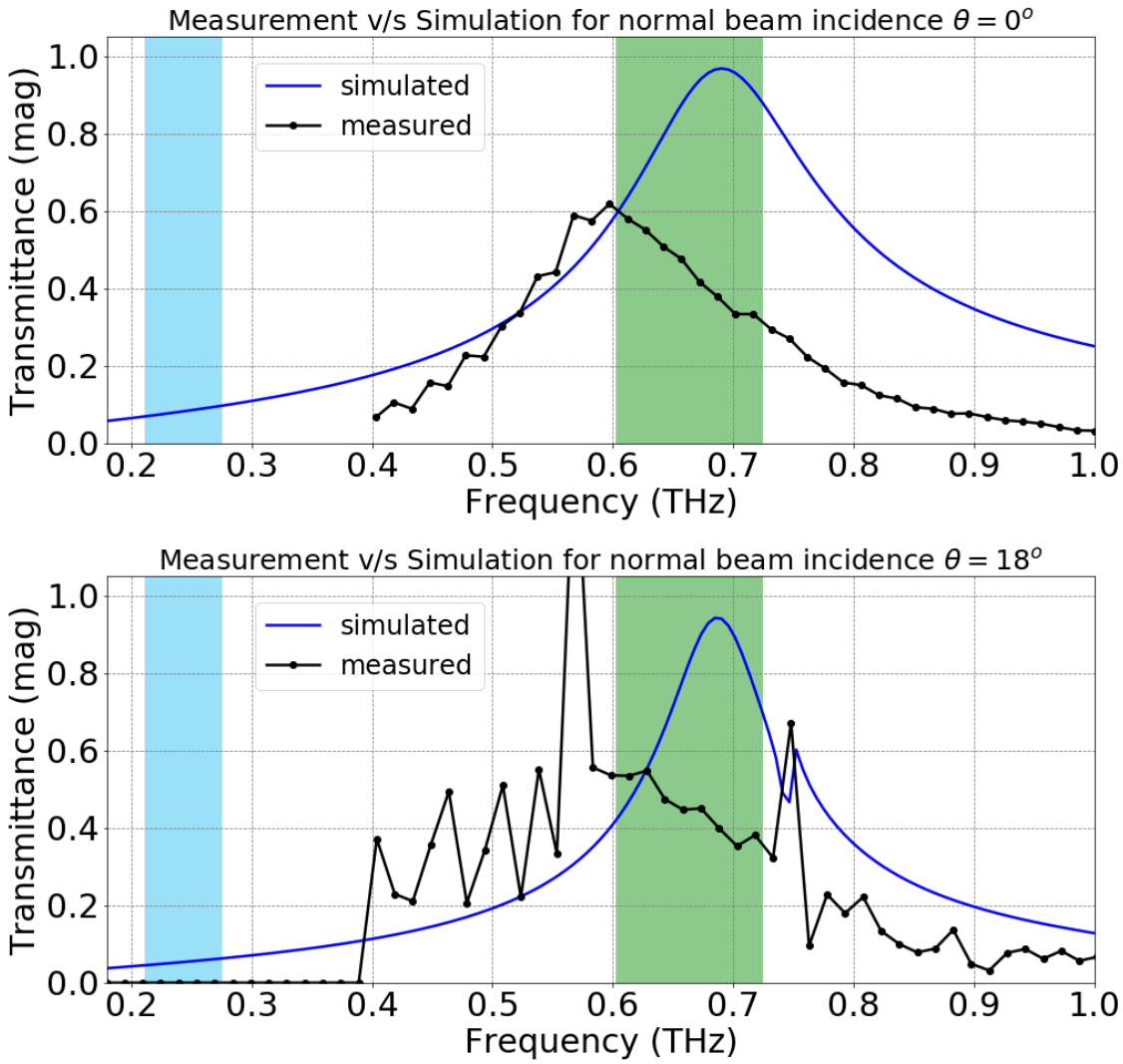

Figure 3.19: ***Experimental results for JC dichroic***
(Top) Comparison between measurements and simulation for normal beam incidence. (Down) Comparison between measurements and simulation for non-normal beam incidence. For the case of normal beam incidence a similar tendency is observed but this featured is missed for non-normal incidence.

In conclusion, the fabrication of this JC dichroic was absolutely not satisfactory because of the fabrication errors that made it unsuitable for any application that aims a low-noise detection.

3.8 Conclusions

In this chapter we have proposed three configurations (Jerusalem-cross, single-hole and flower-type) for a dichroic filter aimed to be used in the optical system presented in chapter 2 to enable ALMA operation in a dual-band mode. All of the proposed dichroics correspond to single-layer structures, where the spectral properties depend on the design parameters, i.e., the aperture size and shape, aperture spacing and plate thickness. Additionally, the expected change of the spectral features for non-normal incidence was experimentally confirmed.

Among all of the proposed configurations only the single-hole, and the flower-type configuration reached the design specifications for almost all the target frequency range. However, at the time of fabrication only the flower-type configuration was successfully made up. The measured performance of this showed a very good agreement with the simulations. This is a very good result since, considering the target frequency range, any commercial option come in the form of multi-layer system. Despite achieving the desired performance, the fabricated flower-type dichroic is not suitable to be integrated into the optical system because it is not totally flat. This issue could be sort out by improving the fabrication process.

The work presented here demonstrates that dichroics based on single layer system represent a good and competitive option for low-noise THz astronomical applications. The advantage of single-layer system over more complicated layer configuration is clear at the time of looking alternatives with lower cost and high repeatability. However, in order to obtain reliable results, high accuracy fabrication method, like laser cutting, must be used. In addition, we believe that as new fabrication technologies arise, this work opens the possibility of looking for new aperture geometries suitable for high-performance dichroic filters.

In order to characterize the combination of the optical system presented in chapter 2, and the dichroic presented in this chapter; a high-performance feed horn antenna is required. Since this type of horn antennas are quite expensive, we consider that developing an antenna 'at home' represents a very interesting challenge. For this reason, in the next chapter, we will focus on the design, construction and characterization of horn antenna aimed to cover the Band 6 frequency range.

Chapter 4

Smooth-Walled Antennas for THz Frequency Range: Design and Evaluation

4.1 Introduction

Traditionally, corrugated conical horn antennas have been the main choice for use in astronomical receivers in the range of millimeter and submillimeter waves. They present low cross-polar level and high coupling efficiency into the fundamental Gaussian mode. However, this type of antenna is difficult to manufacture, inevitably increasing its price and extending the production process. In this work, we present two kinds of feed horn antennas, aimed for use in a frequency range equivalent to ALMA Band 6 (211-275 GHz), which can be fabricated in a much simpler way with conventional machining tools. Specifically, we present the design and performance comparison of smooth-walled spline-profile horns in two geometries, diagonal and conical. Optimization of the designs has been made by means of an algorithm that allowed us to obtain models whose electrical and mechanical characteristics make them competitive when compared with corrugated horns. In particular, they are 40% shorter than conventional corrugated horns suited for this band, representing an advantage given the stringent space constraints of most astronomical receivers. We also demonstrate that they can be coupled efficiently to an astronomical-grade optical system, using ALMA Band-6 receiver as an example. Furthermore, we have constructed the diagonal horn and characterized it thoroughly. Experimental results of the radiation pattern at room temperature show a good cross-polar performance with levels below -20 dB and gaussicity above 96%. Our calculations show a good antenna-efficiency level with losses less than 1%. All these properties demonstrate the feasibility of this type of horns to become the main option at the time of choosing a feed system for cutting-edge astronomical applications.

4.2 Smooth-Walled Spline-Profile Horns

4.2.1 The historical development of horn antennas

Corrugated conical horn antennas have been, traditionally, the main choice when it comes to developing instruments for astronomy applications in the range of millimeter and sub-

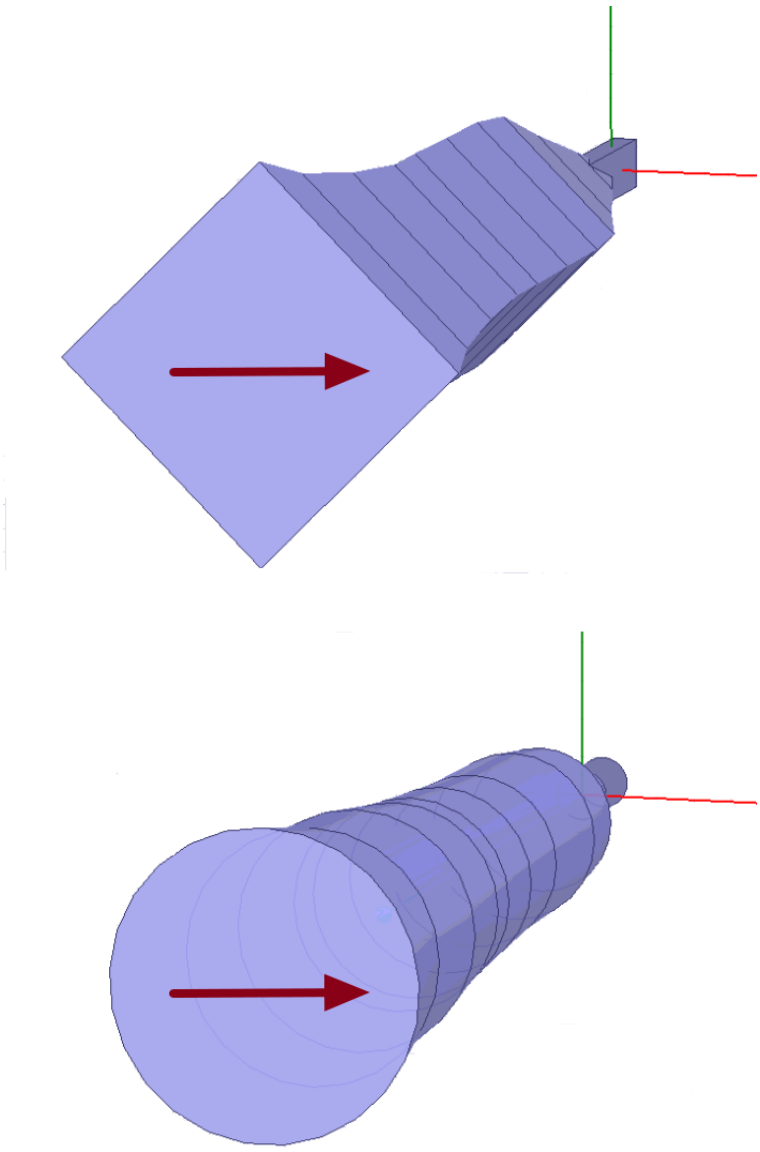

Figure 4.1: ***The two horns under study***

(Top) Diagonal-spline horn connected to a rectangular waveguide. (Bottom) Conical horn connected to a circular waveguide. Electric field orientation in input waveguide of the designs is represented by the brown arrow. It has been located at the aperture just to simplify its visualization. Both designs were optimized in order to reach the goals described in table 4.1.

millimeter waves (including part of the THz frequency spectrum) [95] . They have been selected due to their excellent characteristics. In particular, their coupling to the fundamental Gaussian mode (in short *gaussicity*) is around 98% and cross-polar level lower than -30 dB [47]. Nonetheless, this sort of antennas are difficult to manufacture, inevitably extending the production process and, therefore, increasing their price. There are other options to corrugated horns, e.g., conical and pyramidal horns. However they lack symmetry in the radiation pattern and, additionally, pyramidal horns present astigmatism [96].

The diagonal horn was first described in 1962 [97] and, subsequently, Johansson et.al. [98]

studied the feasibility to construct it using the split-block technique. They concluded that in this way integration to focal plane array could be easily implemented, with a negligible beam distortion. However, having a coupling to fundamental Gaussian mode of around 84% and a cross-polar level of around -15 dB, they are not the best option for astronomical applications. In 2002, Granet et. al [99] introduced the so-called smooth-walled spline-profile horn, as part of an upgrade program of The Australian Telescope [100]. They demonstrated that this horn achieved a performance in W-band that, in certain cases, has a competitive performance compared to its corrugated counterpart. Albeit the machining process was easier than the process to fabricate a corrugated horn, this is still somewhat complicated given the large numbers of steps taken to give the cubic spline shape to the walls. In 2018, Gibson [101] took one step further combining the smooth-walled spline-profile horn with the ease of fabrication of the diagonal horn. The outcome was a new type of horn, designed for THz frequencies, easier to construct, and with a Gaussicity around 97% and cross-polar level better than -20 dB. These features make this horn a good candidate to replace the corrugated horn in THz astronomical applications.

All these efforts reflect the increasing interest in replacing corrugated horns with alternatives that have good performance (even at the expenses of some trade-off), allow reproducibility, are easier to machine, and have an affordable cost. Not only astronomy but also other applications would benefit of such antennas since all of them are aiming to construct receivers at ever higher frequencies and, if possible, in the form of focal plane arrays [102–105]. In this paper, we present the comparison of two types of smooth-walled spline-profile horn antennas, diagonal and circular (figure 4.1), and the construction and characterization of one of them. This work has been focused on the frequency range covered by ALMA Band 6 (211-275 GHz), currently one of the most interesting observation bands for astronomers, with the image of HL-Tau [106] and the first image ever taken of a black hole event horizon [107] as examples of its major achievements. Nevertheless, the methodology described here is applicable to any kind of smoothed-wall horn antenna, no matter the applications nor the operating frequency range. This is particularly interesting because this method is scalable for higher frequencies, where the construction of corrugated horns is extremely difficult due to increasingly shorter wavelengths [108]. Our goal here is to make the horns suitable for astronomical applications, and at the same time, keeping their construction easy and at low cost.

Our work demonstrates that a simplified profile can achieved similar or better performance when compared with other smooth-walled profiles [99, 101]. Simulations show good return losses with no necessity of flaring the input waveguide. Moreover, measurements show an improvement in various figures of merit. The beam has a more circular beam shape, cross-polar performance has levels lower than -20 dB, sidelobes are below -25 dB in the E and H cardinal planes, and the calculated Gaussicity exceeds 96%. Furthermore, we show that the smooth-walled horns studied here can be coupled efficiently to astronomical-grade receivers. As an example, we have calculated the coupling to the existing cold optical system of ALMA Band 6.

4.2.2 Diagonal-spline and Conical-spline horn designs

The starting point to design both horn antennas is the profile of the walls, which defines the features of the radiation pattern. We have followed a similar methodology as described

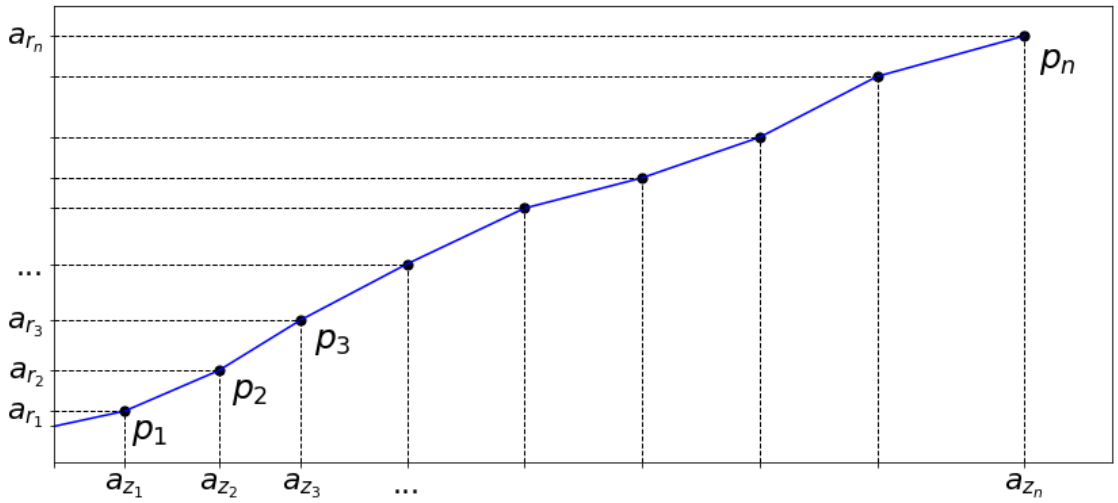

Figure 4.2: ***Basic 1-D profile of the smoothed-wall horn antennas.***
The shape of the horn wall is defined by the set of straight blue lines that connect each node (black dots labelled as p_{i}).

in [109], i.e., define the wall shape using a spline curve and splitting that curve into several segments. Each of these segments are defined by two nodes (labeled as p_{i}), as shown in figure 4.2. In order to simplify the machining even further, we have used straight lines to connect nodes instead of a cubic spline curve. Each node is defined by a pair of coordinates (labeled as a_r and a_z), which are used as parameters for the optimization process. We selected a set of nine nodes to described each horn, as a compromise between achieving the required goals and the use of computational resources. To define the initial position of the nodes, we started from a conventional diagonal, with the appropriate aperture, designed to operate in the desired frequency range. Then, we divided the straight profile into nine equal segments, which defines the initial position of the nodes.

Once the initial wall shape is defined, the next step is creating the volume. On the one hand, for the diagonal-spline horn, the volume is created by rotating the 1-D wall profile in 90° and −90°, then each node is linked to its adjacent neighbors using straight lines. The result is a set of flat rectangular surfaces connecting the nodes that defines half of the volume of the horn. Then, the final volume is obtained by mirroring the resulting surface, by means of selecting the proper symmetry axis. On the other hand, the conical-spline is created by applying a 360° rotational sweep to the initial 1-D wall profile. Both horn geometries are shown in figure 4.1. The diagonal-spline and conical-spline horn designs are fed using a rectangular (0.5 mm × 1.0 mm) and a circular (ϕ 1.30 mm) waveguide, respectively. This election was made to facilitate the subsequent machining process.

The optimization process for both horns was done using an HFSS [87] model, which takes the coordinates of each node as parameters. To make the horns suitable for astronomical applications, we have set the specifications listed in table 4.1 as goals for the optimization. The goal of 2.0 mm for the beam waist was set as a reasonable value that could permit connecting the horn to an optical system. The optimization process starts from an initial set of points a_r and a_z. Then, these values are moved around their initial ones over certain range

Table 4.1: ***Table 1: Design specifications.***

Target Function	Optimization Goal
Cross-polar	−20 dB
Sidelobes	−30 dB
S_{11}	−25 dB
Beam waist	∼2.0 mm

Table 4.2: ***Table 2: Profile parameters than define the wall shape for each horn design.***

	Diagonal-Spline		Conical-Spline	
Parameter	a_z(mm)	a_r(mm)	a_z(mm)	a_r(mm)
p_1	2.5	0.73	3.9	1.88
p_2	5.5	1.55	6.5	2.18
p_3	8.1	2.35	10.4	2.25
p_4	10.1	2.54	13.5	2.45
p_5	12.4	2.56	16.3	2.63
p_6	14.8	2.61	17.7	2.75
p_7	19.5	2.93	21.5	3.19
p_8	23.3	3.51	25.7	3.41
p_9	27.5	4.25	30.3	4.17

until the optimizer finds the set of points that better match the design specifications. This process was done for three key analysis frequencies, 211, 243 and 275 GHz (lowest, middle and highest frequencies of the ALMA Band 6, respectively). The final set of parameters for each horn that better match the design specifications are listed in table 4.2. The aperture and length of each horn are defined by the coordinates of the node p_9. We can see that both designs have a similar dimension for their aperture, but the conical-spline is 2.8 mm (or 9.24%) longer. Considering that the current corrugated horn of Band-6 receiver has a length of 50.0 mm [50], the designs presented here are around 40% shorter. This is a big advantage taking into account the space restrictions presented in mostly all astronomical receivers.

4.3 Performance Evaluation of Designs

4.3.1 Analysis of Far Field Beam Pattern Simulations

Figure 4.3 shows the simulated far field radiation pattern of the diagonal and conical spline horns at their three key analysis frequencies. Both horns show very good symmetry, above −20 dB, for the E, D and H planes. This means that both horns will produce a beam with good circular shape or, equivalently, they present low beam ellipticity. The cross-polar levels for both designs are lower than −20 dB over the entire bandwidth. However, the conical-spline design shows a better performance at all frequencies, reaching levels close to −30 dB. This better cross-polar performance, correlates with lower levels of sidelobes in D plane. For the diagonal-spline geometry, the sidelobe level is below −40 dB in the E and H-plane. The D plane shows higher levels of sidelobes with values above −30 dB for 211 and 243 GHz,

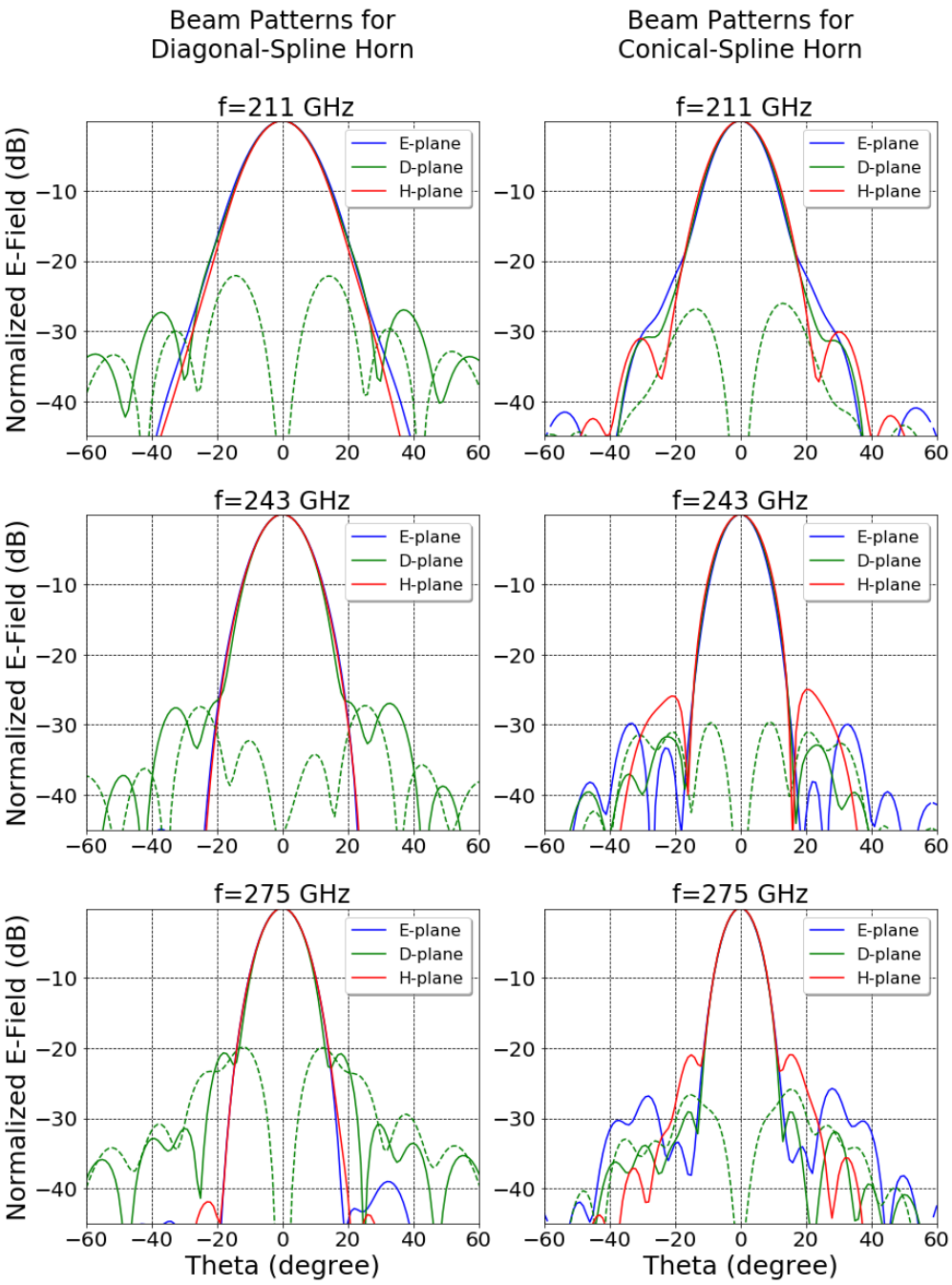

Figure 4.3: ***Simulated radiation beam pattern***

Comparison of far field radiation pattern for diagonal-spline (left column) and conical-spline horns at their key analysis frequencies. Co-polar curves are shown in solid line, and cross-polar curves for D plane are shown in dashed line. Diagonal-spline horn has lower level of sidelobes in E and H planes and a wider beam width. On the other hand, conical-spline horn exhibits lower sidelobes in D-plane, which correlates with lower levels of cross-polar for all the frequencies.

and a level slightly below -20 dB for 275 GHz. For the conical-spline geometry, on the other hand, the sidelobe level is around -30 dB in the E, D and H plane for 211 and 243 GHz. A difference is observed at 275 GHz, where the sidelobe level is slightly below -20 dB in the H-plane. This difference in sidelobe level at different cardinal planes results in the

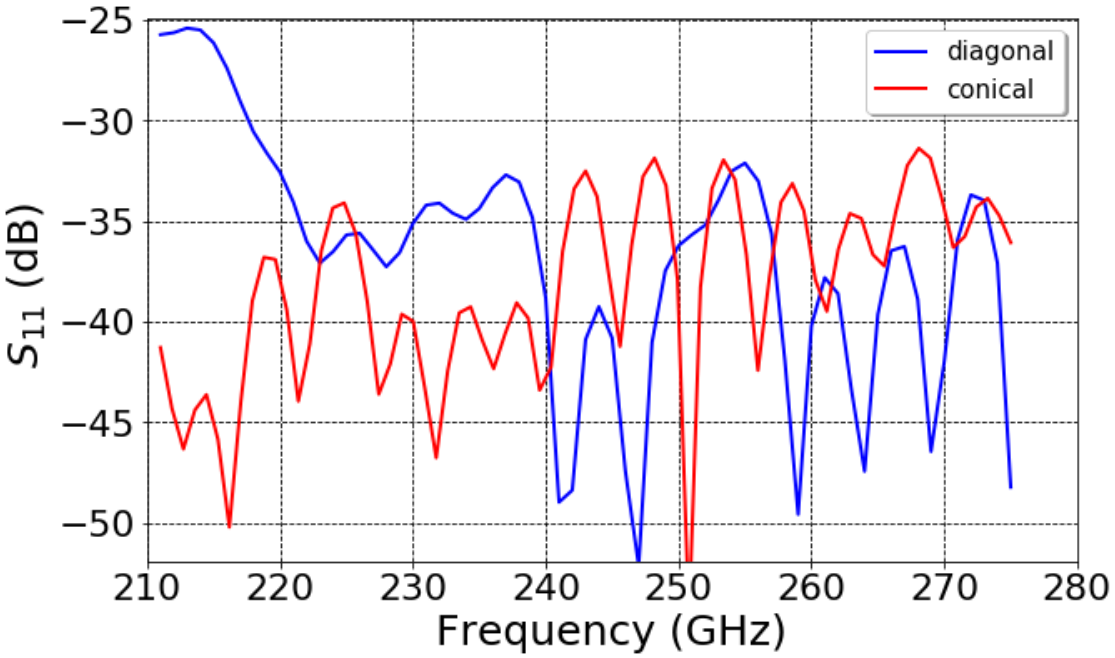

Figure 4.4: ***Simulated return loss***

Simulations of return loss for diagonal-spline (blue) and conical-spline (red) horns. Both designs show levels below −25 dB for the entire frequency range.

diagonal-spline design having a more symmetrical beam shape, but at expenses of having higher levels of cross-polar component.

One additional issue to sort out at the moment of designing these antennas was the relatively wide bandwidth that must be covered. These horns have a fractional bandwidth of 26.3%. A natural degradation can be seen as we move away from the central design frequency (243 GHz). Return losses (figure 4.4) shows a degradation only for the diagonal-spline design. However, this is below −25 dB, making the performance of return loss sufficiently good. From the simulated far field radiation patterns we have calculated the beam waist (w_o), far field divergence angle (θ_o), phase center location (PCL), gain and gaussicity [40]. The results are presented in tables 4.3 and 4.4. The beam waist for the diagonal design is close to 2.0 mm at 211 and 243 GHz, but it shows a small deviation of 0.1 mm from the desired value at 275 GHz. In comparison, the beam waist of conical design shows a larger deviation from the optimization goal. These difference in the beam waist correlates with the differences observed in the far field divergence angle between designs. The calculated PCL (whose values indicate a position inside the horn, taking as reference plane the horn aperture) has a similar value at 211 GHz for both designs, but a significant difference is observed as the frequency increases. The impact of all these differences will be evaluated in next section where, as an example, the horns are coupled to the cold optical system of ALMA Band-6 receiver. The calculated gain is within a range of $21-27$ dB, which is expected for traditional diagonal and conical horn. The values of gaussicity were obtained by calculating the coupling integral, as described in [95], between the far field radiation patterns and their respective Gaussian fit curves. These values are close to 97% at the three key analysis frequency, which make these horns comparable with high performance corrugated horns, whose gaussicity is in the order of 98% [110].

Table 4.3: ***Calculated parameters of the diagonal-spline horn.***

Frequency (GHz)	w_o (mm)	θ_o (°)	PCL (mm)	Gain (dB)	Gaussicity %
211	2.00	12.9	4.34	21.6	97.0
243	2.02	11.1	3.23	23.5	97.2
275	2.10	9.4	0.61	25.0	96.9

Table 4.4: ***Calculated parameters of the conical-spline horn.***

Frequency (GHz)	w_o (mm)	θ_o (°)	PCL (mm)	Gain (dB)	Gaussicity %
211	2.28	11.3	4.51	23.4	97.2
243	2.39	9.4	2.69	25.1	97.0
275	2.63	7.5	2.33	26.5	96.9

4.3.2 Example of Application: Integration into ALMA Band-6 Receiver

Although the horns presented here can be used as feed antennas in any astronomical system working around 243 GHz, as specific example, we have studied their integration with the cold optics of current ALMA Band 6 for illuminating a secondary reflector with the same ALMA Cassegrain configuration. Quasi-optical calculations using the ABCD matrix formalism [41] have been performed to estimate the antenna efficiency when the designed diagonal- or conical-spline horn is coupled to the cold optical system. Figure 4.5 shows the optical train description of the system under study and details of the system of elliptical mirrors used to match the horn beam into the secondary reflector [49]. The distance between the horn aperture and mirror 1 is represented as d_1, whereas d_2 represents the distance between mirrors 1 and 2. The focal points of elliptical mirrors (labeled as P_1, P_2, P_3, and P_4) have been chosen for optimal matching. The distance between the center of an elliptical mirror and one of its focal points P_i is denoted by R_i. Table 4.5 gives the optical train parameters that described the cold optical system of existing ALMA Band-6 receiver [50].

Optimal illumination, i.e., maximum antenna efficiency, is achieved when the edge taper takes a value of around 12.02 dB, given the ALMA Cassegrain configuration [111]. The edge taper has been calculated, according to [40], as

$$T_e = 8.686 \left(\frac{r_s}{w_z} \right)^2,$$

where r_s corresponds to ALMA secondary reflector ($r_s = 375$ mm) and w_z is the beam radius at the secondary reflector position. The ALMA Band-6 corrugated horn was designed to have an edge taper of 12.02 dB over the entire frequency range [50]. This can be achieved if the beam waist and phase center location have constant values for all the frequencies. Figure 4.6 shows the calculated edge taper as a function of frequency for the conical-spline, diagonal-spline and corrugated horns. The edge taper have values ranging between $8.38 - 9.66$ dB

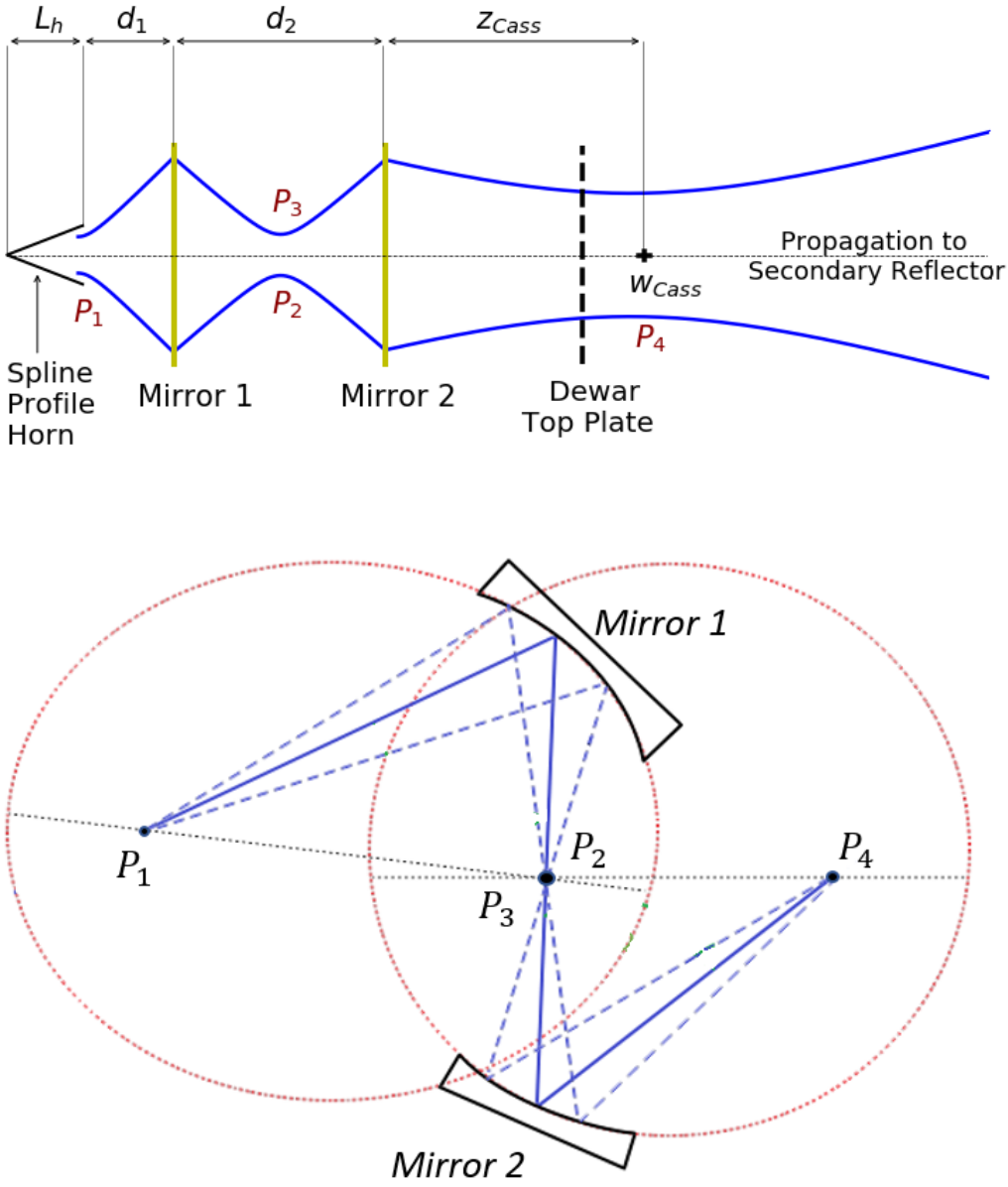

Figure 4.5: ***Optical train description of the ALMA cold optics***

(Top) Optical system of ALMA Band 6, which consists of two elliptical mirrors (represented by yellow lines), and a feed horn antenna. The final beam waist and its position respect to mirror 2 are given by w_{cass} and z_{cass} respectively. (Bottom) Mirror layout of ALMA Band-6 cold optical system. The points P_1 and P_2 represent the position of focal points for mirror 1; P_3 and P_4 have the same relation with mirror 2. The chief ray is shown by solid blue line.

for conical-spline and $11.59 - 13.21$ dB for diagonal-spline. These differences respect to corrugated horn are explained mainly by the shift in the beam waist and the PCL values (tables 4.3 and 4.4). From figure 4.6 we can see that diagonal-spline horn provides a value closer to the desire 12.02 dB. The illumination efficiency loss due to this edge taper variation has been estimated to be lower than 1%, according to [40]. This is sufficiently good for testing a receiver band aimed to fully cover the ALMA Band-6 frequency range.

Table 4.5: ***Optical train parameters for existing Band-6 receivers.***

Optical-train parameter	Value (mm)
L_h	50.00
d_1	60.85
R_1	65.27
R_2	72.91
d_2	140.0
R_3	73.42
R_4	275.39

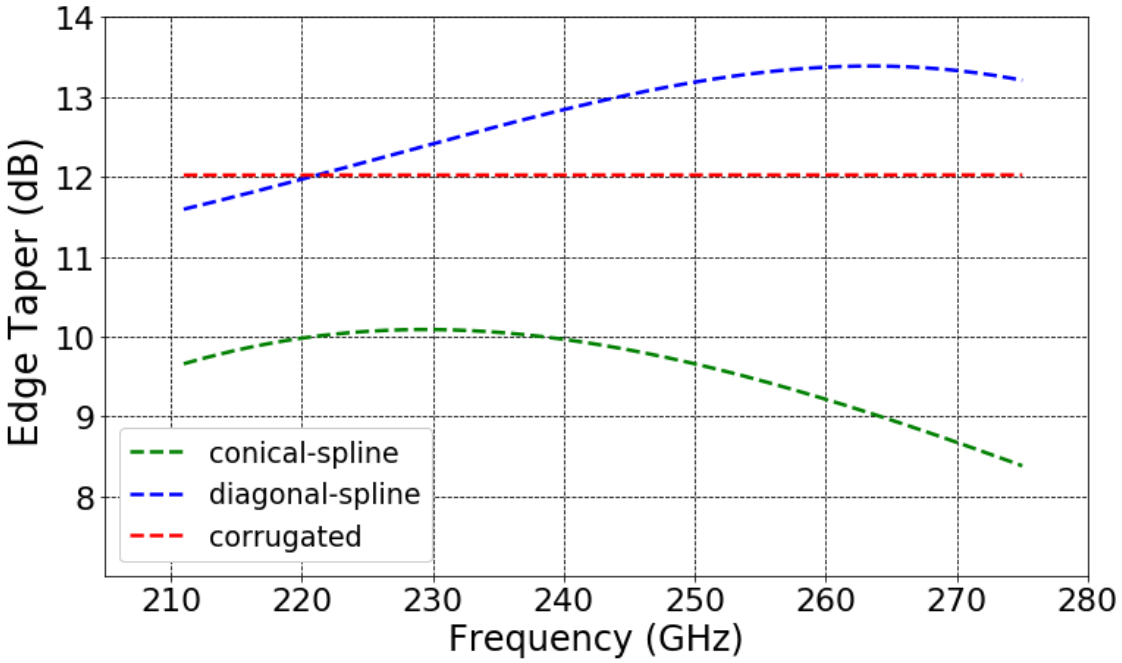

Figure 4.6: ***Edge taper versus frequency***
The plot shows the edge taper as function of frequency when the Band-6 optical system is fed by different horn antennas.

Based on our far field radiation pattern simulations, it is possible to conclude that both horns have similar performance. However, based on our quasi-optical calculation, it can be seen that coupling of the diagonal-spline horn with the cold optical system of Band 6 gives a higher illumination efficiency. With this point in mind, we selected the diagonal design for fabrication and characterization. Furthermore, this design is easier to be fabricated in our workshop and does not require a complicated transition for connection with a rectangular waveguide. In closing this section, it has to be remarked that the conical-spline horn design could be re-optimized to have better illumination efficiency. This could be achieve by including the PCL as an optimization goal in our HFSS model. Another option is to re-design the pair of elliptical mirrors to compensate the PCL shift. However, doing so is out of the scope of this work.

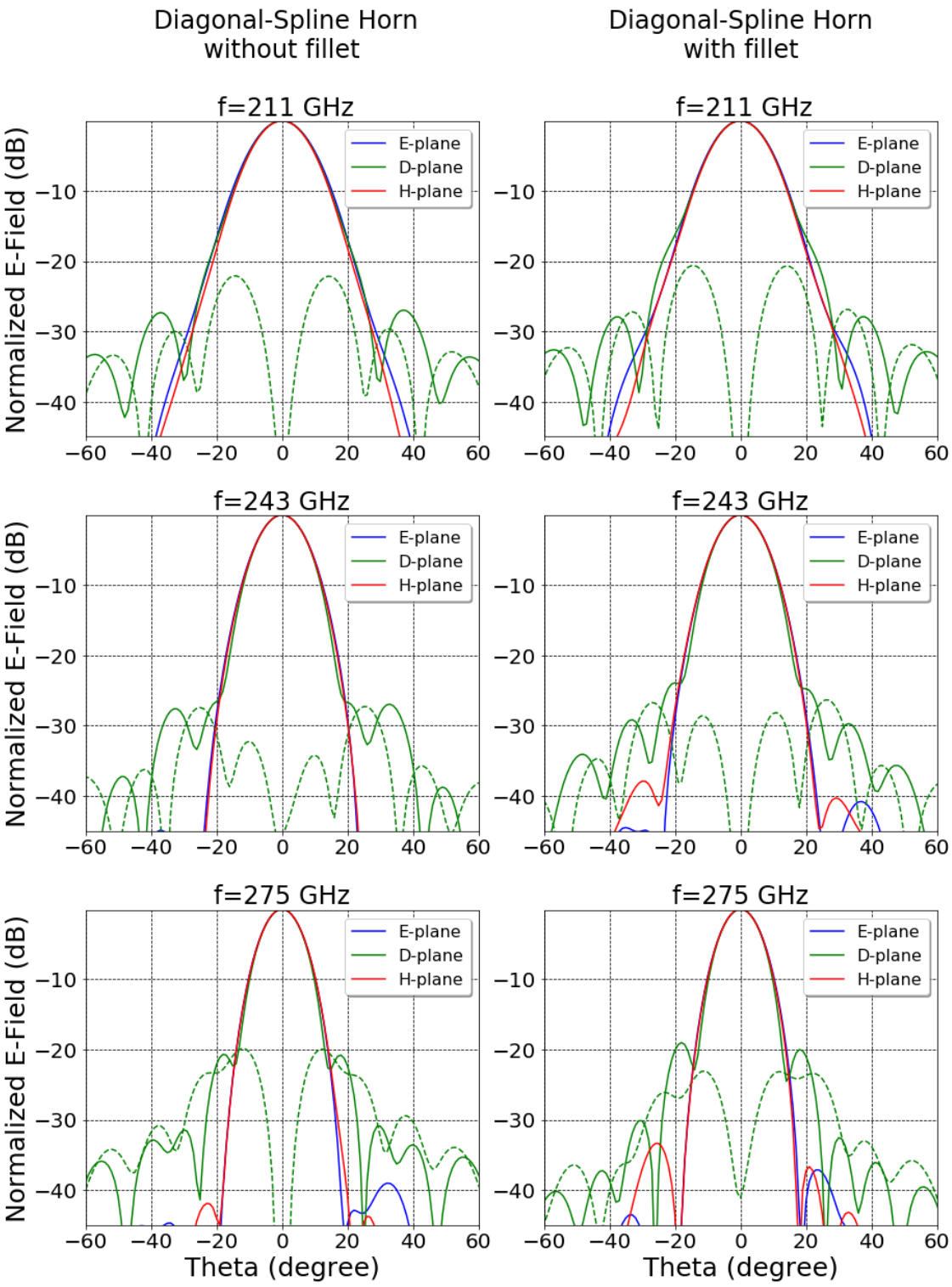

Figure 4.7: ***Simulated far field radiation pattern***

Simulations for the diagonal-spline horn with and without fillet. When the fillet is included the main difference is on cross-polar (dashed line), which suffers a small degradation at 211 GHz and 243 GHz but improves at 275 GHz.

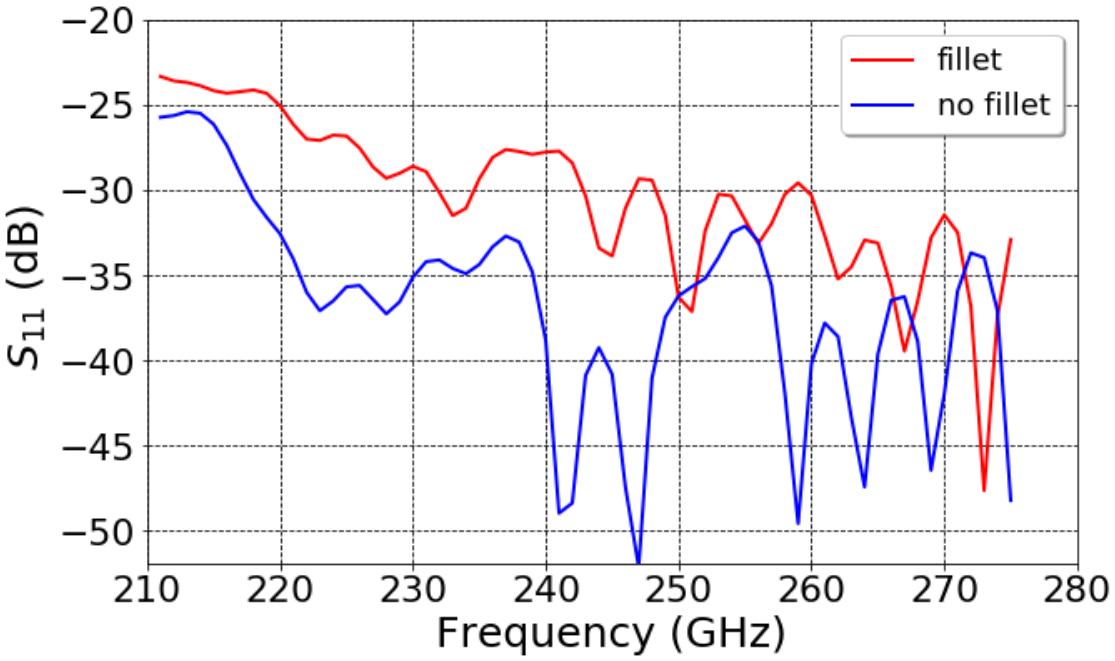

Figure 4.8: ***Return loss comparison.***
Small differences are visible, but performance is till < -23 dB over the entire frequency range.

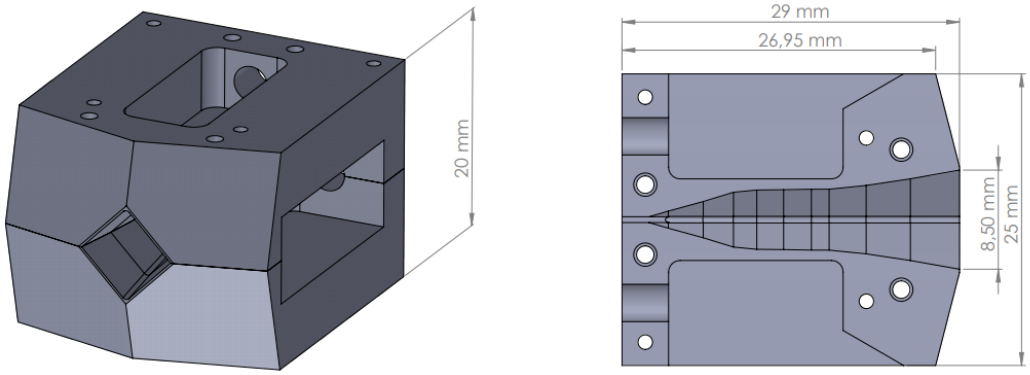

Figure 4.9: ***Final mechanical design of the horn using the split-block technique.***
An anti-reflection chamfer of 30° was implemented to suppress standing waves. The block also includes a transition to the waveguide, which helps to its integration to external circuitry.

4.3.3 Construction

The diagonal-spline horn was constructed using a high-precision computer numerical control (CNC) milling machine in the split block configuration. The use of this technique results in an unavoidable filleting on the intersection line of two walls at the bottom of each block. The radius of the fillet equals that of the used mill, in this case 0.3 mm. This fillet could be avoided if the broaching technique or 5-axis machining with a square end-mill were used to manufacture the horn. However, due to mechanical restrictions in our workshop, this technique was not implemented but, to evaluate the impact of this fillet, new simulations were carried out. Figures 4.7 and 4.8 show the latter simulations in comparison with the original ones. The main impact on the beam pattern lies on the D-plane at 211 GHz and

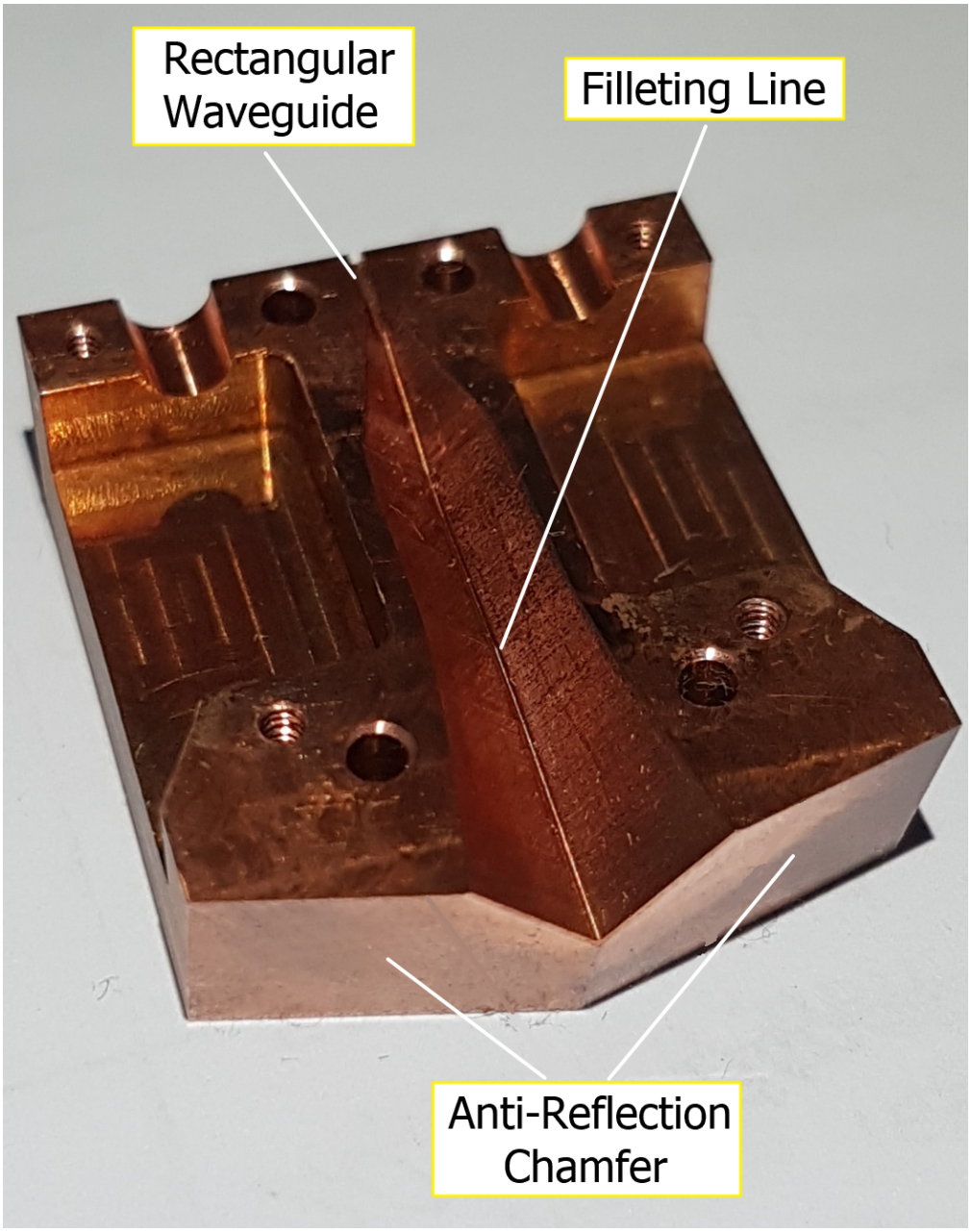

Figure 4.10: ***One of the blocks of the constructed horn.***
Construction took place at the Millimeter Wave Lab from Universidad de Chile.

275 GHz. At 211 GHz, the cross-polar gets a small degradation, but it is still under −20 dB, and the co-polar component only starts making a visible difference at a level of −17 dB. At 275 GHz the cross-polar component is reduced in around 3 dB, which represents significant improvement. The return loss shows the same tendency, i.e., it degrades at low frequencies, but even at its highest point, the value remains below −23 dB. We, therefore, concluded that the necessary modifications that make the design feasible for machining, do not introduce disruptive changes in the overall horn performance.

The mechanical design of the block is shown in figure 4.10, whilst the constructed horn is shown in figure 4.10. It uses flange based on specification UG-387 with tighter tolerances.

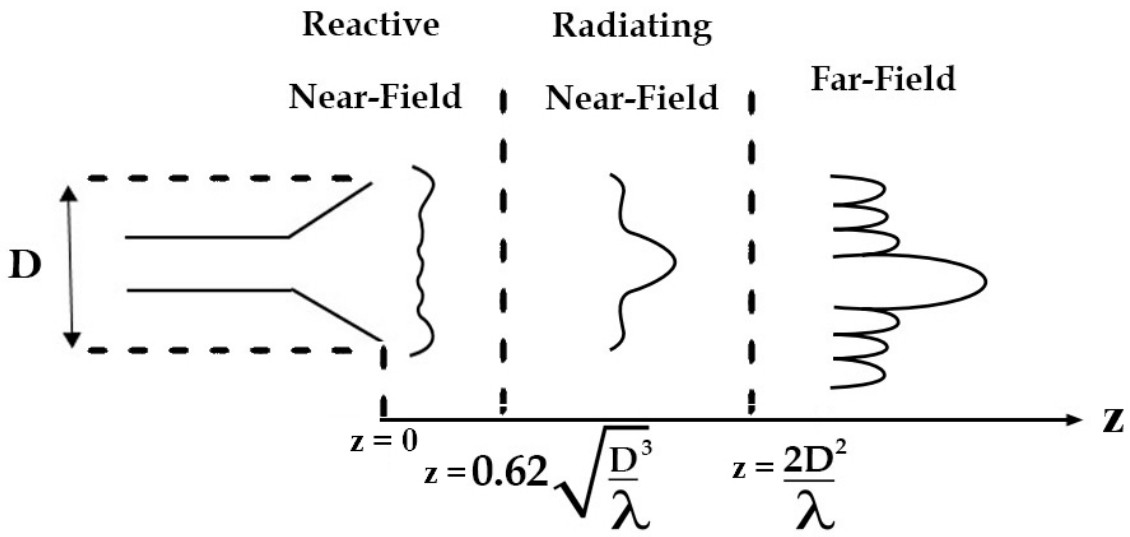

Figure 4.11: ***The propagation regions of an electromagnetic beam***
The distances where the transition between regions take place are indicated in the plot.

This selection was made to facilitate its integration with commercial RF components. An anti-reflection chamfer of 30° was implemented in the block in order to reflect stationary waves out of the optical axis. Additionally, the block includes a waveguide interface in order to facilitate the integration to external circuitry, making the block a few mm longer.

4.4 Experimental methodology and Results

4.4.1 Theoretical background

The fact that the radiating properties of an electromagnetic beam varies with the distance from the antenna, allows to define three regions, which are represented in figure 4.11. The far-field region has a special interest in radio astronomy applications since the signal are received/sent from/to very long distances. The kind of techniques used for characterizing the far-field radiation pattern can be classified into two general categories: direct and indirect [112]. Direct measurements in the far-field region become too demanding when the dimensions of the aperture get significantly large. This increased difficulty level may even lead to an erroneous characterization of the far-field radiation pattern of the antenna-under-test (AUT).

Indirect techniques, also known as near-field measurement techniques, represent a useful tool to obtain a full characterization of the far-field radiation pattern of the AUT. The principle of measuring an electromagnetic beam in its near-field region, and with this, obtaining the far-field region, is based on the relation that both regions compound a Fourier transform pair. Near field measurement techniques are widely used in antennas whose far-field distance becomes too long from the plane where electromagnetic waves are generated. In addition, they provide a fast and accurate method that allows us to obtain a full characterization of the radiation pattern of an antenna. Since the relative short area that must be employed to

obtain a good sample of the field, they can be undergone in small experimental setups. Thus, reducing the operation cost, and lowering the complexity level of the required infrastructure.

Among the many available methods to characterize the constructed diagonal-spline horn antenna, we will use the planar near-field technique [10]. This technique is based on scanning a probe across a plane orthogonal to the axis of propagation of the electromagnetic beam. The recorded information (by a detection setup) of the signal generated by the probe can be used to calculate the complex field coupling coefficient between the probe pattern and the AUT. When this coefficient is known for two orthogonal polarization direction within in the scanned plane, a full characterization of the power density radiated by the AUT can be obtained. A detailed explanation of the implementation of this technique is explained in the following subsection.

A thorough explanation of the electromagnetic formalism behind this measuring technique requires a deep review of plane-wave scattering matrix theory [113], which is beyond of the scope of this chapter. Nevertheless, a simplified version, based on the method described in [114], is presented as follows. An arbitrary electromagnetic field E propagating in free-space can be described as a superposition of planes-waves [14]

$$E(r) = \frac{1}{4\pi^2} \int A(K) \exp^{-\mathrm{i}k.r} \, \mathrm{d}K \tag{4.1}$$

where $K = k_x + k_y$ represents the transverse component of $k = k_x +_y + k_z$ and $A(K)$ is the angular spectrum of planes waves composing the field distribution E(r). Now suppose we only consider a single component of the electric field. Equation 4.1 can then be written as:

$$E(x, y, z) = \frac{1}{4\pi^2} \int_{-\infty}^{+\infty} \int_{-\infty}^{+\infty} A(k_x, k_y) \exp^{-\mathrm{i}k_z z} \exp^{-\mathrm{i}(k_x x + k_y y)} \, \mathrm{d}k_x \mathrm{d}k_y \tag{4.2}$$

The angular spectrum of plane waves in 4.2 only depends on two transverse components of k, since k_z can be expressed in terms of k_x and k_y by $k_z = \sqrt{(k^2 - k_x^2 - k_y^2)}$. $A(k_x, k_y)$ can therefore be obtained by a two-dimensional Fourier Transform of a measurement of $E(x, y)$ at $z = 0$. Equation 4.2 reveals that knowing $A(k_x, k_y)$ is sufficient to obtain a full description of E anywhere. Therefore, measuring the electric field at the aperture ($z = 0$) of the AUT is sufficient to obtain its electric field at the far-field region.

4.4.2 Planar near-field technique

The characterization of the far field radiation pattern can be achieved in two steps, measuring the near-field radiation pattern and, subsequently, using Fourier transformation to obtain the desired far field radiation pattern. To obtain the far field radiation pattern by this method, the amplitude and phase have to be measured in the scanning plane [115]. This can be done by scanning the relative position between RF source and receiver [116]. Additionally, the scanner is returned at the center of the sampling area after measuring each row, then, the amplitude and phase there are measured, and the time is registered. This allows evaluating

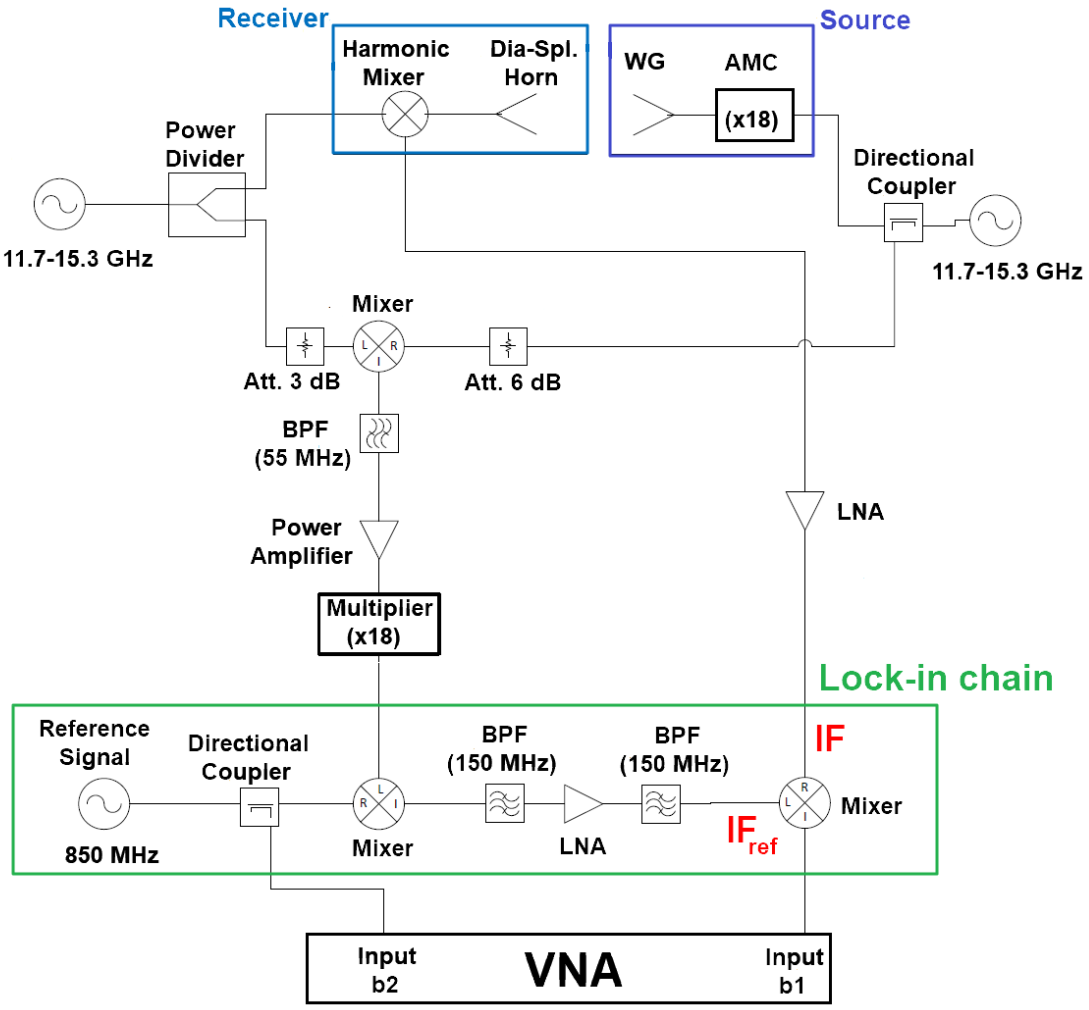

Figure 4.12: ***Schematic of the receiver system used to characterize the horn.*** The receiver is formed by the diagonal-spline horn and a high-harmonic mixer. The RF source is formed by an open-ended waveguide connected to an active multiplication chain.

the amplitude and phase drifts as a function of time. By interpolating the drift data, we can correct the drift in amplitude and phase drift at each measured position.

We have built our own heterodyne receiver system, to operate at room temperature, using the technique described in [117]. The operation principle is as follows, the beam phase can be measured as long as there is a common phase reference between the RF signal and the Local Oscillator (LO) signal. The RF signal is radiated by the system source, whereas the LO signal is used by the receiver to generate an intermediate-frequency (IF) signal. One coupler and one 3 dB splitter are used, respectively, to take samples from the RF and LO signal generator outputs. Then, these samples are mixed and the down-converted output is further multiplied by a factor N, equal to the multiplication factors in the LO and RF chains. This down-converted and multiplied sample signal is then up-converted using a reference signal, which is part of a lock-in chain. We call this signal IF_{ref} to distinguish it from the IF signal of interest generated at high-frequency by the antenna under test. This IF_{ref} and the IF of

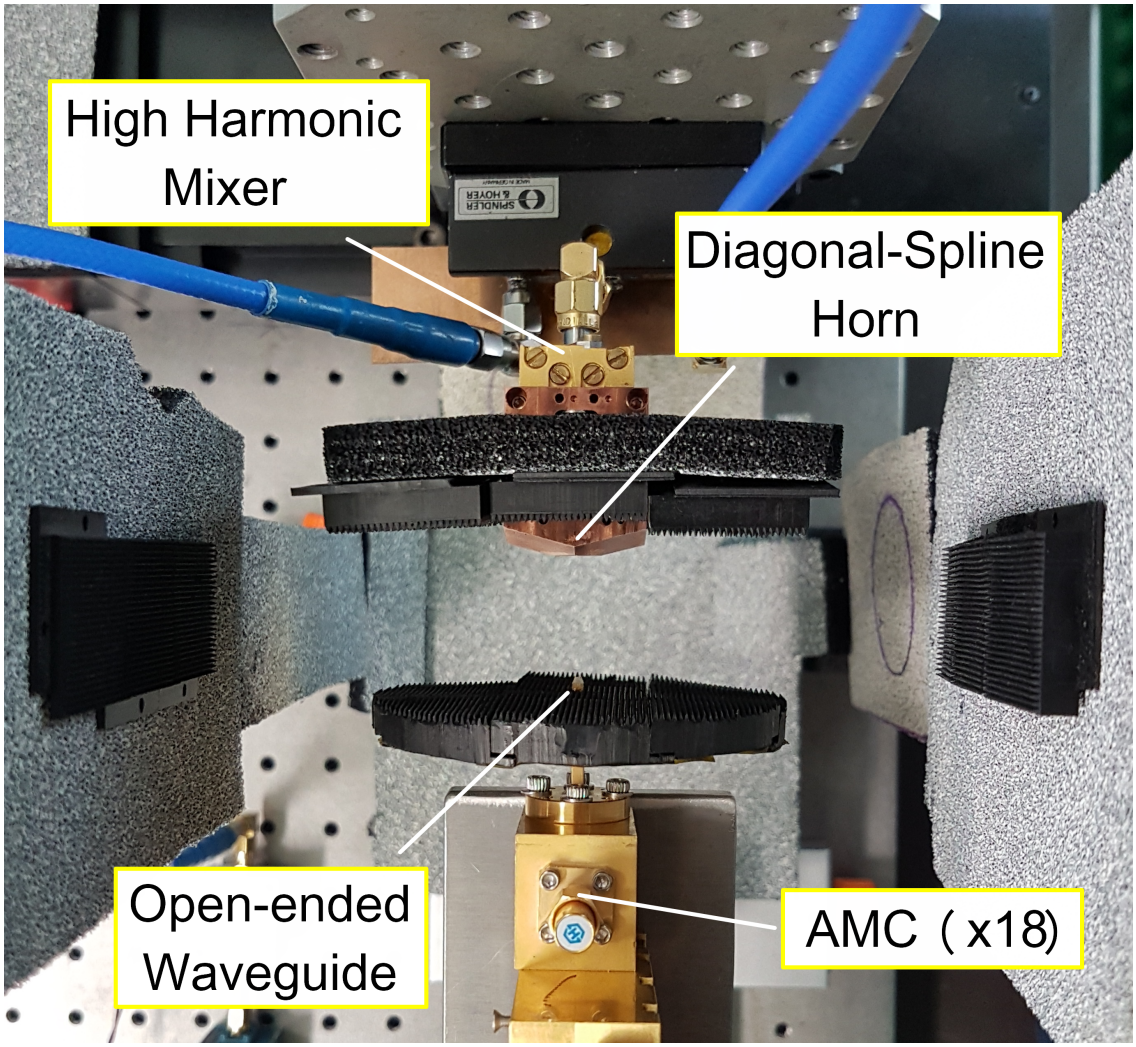

Figure 4.13: ***Experimental set-up to measure near-field radiation pattern***
Details of source-receiver set-up used to measure the near-field radiation pattern. Only the last part of the active multiplication chain connected to the open-ended waveguide is shown in this picture

interest are used in a new down-converting process. The phase of the resulting signal from the lock-in chain will contain information about the beam phase pattern on top of the phase of the reference signal of the lock-in chain. The latter is only used as the phase reference, which can be removed by measuring the ratio between the output signal of the lock-in chain and this unwanted reference. In this way, the phase information related to the LO and RF signal generators is removed from the IF signal. In addition, the phase drift produced by each signal generator is compensated.

4.4.3 Experimental set-up

Figure 4.12 shows the block diagram of the circuitry used to build the receiver system. ALMA Band 6 frequency range can be fully covered using signals generated between 11.7 and 15.3 GHz, in combination with a multiplication chain with a factor $N = 18$ (using one doubler and two triplers). Two signal generators are used to generate the RF and LO signal in this frequency range. The generated signals are divided using one directional coupler

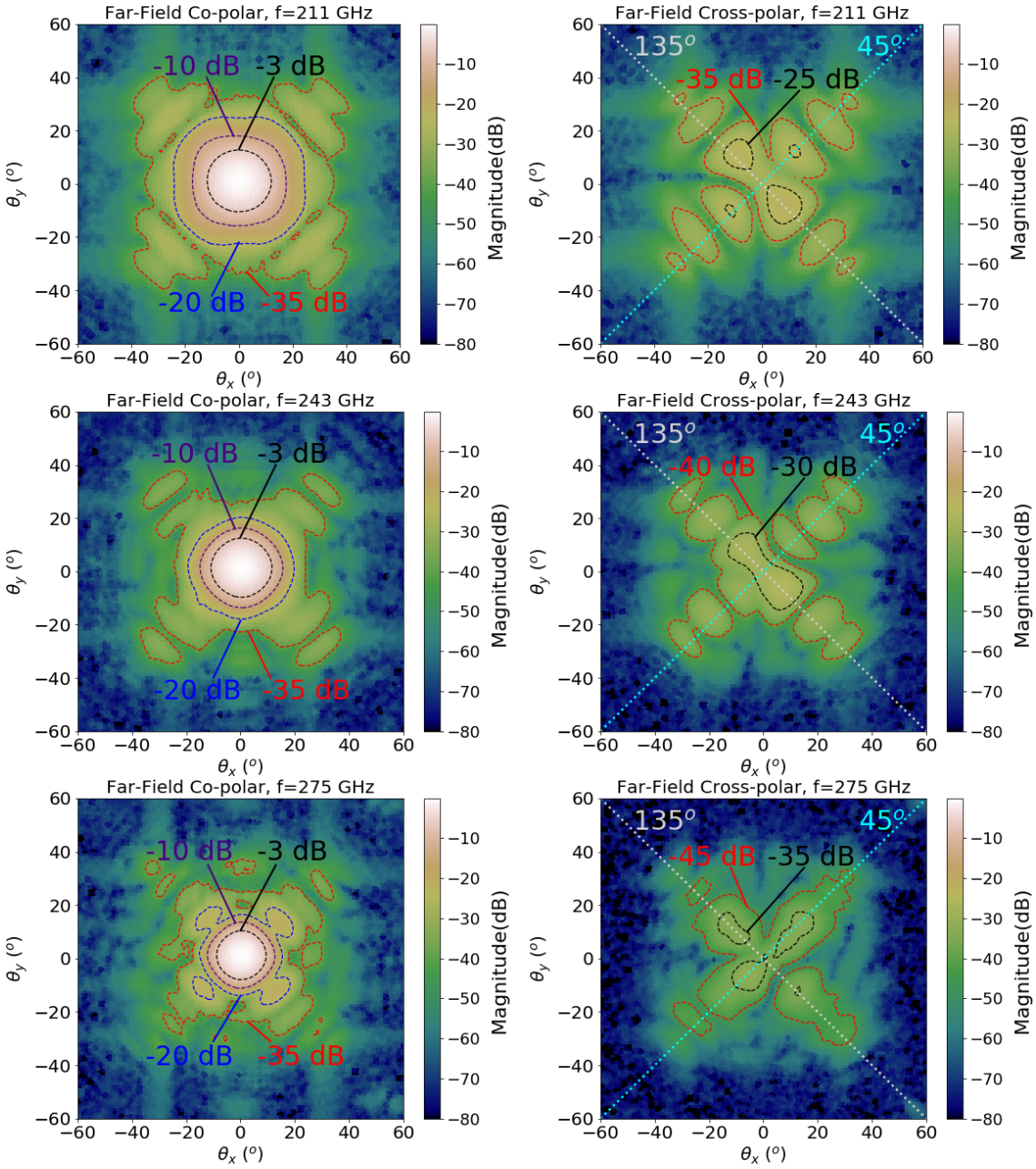

Figure 4.14: ***Experimental results for far field radiation pattern***

Measured co-polar (left column) and cross-polar (right column) patterns at 211 GHz (top), 243 GHz (middle) and 275 GHz (bottom). Contour lines for co-polar measurements show the levels at −3 dB, −10 dB, −20 dB and −35 dB. For cross-polar measurements a range of levels spanning from −25 dB to −45 dB are shown. Additionally, the cross-polar plots show the 45° and 135° planes using cyan and grey color lines, respectively.

and one power divider. The idea is to mix the initial signals to obtain $f_1 - f_2 = \Delta f = 55.56$ MHz. Then, the down-converted signal is multiplied by a factor $N = 18$, obtaining a signal $f_3 = \Delta f \times 18 = 1000$ MHz. Once multiplied, the signal f_3 is mixed with a reference signal of frequency $f_{ref} = 850$ MHz. This provides an IF_{ref} signal of 150 MHz, selected simply because of the available filters. This IF_{ref} undergoes a final mixing process, using as a second input the down-converted signal coming from the receiver system. Since we took a

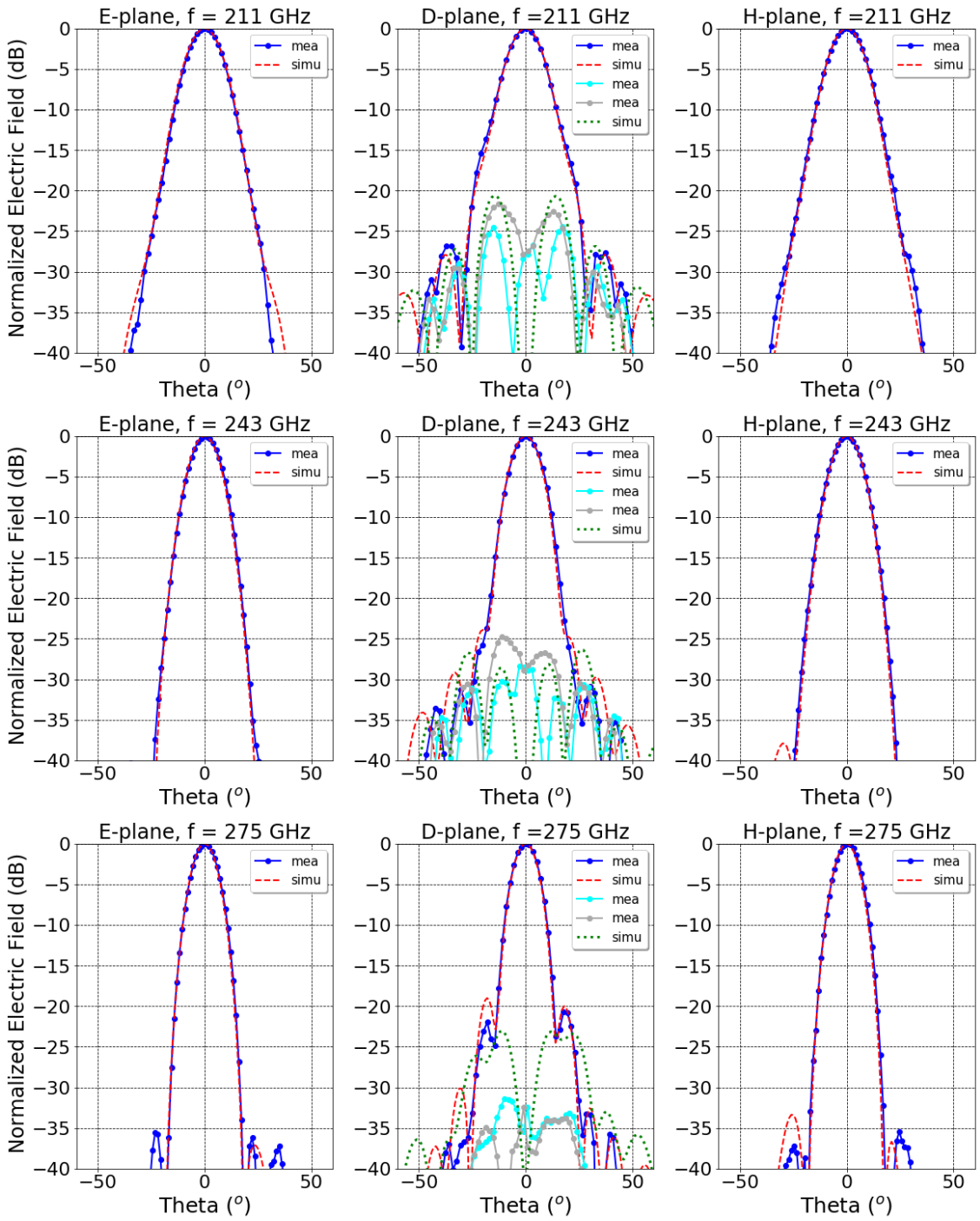

Figure 4.15: ***Comparison between experimental results (dotted lines) and simulations (dashed lines) for far field radiation pattern.***

Co-polar comparison was made taken the cross-section along the E and H planes (left and right column respectively), whereas cross-polar comparison (middle column) was made taken two cross sections at 45°(cyan) and 135°(grey), as shown in figure 4.14, using the same colors to facilitate the visualization.

factor of $N = 18$ for down-converting the RF signal coming from the source, the IF signal provided by the high-harmonic mixer has a frequency equal to f_3. The resulting output is a signal f_{out} whose frequency is equal to f_{ref}. Finally, the phase of the radiation pattern is

obtained using a vector network analyzer to measure the ratio between f_{out} and f_{ref}.

Figure 4.13 shows the near-field measuring set-up. The diagonal-spline horn is directly connected to a high-harmonic mixer, making up the receiver system. An open-ended WR-4.3 waveguide is connected to an active multiplication chain (AMC), with a factor $N = 18$, used as RF source. Microwave absorber has been used to eliminate standing waves. Only the regions around radiating zones have been covered. Based on our experimental results we deem that this is a good alternative to a full implementation of an anechoic chamber. Co-polar measurements were taken by aligning the receiver and source polarizations, and then seeking for the peak power level, whereas for taking cross-polar measurements, the receiver system was rotated in 90° and the minimum power level was sought.

4.4.4 Beam performance analysis

Figure 4.14 shows the far-field experimental results for co- and cross-polar at the key analysis frequencies. The transformation from near to far field was made by implementation of a script in *Python*. The signal-to-noise level is estimated to be around 65 dB. Figure 4.15 shows a comparison of the far field radiation patterns between experimental results and simulation. The plots show an excellent agreement for the co-polar component at all the frequencies in the E, D and H planes. Some small differences are observed only below −30 dB, making them almost negligible. The situation is different for the cross-polar component since more appreciable differences are visible. We have taken two profiles for cross-polar plots at 45° and 135° (green dotted lines at D-plane plots). Those profiles show unbalanced levels. The main explanation for this effect is the asymmetry between the two blocks of the horn. However, the cross-polar levels are, in most cases, lower than the theoretical prediction. Only at 243 GHz the cross-polar is higher than simulated, but the peak value is still below −25 dB, which is certainly a very good result. Additionally, this horn presents sidelobe levels below −40 dB for the E and H planes, and levels below −20 dB for the D plane.

4.5 Conclusions

We have designed two smooth-walled spline-profile horns, conical and diagonal. Simulations demonstrate that they have similar performance but we fabricated and characterized the latter since it adapts better to the design specifications. The measured radiation patterns have shown an excellent agreement with simulations. This horn has very good performance with a gaussicity exceeding 96% and a cross-polar level lower than −20 dB over the entire frequency range. Additionally, we have demonstrated that it can be coupled to astronomical systems by selecting current ALMA Band 6 as an example. In this case, it would illuminate the sub-reflector with an efficiency loss lower than 1%. Moreover, these antennas represent a good choice to illuminate the optical system presented in chapter 2, and thus, testing its performance without the necessity of a complex experimental setup.

The horn presented in this work is one of the first applications of the work presented by Gibson [101], and certainly the first at this specific frequency range. However, with the modifications presented here, our horn has a better performance since it can reach cross-polar levels as low as −30 dB for its higher design frequency. Moreover, the beam shape is clearly more circular is our design and has a larger fractional bandwidth of 26.3% (Gibson's design

achieved only 17.5%).

The difficulty level to machining this horn can be classified as medium, i.e., easier than a corrugated, but harder than a classic conical or diagonal. This ease in machining along with reduced tolerance restrictions, allow reducing the cost and production time of this sort of antennas. Additionally, this type of horn shows big integrability to external circuitry since it can be constructed in a block along with a waveguide.

Finally, we believe that an easier construction process, ease in terms of integrability, high Gaussicity and low level of cross-polar, make this horn a good choice for millimeter and submillimeter receivers, especially when implementing focal plane arrays.

Chapter 5

Summary and Conclusions

In this final chapter, we provide a general summary of the work done through this thesis, the overall research outcomes, and the conclusions.

This thesis concerned the design, optimization, and construction of an optical system aiming to combine the Bands 6 and 9 of ALMA, and so, allowing ALMA operates in dual-band observation mode. The key experimental achievement of this thesis work was the design of all the devices that a dual-band receiver demands, i.e., an optical system allow to re-focus the low-frequency beam into its respective receiver, the dichroic filter that splits the beam (coming from the secondary reflector) and insert as little noise as possible, and the feed optics necessary to illuminate the optical system, and so, corroborating the overall optical performance. In addition, a study of the impact on the normal operation mode of ALMA, and the benefits of implementing a dual-band receiver were presented. All these reached goals were introduced in chapter 1 as the objectives of this thesis work.

5.1 General summary

In this section the conclusions given in chapters 2, 3 and 4 are summarized and presented.

5.1.1 Chapter 2

In this chapter, we have studied the feasibility and practical implementation of simultaneous dual-frequency observations with ALMA. To realize this dual-frequency receiver, a low-distortion optical system was designed in order to combine the target bands. After a tolerance analysis, the optical system was endowed with some micrometer screws over two mirrors (both of them located on the top of the optical system). This feature represents the best option to work as an alignment control system and, any eventual misalignment presented in the system could be corrected by using these screws.

Another outcome of this chapter was the identification of the requirements for the full implementation of this optical system. It was stated that some hardware modifications must be taken in order to enable ALMA to receive a cosmic signal from two receivers simulta-

neously. In addition, the impact on normal ALMA performance was studied. It was found that a small fraction of the operational bandwidth for each band will be lost. Moreover, the integration of this optical system into the ALMA cryostat will produce that either one polarization or sideband of Band 6 will be disabled. Despite these setbacks, once mounted into the cryostat this optical system will not interfere with the standard 'single-band' operation mode of ALMA and, more importantly, will pave the path for a true dual-frequency receiver.

5.1.2 Chapter 3

In this chapter, we proposed three configurations (Jerusalem-cross, single-hole, and flower-type) for a dichroic filter aimed to be used in the optical system presented in chapter 2. All of the proposed designs were optimized to operate at an incidence angle of 18^o and, due to manufacturing limitations, they were designed as single-layer structures.

Among all of the proposed configurations, only the flower-type configuration was successfully fabricated. The measured performance of this showed a very good agreement with the simulations for normal and non-normal beam incidence. However, despite achieving the desired performance the fabricated flower-type dichroic is not suitable to be integrated into the optical system because it is not totally flat. This issue could be sorted out by improving the fabrication process. Nevertheless, this can be addressed in a future instrumentation project that gives continuity to this thesis work.

5.1.3 Chapter 4

In this chapter, we have designed two smooth-walled spline-profile horns with a conical and diagonal aperture. Simulations demonstrate that they have similar performance but we fabricated and characterized the one with diagonal aperture since it adapts better to the design specifications. The constructed horn is certainly one of the first of this type operating at this specific frequency range (211-275 GHz). Moreover, the beam shape has proven to be very circular, and the fractional bandwidth is around 26.3%. The measured radiation patterns have shown excellent agreement with simulations. This horn has very good performance with a gaussicity exceeding 96% and a cross-polar level lower than -20 dB over the entire frequency range.

Furthermore, we have demonstrated that it can be used as feed optics of the current ALMA Band 6 receiver. In this case, it would illuminate the sub-reflector with an efficiency loss lower than 1%. This high-coupling feature makes it a good device to test the optical performance of the constructed dual-frequency optical system.

5.2 Future work

Three key components are necessary in order to test the optical performance of the designed dual-frequency system. However, we have only succeeded in the fabrication of two of them, the optical system and the feed horn for Band 6. Regarding the dichroic, despite demonstrating that almost the entire Band 9 frequency range can be transmitted with efficiency over 90%, it cannot be integrated into the optical system since it is not a flat surface. Nevertheless, we deem that this issue can be easily overcome by fabricating a new system using

the single-hole configuration and increasing the accuracy of the CNC machine. This and the usage of a plate with a thickness of $t = 225$ μm will produce a dichroic which can cover as much as 90% of the frequency range of Band 9. We are aware that this is not optimal but it is sufficiently good to run some test measurements of the optical system that will allow illuminating, simultaneously, the two target bands of ALMA.

Considering that we have a suitable dichroic (as mentioned above), our plan to implement the dual-frequency system in ALMA can be divided into two stages. First, a full demonstration of the dual-frequency system performance at OSF facilities, by using the Front-End Test and Measurement System (FETMS). Once we demonstrate that the performance of the system accomplishes the ALMA requirements, full implementation in a few antennas can take place at the ALMA site. This will allow showing the potential benefits of a dual-frequency system in the science drivers (discussed in chapter 1). One of the most important things to notice is that this dual-frequency system was designed for not interfering with the normal ALMA operation, neither at OSF facilities nor at the Chajnator plateau site. In addition, a brief explanation about how the two mentioned stages can be deployed is presented as follows.

5.3 Conclusions

The integration of the here presented optical system on a few antennas will allow ALMA to operates in a true dual-frequency observation mode. If the phase calibration is proven to be successfully transferred from low to high-frequency, then the longest baseline that ALMA can reach will be available for Band 9. Hence, ALMA will observe with its highest resolution ever achieved so far. In addition to this unique capability enabling ALMA to fully deliver on its promise of high angular resolution imaging, a dual-frequency system, once it exists, brings a number of other possibilities.

I would like to conclude this work with my personal insight regarding the development of technologies for radio astronomy and other potential areas of application. On the one hand, in addition to ALMA, there are currently a variety of astronomical instrumentation projects under development that will take advantage of the technological advances made in recent years. Among them, one of the ideas that is widely supported within the THz instrumentation community is the development of multi-pixel receivers at THz frequencies. These multi-pixel system are aimed for both facilities on planet Earth, and future space missions. This line of research is a good way to continue improving radio astronomy, since the sensitivity levels reached by the latest generation of astronomical receivers are already very close to the limits imposed by the quantum barrier. In addition, having facilities with higher observation speeds will be an extra benefit for the astronomical community, since it will allow them to allocate more observation time without the economic burden of building new observation facilities. On the other hand, THz technology will be a field of increasing development in the coming decades, since it is in this part of the electromagnetic spectrum where the information necessary to answer those unsolved questions that the astronomical community has formulated topics like the early epochs of the universe, the formation of stars and galaxies, and the search of planets with atmospheric conditions similar to Earth.

Bibliography

[1] F. Ghigo, "Karl Jansky and the Discovery of Cosmic Radio Waves," *https://www.nrao.edu/whatisra/hist$_j$ansky.shtml*, *may*2008.

[2] H. Ewen and E. M. Purcell, "Observation of a Line in the Galactic Radio Spectrum: Radiation from Galactic Hydrogen at 1,420 Mc./sec," *Nature*, vol. 168, p. 356, Sept. 1951.

[3] D. Norenberg, S. Crewell, U. Lohnert, T. Rose, and A. Martellucci, "A novel microwave radiometer for assessment of atmospheric propagation conditions for 10 and 90 ghz frequency bands," in *2008 Microwave Radiometry and Remote Sensing of the Environment*, pp. 1–4, March 2008.

[4] R. Chandra, H. Zhou, I. Balasingham, and R. M. Narayanan, "On the opportunities and challenges in microwave medical sensing and imaging," *IEEE Transactions on Biomedical Engineering*, vol. 62, pp. 1667–1682, July 2015.

[5] K. Sassen, "Combined microwave and optical remote sensing of clouds: a review," in *Conference Proceedings Second Topical Symposium on Combined Optical-Microwave Earth and Atmosphere Sensing*, pp. 123–125, April 1995.

[6] R. Bustos, M. Rubio, A. Otárola, and N. Nagar, "Parque astronómico de atacama: An ideal site for millimeter, submillimeter, and mid-infrared astronomy," *Publications of the Astronomical Society of the Pacific*, vol. 126, pp. 1126–1132, dec 2014.

[7] J. R. Pardo, J. Cernicharo, and E. Serabyn, "Atmospheric transmission at microwaves (ATM): an improved model for millimeter/submillimeter applications," *IEEE Transactions on Antennas and Propagation*, vol. 49, pp. 1683–1694, Dec 2001.

[8] E. A. Michael and F. E. Besser, "On the possibility of breaking the heterodyne detection quantum noise limit with cross-correlation," *IEEE Access*, vol. 6, pp. 45299–45316, 2018.

[9] A. R. Thompson, J. M. Moran, and J. Swenson, George W., *Interferometry and Synthesis in Radio Astronomy, 3rd Edition*. 2017.

[10] A. M. Barychev, *Superconductor-Insulator-Superconductor THz Mixer Integrated with a Superconducting Flux-Flow Oscillator*. PhD thesis, Delft University of Technology,

2005.

[11] D. M. Pozar, *Microwave engineering; 3rd ed.* Hoboken, NJ: Wiley, 2005.

[12] V. Belitsky, B. Billade, V. Desmaris, D. Dochev, M. Fredrixon, S. Ferm, G. Johnsen, I. Lapkin, D. Meledin, O. Nyström, A. Pavolotsky, H. Rashid, E. Sundin, and M. Strandberg, "Design and performance of alma band 5 receiver cartridge," in *35th International Conference on Infrared, Millimeter, and Terahertz Waves*, pp. 1–2, Sep. 2010.

[13] *Principles of Long Baseline Stellar Interferometry*, Jan 2000.

[14] E. Hecht, *Optics*. Pearson Education, Incorporated, 2017.

[15] D. Defrère, C. Aerts, M. Kishimoto, and P. Léna, "A recent history of science cases for optical interferometry," *Experimental Astronomy*, vol. 46, pp. 389–399, Dec 2018.

[16] A. A. Michelson and F. G. Pease, "Measurement of the Diameter of α Orionis with the Interferometer.," , vol. 53, pp. 249–259, May 1921.

[17] B. F. Burke and F. Graham-Smith, *An Introduction to Radio Astronomy*. Cambridge University Press, 3 ed., 2009.

[18] N. M. McClure-Griffiths, *The Southern Galactic Plane Survey*, vol. 276 of *Astronomical Society of the Pacific Conference Series*, p. 58. 2002.

[19] T. Cornwell and E. B. Fomalont, *Self-Calibration*, vol. 180 of *Astronomical Society of the Pacific Conference Series*, p. 187. 1999.

[20] E. Thiebaut and J.-F. Giovannelli, "Image reconstruction in optical interferometry," *IEEE Signal Processing Magazine*, vol. 27, p. 97–109, Jan 2010.

[21] ALMA Partnership, E. B. Fomalont, C. Vlahakis, S. Corder, A. Remijan, D. Barkats, R. Lucas, T. R. Hunter, C. L. Brogan, Y. Asaki, S. Matsushita, W. R. F. Dent, R. E. Hills, N. Phillips, A. M. S. Richards, P. Cox, R. Amestica, D. Broguiere, W. Cotton, A. S. Hales, R. Hiriart, A. Hirota, J. A. Hodge, C. M. V. Impellizzeri, J. Kern, R. Kneissl, E. Liuzzo, N. Marcelino, R. Marson, A. Mignano, K. Nakanishi, B. Nikolic, J. E. Perez, L. M. Pérez, I. Toledo, R. Aladro, B. Butler, J. Cortes, P. Cortes, V. Dhawan, J. Di Francesco, D. Espada, F. Galarza, D. Garcia-Appadoo, L. Guzman-Ramirez, E. M. Humphreys, T. Jung, S. Kameno, R. A. Laing, S. Leon, J. Mangum, G. Marconi, H. Nagai, L. A. Nyman, M. Radiszcz, J. A. Rodón, T. Sawada, S. Takahashi, R. P. J. Tilanus, T. van Kempen, B. Vila Vilaro, L. C. Watson, T. Wiklind, F. Gueth, K. Tatematsu, A. Wootten, A. Castro-Carrizo, E. Chapillon, G. Dumas, I. de Gregorio-Monsalvo, H. Francke, J. Gallardo, J. Garcia, S. Gonzalez, J. E. Hibbard, T. Hill, T. Kaminski, A. Karim, M. Krips, Y. Kurono, C. Lopez, S. Martin, L. Maud, F. Morales, V. Pietu, K. Plarre, G. Schieven, L. Testi, L. Videla, E. Villard, N. Whyborn, M. A. Zwaan, F. Alves, P. Andreani, A. Avison, M. Barta, F. Bedosti, G. J. Bendo, F. Bertoldi, M. Bethermin, A. Biggs, J. Boissier, J. Brand, S. Burkutean, V. Casasola, J. Conway, L. Cortese, B. Dabrowski, T. A. Davis, M. Diaz Trigo,

F. Fontani, R. Franco-Hernandez, G. Fuller, R. Galvan Madrid, A. Giannetti, A. Ginsburg, S. F. Graves, E. Hatziminaoglou, M. Hogerheijde, P. Jachym, I. Jimenez Serra, M. Karlicky, P. Klaasen, M. Kraus, D. Kunneriath, C. Lagos, S. Longmore, S. Leurini, M. Maercker, B. Magnelli, I. Marti Vidal, M. Massardi, A. Maury, S. Muehle, S. Muller, T. Muxlow, E. O'Gorman, R. Paladino, D. Petry, J. E. Pineda, S. Randall, J. S. Richer, A. Rossetti, A. Rushton, K. Rygl, A. Sanchez Monge, R. Schaaf, P. Schilke, T. Stanke, M. Schmalzl, F. Stoehr, S. Urban, E. van Kampen, W. Vlemmings, K. Wang, W. Wild, Y. Yang, S. Iguchi, T. Hasegawa, M. Saito, J. Inatani, N. Mizuno, S. Asayama, G. Kosugi, K. I. Morita, K. Chiba, S. Kawashima, S. K. Okumura, N. Ohashi, R. Ogasawara, S. Sakamoto, T. Noguchi, Y. D. Huang, S. Y. Liu, F. Kemper, P. M. Koch, M. T. Chen, Y. Chikada, M. Hiramatsu, D. Iono, M. Shimojo, S. Komugi, J. Kim, A. R. Lyo, E. Muller, C. Herrera, R. E. Miura, J. Ueda, J. Chibueze, Y. N. Su, A. Trejo-Cruz, K. S. Wang, H. Kiuchi, N. Ukita, M. Sugimoto, R. Kawabe, M. Hayashi, S. Miyama, P. T. P. Ho, N. Kaifu, M. Ishiguro, A. J. Beasley, S. Bhatnagar, I. Braatz, J. A., D. G. Brisbin, N. Brunetti, C. Carilli, J. H. Crossley, L. D'Addario, J. L. Donovan Meyer, D. T. Emerson, A. S. Evans, P. Fisher, K. Golap, D. M. Griffith, A. E. Hale, D. Halstead, E. J. Hardy, M. C. Hatz, M. Holdaway, R. Indebetouw, P. R. Jewell, A. A. Kepley, D. C. Kim, M. D. Lacy, A. K. Leroy, H. S. Liszt, C. J. Lonsdale, B. Matthews, M. McKinnon, B. S. Mason, G. Moellenbrock, A. Moullet, S. T. Myers, J. Ott, A. B. Peck, J. Pisano, S. J. E. Radford, W. T. Randolph, U. Rao Venkata, M. G. Rawlings, R. Rosen, S. L. Schnee, K. S. Scott, N. K. Sharp, K. Sheth, R. S. Simon, T. Tsutsumi, and S. J. Wood, "The 2014 ALMA Long Baseline Campaign: An Overview," , vol. 808, p. L1, Jul 2015.

[22] A. Wootten and A. R. Thompson, "The atacama large millimeter/submillimeter array," *Proceedings of the IEEE*, vol. 97, pp. 1463–1471, Aug 2009.

[23] M. L. Meeks and A. E. Lilley, "The microwave spectrum of oxygen in the earth's atmosphere," *Journal of Geophysical Research (1896-1977)*, vol. 68, no. 6, pp. 1683–1703, 1963.

[24] D. F. Buscher and M. Longair, *Practical Optical Interferometry: Imaging at Visible and Infrared Wavelengths*. Cambridge Observing Handbooks for Research Astronomers, Cambridge University Press, 2015.

[25] S. Matsushita, Y. Asaki, E. B. Fomalont, K.-I. Morita, D. Barkats, R. E. Hills, R. Kawabe, L. T. Maud, B. Nikolic, R. P. J. Tilanus, C. Vlahakis, and N. D. Whyborn, "ALMA Long Baseline Campaigns: Phase Characteristics of Atmosphere at Long Baselines in the Millimeter and Submillimeter Wavelengths," , vol. 129, p. 035004, Mar 2017.

[26] L. T. Maud, R. P. J. Tilanus, T. A. van Kempen, M. R. Hogerheijde, M. Schmalzl, I. Yoon, Y. Contreras, M. C. Toribio, Y. Asaki, W. R. F. Dent, E. Fomalont, and S. Matsushita, "Phase correction for ALMA. Investigating water vapour radiometer scaling: The long-baseline science verification data case study," , vol. 605, p. A121, Sep 2017.

[27] Y. Asaki, S. Matsushita, E. B. Fomalont, S. A. Corder, L. Åke Nyman, W. R. F.

Dent, N. M. Philips, A. Hirota, S. Takahashi, B. Vila-Vilaro, B. Nikolic, T. R. Hunter, A. Remijan, and C. Vlahakis, "ALMA long baseline phase calibration using phase referencing," in *Ground-based and Airborne Telescopes VI* (H. J. Hall, R. Gilmozzi, and H. K. Marshall, eds.), vol. 9906, pp. 2005 – 2022, International Society for Optics and Photonics, SPIE, 2016.

[28] E. Fomalont, V. Impellizzer, and C. Wilson, "Technical description and implementation of band to band phase transfer," *ALMA Technical Note Number 8*, 2014.

[29] Y. Asaki, M. Saito, R. Kawabe, K. Morita, and T. Sasao, "Phase compensation experiments with the paired antennas method," *Radio Science*, vol. 31, pp. 1615–1625, Nov 1996.

[30] B. Nikolic, R. C. Bolton, S. F. Graves, R. E. Hills, and J. S. Richer, "Phase correction for ALMA with 183 GHz water vapour radiometers," , vol. 552, p. A104, Apr 2013.

[31] S. Wedemeyer-Böhm, H. G. Ludwig, M. Steffen, J. Leenaarts, and B. Freytag, "Inter-network regions of the Sun at millimetre wavelengths," , vol. 471, pp. 977–991, Sep 2007.

[32] M. Loukitcheva and S. White, "The solar chromosphere as seen in high-resolution millimeter observations," *Stepanov, A. V.; Benevolenskaya, E. E.; Kosovichev, A. G.: Multi-Wavelength Investigations of Solar Activity, Proc. IAU Symp. 223, University Press, 643-644 (2004)*, vol. 2004, 06 2004.

[33] S. Wedemeyer, T. Bastian, R. Brajša, H. Hudson, G. Fleishman, M. Loukitcheva, B. Fleck, E. P. Kontar, B. De Pontieu, P. Yagoubov, S. K. Tiwari, R. Soler, J. H. Black, P. Antolin, E. Scullion, S. Gunár, N. Labrosse, H. G. Ludwig, A. O. Benz, S. M. White, P. Hauschildt, J. G. Doyle, V. M. Nakariakov, T. Ayres, P. Heinzel, M. Karlicky, T. Van Doorsselaere, D. Gary, C. E. Alissandrakis, A. Nindos, S. K. Solanki, L. Rouppe van der Voort, M. Shimojo, Y. Kato, T. Zaqarashvili, E. Perez, C. L. Selhorst, and M. Barta, "Solar Science with the Atacama Large Millimeter/Submillimeter Array—A New View of Our Sun," , vol. 200, pp. 1–73, Apr 2016.

[34] R. Blundell, "The Submillimeter Array Antennas and Receivers," *arXiv e-prints*, pp. astro–ph/0508492, Aug 2005.

[35] A. Krabbe, "SOFIA telescope," in *Airborne Telescope Systems* (R. K. Melugin and H.-P. Roeser, eds.), vol. 4014, pp. 276 – 281, International Society for Optics and Photonics, SPIE, 2000.

[36] M. Carter, B. Lazareff, D. Maier, J. Y. Chenu, A. L. Fontana, Y. Bortolotti, C. Boucher, A. Navarrini, S. Blanchet, A. Greve, D. John, C. Kramer, F. Morel, S. Navarro, J. Peñalver, K. F. Schuster, and C. Thum, "The EMIR multi-band mm-wave receiver for the IRAM 30-m telescope," , vol. 538, p. A89, Feb 2012.

[37] "Large Latin American Millimeter Array," *Retrieved from https://www.llamaobservatory.org/en/.*

[38] H. Kobayashi, T. Sasao, N. Kawaguchi, S. Manabe, T. Omodaka, O. Kameya, K. Shibata, T. Miyaji, M. Honma, Y. Tamura, T. Hirota, S. Kuji, K. Horiai, S. Sakai, K.-i. Sato, K. Iwadate, Y. Kanya, H. Ujihara, T. Jike, and T. Kasuga, "Vera: A new vlbi instrument free from the atmosphere," vol. 306, p. 367, 01 2003.

[39] Y. C. Minh, D. G. Roh, S. T. Han, and H. G. Kim, *Construction of the Korean VLBI Network (KVN)*, vol. 306 of *Astronomical Society of the Pacific Conference Series*, p. 373. 2003.

[40] P. F. Goldsmith and IEEE Microwave Theory and Techniques Society, *Quasioptical systems: Gaussian Beam Quasioptical Propagation and Applications*. Wiley-IEEE Press, Piscataway, New Jersey, 1998.

[41] B. E. A. Saleh and M. C. Teich, *Fundamentals of Photonics (Second Edition)*. Wiley-Interscience, 1991.

[42] F. Kaufman and C. Christodoulou, "The effect of temperature variation on the performance of metallic mesh reflector surfaces," in *Digest on Antennas and Propagation Society International Symposium*, pp. 250–253 vol.1, June 1989.

[43] J. Sheen, "Losses of the parallel-plate dielectric resonator," *IET Microwaves, Antennas Propagation*, vol. 2, pp. 221–228, April 2008.

[44] J. Ruze, "Antenna tolerance theory—a review," *Proceedings of the IEEE*, vol. 54, pp. 633–640, April 1966.

[45] J. A. Murphy, A. Egan, and S. Withington, "Truncation in millimeter and submillimeter-wave optical systems," *IEEE Transactions on Antennas and Propagation*, vol. 41, pp. 1408–1413, Oct 1993.

[46] W. Kunysz, "Antenna phase center effects and measurements in gnss ranging applications," in *2010 14th International Symposium on Antenna Technology and Applied Electromagnetics the American Electromagnetics Conference*, pp. 1–4, July 2010.

[47] A. Ludwig, "The definition of cross polarization," *IEEE Transactions on Antennas and Propagation*, vol. 21, pp. 116–119, January 1973.

[48] T. Yoshimura, A. Hori, Y. Yoshida, Y. Arai, H. Kurokawa, T. Namiki, and K. Asama, "Coupling efficiencies in reflective self-organized lightwave network (r-solnet) simulated by the beam propagation method," *IEEE Photonics Technology Letters*, vol. 17, pp. 1653–1655, Aug 2005.

[49] A. Baryshev, M. Carter, W. Jellema, and R. Hesper, "Design and evaluation of ALMA band 9 quasioptical system," in *5th International Conference on Space Optics* (B. Warmbein, ed.), vol. 554 of *ESA Special Publication*, pp. 365–371, Jun 2004.

[50] J. Lamb, A. Baryshev, M. C. Carter, L. R. D'Addario, B. N. Ellison, B. Grammer, W. Lazareff, Y. Sekimoto, and C. Y. Tham, "Alma receiver optics design," *ALMA memo#362*, 2001.

[51] J. A. Murphy, "Distortion of a simple Gaussian beam on reflection from off-axis ellipsoidal mirrors," *International Journal of Infrared and Millimeter Waves*, vol. 8, pp. 1165–1187, Sep 1987.

[52] Z. L. 2016, "Opticstudio,"

[53] R. Ulrich, "Far-infrared properties of metallic mesh and its complementary structure," *Infrared Physics*, vol. 7, no. 1, pp. 37 – 55, 1967.

[54] R. Cahill and E. A. Parker, "Performance of millimetre-wave frequency selective surfaces in large incident angle quasioptical systems," *Electronics Letters*, vol. 28, pp. 788–789, April 1992.

[55] D. Pozar, *Microwave Engineering, 4th Edition*. Wiley, 2011.

[56] A. W. L. A. R. Kerr, J. Effland and J. Mangum, "Towards a second generation sis receiver for alma band 6," tech. rep., 520 Edgemont Rd, Charlottesville, VA 22903, 2015.

[57] Baryshev, A. M., Hesper, R., Mena, F. P., Klapwijk, T. M., van Kempen, T. A., Hogerheijde, M. R., Jackson, B. D., Adema, J., Gerlofsma, G. J., Bekema, M. E., Barkhof, J., de Haan-Stijkel, L. H. R., van den Bemt, M., Koops, A., Keizer, K., Pieters, C., Koops van het Jagt, J., Schaeffer, H. H. A., Zijlstra, T., Kroug, M., Lodewijk, C. F. J., Wielinga, K., Boland, W., de Graauw, M. W. M., van Dishoeck, E. F., Jager, H., and Wild, W., "The alma band 9 receiver - design, construction, characterization, and first light," *A&A*, vol. 577, p. A129, 2015.

[58] D. Farrah, K. Ennico Smith, D. Ardila, C. M. Bradford, M. Dipirro, C. Ferkinhoff, J. Glenn, P. Goldsmith, D. Leisawitz, T. Nikola, N. Rangwala, S. A. Rinehart, J. Staguhn, M. Zemcov, J. Zmuidzinas, J. Bartlett, S. Carey, W. J. Fischer, J. Kamenetzky, J. Kartaltepe, M. Lacy, D. C. Lis, L. Locke, E. Lopez-Rodriguez, M. MacGregor, E. Mills, S. H. Moseley, E. J. Murphy, A. Rhodes, M. Richter, D. Rigopoulou, D. Sanders, R. Sankrit, G. Savini, J.-D. Smith, and S. Stierwalt, "Review: Far-Infrared Instrumentation and Technology Development for the Next Decade," *arXiv e-prints*, p. arXiv:1709.02389, Sep 2017.

[59] P. H. Siegel, "Terahertz technology," *IEEE Transactions on Microwave Theory and Techniques*, vol. 50, pp. 910–928, March 2002.

[60] P. H. Siegel, "Thz instruments for space," *IEEE Transactions on Antennas and Propagation*, vol. 55, pp. 2957–2965, Nov 2007.

[61] W. Wild, "Terahertz heterodyne technology for astronomy and planetary science," in *2007 Joint 32nd International Conference on Infrared and Millimeter Waves and the 15th International Conference on Terahertz Electronics*, pp. 323–325, Sep. 2007.

[62] P. G. Steffes and B. M. Karpowicz, "Microwave remote sensing of planetary atmospheres: From staelin and barrett to the nasa juno mission," in *IGARSS 2008 - 2008 IEEE International Geoscience and Remote Sensing Symposium*, vol. 1, pp. I–130–I–

133, July 2008.

[63] S. S. Dhillon, M. S. Vitiello, E. H. Linfield, A. G. Davies, M. C. Hoffmann, J. Booske, C. Paoloni, M. Gensch, P. Weightman, G. P. Williams, E. Castro-Camus, D. R. S. Cumming, F. Simoens, I. Escorcia-Carranza, J. Grant, S. Lucyszyn, M. Kuwata-Gonokami, K. Konishi, M. Koch, C. A. Schmuttenmaer, T. L. Cocker, R. Huber, A. G. Markelz, Z. D. Taylor, V. P. Wallace, J. A. Zeitler, J. Sibik, T. M. Korter, B. Ellison, S. Rea, P. Goldsmith, K. B. Cooper, R. Appleby, D. Pardo, P. G. Huggard, V. Krozer, H. Shams, M. Fice, C. Renaud, A. Seeds, A. Stöhr, M. Naftaly, N. Ridler, R. Clarke, J. E. Cunningham, and M. B. Johnston, "The 2017 terahertz science and technology roadmap," *Journal of Physics D: Applied Physics*, vol. 50, p. 043001, jan 2017.

[64] N. Hurtado, U. U. Graf, H. Adams, C. E. Honingh, K. Jacobs, P. Pütz, R. Güsten, and J. Stutzki, "Optics and cryogenics for the 1.1 THz multi-pixel heterodyne receiver for APEX," in *Millimeter, Submillimeter, and Far-Infrared Detectors and Instrumentation for Astronomy VII* (W. S. Holland and J. Zmuidzinas, eds.), vol. 9153, pp. 716 – 729, International Society for Optics and Photonics, SPIE, 2014.

[65] D. Farrah, K. E. Smith, D. Ardila, C. M. Bradford, M. Dipirro, C. Ferkinhoff, J. Glenn, P. Goldsmith, D. Leisawitz, T. Nikola, and et al., "Review: far-infrared instrumentation and technological development for the next decade," *Journal of Astronomical Telescopes, Instruments, and Systems*, vol. 5, p. 1, Apr 2019.

[66] M. C. Wiedner, I. Mehdi, A. Baryshev, V. Belitsky, V. Desmaris, A. M. DiGiorgio, J. Gallego, M. Gerin, P. Goldsmith, F. Helmich, W. Jellema, A. Laurens, C. Risacher, A. Cooray, and M. Meixner, "A proposed heterodyne receiver for the origins space telescope," *IEEE Transactions on Terahertz Science and Technology*, vol. 8, no. 6, pp. 558–571, 2018.

[67] M. J. Rioja, R. Dodson, T. Jung, and B. W. Sohn, "The power of simultaneous multifrequency observations for mm-vlbi: Astrometry up to 130 ghz with the kvn," *The Astronomical Journal*, vol. 150, p. 202, Dec 2015.

[68] T. R. Hunter, J. W. Barrett, R. Blundell, R. D. Christensen, R. S. Kimberk, S. P. Leiker, D. P. Marrone, S. N. Paine, D. C. Papa, N. Patel, P. Riddle, M. J. Smith, T. K. Sridharan, C. Y. E. Tong, K. H. Young, and J.-H. Zhao, "Dual frequency 230/690 ghz interferometry at the submillimeter array," 2005.

[69] S. S. Dhillon, M. S. Vitiello, E. H. Linfield, A. G. Davies, M. C. Hoffmann, J. Booske, C. Paoloni, M. Gensch, P. Weightman, G. P. Williams, E. Castro-Camus, D. R. S. Cumming, F. Simoens, I. Escorcia-Carranza, J. Grant, S. Lucyszyn, M. Kuwata-Gonokami, K. Konishi, M. Koch, C. A. Schmuttenmaer, T. L. Cocker, R. Huber, A. G. Markelz, Z. D. Taylor, V. P. Wallace, J. A. Zeitler, J. Sibik, T. M. Korter, B. Ellison, S. Rea, P. Goldsmith, K. B. Cooper, R. Appleby, D. Pardo, P. G. Huggard, V. Krozer, H. Shams, M. Fice, C. Renaud, A. Seeds, A. Stöhr, M. Naftaly, N. Ridler, R. Clarke, J. E. Cunningham, and M. B. Johnston, "The 2017 terahertz science and technology roadmap," *Journal of Physics D: Applied Physics*, vol. 50, p. 043001, jan 2017.

[70] D. M. Mittleman, "Perspective: Terahertz science and technology," *Journal of Applied Physics*, vol. 122, no. 23, p. 230901, 2017.

[71] Chao-Chun Chen, "Transmission of microwave through perforated flat plates of finite thickness," *IEEE Transactions on Microwave Theory and Techniques*, vol. 21, pp. 1–6, Jan 1973.

[72] M. Beruete, M. Sorolla, I. Campillo, and J. S. Dolado, "Increase of the transmission in cut-off metallic hole arrays," *IEEE Microwave and Wireless Components Letters*, vol. 15, pp. 116–118, Feb 2005.

[73] P. A. R. Ade, G. Pisano, C. Tucker, and S. Weaver, *A review of metal mesh filters*, vol. 6275 of *Society of Photo-Optical Instrumentation Engineers (SPIE) Conference Series*, p. 62750U. 2006.

[74] J. W. Archer, "A novel quasi-optical frequency multiplier design for millimeter and submillimeter wavelengths," *IEEE Transactions on Microwave Theory and Techniques*, vol. 32, pp. 421–427, Apr 1984.

[75] A. C. d. Lima and E. A. Parker, "Fabry-perot approach to the design of double layer fss," *IEE Proceedings - Microwaves, Antennas and Propagation*, vol. 143, pp. 157–162, April 1996.

[76] R. Ulrich, "Far-infrared properties of metallic mesh and its complementary structure," *Infrared Physics*, vol. 7, no. 1, pp. 37 – 55, 1967.

[77] N. Marcuvitz, I. of Electrical Engineers, I. of Engineering, Technology, M. I. of Technology, P. P. Limited, M. I. of Technology. Radiation Laboratory, U. S. O. of Scientific Research, and D. N. D. R. Committee, *Waveguide Handbook*. Electromagnetics and Radar Series, McGraw-Hill, 1951.

[78] C. Cunningham, "Resonant grids and their use in the construction of submillimetre filters," *Infrared Physics*, vol. 23, no. 4, pp. 207 – 215, 1983.

[79] J. E. Harvey and R. N. Pfisterer, "Understanding diffraction grating behavior: including conical diffraction and Rayleigh anomalies from transmission gratings," *Optical Engineering*, vol. 58, no. 8, pp. 1 – 21, 2019.

[80] T. Manabe, K. Kikuchi, S. Ochiai, and T. Nishibori, "Dual-polarization jerusalem-cross slot type fss for a submillimeter-wave band," in *2015 International Symposium on Antennas and Propagation (ISAP)*, pp. 1–3, Nov 2015.

[81] R. Collin, I. Antennas, and P. Society, *Field Theory of Guided Waves*. IEEE/OUP series on electromagnetic wave theory, IEEE Press, 1990.

[82] C. Winnewisser, F. T. Lewen, M. Schall, M. Walther, and H. Helm, "Characterization and application of dichroic filters in the 0.1-3-thz region," *IEEE Transactions on Microwave Theory and Techniques*, vol. 48, pp. 744–749, April 2000.

[83] D. H. Kim, W. Mohyuddin, D. S. Woo, H. C. Choi, and K. W. Kim, "Design of a 75–140 ghz high-pass printed circuit board dichroic filter," *Review of Scientific Instruments*, vol. 88, no. 3, p. 034704, 2017.

[84] A. Hessel and A. A. Oliner, "A new theory of wood's anomalies on optical gratings," *Appl. Opt.*, vol. 4, pp. 1275–1297, Oct 1965.

[85] M. Bozzi, *Electromagnetic Modeling of Quasi–Optical Filters and Frequency Multipliers*. PhD thesis, UNIVERSITÀ DEGLI STUDI DI PAVIA, 2000.

[86] A. Dalkiliç, "Analysis and design of conformal frequency selective surface," Master's thesis, MIDDLE EAST TECHNICAL UNIVERSITY, 2014.

[87] A. Corp., "Hfss ansoft, ver. 19.1.0," *Pittsburgh, PA, USA, Tech. Rep.*, 2018.

[88] P. A. R. Ade, C. E. Tucker, G. Pisano, and S. Weaver, "Modelling and measurement of frequency selective surfaces," in *2007 Joint 32nd International Conference on Infrared and Millimeter Waves and the 15th International Conference on Terahertz Electronics*, pp. 771–772, Sep. 2007.

[89] C. Winnewisser, F. Lewen, and H. Helm, "Transmission characteristics of dichroic filters measured by thz time-domain spectroscopy," *Applied Physics A*, vol. 66, pp. 593–598, 1998.

[90] S. P. Singh, A. K. Jha, and M. J. Akhtar, "Design of broadband superstrate fss for terahertz imaging and testing applications," in *2016 IEEE MTT-S International Microwave and RF Conference (IMaRC)*, pp. 1–4, Dec 2016.

[91] D. S. Wang, B. J. Chen, P. Zhao, and C. H. Chan, "High-selectivity frequency selective surfaces at millimeter-wave and terahertz frequencies," in *Global Symposium on Millimeter-Waves (GSMM)*, pp. 1–3, May 2015.

[92] S. P. Morgan, "Effect of surface roughness on eddy current losses at microwave frequencies," *Journal of Applied Physics*, vol. 20, no. 4, pp. 352–362, 1949.

[93] D. A. Naylor, B. G. Gom, M. K. Tahic, and G. R. Davis, "Astronomical spectroscopy using an aliased step-and-integrate Fourier transform spectrometer," in *Millimeter and Submillimeter Detectors for Astronomy II* (J. Zmuidzinas, W. S. Holland, and S. Withington, eds.), vol. 5498, pp. 685 – 694, International Society for Optics and Photonics, SPIE, 2004.

[94] J. Shafii and R. J. Vernon, "Investigation of mode coupling due to ohmic wall losses in overmoded uniform and varying-radius circular waveguides by the method of cross sections," *IEEE Transactions on Microwave Theory and Techniques*, vol. 50, no. 5, pp. 1361–1369, 2002.

[95] J. F. Johansson, "A Comparison of Some Feed Types," vol. 75, pp. 82–89, 1995.

[96] E. Muehldorf, "The phase center of horn antennas," *IEEE Transactions on Antennas*

and Propagation, vol. 18, pp. 753–760, November 1970.

[97] A. Love, "The diagonal horn antenna," *Microwave Journal*, vol. 5, pp. 117–112, 1962.

[98] J. F. Johansson and N. D. Whyborn, "The diagonal horn as a sub-millimeter wave antenna," *IEEE Transactions on Microwave Theory and Techniques*, vol. 40, pp. 795–800, May 1992.

[99] C. Granet, G. L. James, R. Bolton, and G. Moorey, "A smooth-walled spline-profile horn as an alternative to the corrugated horn for wide band millimeter-wave applications," *IEEE Transactions on Antennas and Propagation*, vol. 52, pp. 848–854, March 2004.

[100] G. James, "The feed system," *Special Issue: The Australian Telescope: J. Elect. Electron. Eng.*, vol. 12, no. 2, pp. 137–145, 1992.

[101] H. J. Gibson, B. Thomas, L. Rolo, M. C. Wiedner, A. E. Maestrini, and P. de Maagt, "A novel spline-profile diagonal horn suitable for integration into thz split-block components," *IEEE Transactions on Terahertz Science and Technology*, vol. 7, pp. 657–663, Nov 2017.

[102] G. M. Rebeiz, L. P. B. Katehi, W. Y. Ali-Ahmad, G. V. Eleftheriades, and C. C. Ling, "Integrated horn antennas for millimeter-wave applications," *IEEE Antennas and Propagation Magazine*, vol. 34, pp. 7–16, Feb 1992.

[103] G. Yassin, P. Kittara, A. Jiralucksanawong, S. Wangsuya, J. Leech, and M. Jones, "A High Performance Horn for Large Format Focal Plane Arrays," in *Eighteenth International Symposium on Space Terahertz Technology* (A. Karpov, ed.), p. 199, 2007.

[104] J. Leech, B. K. Tan, G. Yassin, P. Kittara, and S. Wangsuya, "Experimental investigation of a low-cost, high performance focal-plane horn array," *IEEE Transactions on Terahertz Science and Technology*, vol. 2, pp. 61–70, Jan 2012.

[105] V. Vilnrotter, M. Britcliffe, and D. Hoppe, "Focal plane array receiver for deep-space communication," in *2008 IEEE Aerospace Conference*, pp. 1–10. doi:10.1109/AERO.2008.4526309, March 2008.

[106] ALMA Partnership, C. L. Brogan, L. M. Pérez, T. R. Hunter, W. R. F. Dent, A. S. Hales, R. E. Hills, S. Corder, E. B. Fomalont, C. Vlahakis, Y. Asaki, D. Barkats, A. Hirota, J. A. Hodge, C. M. V. Impellizzeri, R. Kneissl, E. Liuzzo, R. Lucas, N. Marcelino, S. Matsushita, K. Nakanishi, N. Phillips, A. M. S. Richards, I. Toledo, R. Aladro, D. Broguiere, J. R. Cortes, P. C. Cortes, D. Espada, F. Galarza, D. Garcia-Appadoo, L. Guzman-Ramirez, E. M. Humphreys, T. Jung, S. Kameno, R. A. Laing, S. Leon, G. Marconi, A. Mignano, B. Nikolic, L.-A. Nyman, M. Radiszcz, A. Remijan, J. A. Rodón, T. Sawada, S. Takahashi, R. P. J. Tilanus, B. Vila Vilaro, L. C. Watson, T. Wiklind, E. Akiyama, E. Chapillon, I. de Gregorio-Monsalvo, J. Di Francesco, F. Gueth, A. Kawamura, C.-F. Lee, Q. Nguyen Luong, J. Mangum, V. Pietu, P. Sanhueza, K. Saigo, S. Takakuwa, C. Ubach, T. van Kempen, A. Wootten, A. Castro-Carrizo, H. Francke, J. Gallardo, J. Garcia, S. Gonzalez, T. Hill, T. Kaminski, Y. Kurono, H.-

Y. Liu, C. Lopez, F. Morales, K. Plarre, G. Schieven, L. Testi, L. Videla, E. Villard, P. Andreani, J. E. Hibbard, and K. Tatematsu, "The 2014 ALMA Long Baseline Campaign: First Results from High Angular Resolution Observations toward the HL Tau Region," *The Astrophysical Journal Letters*, vol. 808, p. L3, July 2015.

[107] Event Horizon Telescope Collaboration, K. Akiyama, A. Alberdi, W. Alef, K. Asada, R. Azulay, A.-K. Baczko, D. Ball, M. Baloković, J. Barrett, and et al., "First M87 Event Horizon Telescope Results. VI. The Shadow and Mass of the Central Black Hole," *The Astrophysical Journal Letters*, vol. 875, p. L6, Apr. 2019.

[108] B. N. Ellison, M. L. Oldfield, D. N. Matheson, B. J. Maddison, C. M. Mann, and A. F. Smith, "Corrugated Feedhorns at Terahertz Frequencies - Preliminary Results," in *Fifth International Symposium on Space Terahertz Technology*, pp. 851–860. Retrieved from https://ui.adsabs.harvard.edu/abs/1994stt..conf..851E, 1994.

[109] C. Granet, G. James, R. Bolton, and G. Moorey, "Smooth-walled spline-profile horn for radio astronomy," *Proc. JINA 2002 International Symposium on Antennas*, vol. 1, pp. 375–378, 2002.

[110] A. Hammar, Y. Karandikar, P. Forsberg, A. Emrich, and J. Stake, "A 340 ghz high gaussicity smooth spline horn antenna for the steamr instrument," in *2014 IEEE Antennas and Propagation Society International Symposium (APSURSI)*, pp. 649–650, July 2014.

[111] FEND-40.02.00-00-011-A-REP, "Alma receiver optics design electromagnetic analysis," 2003.

[112] A. Maheshwari, S. Behera, T. Romila, S. Maiti, and A. Mukherjee, "Near field to far field transformation by asymptotic evaluation of aperture radiation field," pp. 745–749, 07 2014.

[113] D. M. Kerns, *Plane-Wave Scattering-Matrix Theory of Antennas Antenna-Antenna Interactions*, vol. 162. National Bureau of Standards.

[114] W. Jellema, *Optical Design and Performance Verification of Herschel-HIF*. PhD thesis, Groningen, NL, 2015.

[115] A. Yaghjian, "An overview of near-field antenna measurements," *IEEE Transactions on Antennas and Propagation*, vol. 34, pp. 30–45, January 1986.

[116] Y. Fujii, A. Gonzalez, M. Kroug, K. Kaneko, A. Miyachi, T. Yokoshima, K. Kuroiwa, H. Ogawa, K. Makise, Z. Wang, and Y. Uzawa, "The first six alma band 10 receivers," *IEEE Transactions on Terahertz Science and Technology*, vol. 3, pp. 39–49, Jan 2013.

[117] A. Gonzalez, Y. Fujii, T. Kojima, and S. Asayama, "Reconfigurable near-field beam pattern measurement system from 0.03 to 1.6 thz," *IEEE Transactions on Terahertz Science and Technology*, vol. 6, pp. 300–305, March 2016.